

https://dspace.org/

Characterization of direct current discharge based electric microthrusters

Wright, William Patrick

2017

https://hdl.handle.net/10539/25133

Wright, William Patrick (2017) Characterization of direct current discharge based electric microthrusters, University of the Witwatersrand, Johannesburg, https://hdl.handle.net/10539/25133

Downloaded from a DSpace repository. https://dspace.org/

Characterization of direct current discharge based electric microthrusters

William Patrick Wright

A thesis submitted to the Faculty of Science, University of the Witwatersrand, Johannesburg, in fulfilment of the requirements for the degree of Doctor of Philosophy.

School of Physics

University of the Witwatersrand

March 2017

Declaration

I declare that this thesis is my own, unaided work, other than where specifically acknowledged. It is being submitted in fulfilment of the requirements for the degree of Doctor of Philosophy to the University of the Witwatersrand, Johannesburg. It has not been previously submitted for any degree or examination at any other university.

Signed this_____day of_____2017

_____

William Patrick Wright

Abstract

In this work, a novel electrostatic microthruster concept, based on a direct current gaseous discharge, is proposed. The design draws inspiration from the previously developed CorIon system, which utilizes a coupling of the corona ionization mechanism and the acceleration mechanism. The new design is an attempt to develop a space propulsion system for use on microsatellites, such as CubeSats. A proof of concept system is tested to determine if the direct current discharge can be used as a plasma generator for use in electric space propulsion systems. A system representative of the proposed microthruster concept is tested to determine if it operates in a way that will generate thrust, and boundaries on the systems stable operating parameters are ascertained. Lifetime, repeatability and erosion tests are performed on both the proof of concept system, and the microthruster design to determine if the system is an improvement on the CorIon system. A thrust measurement stand is designed and constructed that utilizes a novel magnetic coupling mechanism to measure the thrust produced by a microthruster. The thrust measurement stand is tested with a cold gas thruster to study the thrust stands repeatability characteristics, and if it produces the expected results for such a system. A theoretical model for the thrust measurement stand is developed, so that the output of the thrust stand can be predicted for various loading conditions. Thrust measurements are performed on the microthruster design as different operating parameters are varied. Measurements of the power used by the microthruster design are taken as different operating parameters are varied. Ion current density measurements of the microthruster design are performed as different operating parameters are varied. Ion current density distribution measurements of the microthruster design are performed. Simulations of the microthruster design are developed, using COMSOL Multiphysics, to confirm the hypothesized mechanism of operation of the microthruster design, and to explain the trends observed in experimental data. Two types of simulation are constructed: a base case, where general features in the physical quantities extracted from the simulations are discussed, and simulations where operating parameters are varied, to study the effects these parameters have on the extracted physical quantities. Thrust values are extracted from the simulations and compared with the experimentally measured thrust. Future research to be conducted involving the novel microthruster design is listed.

Acronyms

Here, a list of commonly used acronyms in the text is presented. The meaning of each acronym is given followed by the number of the page of its first use.

MEMS - microelectromechanical systems - 2

VAT - vacuum arc thruster - 3

DC - direct current - 6

AC - alternating current - 6

GIT - gridded ion thruster - 10

PPT - pulsed plasma thruster - 13

FEEP - field emission electric propulsion - 13

IV - current-voltage - 30

BNC - Bayonet Neill-Concelman - 36

USB - universal serial bus - 41

GPIB - general purpose interface bus - 42

PVC - polyvinyl chloride - 42

ICD - ion current density - 43

ICDD - ion current density distribution - 44

PLA - polylactic acid - 48

ABS - acrylonitrile butadiene styrene - 48

RS-232 - recommended standard 232 - 54

SEM - scanning electron microscope - 68

UV - ultraviolet - 94

PIC - particle-in-cell - 103

LISA - laser interferometer space antenna - 178

SPT - stationary plasma thruster - 182

TAL - anode layer thruster - 182

Mathematical Symbols

Here, a list of some of the commonly occurring mathematical symbols used in this text is given, along with their conventional meaning. Specific variations to these meanings are described in the main text.

I_{sp} - specific impulse

F_T - magnitude of thrust produced

$\dot{m}$ - mass flow rate

g - magnitude of acceleration due to gravity

v_{ex} - magnitude of propellant exhaust velocity

p - pressure

A - area

ε_0 - permittivity of free space

ρ - mass density

n_s - number density of species s

m_s - mass of species s

T_s - temperature of species s

κ - Boltzmann's constant

λ_D - Debye Length

e - charge of an electron

α - first Townsend coefficient

γ - secondary electron emission coefficient

V_b - breakdown voltage

ΔE - ionization energy

Acknowledgements

First and foremost, I would like to thank my friends and family for all their love, care and support throughout the duration of this project. Without your encouragement, I would not be where I am now.

To my parents, Avril and Luigi Wright, I would like to thank you for being patient and understanding throughout the last three years. Thank you for continuing to provide me with a roof over my head, and making sure that I was fed and clothed without insisting that I leave the nest. I appreciate that many other parents would question the sanity of their child if they choose to pursue a doctoral degree, and while the question of my sanity is still up for debate, you were more than happy to entertain my choice without hesitation. Finally, I would like to thank you for providing me the opportunity to figure out my next step without any pressure to make an immediate choice. The time off will be needed and very welcome.

To my sister, Helen Wright, even though you only moved out towards the end of the of my doctorate, I would like to thank you for our Wednesday night suppers at your house. They provided me with a space where I could regularly blow off steam and not have to think about physics for a little while. Thank you for offering to proof read my thesis, and for pointing out where I was writing absolute nonsense.

To my girlfriend, Zulian Joubert, you only entered my life in the final months of my doctorate, but during those final months you offered kindness, care, love and support that was enough to fill the entire duration of my doctorate and more. Your encouragement and patience knows no bounds and you were always willing to help at the drop of a hat, no matter what was going on in your own life. Your help with editing during the 11th hour was a life saver and I hope to be able to return the favour when your turn comes, as well as make up for lost dinner dates and concert recitals.

To my office mates, both old and new, I would like to thank you for helping to create a pleasant work environment. Everyone was always happy to have ideas bounced off of them, frustrations vented to them and a favour asked of them. It was never always about

the physics with exchanges on music, soccer and politics regularly filling the office.

To my friends, both old and new, I would like to thank you for helping me to unwind during what has been quite a stressful and difficult experience. While a lot of you have moved on to new chapters in your lives, I will always value how you helped me get through this experience, by providing a laugh, support, a shoulder to cry on, or just an ice cold beer. Hopefully life will take each of you on many new adventures, and with some luck, I may be able to be a part of some of them.

Finally, I would like to thank my supervisor, Dr. Philippe Ferrer, for giving me the opportunity to undertake this research. Your guidance and mentoring was invaluable. Thank you for being patient with me. Without your approach to supervising, I am not sure that I would have made it through the experience of a doctoral degree in one piece.

The financial assistance of the National Research Foundation (NRF) towards this research is hereby acknowledged. Opinions expressed and conclusions arrived at are those of the author, and are not necessarily to be attributed to the NRF.

A conference proceedings publication, two peer reviewed journal articles and two pre-patent applications resulted from the work described in this thesis:

'Characterization of corona ionization based microthrusters' by W. P. Wright and P. Ferrer, Proceedings of the 34th International Electric Propulsion Conference, IEPC-2015-234, Hyogo-Kobe, Japan, 2015. Electric Rocket Propulsion Society.

'Electric micropropulsion systems' by W. P. Wright and P. Ferrer, Progress in Aerospace Sciences, 74:48-61, 2014.

'A magnetic coupling thrust stand for microthrust measurements' by W. P. Wright and P. Ferrer, Measurement Science and Technology, 27:015901, 2016.

'An electrostatic thruster for micropropulsion' by W. P. Wright and P. Ferrer, South Africa, Pat. No. 2014/08858, 1/12/2014.

'A magnetic coupling thrust stand for microthrust measurements' by W. P. Wright and P. Ferrer, South Africa, Pat. No. 2015/07894, 22/10/2015.

Contents

Declaration i

Abstract ii

Acronyms iii

Mathematical Symbols v

Acknowledgements vii

1. Introduction 1

1.1. Small Spacecraft . . . 1

1.1.1. CubeSats . . . 2

1.2. The CorIon Concept . . . 3

1.2.1. Principle of Operation . . . 4

1.2.2. Advantages . . . 4

1.2.3. Disadvantages . . . 5

1.3. Direct Current Discharge Based Microthruster . . . 5

1.4. Chapter Summary . . . 8

2. Literature Review 9

2.1. Miniature Propulsion Systems . . . 9

2.1.1. Propulsion Concepts . . . 10

2.2. Types of Electric Micropropulsion . . . 12

2.2.1. Gridded Ion Thrusters . . . 13

2.2.2. Hall Thrusters . . . 13

2.2.3. Pulsed Plasma Thrusters . . . 14

2.2.4. Colloid Thrusters . . . 14

2.2.5. Field Emission Electric Propulsion . . . 14

2.2.6. Laser Ablation Thrusters . . . 15

2.2.7. Vacuum Arc Thrusters . . . 15

2.3. Introductory Plasma Physics 16
2.3.1. What is a Plasma? 16
2.3.2. Various Plasma Types 16
2.3.3. Fundamental Properties and Characteristics of Plasmas 19
2.4. Physics of Direct Current Glow Discharges 25
2.4.1. Features 25
2.4.2. Light Emission 26
2.4.3. Axial Variation of Parameters 28
2.4.4. The Guiding Effect of Surface Charge 29
2.4.5. Current-Voltage Characteristics 29

3. Experimental: Apparatus and Procedure 35
3.1. Apparatus 35
3.1.1. Vacuum System 35
3.1.2. Mass Flow Measurement Systems 36
3.1.3. Power Supply 40
3.1.4. Experimental Control and Data Acquisition System 40
3.1.5. Thruster Mounting Table 41
3.1.6. Faraday Cup Probe 42
3.1.7. Thrusters 46
3.2. Thrust Measurement Stand 48
3.2.1. Description 49
3.2.2. Principle of Operation 52
3.2.3. Calibration Procedure 52
3.2.4. Theoretical Model 56
3.2.5. Adjusting Sensitivity 59
3.2.6. Thrust Measurement 59
3.2.7. Costing 62
3.3. Procedure 63
3.3.1. Mounting Thrusters to the Thruster Mounting Table 63
3.3.2. Mounting Thrusters to the Thrust Measurement Stand 63
3.3.3. Evacuating the Vacuum Chamber 65
3.3.4. Mass Flow Rate, Voltage and Current Tests 65
3.3.5. Lifetime and Erosion Tests 66
3.3.6. Repeatability 67
3.3.7. Thrust Measurements 68
3.3.8. Ion Current Density Measurements 69

4. Experimental: Results and Discussion **72**
4.1. Mass Flow Rate, Voltage and Current Tests . . . 72
4.1.1. Proof of Concept Straight Discharge Tube . . . 72
4.1.2. 'U-Shaped' Thruster . . . 75
4.2. Lifetime, Erosion and Repeatability Tests . . . 79
4.2.1. Proof of Concept Straight Discharge Tube . . . 80
4.2.2. 'U-Shaped' Thruster . . . 83
4.3. Thrust Measurement . . . 87
4.3.1. Varying Mass Flow Rate . . . 87
4.3.2. Varying Current . . . 90
4.3.3. Varying Voltage . . . 92
4.4. Ion Current Density Measurements . . . 93
4.4.1. Varying Operating Parameters . . . 95
4.4.2. Ion Current Density Distribution . . . 99

5. Simulations: Framework and Development **102**
5.1. COMSOL Multiphysics . . . 102
5.1.1. General Overview . . . 102
5.1.2. The Plasma Module . . . 104
5.1.3. The Computational Fluid Dynamics Module . . . 109
5.1.4. The Heat Transfer Module . . . 110
5.2. Simulation Geometry . . . 112
5.3. Simulation Parameters . . . 113
5.3.1. Base Case . . . 113
5.3.2. Initial and Boundary Conditions . . . 114
5.3.3. Mesh Choice . . . 116
5.3.4. Varying Parameter Simulations . . . 116

6. Simulations: Results and Discussion **118**
6.1. Base Case . . . 118
6.1.1. Electron Number Density . . . 118
6.1.2. Ion Number Density . . . 120
6.1.3. Electric Potential . . . 121
6.1.4. Electron Temperature . . . 122
6.1.5. Ion Flux . . . 122
6.1.6. Neutral Gas Velocity . . . 123
6.1.7. Neutral Gas Temperature . . . 123
6.2. Varying Parameter Simulations . . . 123
6.2.1. Voltage . . . 124

6.2.2. Mass Flow Rate . . . 131
6.3. Thrust Extraction . . . 138
6.3.1. Results . . . 138
6.3.2. General Comments . . . 141
6.4. Estimated Power Lost to Heating . . . 142
6.4.1. Calculation . . . 142

7. Conclusions **146**
7.1. Experimental . . . 146
7.1.1. Proof of Concept . . . 146
7.1.2. 'U-Shaped' Thruster . . . 147
7.1.3. Lifetime . . . 147
7.1.4. Erosion . . . 148
7.1.5. Repeatability . . . 148
7.1.6. Thrust Measurement Stand Development . . . 149
7.1.7. Thrust and Power Measurements . . . 149
7.1.8. Cold Gas Thrust . . . 149
7.1.9. Hot Gas Thrust . . . 150
7.1.10. Ion Current Density Measurements . . . 151
7.1.11. Ion Current Density as Operating Parameters are Varied . . . 151
7.1.12. Ion Current Density Distribution . . . 152
7.2. Simulation . . . 153
7.2.1. Base Case . . . 153
7.2.2. Varying Simulation Parameters . . . 155
7.2.3. Thrust Extraction . . . 157
7.2.4. Power Lost To Heating . . . 158
7.3. Summary and Future Work . . . 158
7.3.1. Summary . . . 159
7.3.2. Future Work . . . 160

References **162**

A. Appendix - Electric Micropropulsion: Latest Developments to Date **185**
A.1. Ion Thrusters . . . 185
A.2. Pulsed Plasma Thrusters . . . 187
A.3. Hall Thrusters . . . 188
A.4. Colloid Thrusters . . . 190
A.5. Field Emission Electric Propulsion . . . 191
A.6. Laser Ablation Thrusters . . . 192
A.7. Vacuum Arc Thrusters . . . 193

B. Appendix - Theoretical Model of Thrust Balance **194**

C. Appendix - Thrust Extraction **198**

List of Figures

1.1. A photograph showing a CubeSat. The CubeSat consists of a single module that was developed at the University of Montana [23] 3
1.2. A schematic diagram demonstrating the principle of operation of the CorIon concept thruster 4
1.3. A schematic diagram demonstrating the principle of operation of the direct current discharge based microthruster. 7

2.1. A schematic diagram of the gridded ion thruster developed at the Pennsylvania State University: a) in 3D and b) as a longitudinal cross-section [47] 13
2.2. A schematic diagram demonstrating the principle of operation of a laser ablation thruster. [54] 15
2.3. A diagram depicting the relationship between the electron temperature and electron number density of a variety of different naturally occurring plasmas [60]. 17
2.4. A diagram depicting the relationship between the electron temperature and electron number density of a variety of different plasmas that can be created in the laboratory [60] 17
2.5. A schematic diagram showing how the properties of a glow discharge vary with distance from the cathode: a) glow intensity; b) potential; c) longitudinal electric field; d) electronic and ionic current densities; e) electronic and ionic number densities and f) space charge [69] 27
2.6. A schematic diagram showing the current-voltage characteristics of a conventional direct current glow discharge. As the discharge current is increased the discharge transitions through a number of modes shown to be: 1) a Townsend dark discharge; 2) a normal glow; 3) an abnormal glow and 4) an arc discharge [70] 30
2.7. Paschen curves for gases commonly used in direct current discharges [71] 32

3.1. A photograph depicting the vacuum chamber used in this work. 36

3.2. A diagrammatic representation of the in-house developed, mass flow rate measurement system 38
3.3. An example calibration curve for the in-house developed, mass flow rate measurement system. 39
3.4. A diagrammatic representation of the thruster mounting table used in the acquisition of experimental data. 42
3.5. An engineering drawing depicting the various constituent components of the Faraday cup probe [79]. 43
3.6. A photograph showing the Faraday cup probe inside the vacuum chamber and mounted to the adjustable probe stand [79]. 44
3.7. A schematic circuit diagram depicting how the various voltage sources and the digital oscilloscope are connected to the Faraday cup probe, adapted from [79]. 45
3.8. A diagrammatic representation of an example, proof of concept, straight discharge tube, tested throughout these experiments 47
3.9. A diagrammatic representation of an example, 'U-shaped' thruster body, tested throughout these experiments 48
3.10. A diagrammatic representation of an example, 'U-shaped' thruster face-plate, tested throughout these experiments 49
3.11. The thrust measurement stand rendered in 3D. The mass balance used to take measurements is positioned underneath the thrust support member. 50
3.12. A schematic diagram of the thrust measurement stand. 51
3.13. The zero drift experienced by the thrust measurement stand over a period of approximately 30 minutes. 54
3.14. Magnetic induction damper stabilization as indicated using the output from the thrust measurement stand. 54
3.15. The raw data obtained from the thrust stand for a single full calibration. The masses corresponding to the peaks from left to right are from largest to smallest and the unknown mass is the final peak. 55
3.16. A sample calibration curve obtained from the thrust measurement stand. 55
3.17. A free body diagram of the thrust measurement stand showing all of the forces considered. 56
3.18. A plot of the angular displacement of the lever arm against the known test masses used in calibration. The torsion spring constant of the fulcrum can be determined from this plot. Errors in the calibration mass are too small to appear on the plot. 58
3.19. A plot showing the effect of magnet position on thrust stand sensitivity. . 60
3.20. A plot of the measured thrust of a simple cold gas thruster as the mass flow rate is varied. 61

3.21. A plot comparing the thrust measurements of the three identical thrust tests to check for repeatability 62
3.22. A photograph depicting an assembled, proof of concept, straight, discharge tube ready to be mounted to the thruster mounting table. 64
3.23. A photograph depicting an assembled, 'U-shaped' thruster ready to be mounted to the thrust measurement stand. Note the hexagonal grain in the plastic, an artefact of the 3D printing process. 64
3.24. A diagram illustrating the 6 probe positions ion current density measurements are taken from. In each case the probe is rotated so that the probe entrance faces the thruster. 71

4.1. A photograph of a proof of concept, straight, discharge tube in operation. 73
4.2. A series of graphs depicting: A) the voltage versus current curves for the proof of concept system at two different mass flow rates, B) the power versus current curves for the proof of concept system at two different mass flow rates and C) the resistance versus current curves for the proof of concept system at two different mass flow rates 74
4.3. A photograph of a 'U-shaped' thruster in operation. 75
4.4. A series of video stills depicting the 'U-shaped', direct current discharge based thruster in the various observed modes of operation: A) the discharge confined to the thruster channel with no visible plumes; B) the thruster exhibiting a stable direct current discharge mode of operation with a plume visible; C) the thruster in a 'corona' discharge mode of operation with a plume visible; D) the thruster exhibiting continued plume formation while arcing is occurring between electrodes and E) the thruster experiencing arcing between electrodes and discharge expansion into the supply pipe. . 77
4.5. Electron microscope images of the inner rims of: A) a control electrode that was not subjected to plasma exposure and B) an electrode that was used to generate and was exposed to the discharge in the proof of concept, straight, discharge tube. 81
4.6. Optical microscope images of the needles used as electrodes in the CorIon system: A) before firing and B) after firing. Note the lack of obstructions in the needle before firing and the discoloration of the needles after firing. 82
4.7. Photographs of the 'U-shaped' thruster that failed while conducting lifetime tests: A) a top down view of the outlets of the thruster; B) a side profile of the thruster, showing the face into which the gas insert is attached and C) a top down view of the thruster having been disassembled so that the damage can be further studied. 85

4.8. Electron microscope images of the inner rims of: A) the electrode connected to the positive terminal of the high voltage power supply; B) the grounded electrode and C) a control electrode. 86
4.9. A graph depicting the cold gas thrust test of the 'U-shaped' thruster design as the mass flow rate is varied. A linear expression is fitted to the data. . 88
4.10. A graph comparing the thrust measurements of the 'U-shaped' thruster before the power supply is activated (cold gas) and after the power supply is activated (hot gas) as the mass flow rate is varied. 89
4.11. A graph showing how the power obtained from measuring the voltage and current at the thruster electrodes varies as the mass flow rate is varied. . 91
4.12. A graph comparing the thrust measurements of the 'U-shaped' thruster before the power supply is activated (cold gas) and after the power supply is activated (hot gas) as the discharge current is varied. 91
4.13. A graph showing how the power obtained from measuring the voltage and current at the thruster electrodes varies as the discharge current is varied. 92
4.14. A graph comparing the thrust measurements of the 'U-shaped' thruster before the power supply is activated (cold gas) and after the power supply is activated (hot gas) as the discharge voltage is varied. 93
4.15. A graph showing how the power obtained from measuring the voltage and current at the thruster electrodes varies as the discharge voltage is varied. 94
4.16. Graphs depicting the common lineshapes observed in the raw data obtained from ion current density measurements: A) the lineshape depicting a single peaked, sawtooth-like curve; B) the lineshape depicting a double-peaked curve and C) the curve depicted in B) magnified, so that the double-peak is clearly seen. 95
4.17. A graph depicting the measured ion current density generated by the 'U-shaped' thruster as the mass flow rate is varied. The ion current densities obtained from both the first and second peaks are shown. 97
4.18. A graph depicting the measured ion current density generated by the 'U-shaped' thruster as the discharge current is varied. The ion current densities obtained from both the first and second peaks are shown. 98
4.19. A graph depicting the measured ion current density generated by the 'U-shaped' thruster as the discharge voltage is varied. The ion current densities obtained from both the first and second peaks are shown. 99
4.20. A graph depicting the ion current density distribution generated by the 'U-shaped' thruster determined from the first peak of the measured ion current signals. 100

4.21. A graph depicting the ion current density distribution generated by the 'U-shaped' thruster determined from the second peak of the measured ion current signals. 101

5.1. A diagrammatic representation of an arbitrary domain divided up into triangular mesh elements [126] 103
5.2. An example geometry used to study the 'U-shaped', direct current discharge based, electric microthruster. The units of the horizontal and vertical axes are meters 113
5.3. An example of the mesh geometry used to study the 'U-shaped', direct current discharge based, electric microthruster. The units of the horizontal and vertical axes are meters 116

6.1. The results of the simulation of the 'U-shaped', direct current discharge based, electric microthruster: A) electron number density (in particles/m^3); B) ion number density (in particles/m^3); C) electric potential (in V); D) electron temperature (in V); E) ion flux; F) neutral gas velocity (in m/s) and G) neutral gas temperature (in K) 119
6.2. The electric potential obtained from the simulation of the 'U-shaped', direct current discharge based, electric microthruster, as the discharge voltage is varied between the values of A) 250 V; B) 300 V; C) 350 V and D) 400 V 124
6.3. The electron number density obtained from the simulation of the 'U-shaped', direct current discharge based, electric microthruster, as the discharge voltage is varied between the values of A) 250 V; B) 300 V; C) 350 V and D) 400 V 125
6.4. The electron temperature obtained from the simulation of the 'U-shaped', direct current discharge based, electric microthruster, as the discharge voltage is varied between the values of A) 250 V; B) 300 V; C) 350 V and D) 400 V 126
6.5. The ion number density obtained from the simulation of the 'U-shaped', direct current discharge based, electric microthruster, as the discharge voltage is varied between the values of A) 250 V; B) 300 V; C) 350 V and D) 400 V 127
6.6. The ion flux obtained from the simulation of the 'U-shaped', direct current discharge based, electric microthruster, as the discharge voltage is varied between the values of A) 250 V; B) 300 V; C) 350 V and D) 400 V . . . 128

6.7. The neutral gas temperature profile obtained from the simulation of the 'U-shaped', direct current discharge based, electric microthruster, as the discharge voltage is varied between the values of A) 250 V; B) 300 V; C) 350 V and D) 400 V 129
6.8. The neutral gas velocity profile obtained from the simulation of the 'U-shaped', direct current discharge based, electric microthruster, as the discharge voltage is varied between the values of A) 250 V; B) 300 V; C) 350 V and D) 400 V 130
6.9. The neutral gas velocity profile obtained from the simulation of the 'U-shaped', direct current discharge based, electric microthruster, as the mass flow rate of the gaseous propellant is varied between the values of A) 0.2 mg/s; B) 0.4 mg/s; C) 0.6 mg/s and D) 0.8 mg/s 131
6.10. The neutral gas temperature profile obtained from the simulation of the 'U-shaped', direct current discharge based, electric microthruster, as the mass flow rate of the gaseous propellant is varied between the values of A) 0.2 mg/s; B) 0.4 mg/s; C) 0.6 mg/s and D) 0.8 mg/s 132
6.11. The electron density profile obtained from the simulation of the 'U-shaped', direct current discharge based, electric microthruster, as the mass flow rate of the gaseous propellant is varied between the values of A) 0.2 mg/s; B) 0.4 mg/s; C) 0.6 mg/s and D) 0.8 mg/s 133
6.12. The electron temperature profile obtained from the simulation of the 'U-shaped', direct current discharge based, electric microthruster, as the mass flow rate of the gaseous propellant is varied between the values of A) 0.2 mg/s; B) 0.4 mg/s; C) 0.6 mg/s and D) 0.8 mg/s 134
6.13. The electric potential profile obtained from the simulation of the 'U-shaped', direct current discharge based, electric microthruster, as the mass flow rate of the gaseous propellant is varied between the values of A) 0.2 mg/s; B) 0.4 mg/s; C) 0.6 mg/s and D) 0.8 mg/s 135
6.14. The ion number density profile obtained from the simulation of the 'U-shaped', direct current discharge based, electric microthruster, as the mass flow rate of the gaseous propellant is varied between the values of A) 0.2 mg/s; B) 0.4 mg/s; C) 0.6 mg/s and D) 0.8 mg/s 136
6.15. The ion flux profile obtained from the simulation of the 'U-shaped', direct current discharge based, electric microthruster, as the mass flow rate of the gaseous propellant is varied between the values of A) 0.2 mg/s; B) 0.4 mg/s; C) 0.6 mg/s and D) 0.8 mg/s 137
6.16. A diagram depicting the entire simulation geometry and all of the labelled boundaries considered in calculating the thrust generated by the simulated thruster. 139

6.17. The cold gas thrust extracted from the simulations as the mass flow rate through the system is varied. A linear curve is fitted to the data. 139
6.18. A comparison between the hot gas thrust and the cold gas thrust extracted from the simulations as the mass flow rate is varied 140
6.19. A comparison between the hot gas thrust and the cold gas thrust extracted from the simulations as the discharge voltage is varied 141
6.20. A plot showing the spatial variation of the electric potential under the conditions used in these calculations. The division of the vacuum region into several smaller regions is shown. 143
6.21. A plot showing the spatial variation of the ion number density under the conditions used in these calculations. The division of the vacuum region into several smaller regions is shown. 144

B.1. A reprint of the free body diagram of the thrust balance showing all of the forces considered. 194

C.1. The simulation domain studied in this work. The highlighted regions represent the boundary of the control volume. 200
C.2. The simulation domain studied in this work. The highlighted regions represent the boundaries over which the pressure is considered 202

List of Tables

3.1. A comparison between the measured calibration masses and the predicted calibration masses obtained from the model of the thrust measurement stand. 59

4.1. A table showing the repeatability results of the proof of concept, straight, discharge tube. 83
4.2. A table showing the repeatability results of the 'U-shaped' thruster. . . . 87
4.3. A table showing a comparison between some performance parameters of competing electric micropropulsion systems. 90

5.1. A list of the reactions occurring in the plasma chemistry of argon as found in [149]. 114
5.2. A list of the surface reactions occurring in the plasma chemistry of argon, as the different particle species interact with the boundaries. 115

1. Introduction

In this chapter, a conceptual overview of the research performed in this work is given. The research is justified by providing context around the limitations placed on small spacecraft subsystems. The conceptual propulsion system to be studied throughout this work is presented, and a summary of the contents of the following chapters is provided.

1.1. Small Spacecraft

Small spacecraft are becoming more viable and attractive space platforms. This is because many now have the capabilities to satisfy the requirements of modern space missions. This is seen in the growing tendency for both military [1] and civilian space agencies [2], [3], [4], [5] to include small spacecraft in their mission proposals. These spacecraft are required to perform complicated and delicate manoeuvres, such as formation flying [6], while being able to maintain fine attitude control [7]. Cost is a primary motivating factor for the shift to utilizing smaller spacecraft. Launch costs are reduced as a smaller spacecraft means a smaller mass that needs to be launched into space. Fewer materials are required for smaller spacecraft construction, and the possible reductions in complexity associated with smaller spacecraft lead to a reduction in manufacturing costs [8]. The reduced cost of satellites and launches allows the private sector greater access to space, with more frequent launches and more flexible missions profiles. There is also the potential for distributed workloads across many smaller spacecraft [9].

Unfortunately, technological challenges accompany the benefits associated with smaller spacecraft. The miniaturization of spacecraft requires the miniaturization of many crucial spacecraft subsystems, such as scientific instruments [10] and power generation and processing systems [11]. Of particular interest in this work is the miniaturization of spacecraft propulsion systems.

Many different propulsion systems have been developed since the inception of space travel [12], [13]. These systems have found use in manned space flight [14], as well as on robotic

space probes used for scientific research [15], [16]. To develop propulsion systems for small spacecraft, scientists and engineers have typically begun by attempting to miniaturize existing technologies. However, many of these systems are physically prohibited from operating at small sizes due to scaling problems [17]. Other research groups have attempted to develop propulsion systems that are already miniaturized. These systems will typically rely on novel chemical and physical mechanisms to generate thrust [18]. In this work, a novel miniature space propulsion concept will be presented and tested.

It is useful to consider what is required of a space micropropulsion system. In order to do so, the term 'small spacecraft' should be defined to provide context. Different classifications of what constitutes a small spacecraft have been proposed [9], [19]. The consensus is that when categorizing small spacecraft, mass is an essential property to be considered. The mass of a small spacecraft should be limited to less than 100 kg. They can be further separated into three categories, according to their masses, as per [9]. These categories are given below:

- Microspacecraft - spacecraft that have masses in the range of 5 kg - 20 kg.
- Nanospacecraft - spacecraft that have masses in the range of 1 kg - 5 kg.
- Picospacecraft - spacecraft that have masses less than 1 kg.

Generally, the above mass restrictions prevent large power conditioning systems from being used and power supplies are limited to 100 W [9]. The physical dimensions of such small spacecraft are also limited. New microfabrication techniques, such as plasma etching and photolithography, were used as early as 1991 to develop Microelectromechanical systems (MEMS), which can operate within the mass and power restrictions of small spacecraft [20].

1.1.1. CubeSats

Of particular relevance to this work, is the CubeSat nanosatellite platform. CubeSats are a new, commercially available nanosatellite platform, whose affordability makes them attractive to both private and academic institutions, as a tool to perform research from orbit. The CubeSat platform consists of individual cubic modules that have a mass of approximately 1 kg and a volume of approximately 1 litre [21]. A CubeSat can consist of either a single module, or of a combination of these cubic modules in a variety of different configurations. Figure 1.1 shows a CubeSat that consists of a single module, developed

at the University of Montana. CubeSats provide countries without well established space programs the opportunity to conduct their own space missions [22]. At the time of writing, CubeSats are typically launched without a propulsion system [23]. This is problematic as, even if missions do not need propulsion capabilities, there is discussion amongst regulatory bodies regarding the potential mandatory inclusion of de-orbiting capabilities on all satellites [24]. This means that CubeSats will require either a propulsion system to allow for de-orbiting or a passive end of life disposal mechanism, whether missions require them or not. Even though a number of systems, such as vacuum arc thrusters (VATs) [25] and electrospray/colloid thrusters [26], have been proposed for future missions, there are currently no options that adequately meet the strict mass and power requirements of the CubeSat platform. The main feature of this work is to draw inspiration from a corona ionization based, miniaturized propulsion system, previously developed at the University of the Witwatersrand, and to develop a micropropulsion system that could satisfy the limitations of the CubeSat platform. The system from which inspiration is drawn, known as the CorIon system, is briefly discussed below.



Figure 1.1.: A photograph showing a CubeSat. The CubeSat consists of a single module that was developed at the University of Montana [23]

1.2. The CorIon Concept

As stated previously, there are a number of reasons why the current generation of available micropropulsion systems are unsuitable for use on CubeSats. Aside from the physical size and masses of the systems themselves, fuel and power efficiency are also important factors to be taken into consideration. One system that could potentially meet the lower power consumption, high fuel efficiency, low mass and small size requirements of CubeSat missions, is the CorIon thruster concept, currently under development at the University of the Witwatersrand's Space Propulsion Research Laboratory, based at the School of Physics. A more comprehensive description of the progress on the project can be found elsewhere [27], [28], [29], but a brief summary follows.

1.2.1. Principle of Operation

CorIon is a portmanteau of 'corona ionization', which is the primary ionization mechanism used to generate thrust in the system. The system uses a coupling of the ionization and acceleration mechanisms to achieve miniaturization. The bipolar design of the thruster consists of two metallic needles, embedded in an insulating material, as shown in the schematic diagram in Figure 1.2. The needles are connected to a gas flow system, which supplies propellant, and a high voltage power supply. When a high potential is maintained across the needles, the high electric field created by the stressed electrodes ionizes the gaseous propellant as it leaves the needle tips, via positive and negative corona ionization. The same electric fields then accelerate the resulting ions and electrons away from the system, generating thrust.

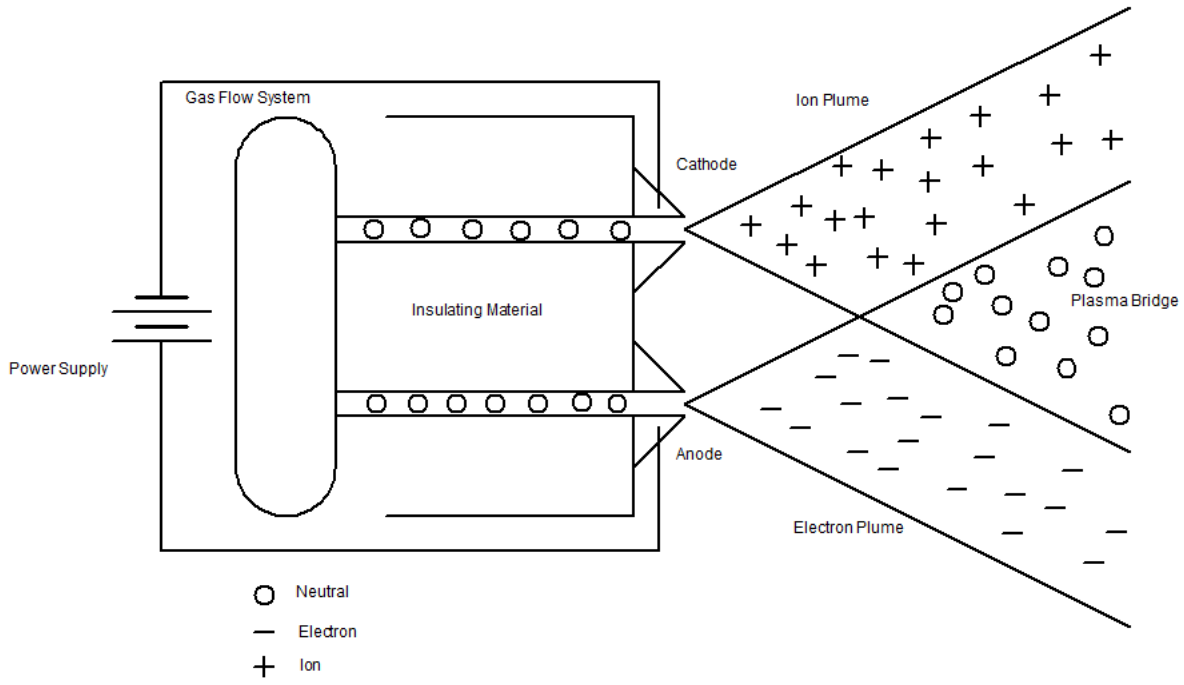

Figure 1.2.: A schematic diagram demonstrating the principle of operation of the CorIon concept thruster

1.2.2. Advantages

The system has a number of favourable qualities that make it an attractive option as a micropropulsion system for use on CubeSats. Due to the bipolar nature of operation, with the correct flow rates through each needle, there should be no need for a neutralizer. This is due to of the hypothesized formation of a plasma bridge upstream from the needles. This will result in a quasi-neutral plasma, which will not charge the external

surface of the spacecraft. The system is also able to use any gaseous propellant, making it versatile. The corona ionization mechanism is an efficient process by nature [27], with a low energy cost to produce an electron-ion pair [30]. This has potential to yield an efficient thruster.

The system is uncomplicated and easy to build. This simplicity lends itself to good reliability, especially with regard to support subsystems such as power supply and conditioning systems. The electrodes themselves are needles with exterior diameters less than 1 mm. This means the system can be made small and light. Finally, with some modifications, the system can be made stackable. This allows a greater total thrust to be generated with the use of multiple thrusters. Initial experiments performed on the system have given promising results [27], [28], [29].

1.2.3. Disadvantages

Unfortunately, the CorIon system in its current form suffers from an instability that inhibits its development into a fully fledged propulsion system. Due to the needle's small size, a very high power density is present at the needle tips when ionization occurs. While this is desirable, the newly generated ions impact on the needle tips with a high energy, resulting in sputtering of the needles and a corresponding high erosion rate. This erosion affects the shape of the needle tips, which in turn affects the electric field and gas flow characteristics of the system. This results in changing plasma characteristics, which alter the system's performance and the properties of the plasma bridge. This hampers continued operation. In some cases, the erosion results in the blocking of the needle tips with debris, halting operation entirely. These processes have limited the repeatability of experiments, as well as limiting the thruster's lifetime to approximately 15 minutes. It is clear that if the system is to be developed further, a reworking of the system's design is necessary.

1.3. Direct Current Discharge Based Microthruster

A candidate for the reworking of the CorIon design is inspired by a conventional glow discharge tube. Glow discharges have been studied for nearly 100 years, and the physical principles that describe them are well understood [31]. A plasma is generated in a low-pressure gas, confined to an insulating container, via a Townsend discharge. The Townsend discharge is brought about by the electric field set up by a pair of oppositely

charged electrodes. Various discharge regimes can be achieved by varying the voltage drop across the electrodes, including a stable glow discharge regime, an arc discharge regime and a pulsed mode, used in electronics when the direct current (DC) voltage signal is replaced by an alternating current (AC) signal [32]. If the system were to be adapted into a propulsion system, these various discharge regimes could offer a variety of different operating modes, making the system versatile. The system also offers stability previously lacking in the original CorIon design, as systems operating in the stable glow discharge regime can log thousands of hours of continuous operation and have excellent repeatability [32]. The system can be adapted to operate in a bipolar design with some modifications to the geometry.

The preferred incarnation of this design would be a cylindrical, 'U-shaped' discharge tube, with its normally closed ends opened to the vacuum of space, and ring-shaped electrodes attached to the open ends of the discharge tube. A gas flow inlet will be added to replenish the exhausted propellant. The ring electrodes placed at the open ends will create the electric field used to initiate and maintain ionization. It is hypothesized that a similar glow discharge to the one occurring in a conventional discharge tube will occur in the propellant gas, but since the plasma is not confined, ions and electrons will be attracted to the grounded and positively charged electrodes respectively, and will be accelerated away from the thruster, generating thrust. This is similar to the ionization-acceleration coupling exploited by the CorIon system. Neutralization of the charged particles leaving the proposed design is expected to occur in a similar way to the CorIon system, with the formation of a plasma bridge. Figure 1.3 shows a schematic diagram of this 'U-shaped', DC discharge based, microthruster concept. This system is expected to address the failings of the CorIon system by reducing the power density at the electrodes, resulting in reduced erosion and longer operating lifetimes with greater repeatability. Along with these improvements, the CorIon's advantages, such as a small mass and simple design, will be retained.

The primary goals of this work are:

- to test a proof of concept, DC discharge system to determine if the DC discharge is a viable plasma source in a vacuum for use in a space propulsion system
- to test a 'U-shaped', DC discharge based microthruster design to determine if it can operate as hypothesized above
- to determine how the 'U-shaped', DC discharge based microthruster behaves using various operating parameters, so that stable operating characteristics can be ascertained

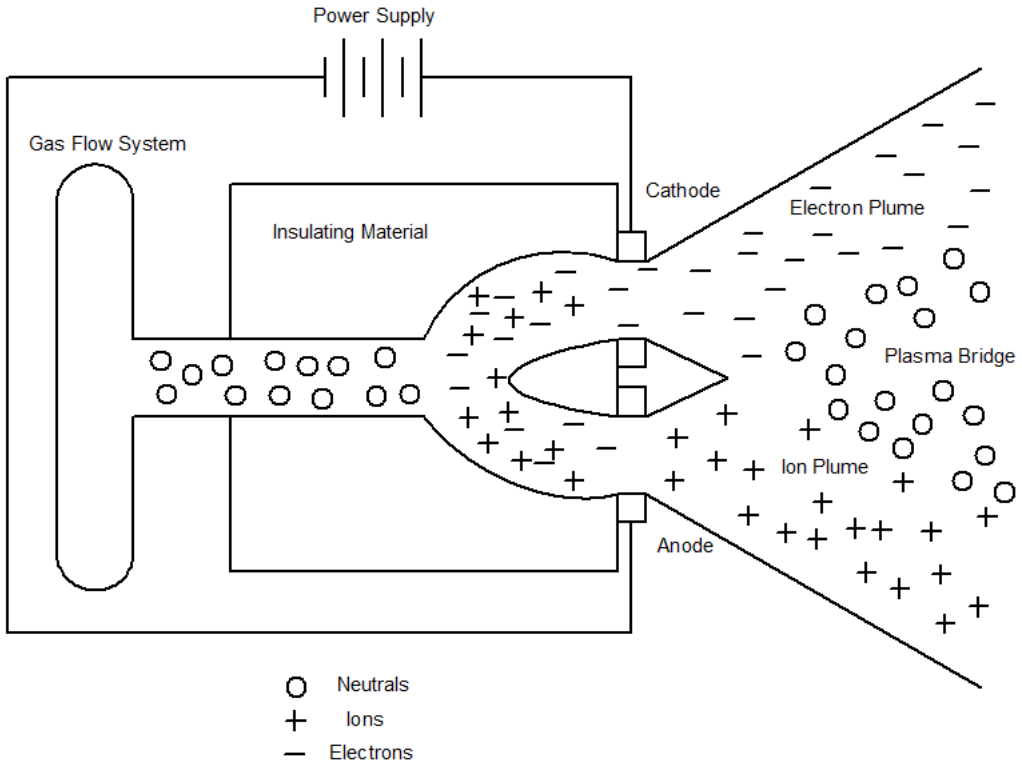

Figure 1.3.: A schematic diagram demonstrating the principle of operation of the direct current discharge based microthruster.

- to test the repeatability, lifetime and erosion characteristics of the 'U-shaped', DC discharge based microthruster to determine if it addresses the shortfalls of the CorIon system

- to design, build and analyze a thrust measurement system capable of measuring the thrust produced by the 'U-shaped', DC discharge based microthruster

- to measure the thrust produced by the 'U-shaped', DC discharge based microthruster as the operating parameters of the system are varied

- to perform plasma diagnostic measurements on the thruster to characterise the properties of the plasma generated by the system

- to simulate the system using computational techniques in order to confirm the hypothesis of the system's mechanism of operation, and gain further insight into its behavior.

1.4. Chapter Summary

Here, a brief summary of the content of each chapter is presented. Chapter 1 serves as an introduction to this work and provides context for the chapters to follow. The basic details of the system to be studied are presented and an outline of the research that follows is given.

Chapter 2 provides a theoretical context for this work by giving background information on the various fields of study that are associated with the research to follow. A number of different fields are reviewed, ranging from fundamental plasma physics, to an overview of other propulsion systems that are currently in development.

In chapter 3, the details of all experimental work are given, including the apparatus, construction of the thrusters to be studied, and detailed experimental procedures, explaining how each test was performed. A section is dedicated to the description and analysis of the thrust measurement system developed for this work.

Chapter 4 presents the experimental results of the tests described in chapter 3. These results include thrust measurements as different operating parameters are varied, erosion tests and plasma diagnostics. These results are accounted for with hypotheses and sources from the literature.

Chapter 5 discusses the simulation framework that was used to computationally study the thruster presented in this work. A brief overview of the software used, as well as the specific geometry and parameters that define the simulation are given.

Chapter 6 presents the results of the simulations. Various plots of the output of the simulation are shown and experimental results are reconciled with the data obtained from the simulations. The simulation results are compared with sources from the literature.

Finally, chapter 7 gives the conclusions derived from this work, and suggests future work that could be undertaken to better understand this system and develop it into a working prototype.

Chapter 7 is followed by a list of references and a number of appendices that contain additional supporting information.

2. Literature Review

In this chapter, a review of the relevant literature pertaining to the scientific fields covered in this work, is presented. These fields include introductory plasma physics, the physics of DC glow discharges, some features of established electric micropropulsion systems, and general propulsion system concepts.

2.1. Miniature Propulsion Systems

To miniaturize robotic spacecraft, each of the subsystems the spacecraft consists of needs to be considered and miniaturized in turn. One subsystem of particular interest is the spacecraft propulsion system. Size reduction of conventional propulsion systems, such as chemical rockets and larger electric propulsion systems, is often marred by scaling problems. These scaling problems can prevent systems from being able to function correctly. An example of this problem is the gridded ion thruster (GIT), where miniaturization necessitates making the ionization chamber smaller than the mean free path of the electrons in the chamber, preventing ionization from taking place [17]. These issues can be overcome, but require complex additions to thruster designs, such as the inclusion of magnetic fields in the example above. Here, magnetic fields confine the electrons to a smaller volume via the Lorentz force, which shortens their mean free path, allowing ionization to take place [33]. Another option would be to develop novel propulsion concepts that are designed specifically to operate at smaller sizes. An example would be micrometer sized, solid propellant thrusters, developed using micromachining techniques [18].

Some of the most popular propulsion technologies are: Chemical propulsion systems, which make use of the energy stored in the chemical bonds of propellant molecules to produce thrust [34] (this energy is released via exothermic reactions); Electric propulsion systems, which utilize electric and magnetic fields to generate plasmas and accelerate charged ions away from the thruster, producing thrust [35] and Nuclear propulsion systems that utilize the decay of atomic nuclei to generate thrust in a number of unique ways.

Electric propulsion systems will be considered in this work. This is because, while chemical systems are tried and tested technologies, and chemical micropropulsion systems are being developed [36], there is a fundamental limit on the exhaust velocity of the propellant that can be achieved in this manner. This limit is the binding energy of the propellant molecules. Electric propulsion systems do not suffer from this drawback as, in general, the only bound on the propellant exhaust velocity is the strength of the accelerating fields and the amount of power that can be used to create them [27]. Nuclear systems are not being considered, as the technology is not yet mature enough to be developed into fully functional micropropulsion systems [37].

2.1.1. Propulsion Concepts

A number of attributes are common among propulsion systems of varying types, which enable them to be studied more effectively. These common features allow different propulsion systems to be compared, so that their usefulness in different applications can be determined [9], [38]. Mass, specific impulse, total thrust, power consumption and efficiency are some of the most significant of these common properties.

The specific impulse of a system is a measure of its fuel efficiency, and indicates the thrust that the system produces per unit fuel expended, per unit time [39]. However, specific impulse may not be used as an indicator of thruster suitability alone, as a system may produce an inadequate thrust for a given application while still having a high specific impulse. The specific impulse in conjunction with the total impulse, or total thrust, can be used to determine the suitability of a thruster. The most versatile systems are capable of operating when the specific impulse and thrust can be varied [40]. The mathematical definition of specific impulse is obtained by defining the thrust produced by a system in terms of the propellant mass flow rate and the exhaust velocity of the expelled propellant:

$$I_{sp} = \frac{F_T}{\dot{m}_p g} = \frac{v_{ex}}{g} \tag{2.1}$$

where F_T is the thrust produced, $\dot{m}_p$ is the mass flow rate of the propellant, g is acceleration due to gravity and v_{ex} is the exhaust velocity of the propellant.

Considering that the main use of micropropulsion systems will likely be as primary propulsion systems on small spacecraft (microspacecraft and smaller), the mass restrictions imposed in the definitions of these kinds of spacecraft will place limitations on the mass

of the propulsion system. Inventive thinking is required to keep the propulsion system within mass limits

The use of solar cells on smaller spacecraft promises to minimize the effect a thruster's power consumption has when determining the suitability of a system for a specific application. This is because the solar cells are generally able to supply sufficient power to satisfy the power requirements of most propulsion systems [41]. However, this advantage is mitigated by the complex and heavy power processing equipment that is required for thrusters with high power requirements. This means that more useful quantities when comparing propulsion systems are the thrust to power ratio and the power per unit mass.

There are a number of efficiencies which are of interest when characterizing a space propulsion system, the two most important being the electrical efficiency and the mass utilization efficiency. With these two quantities, the total thrust efficiency of the propulsion system can be calculated. The electrical efficiency is the ratio of the output power created by the thruster to the total input power. The fuel or mass utilization efficiency gives an indication of how much of the expended propellant is used to generate thrust [42]. The mass utilization efficiency is a complex quantity to calculate, as neutral particles are also typically involved in thrust generation and need to be taken into account.

Thrust

The amount of thrust a propulsion system produces is the most important attribute for consideration. The amount of thrust a system produces will determine its usefulness and suitability for specific applications. For example, a thruster that produces μN of thrust will be unsuitable as a primary propulsion system for a space probe with a mass of several tons, designed to perform complex, high velocity manoeuvres in the outskirts of the solar system.

A number of mathematical models have been developed to describe the thrust of specific systems, an example being the general thrust equation [43], which is used to describe the thrust produced by a rocket. This is achieved by considering momentum transfer and pressure effects from expelled propellant:

$$F_T = \dot{m}_p v_{ex} - A(p_e - p_0) \tag{2.2}$$

where A is the propellant exit area, p_e is the exit pressure of the propellant and p_0 is the free stream pressure of the propellant. Another example of an expression used to calculate thrust, is the expression used to predict the net thrust on a GIT:

$$F_T = -\frac{1}{2}\varepsilon_0 \left(E_{accel}^2 - E_{screen}^2\right) \tag{2.3}$$

where E_{accel} is the electric field at the acceleration grid and E_{screen} is the electric field at the screen grid [35]. A general method to determine the thrust for an arbitrary body, via an arbitrary thrust generation mechanism has been developed by considering conservation of momentum equations applied to a generalized body that is to moved due to an arbitrary thrust:

$$\vec{F_T} = \iiint_{V_c} \vec{b} dV + \oiint_{\partial V_c} \rho \vec{v}([\vec{w} - \vec{v}] \cdot \hat{n}) dA + \oiint_{\partial V_c} \boldsymbol{\sigma} \cdot \hat{n} dA \tag{2.4}$$

where V_c is the volume enclosing the generalized body that is to be moved, $\vec{b}$ is a body force density or a vector momentum density, dV is a volume differential, ∂V_c is the boundary of the volume V_c, ρ is the mass density of the system, v is the propellant velocity, $\vec{w}$ is the velocity at which ∂V_c moves, $\hat{n}$ is the unit vector normal to ∂V_c, dA is an area differential and $\boldsymbol{\sigma}$ is the stress tensor [44].

There are three sources of thrust in this general system. Thrust generated from the first term relate to body forces, such as the force of gravity. Thrusts generated from the second term relate to momentum flux across the boundary of V_c and thrusts generated from the third term relate to applied stresses over the boundary of V_c. More details on this method can be found elsewhere [44].

2.2. Types of Electric Micropropulsion

A number of electric micropropulsion systems have been developed and can be divided into two broad categories: Miniaturized versions of pre-existing systems, which include the Hall thruster, the GIT and pulsed plasma thrusters (PPTs), and novel systems, which include the colloid thruster, field emission electric propulsion (FEEP), laser ablation thrusters and VATs. These systems represent the most widely studied options and each system in each category will be explained briefly below. Appendix A. contains information on some of the latest developments in the research undertaken in developing these systems

further.

2.2.1. Gridded Ion Thrusters

The GIT utilizes a variety of different mechanisms to ionize a gaseous propellant in an ionization chamber. These mechanisms include ionzation via hollow cathode generated electrons [35], radio frequency electron acceleration [45] and microwave heating [46]. The common attribute connecting these ionization mechanisms is that the resulting ions are accelerated away from the plasma generator and focused using ion optics, which consist of stages of oppositely charged electrostatic grids. The grids also serve to repel electrons and confine them to the plasma generator, improving the efficiency of the generator. However, this means an external neutralizer, in the form of a hollow cathode, is needed. A schematic diagram of a GIT is shown in Figure 2.1

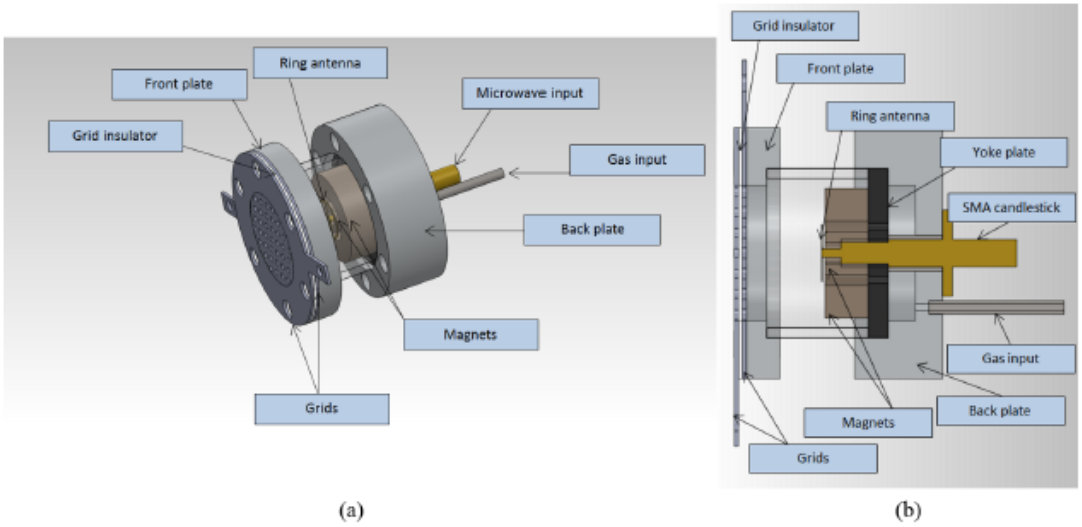

Figure 2.1.: A schematic diagram of the gridded ion thruster developed at the Pennsylvania State University: a) in 3D and b) as a longitudinal cross-section [47]

2.2.2. Hall Thrusters

The Hall thruster operates by trapping electrons emitted by a hollow cathode, using radial magnetic fields. When a gaseous, inert propellant is fed through the anode and into the annular thruster channel, electrons emitted by the hollow cathode outside the thruster are attracted to the anode, but become trapped in the radial magnetic field [48]. These electrons both ionize the propellant and are drawn into the ion beam, resulting in

a quasi-neutral plasma [35]. Ions produced by the ionization are accelerated away from the thruster by the electric field set up between the anode and the cathode, generating thrust.

2.2.3. Pulsed Plasma Thrusters

The main feature of the PPT is that it operates via the ablation and ionization of a solid propellant, as opposed to a liquid or a gas. This is advantageous in that it eliminates many propellant storage issues. An igniter is used to initially ablate material from the surface of the solid propellant. This partially ionized propellant closes the circuit between two oppositely charged electrodes, maintained at a high potential in a vacuum environment. The resulting arc, which passes through the propellant, ionizes it further, and the associated electromagnetic fields accelerate the plasma away from the thruster, generating thrust [49], [50].

2.2.4. Colloid Thrusters

Colloid thrusters exploit electrospray techniques to extract charged droplets from the surface of an ionic liquid propellant. The ionic liquid propellant is charged via contact with an electrode, and oppositely charged gridded electrodes are positioned a distance away from the surface of the propellant. The high electric field set up between the propellant surface and the gridded electrodes result in the formation of Taylor cones and, above a certain threshold voltage, charged liquid droplets can be extracted from the tips of the Taylor cones. These droplets are accelerated away from the thruster by the gridded electrode and generate thrust [51].

2.2.5. Field Emission Electric Propulsion

FEEP shares some common features with colloid thrusters. Both systems utilize a liquid propellant. In the case of FEEP, a liquid metal propellant, such as caesium, is used. The liquid metal propellant is in contact with a charged electrode, typically a capillary tube, while an oppositely charged electrode is placed a distance from the surface of the propellant. The high electric field set up between this external electrode and the surface of the propellant, results in the formation of Taylor cones. Above a certain threshold voltage, metal ions are extracted from the Taylor cones on the surface of the propellant,

and are accelerated away from the thruster by the external electrode, thus generating thrust [52].

2.2.6. Laser Ablation Thrusters

Thrusters that utilize laser ablation techniques to generate thrust are a relatively new development in space propulsion technology. A laser diode is used to produce monochromatic light, which is shone on the reverse side of a transparent tape. The other side of the transparent tape is coated in a solid propellant. The propellant is ablated and ionized by the radiation imparted by the laser diode in a controlled detonation, which generates thrust [53]. A schematic diagram of a laser ablation thruster is shown in Figure 2.2.

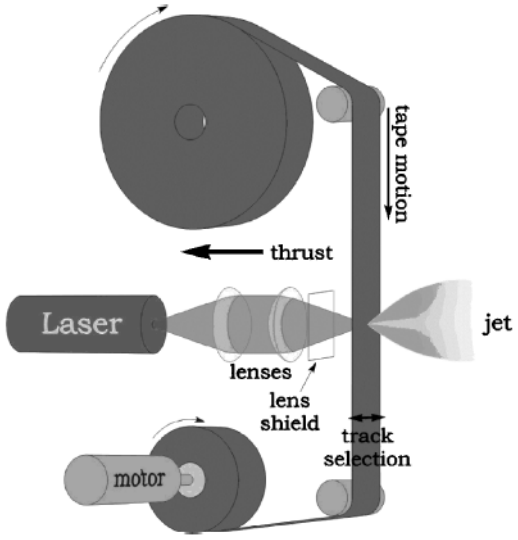

Figure 2.2.: A schematic diagram demonstrating the principle of operation of a laser ablation thruster. [54]

2.2.7. Vacuum Arc Thrusters

Similarly to the PPT, the VAT is able to generate thrust by using a solid propellant. A high potential is maintained across two metallic electrodes in a near vacuum. Above a threshold voltage, a vacuum arc develops between the two electrodes, causing material from the surface of the cathode to be ablated and ionized. The resulting plasma is accelerated away from the thruster by the high electric field generated by the vacuum arc. Additional electric and magnetic fields can be used to further increase the thrust generated [55].

2.3. Introductory Plasma Physics

Because the proposed thruster, and the majority of electric micropropulsion system concepts, involve the generation of plasmas and the acceleration of the constituent ions, an understanding and appreciation of some fundamental concepts in plasma physics is essential to develop the proposed thruster concept further, and gain an intimate understanding of how it operates.

2.3.1. What is a Plasma?

A plasma, typically referred to as the fourth state of matter, is most simply defined as an ionized gas [56]. However, complete ionization is not a requirement for matter to be considered a plasma. This means that a plasma can consist of a mixture of neutral atoms, positively charged ions, negatively charged ions, metastable atoms and electrons. The presence of moving, unbound charged particles in the plasma means that plasmas both create and are effected by electric and magnetic fields. The collective behavior of a plasma is governed by both these internally generated and externally imposed electromagnetic fields [57]. Plasma is the most abundant state of ordinary matter in the universe, with compositional estimates quoted as high as 99 % [58]. Many attempts have been made to study the properties of these astrophysical plasmas using experimental techniques [59].

2.3.2. Various Plasma Types

Plasmas arise from a variety of different sources and can be created both by natural phenomena, and in laboratories with experimental equipment. Figures 2.3 and 2.4 depict the relationship between two of the defining parameters of some of the many plasmas that exist in nature and that can be artificially created in the laboratory. Some of these plasmas are now discussed.

Naturally Occurring Plasmas

Ionosphere The ionosphere is a region of the earth's atmosphere that consists of a high number of free electrons and ions, created predominantly by energy absorbed from ultraviolet radiation produced by the sun. The state of the ionosphere is dependent on

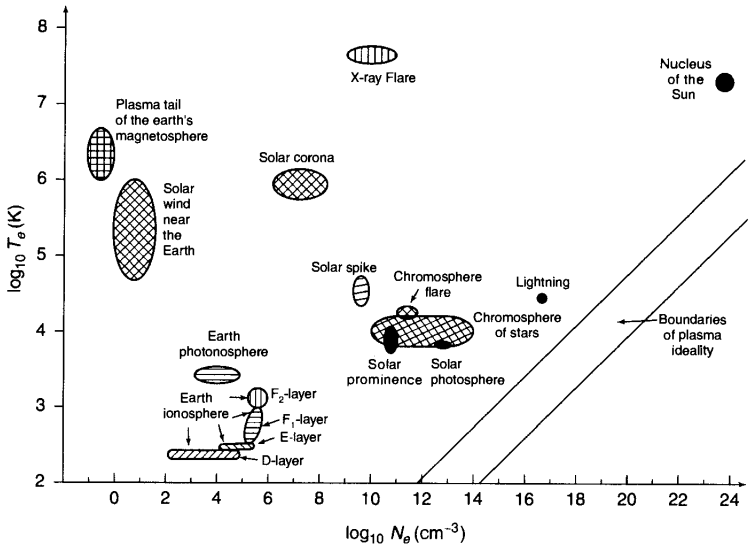

Figure 2.3.: A diagram depicting the relationship between the electron temperature and electron number density of a variety of different naturally occurring plasmas [60].

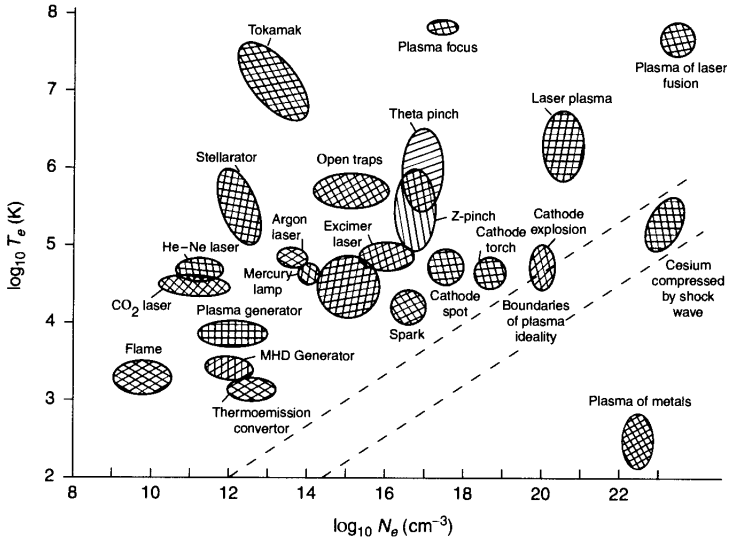

Figure 2.4.: A diagram depicting the relationship between the electron temperature and electron number density of a variety of different plasmas that can be created in the laboratory [60]

many factors, including latitude, longitude, time of day, season and solar activity. The ionosphere plays an important role in radio communication across the earth [61].

Magnetosphere The magnetosphere is the region around any astronomical object where charged particles are influenced by the object's magnetic field. The earth possesses a magnetosphere, which is sometimes considered to be a part of the ionosphere, but is of distinct interest, as it interacts with the ionic solar wind produced by the sun [62].

Solar Corona The solar corona is an aura of plasma that surrounds the sun and is most easily observed by a layperson during a solar eclipse. The solar corona has a temperature ranging into millions of kelvin, much hotter than the surface of the sun (the photosphere, whose temperature measures in the region of thousands of kelvin). The exact reason for this temperature difference is the subject of much debate [63]. The high temperature of the corona also leads to novel spectral features, which can be explained by the presence of highly ionized iron.

Lightning Lightning is a form of electrostatic discharge, typically observed during storms. Lightning can occur between clouds (typically negatively charged) and the earth (typically positively charged), between different clouds and between differently charged sections of the same cloud [64]. The lightning results in the equalization of charge between the bodies involved and the flash of light observed is due to the ionization of the air through which the discharge travels. This ionization rapidly heats the air surrounding the discharge, resulting in the accompanying thunder clap.

Man Made Plasmas

Inductively Coupled Plasma An inductively coupled plasma is a plasma that is created using time-varying magnetic fields to stimulate electromagnetic induction inside the gas from which the plasma is to be generated. The magnetic field is created by passing high frequency electric currents through an induction coil, positioned nearby or around the source gas. Often, the discharge is initiated using a spark, but is sustained by the energy obtained from the fluctuating magnetic field. This energy is passed to the free electrons created by the initial spark [65]. Different antenna shapes can be used to sustain the plasma. Inductively coupled plasmas are used in atomic emission spectroscopy, a type of mass spectrometry, and reactive-ion etching.

Capacitively Coupled Plasma A capacitively coupled plasma is formed when two metal electrodes are placed inside a flowing gas stream, from which the plasma is to be generated. The metal electrodes are separated by a small distance, one of them grounded, and one of them connected to a radio frequency power supply. This configuration is similar to that of a capacitor. Free electrons in the flowing gas can be accelerated by the resulting radio frequency field. These energetic electrons ionize the flowing gas, thereby creating the plasma [66].

Microwave-Induced Plasma A microwave-induced plasma can be created without the use of electrodes via gigahertz range electromagnetic radiation. A tuned resonant cavity is used to produce a standing electromagnetic wave, while seed electrons are introduced into the gas in which the plasma is to be generated [67]. The electric field set up by the standing wave accelerates electrons and imparts them with enough energy to ionize neutral atoms, creating the plasma.

Laser-Induced Plasma A laser-induced plasma can be created from any material, regardless of its state, be it solid, liquid or gas. A highly energetic laser source is used to atomize and further excite the sample under study. A plasma is formed once the laser achieves the threshold for optical breakdown. This threshold is dependent on the properties of the environment and the material being studied [68].

2.3.3. Fundamental Properties and Characteristics of Plasmas

There are a number of important physical quantities that can be used to specify a plasma and describe all plasma phenomena. These properties are analogous to the pressure, density and temperature used to describe the state of conventional materials.

Number Density and Temperature

The description of a plasma requires more than just three parameters like a conventional material. In fact, for a plasma consisting of a number of electrons and a variety of different ionic species, the number densities of all species must be specified. These densities must all be regarded as independent variables, as each species will react differently to electromagnetic forces.

As with other states of matter, the temperature of the plasma under study is related to the average, random kinetic energy of the constituent particle species. If the system under consideration is in thermal equilibrium, then the velocity distribution of a particle species s can be taken to be Maxwellian:

$$f_s(v) = n_s \left(\frac{m_s}{2\pi\kappa T_s} \right)^{3/2} e^{-\frac{m_s v^2}{2\kappa T_s}} \tag{2.5}$$

where m_s is the mass of the particle species s, v is the velocity under consideration, T_s is the temperature of the particle species s and κ is Boltzmann's constant. The velocity distribution is normalized in such a way that the number density of all particles of species s, n_s, is obtained when the velocity distribution is integrated over all velocities:

$$\int_{-\infty}^{\infty} f_s(v) dv_x dv_y dv_z = n_s \tag{2.6}$$

It can be shown that the root-mean-square velocity can be written in terms of the thermal speed C_s. This Gives $v_{rms} = \sqrt{3} C_s$ and the thermal speed is:

$$C_s = \sqrt{\frac{\kappa T_s}{m_s}} \tag{2.7}$$

Finally, the average kinetic energy of the particles of species s can be written in terms of the species temperature:

$$\left\langle \frac{1}{2} m_s v^2 \right\rangle = \frac{3}{2} \kappa T_s \tag{2.8}$$

Substantial differences in temperature may occur between different particle species in a plasma. This is due to the different rates of energy transfer between particles of the same species, for example, between electrons, and between particles of different species, for example, between electrons and ions. These different energy transfer rates are due to differing species masses, and can create a slow transition to thermal equilibrium, which introduces complicated non-equilibrium effects.

Debye Length

If the temperature and number density of the species that constitute the plasma are known, then the existence of a fundamental length scale that characterizes the plasma, can be demonstrated. This is done by inserting a negative test charge, Q, into a homogeneous plasma. Electrostatic forces cause the repulsion of electrons from the test charge and the attraction of ions towards it, resulting in a polarization charge, which acts to shield the plasma from the test charge. This type of shielding is known as Debye shielding and the characteristic length over which it occurs is known as the Debye length.

Consider a homogeneous plasma, consisting of a background of positive ions of number density n_0 and electrons of temperature T_e and number density n_e, into which a negative test charge Q is inserted. Possion's Equation can now be solved, yielding a value for the electric potential:

$$\Phi = \frac{1}{4\pi\varepsilon_0}\frac{Q}{r}e^{-r/\lambda_D} \tag{2.9}$$

where ε_0 is the permittivity of free space, r is the radial distance from the test charge, and λ_D is the Debye length:

$$\lambda_D^2 = \frac{\varepsilon_0 \kappa T_e}{n_0 e^2} \tag{2.10}$$

where e is the elementary charge of an electron. The potential shown in Equation 2.9 is known as the Debye-Hückel potential. It is obtained from the Poisson Equation by assuming a Maxwellian velocity distribution, with kinetic and potential energy accounted for, at an infinite distance away from the test charge. Further, it is assumed that the electric potential is small when compared to the electron temperature and that the potential is spherically symmetric.

Plasma Sheaths

As was shown previously, the thermal speed of a species in a plasma is given by Equation 2.7. By considering the form of this expression, it is noted that electrons will have a much higher thermal speed than ions, due to their significantly smaller mass. As a consequence of this, if an object is placed inside a plasma, it will receive a net negative charge on its surface due to being bombarded by a greater number of electrons than ions. This net

negative charge will result in the repulsion of electrons and attraction of positively charged ions. When the attracted ion current equals the repelled electron current, equilibrium is reached. This situation is similar to the case where a negative test charged is placed in the plasma. The electrically polarized region, which is formed around the object, is called a plasma sheath. If the surface of the object in the plasma can be approximated as planar, then the equilibrium potential of the surface can be determined by equating the electron and ion currents:

$$V = -\frac{\kappa T_e}{2e}\left[ln\left(\frac{m_i}{m_e}\right) + ln\left(\frac{T_e}{T_i}\right)\right] \tag{2.11}$$

where T_i is the ion temperature, m_i is the mass of the ion and m_e is the electron mass. It is a non-trivial exercise to determine the equilibrium potential for other surfaces. If other physical phenomena, such as secondary electron emission due to ion impact, result in changes to the equilibrium currents, these effects should be taken into account. It should be noted that while Equation 2.11 is valid for Maxwellian electrons, its applicability in practical situations is limited because typically $T_i << T_e$. This means that the ions must enter the sheath with the Bohm velocity if a stable plasma sheath is to form. This requires a pre-sheath potential adjacent to the sheath, and therefore the surface potential is modified by ions striking the surface at a different rate.

Plasma Frequency

Consider a homogeneous plasma, consisting of a static background of ions and moving electrons. If the electrons are displaced from their equilibrium position, an electrostatic restoring force will act to restore the electrons back to their equilibrium position. This force can be approximated by Hooke's law, as the magnitude of the charge imbalance is directly proportional to the displacement. The system will undergo harmonic oscillation, due to the inertia possessed by the electrons. These oscillations are called Langmuir oscillations and occur with a frequency termed the electron plasma frequency:

$$\omega_{pe}^2 = \frac{n_0 e^2}{\varepsilon_0 m_e} \tag{2.12}$$

Equation 2.12 represents the specific case of electrons, but if a plasma contains multiple species, then a plasma frequency can be defined for each species. However, this does not mean that each species oscillates independently of one another. The thermal speed

of a species, its Debye Length and its plasma frequency are all related by the simple expression:

$$\omega_{ps}\lambda_{Ds} = C_s \tag{2.13}$$

Cyclotron Frequency

If a moving, charged particle of mass m and charge q is subjected to an external magnetic field of magnitude B, it will move with uniform circular motion around the magnetic field lines with a characteristic frequency known as the cyclotron frequency:

$$\omega_c = \frac{|q|B}{m} \tag{2.14}$$

This phenomenon is observed in both electron and ion behavior.

Collision Frequency

Due to the nature of a plasma, which can consist of a number of different charged and neutral species, it is convenient to define a collision frequency, denoted as ν_{rs}. This frequency represents the average rate at which particles of type r, collide with particles of type s. Collisions can be grouped together into two categories, collisions between charged particles and neutrals, and collisions between charged particles. Each of these categories displays unique behavior and will be treated individually.

Collisions Between Charged and Neutral Particles Due to the lack of a long range electrostatic force, collisions between charged particles, denoted as c particles, and neutral particles, denoted as n particles, are characterized by short range forces. By assuming that the neutrals are hard, immobile spheres, the collision frequency can be calculated using:

$$\nu_{nc} = n_n C_c \sigma_n \tag{2.15}$$

where σ_n is the collision cross-section of the neutral species and n_n is the neutral species'

number density. The thermal speed of charged species is also present in Equation 2.15, and represents how the collision frequency is temperature dapendent.

When comparing the importance of charged-neutral collisions to other plasma processes in governing the plasma's behavior, the charged neutral collision frequency should be compared to the characteristic time scale of the plasma process of interest, τ. If the product $\nu\tau$ is less than one, then the plasma is said to be weakly collisional, with a slow transfer of energy to neutrals. This is achieved by reducing the density of the neutral species. Conversely, a highly collisional regime is obtained when $\nu\tau$ is greater than one, and plasma processes are typically of a lesser importance when describing the plasma's behavior.

Collisions Between Charged Particles Collisions between charged particles involve the long range Coulomb force. It is therefore useful to define a differential scattering cross-section. This is the number of particles scattered into a differential solid angle, $d\Omega$, divided by the incident beam intensity:

$$d\Omega = 2\pi \sin\chi d\chi \tag{2.16}$$

where χ is the angle between the incident beam and the scattered particle. By considering an electron scattering off of a much heavier ion, the differential cross-section, σ_C, is:

$$\sigma_C(\chi) = \frac{1}{4}\left(\frac{e^2}{4\pi\varepsilon_0 m_e v^2}\right)^2 \frac{1}{\sin^4(\chi/2)} \tag{2.17}$$

This is the Rutherford formula, which varies by the inverse of the thermal speed to the power of four. This means that the collision frequency varies as $1/T^{3/2}$, which implies that as the temperature increases, the rate of collisions between charged particles decreases. This is the opposite behavior to that observed for collisions between charged and neutral particles. It can be shown that the collision frequency between electrons and ions is:

$$\nu_{ei} = \frac{n_0 e^4}{32\pi^{1/2}\varepsilon_0^2 m_e^{1/2}(2\kappa T_e)^{3/2}} \ln(12\pi n_0 \lambda_D^3) \tag{2.18}$$

2.4. Physics of Direct Current Glow Discharges

The novel thruster concept proposed in this work will utilize a DC glow discharge to ionize a gaseous propellant. The resulting charged species will be accelerated away from the thruster, generating thrust. Therefore, a thorough understanding of the physics of DC discharges is essential to transform the idea into a working, proof of concept system.

2.4.1. Features

Stable, DC glow discharges are one of the most well studied plasma phenomena, and have been used in one form or another for approximately 100 years. Their applications have ranged from light sources, to electronic components in circuits. The discharge is characterized by its ability to be self-sustaining, via secondary electron emission from a cold cathode, subjected to ion bombardment. In its most common incarnation, DC glow discharges are made to occur in a cylindrical, insulating container that encloses a gas, at a pressure typically less than atmospheric pressure, and two electrodes, one positively charged and one grounded, are situated at opposite ends of the container. This apparatus is normally referred to as a discharge tube.

A number of distinct zones in space characterize a DC glow discharge, with each region possessing different physical properties. A large positive space charge, following a significant potential drop near the cathode, are both distinctive features of a DC glow discharge. This potential drop is known as the cathode fall region. The thickness of the cathode fall region increases as the density of the background gas decreases. A homogeneous plasma region, known as the positive column, can form if the distance between the electrodes is large enough to prevent the cathode layer from filling the entire space between the electrodes. The positive column is electrically neutral and is considered to be the most common example of a weakly ionized, non-equilibrium plasma. Separating the positive column and the anode is a region known as the anode layer. As the pressure is increased in a glow discharge, all the regions thin out and shift closer to the cathode. While the cathode layer is essential for the formation of a DC glow discharge to occur, the positive column is not. [69].

2.4.2. Light Emission

A glow discharge can be divided up into a number of different layers that are observed to either radiate light or remain dark. The luminous layers that a glow discharge exhibits are shown schematically in Figure 2.5. These layers are most easily discernible at lower pressures and can consist of striated features, or can be homogeneous, as is the case with the positive column. If the discharge is created under circumstances that prevent the formation of a positive column, then the light that is observed emanates from the region termed the negative glow.

The colour of a glow discharge is dependent on the composition of the gas that the discharge is occurring in and is a reflection of its atomic spectrum, for example, nitrogen will exhibit a purple glow, whereas neon will exhibit an orange glow. The colours in the discharge can also be observed to change between regions of the discharge, for example, the colour given off by a helium glow discharge can be resolved to a red cathode layer, a green negative glow and a reddish-purple positive column.

As electrons are emitted from the cathode, due to secondary emission from ion impacts, they initially have a low energy, of approximately 1 eV, which is too low for atomic excitation. This means that no light is emitted and the region adjacent to the cathode is termed the Aston dark space. As the electrons are accelerated by the electric field, they are able to gain enough energy to begin exciting neutral atoms, causing light to be emitted according to the background gas' atomic spectra. The resulting region is referred to as the cathode glow. Sometimes, different layers may appear to correspond to different levels of atomic excitation and each layer will have a different colour. As the electrons are further accelerated, they move into a region where they have too much energy for excitation to occur and light emission ceases. This region is known as the cathode dark space and is the predominant area of ionization of the background gas. New electrons are created here and the resulting ions travel much more slowly, resulting in a build up of positive space charge, which helps to demarcate the physical boundary of the cathode layer.

The electron flux out of the cathode layer is quite high, due to the increase in electron population from the avalanche process inside the cathode layer. The energies of these electrons are in the range required for atomic excitation, and the region known as the negative glow results. As electrons are ejected from the cathode, they start with a lower energy that increases as the electrons are accelerated. This means that inside the cathode glow, spectral lines that correspond to lower energy excitations are observed first and higher energy spectral lines are observed as the electrons are accelerated. The

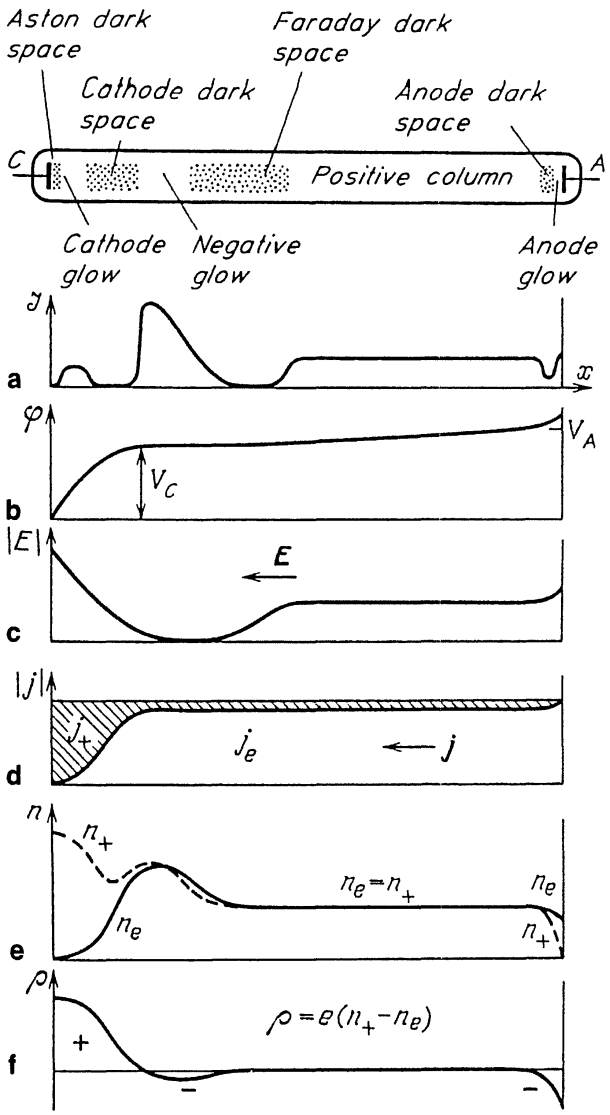

Figure 2.5.: A schematic diagram showing how the properties of a glow discharge vary with distance from the cathode: a) glow intensity; b) potential; c) longitudinal electric field; d) electronic and ionic current densities; e) electronic and ionic number densities and f) space charge [69]

opposite occurs in the negative glow, where electrons begin to lose energy due to excitation collisions, meaning that high energy spectral lines dominate the beginning of the cathode glow and low energy spectral lines are observed deeper in the negative glow, eventually giving way to the Faraday Dark space.

Some electrons that leave the cathode layer are highly energetic, due to no participation in any excitation or ionizing collisions. This is in contrast with the moderately energetic electrons that are typically present in the negative glow. These energetic electrons can cause ionization to occur inside the Faraday dark space, resulting in a higher electron number density than is present in the positive column.

The remaining energetic electrons that have managed to traverse their way through the discharge are able to excite atoms in the region known as the positive column. This results in light emission from this area of the discharge. Generally, the velocity distribution in the positive column is random, but there is a slight asymmetry present towards the anode. Being positively charged, the anode will have a tendency to attract electrons and repel ions, resulting in the formation of a region of negative space charge. The acceleration of electrons towards the anode results in the excitation of neutral atoms near the anode, causing the luminescence of the anode glow.

2.4.3. Axial Variation of Parameters

Figure 2.5. also shows schematically how a variety of important plasma parameters vary along the length of the discharge tube. These parameters are: the plasma potential, the longitudinal electric field, the electronic and ionic current densities, the electronic and ionic number densities, and the space charge. These profiles have been predicted through theoretical analysis and have been confirmed experimentally using Langmiur probe measurements [69]. They indicate the boundary between different physical regions of the discharge, as opposed to the regions defined by the amount of light emission. For example, the large positive space charge and electric field of the cathode layer discussed previously, are clearly observed in the curves at the cathode boundary of the negative glow. This shows how the cathode layer includes the Aston dark space, the cathode glow and the cathode dark space, which are all defined by the light they emit.

2.4.4. The Guiding Effect of Surface Charge

While the most common incarnation of a discharge tube utilizes a cylindrical container, DC discharges have been sustained in tubes that are manufactured into very complex shapes, as is evident in the marketing and advertising industry. This is an interesting phenomenon, considering that the charged particles that maintain the discharge are bound to move along the electric field lines set up by the electrodes. These electric field lines are not bound by the shape of the discharge tube, and will intersect the walls of the tube many times in some cases. The phenomenon is explained by the existence of plasma sheaths in the plasma. The electrons in the plasma are initially bound to the electric field lines set up by the electrodes that sustain the discharge. As the electric field lines intersect with an insulating wall, the electrons will impact with the wall and impart an overall negative surface charge on the wall. This creates a plasma sheath at the boundary between the bulk plasma and the wall. The electric field lines set up by this sheath will guide charged species along the length of the tube, through the complex geometries the tube is constructed in. This allows the discharge to be sustained.

2.4.5. Current-Voltage Characteristics

Figure 2.6 depicts a schematic of the current-voltage (IV) characteristics of a low pressure DC discharge. As the discharge current is increased, the discharge transitions through a number of different discharge modes. These include a dark Townsend discharge, a normal glow, an abnormal glow and an arc discharge.

Townsend Avalanches and The Breakdown Voltage

Consider a cylindrical discharge tube, filed with a gas at a low pressure, with electrodes positioned at either end and connected to a power supply. The discharge voltage is progressively increased from 0 V. The initial electron population is formed spontaneously through other environmental processes (for example photo-ionization). Those electrons that are initially present near the cathode are transported towards the anode by the homogeneous field that forms due to the increasing voltage. Electrons may be lost to the walls of the discharge tube or may be captured by electronegative atoms, forming ions, but these losses decrease as the voltage (and therefore electric field) is increased. This means that initially, the current that flows between the electrodes increases as the voltage is increased. Eventually, a cut-off voltage is reached, where all of the charge

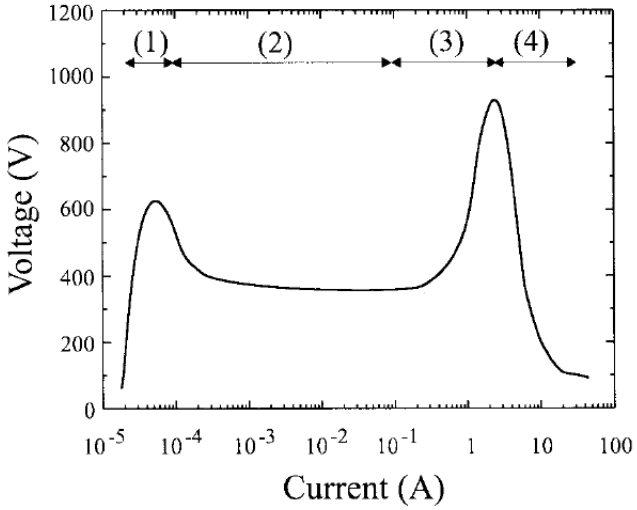

Figure 2.6.: A schematic diagram showing the current-voltage characteristics of a conventional direct current glow discharge. As the discharge current is increased the discharge transitions through a number of modes shown to be: 1) a Townsend dark discharge; 2) a normal glow; 3) an abnormal glow and 4) an arc discharge [70]

particles that are spontaneously generated in the discharge tube are collected by the electrodes, and further increases in voltage do not yield an increase in current. This is a non-self sustaining discharge, as the current is dependent on the outside factors that spontaneously generate the charged particles. As the voltage is increased further, the charged species are accelerated to higher velocities, until a point is reached where they possess enough energy to be able to ionize neutral atoms in the background gas, thus producing more charged species, which can contribute to the measured current. This amplifying effect results in the current:

$$i = i_0 e^{\alpha d} \tag{2.19}$$

where i_0 is the initial current generated spontaneously by environmental sources, α is the first Townsend coefficient and d is the distance between the electrodes. As the voltage is increased further, secondary electron production mechanisms begin to take effect. Similarly to how electrons are accelerated towards the anode, ions are accelerated towards the cathode. When they impact on the cathode with enough energy, electrons can be released from the surface of the cathode material. This process is known as secondary emission and can be initiated by excited atoms and photons as well. Other secondary electron production mechanisms can take place, but secondary emission will dominate the measured discharge current. This is because electrons that are emitted from the cathode

can potentially traverse the entire length of the discharge and generate more electrons via the primary process of impact ionization. When secondary emission effects are taken into account, the measured current is:

$$i = \frac{i_0 e^{\alpha d}}{(1 - \gamma(e^{\alpha d} - 1))} \tag{2.20}$$

where γ is the secondary electron emission coefficient. Equation 2.20 becomes meaningless when the denominator is negative. This occurs when the voltage is increased further, but if the voltage is kept such that the denominator is positive and non-zero, the current is steady, but not self sustaining. The transition from a non-self sustaining discharge to a self sustaining discharge is given when the denominator is zero:

$$\alpha d = ln\left(\frac{1}{\gamma} + 1\right) \tag{2.21}$$

This transition is known as breakdown and occurs at the voltage determined from Equation 2.21. Technically, the discharge only becomes self-sustaining at a slight over-voltage from the breakdown voltage, as the condition for breakdown only ensures that the electron population can reproduce itself and not grow. The process of growth of electrons will continue until it is stopped by the ohmic resistance of the circuit (which will receive the majority of the voltage drop supplied by the source) or matched by the recombination of ions and electrons. When the voltage drops and the current no longer grows, the discharge is said to be a dark Townsend discharge, and the process of breakdown described above is known as a Townsend avalanche. The expression which shows how the current grows with time under a slight but constant over-voltage is:

$$i(t) = i_0 e^{\alpha d}\left(\frac{\mu}{\mu - 1} e^{\left(\frac{\mu - 1}{\mu}\frac{t}{\tau}\right)} - \frac{1}{\mu - 1}\right) \tag{2.22}$$

where τ is the time necessary for an ion to travel from the anode to the cathode and μ is the reproduction coefficient:

$$\mu = \gamma(e^{\alpha d} - 1) \tag{2.23}$$

Equation 2.22 shows that breakdown occurs exponentially faster as the over-voltage increases. This is because the Townsend coefficient is a steep function of electric field and

the reproduction coefficient is dependant on the Townsend co-efficient.

Paschen's Law

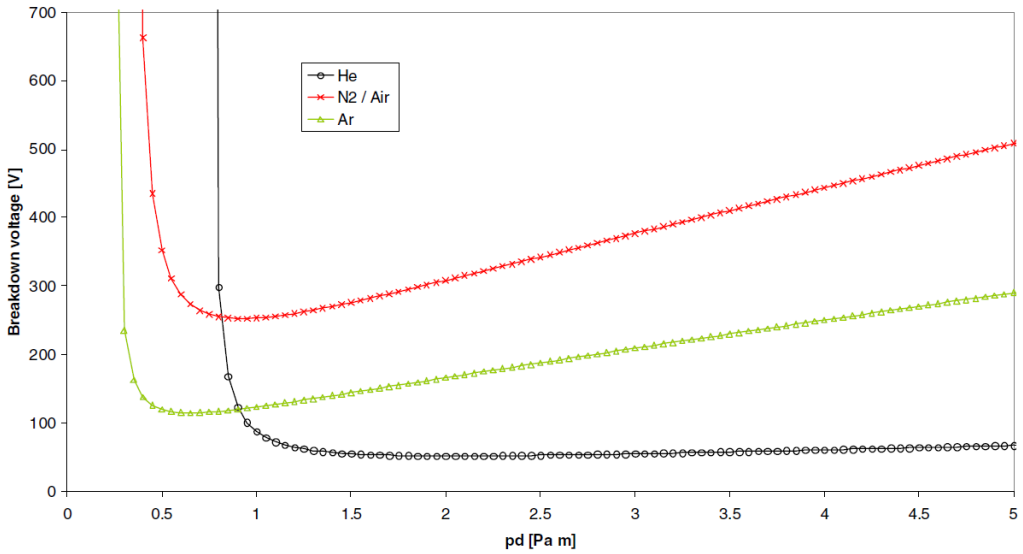

Figure 2.7.: Paschen curves for gases commonly used in direct current discharges [71]

The breakdown voltage (V_b) is determined by a number of factors that are specific to the discharge, namely the background gas, the gas pressure, the gap between the electrodes and the cathode material. An expression that relates these quantities is found in the empirically determined Paschen curve [71], a number of which are shown for common gases used in DC discharges in Figure 2.7, and the expression for which is:

$$V_b = \frac{Bpd}{ln(Apd) - ln\left(ln\left(1 + \frac{1}{\gamma}\right)\right)} \tag{2.24}$$

where p is the pressure of the background gas, A is the first Paschen coefficient and B is the second Paschen coefficient. The first Paschen coefficient is:

$$A = 0.224 \frac{3e^4}{16\pi\varepsilon_0^2 \Delta E^2 k_b T} \tag{2.25}$$

where ΔE is the ionization energy of the background gas and T is the temperature of the background gas. The second Paschen coefficient is:

$$B = \frac{5\pi a_r^2 \Delta E}{4 k_b T e} \tag{2.26}$$

where a_r is the atomic radius of the background gas atoms. By considering the Paschen curves shown in Figure 2.7, one can see that a minimum breakdown voltage can be achieved for a specific value of the product between the pressure of the background gas, and the distance between the electrodes.

Discharge Types

In a real circuit, some sort of ohmic resistance (be it controlled or material dependant) exists that will hamper the flow of electric current. This resistance will set a limit on the achievable current for a given voltage drop across the circuit, and, since the type of discharge that forms is dependant on the current (which is an indicator of the degree of ionization), the resistance imposes a limit on the type of discharge that will form after breakdown has occurred.

Townsend Dark Discharge This type of discharge corresponds to region 1 in Figure 2.6. and occurs in any discharge tube at very low currents. This kind of discharge can be engineered by imposing a very high circuit resistance on the discharge, which will limit the current that can flow through the circuit. This results in a negligible electron and ion density, which will prevent the development of space charge regions and will leave the electric field set up by the electrodes undistorted. If the distance between the electrodes is small, the field can be assumed to be identical to how it would be in the absence of ionization. The discharge is made self sustaining by applying the breakdown voltage across the electrodes, which ensures that the electron and ion populations are simply maintained and not allowed to increase or decrease. Due to the very low rate of ionization, no light emission is observed from this kind of discharge.

Glow Discharge A glow discharge is realised by increasing the voltage drop supplied by the source, or by decreasing the circuit resistance, thereby allowing more current to flow. The transition to a glow discharge is marked by a drop in the measured voltage across the discharge as the current increases, and is visible in region 2 in Figure 2.6. After this drop, the voltage remains almost constant with increasing current. The higher the pressure, the greater the region of relatively constant current. As the current is varied, the density of the discharge at the cathode remains unchanged. However, the density in

other areas of the discharge is observed to change, and the luminous spot on the cathode is observed to grow as the current is increased.

Abnormal Discharge When the luminous spot on the cathode has grown to cover the entire cathode surface, the discharge voltage will begin to grow so as to extract more current from the cathode, and a transition to an abnormal discharge is observed. This corresponds to region 3 in Figure 2.6.

Arc Discharge When the current finally reaches a critical value, the abnormal discharge cascades down into an arc discharge which corresponds to region 4 in Figure 2.6.

3. Experimental: Apparatus and Procedure

In order to test the proposed thruster concept's viability in a practical setting, experimental testing needs to be undertaken. These experiments range from basic firing tests on proof of concept systems, to thrust tests designed to measure the thrust produced by the fully functional novel system proposed in this work. In this chapter, the experimental apparatus used to perform these measurements is discussed, along with the experiment particulars and procedures. A section is dedicated entirely to the thrust measurement stand, as this thrust measurement system operates on a novel principle, and was developed and tested in-house.

3.1. Apparatus

All pieces of apparatus used throughout the testing process are discussed below.

3.1.1. Vacuum System

All tests were performed in a stainless steel, ring vacuum chamber, with a hemispherical lid and dimensions of 760 mm diameter x 200 mm height. The ring chamber has a number of access ports situated around its circumference. These access ports can either be sealed, to ensure the required vacuums can be obtained, or fitted with different interfaces, to allow for viewing of, and access to the interior of the vacuum chamber. For these experiments, a viewing port, consisting of a glass window, was used to obtain photographs and video footage of the interior of the chamber. A high voltage connector interface was used to connect the thruster inside the chamber to the high voltage power supply outside the chamber, and a Bayonet Neill-Concelman (BNC) connector interface was used to allow diagnostic probes inside the chamber to be connected to external circuits. The

high voltage connectors consist of two copper rods that are insulated from the chamber and each other by ceramic isolators. These ceramic isolators enclose the copper rods at the points of contact with the vacuum chamber. The rods and insulators are attached to a stainless steel disc, which can be mounted to one of the access ports around the chamber.

The vacuum required to create an artificial space environment is achieved by using a combination of an Alcatel 2012A roughing pump and a Leybold-Heraeus water cooled diffusion pump. Initially, the chamber is pumped down with the roughing pump until a vacuum of approximately 0.05 torr is achieved. Following this, the diffusion pump is exposed to the vacuum chamber, and vacuums as high as 10^{-4} torr can be obtained. Typically, the vacuums obtained are slightly softer than this, due to the out-gassing of plastic components [72]. A Kurt J. Lesker 275i vacuum gauge is used to measure lower vacuums, and a Leybold-Heraeus PM 41 Penning vacuum gauge is used to measure higher vacuums.

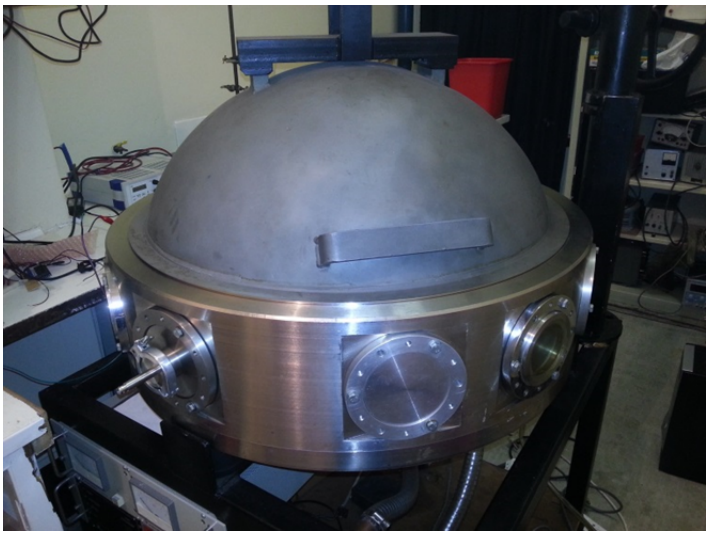

Figure 3.1.: A photograph depicting the vacuum chamber used in this work.

3.1.2. Mass Flow Measurement Systems

Two different mass flow measurement systems were used throughout this work. For initial testing of each thruster, air obtained from the atmosphere was used as a propellant. This was to allow for adequate experimentation with the system, especially when understanding viable operating parameters, without having to be concerned with wasting more conventional propellant gases. Tests using air as a propellant were performed using a mass flow measurement system developed in-house. For all subsequent diagnostic tests,

argon was used as the propellant gas. Using argon with the in-house mass flow measurement system would have required significant modification and re-calibration. Therefore, an MKS Instruments Type 1179 MFC and an MKS Instruments 647C MGC were connected to a pressurized argon tank, and were used to control the mass flow rate of argon. The in-house developed mass flow measurement system is described below.

Orifice Plate Mass Flow Meter

In order to measure the mass flow rate of the gaseous propellant supplied to the thruster under study, a mass flow measurement system was developed in-house. This system is based on an orifice flow meter concept [73]. In principle, the flow meter consists of two chambers that are separated by a barrier. An aperture is made in the barrier that is considerably smaller than the surface area of the barrier itself. The barrier is now known as the orifice plate. If a pressure difference can be established between the two chambers and then measured, the mass flow rate of the liquid or gas flowing through the aperture can be determined:

$$\dot{m} = CA\sqrt{2\rho\Delta P} \tag{3.1}$$

where C is the orifice flow coefficient, A is the area of the aperture, ρ is the density of the substance flowing through the meter and ΔP is the pressure difference measured between the two chambers.

Design A diagrammatic representation of the orifice flow meter is shown in Figure 3.2. The orifice flow meter is rectangular in shape. It is 65 mm long, 40 mm wide and 40 mm high. Each chamber consists of a hollowed out aluminium block. The orifice plate, also made from aluminium, is sandwiched between these two blocks, with a rubber gasket on each side of it to ensure an airtight seal. Two holes are drilled through the length of the aluminium blocks at the corners of the orifice flow meter. The holes also pass through the orifice plate. Bolts are inserted into these holes and are secured from both ends using nuts. This configuration holds the system together and prevents leaks by applying pressure to the rubber gaskets. There are two open pipes attached to each aluminium block, one for the attachment of a gas inlet or outlet, and one that allows for the connection of a manometer to measure the pressure difference between the two chambers. In these experiments, an Extech HD750 Differential Pressure Manometer was used for this purpose.

The outlet of the mass flow measurement system is connected to the vacuum chamber via a micrometer needle valve. The vacuum generated inside the vacuum chamber creates the pressure difference needed to incite gas flow through the system. The flow rate is accurately controlled using the micrometer needle valve. Since the propellant used with this system was air, the gas inlet to the flow meter was left open to the atmosphere.

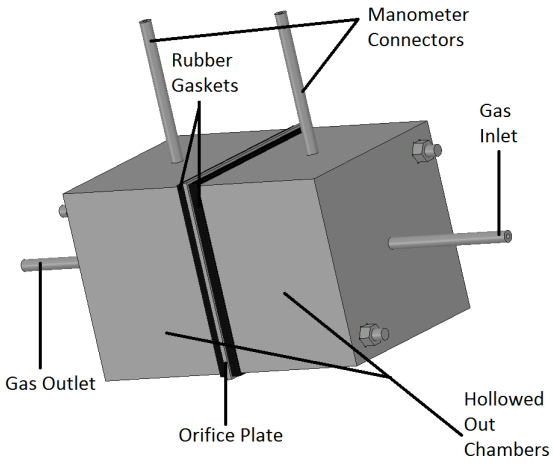

Figure 3.2.: A diagrammatic representation of the in-house developed, mass flow rate measurement system

Calibration By using Equation 3.1, a calibration curve can be plotted that allows for the mass flow rate of a given gas to be determined for a measured pressure difference. Calibration also allows for the orifice flow coefficient to be extracted from the resulting curve fit.

The mass flow rate through the system was determined by measuring the amount of time taken for the vacuum to displace a set volume of air from a 100 ml measuring cylinder upturned in a container of water. This configuration traps an air bubble inside the measuring cylinder. A pipe is connected to the gas inlet of the mass flow measurement system and inserted into the measuring cylinder before it is upturned in the container of water. This allows air to be siphoned from the bubble when it is exposed to the vacuum. The rate at which air is siphoned from the bubble is controlled by manipulating the micrometer needle valve. As air is syphoned from the bubble by the vacuum, the graduations on the measuring cylinder provide a way to measure the volume of air that is extracted from the cavity.

A stopwatch is used to measure the amount of time taken for the vacuum to siphon 5 ml of air from the cavity. Sources of human error using this method are: the use of the eye to determine when 5 ml of air has been siphoned, and the human reaction time when timing

a new reading. These effects are mitigated by taking a number of readings per pressure difference and averaging the results. This process provides a mass flow rate in ml/s, which can be converted to mg/s, as the density of air at a given temperature and height above sea level is known. An example calibration curve is shown in Figure 3.3, with the expression that was fitted to the calibration data given in Equation 3.2. All of the constants present in Equation 3.1 are combined to give the numerical coefficient in Equation 3.2. This method of calibration is not ideal, as there is potential for the vacuum system to be damaged should liquids be sucked into the vacuum chamber, but with careful operation, this calibration technique can produce accurate results with minimal time spent on the calibration process.

$$\dot{m} = 0.0662\sqrt{\Delta P} \tag{3.2}$$

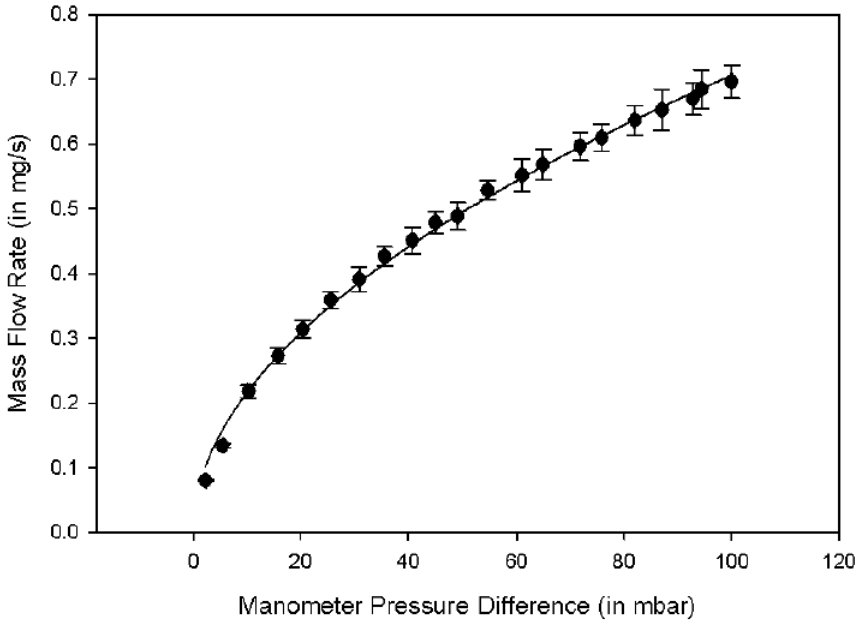

Figure 3.3.: An example calibration curve for the in-house developed, mass flow rate measurement system.

Commercial Mass Flow Measurement System

The commercially available mass flow measurement system used in this work consists of an MKS Instruments Type 1179 MFC mass flow controller, controlled by an MKS Instruments 647C MGC multigas controller. The Type 1179 MFC uses a differential heat transfer technique to measure the mass flow rate of gases through the system. The desired mass flow rate is achieved using an electronically automated valve.

Once an appropriate vacuum has been obtained inside the vacuum chamber, the 647C MGC multigas controller is turned on. The differential heat transfer system is allowed a warm up period of two minutes to ensure the accurate operation of the mass flow controller. Then, the gas flow is turned on at the course pressure regulator of the argon gas cylinder connected to the Type 1179 MFC mass flow controller. The outlet pressure from the gas cylinder must not exceed 40 psi if the system is to be operated safely. Following this, the Type 1179 MFC can be exposed to the vacuum chamber via a needle valve placed between the mass flow controller and the vacuum chamber. This will create the pressure differential required for gas to flow. The required gas flow is set using the 647C MGC, and the gas flow can be activated and deactivated from the 647C MGC when required. The 647C MGC measures the mass flow rate in sccm as opposed to mg/s. When readings are performed with the commercial mass flow measurement system, the desired mass flow rate must be converted to sccm.

3.1.3. Power Supply

A high voltage power supply is required to provide the thruster under study with the necessary voltage to ionize a gaseous propellant. A Hivolt T1EP 100 605 p high voltage power supply fulfils this purpose. This power supply is able to deliver a maximum current of 6 mA at 10000 V, with facilities to allow for the independent limiting of both current and voltage. The power supply also has a universal serial bus (USB) connector, which allows it to be controlled as part of a greater experimental control and data acquisition system. This system is discussed below

3.1.4. Experimental Control and Data Acquisition System

Accurate control and measurement of the electrical operating parameters of the thruster is required so that the behavior of the thruster being studied can be understood. Unfortunately, this is not offered by the controls on the front panel of the high voltage power supply. The required level of control can be obtained through the USB interface. To utilize this functionality, software was written, in LabVIEW, to allow for the accurate setting of voltage and current parameters. LabVIEW is a software package, developed by National Instruments, typically used to create software to automate the process of experimental data capture.

To measure the voltage drop across and current through the electrodes of the thruster under study, two digital multimeters (a Fluke 8840A and an Agilent 34401A) are con-

nected to the analogue measurement outputs of the high voltage power supply. The voltages obtained at the analogue measurement outputs are scaled down, so as not to damage the measurement equipment. To relate these scaled voltages to the desired voltage and current readings, linear calibration curves are generated across the entire range of operational voltages and currents the power supply can produce. The measurements are recorded from these digital multimeters using general purpose interface bus (GPIB) connections and software written in LabVIEW.

In order to obtain a visual record of the behavior of the thruster being studied under different operating conditions, a digital camera was used to record video footage of the thruster firing. The digital camera used was a Logitech C525 HD Webcam. The digital camera was mounted to the viewing port on the side of the vacuum chamber, which allows for visual access to the chamber interior. The recording of the video footage was controlled manually using Logitech's Webcam Software.

3.1.5. Thruster Mounting Table

A thruster mounting table was developed to allow for thrusters to be mounted in the chamber for testing, without exposing any electrical connections to the plasma resulting from thruster firing. Exposed connections could also result in unwanted ionization of neutrals, via corona ionization, which could affect efficiency results.

Figure 3.4 depicts a diagrammatic representation of the thruster mounting table. The thruster mounting table measures 30 cm long, 6 cm wide, 2 cm high and sits 10 cm off the floor of the vacuum chamber. It consists of a rectangular block of polyvinyl chloride (PVC) plastic cut in half longitudinally. The lower half is secured to the base of the vacuum chamber via two vertical blocks of PVC plastic, mounted at one end of and halfway along the lower half of the mounting table respectfully. These two blocks are connected together using a metal mounting bracket, secured to the floor of the vacuum chamber. The lower half of the mounting table has two channels hollowed out of its upper surface to allow for electrical leads to run along the length of the thruster mounting table. These leads are isolated from the environment once the two halves of the thruster mounting table are secured together. The leads allow for the connection of a thruster at one end of the table, to the high voltage connectors at the other end. This connection is facilitated by two enlarged cavities that are drilled out of the two halves of the thruster mounting table. These cavities are large enough for the copper high voltage connectors to be inserted, and contact is made with the wires running the length of the thruster mounting table via pressure contacts. The upper half of the mounting table is secured

to the lower half using nylon screws at a number of points around the perimeter of the mounting table. Further insulation from the outside vacuum environment is obtained using silicone sealant, which has been shown to be both vacuum stable [74] and an excellent electrical insulator [75]. Electrical contact is made with the thruster to be studied via pressure contacts, consisting of two steel screws that are inserted through the top half of the thruster mounting table, and into the leads running through the centre of the mounting table.

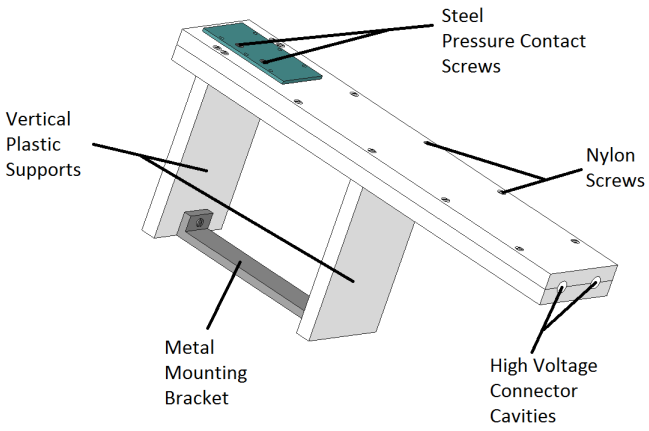

Figure 3.4.: A diagrammatic representation of the thruster mounting table used in the acquisition of experimental data.

3.1.6. Faraday Cup Probe

The Faraday cup probe is an instrument used to study some of the various ion properties of plasma plumes. This is in contrast to the various types of Langmiur probe, which are typically used to study the electron properties of plasmas (although some ion properties can be deduced using Langmuir probes) [76]. The Faraday cup probe takes ion current measurements, which provide an indication of the ion production rate and the number of ions produced.

Typically, the probe consists of a negatively biased collector plate or grid, which attracts ions produced by the plasma source. As ions impact on the collector, they impart a charge on the plate that is neutralized by electrons, which flow from the grounded connection in the circuit. For complete neutralization to take place, the electron current must equal the ion current. This current can be measured by connecting a terminating resistor between the collector and ground and measuring the voltage drop across it. Due to the limited surface area of the collector, the current that is measured is not the entire ion current generated by the plasma source. To incorporate this, ion current densities (ICDs) are

extracted from the measurements obtained using the Faraday cup probe.

One of the advantages of the Faraday cup probe, is that it can be positioned to face the plasma source from different angles. This means the ICD emanating from different regions of the plasma source can be measured, allowing for an ion current density distribution (ICDD) to be generated [77]. When studying thruster performance, ICDD allows for the direction of the ionic thrust component to be determined.

The charged states of different ions constituting the plasma can be determined using a Faraday cup probe, but due to the complex additional equipment required to take such readings (such as ion optics to focus the ion beam onto the probe) [78] these readings will not be performed in this work.

Probe Description

The Faraday cup probe used in this work was originally developed to study the ion properties of the vacuum arc plasma generated by VAT design improvements, and hence characterize the VAT's performance. A detailed description of the probe's operational behavior and performance analysis can be found elsewhere [79].

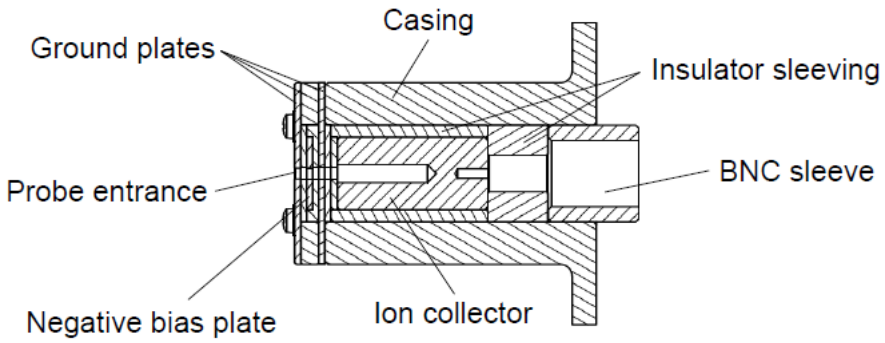

Figure 3.5.: An engineering drawing depicting the various constituent components of the Faraday cup probe [79].

Figure 3.5 shows an engineering drawing of the interior of the Faraday cup probe. The negatively biased ion collector consists of a copper cylindrical inner cup, with a length of 15 mm and a diameter of 3 mm, which conically tapers to a point at the termination of the cup inside the probe. This design ensures electrons created from secondary emission due to ion impact, and reflected ions do not escape the probe. The negative bias will attract incoming, positively charged ions and repel incoming electrons.

An additional electron rejecter plate is installed in front of the collector. This plate is

made from a 0.9 mm thick copper plate. The negative bias acts to further repel electrons and attract positive ions. Grounded aluminium plates are positioned on either side of the electron rejecter plate. This is to counterbalance the electric field of the electron rejecter plate.

The entrance hole to the probe and the hole in the electron rejecter plate have a diameter of 1.8 mm. This is the smallest orifice accurately obtainable with the manufacturing capabilities available. A smaller orifice would have been preferable, so as to limit the shielding effect of the resulting plasma sheath on the probe.

The collector and the electron rejecter plate are connected to external circuits via BNC coaxial cable connectors attached to the probe. Signals read by the probe are fed through coaxial cables to the circuit powering the probe, outside of the vacuum chamber via the BNC connector interface.

All the various electrically connected components are separated from one another using 0.9 mm thick rings of ultra-high molecular weight polyethylene plastic, and all of these components are housed together in an aluminium casing. This casing protects all the components of the probe, and enables the probe to be mounted to a vertical, adjustable stand. This stand allows for the probe to be positioned at different heights. The probe inside its aluminium casing, attached to the adjustable stand is shown in Figure 3.6.

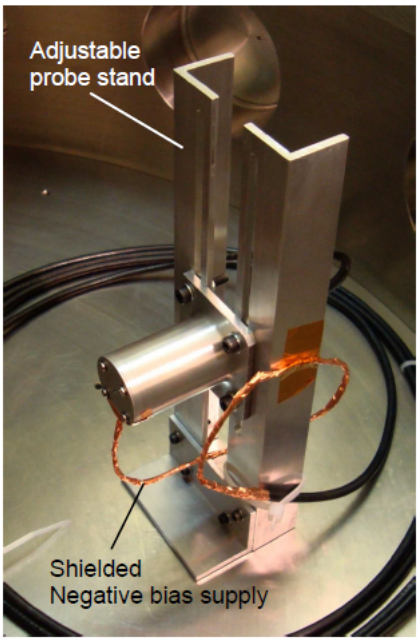

Figure 3.6.: A photograph showing the Faraday cup probe inside the vacuum chamber and mounted to the adjustable probe stand [79].

Probe Circuit

Figure 3.7 shows a schematic circuit diagram of the electrical circuit used to take ion current density measurements.

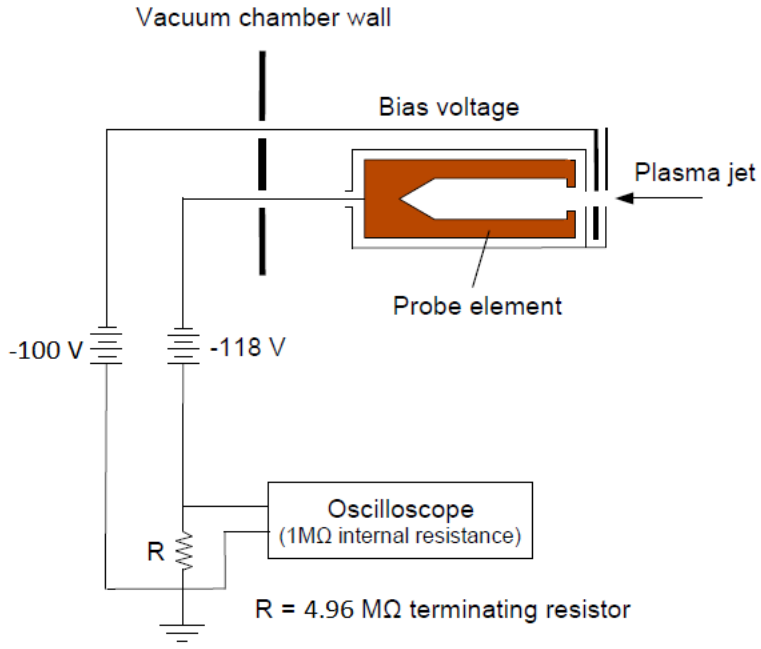

Figure 3.7.: A schematic circuit diagram depicting how the various voltage sources and the digital oscilloscope are connected to the Faraday cup probe, adapted from [79].

Two shielded packs of 9 V batteries were used to generate the negative bias required by the collector and the electron rejecter plate. The collector had a bias of -118 V applied to it, while the electron rejecter plate had a bias of -100 V applied to it. A Rigol DS1052E digital oscilloscope was used to measure the voltage drop across a shielded 4.96 MΩ terminating resistor. However, it is noted that the oscilloscope itself introduces a parallel resistance to the circuit that must be taken into account. This means the true terminating resistance is:

$$R_{true} = \frac{R_0 R}{R_0 + R} \tag{3.3}$$

where R is the terminating resistance and R_0 is the oscilloscope resistance (which in this case measures 1 MΩ). The terminating resistance can be altered to change the voltage drop measured by the oscilloscope, meaning a wide range of ion currents can be measured with this apparatus. Finally, the ion current measured by the probe is given by Ohm's Law:

$$I_{ic} = \frac{V_{tr}}{R_{true}} \tag{3.4}$$

3.1.7. Thrusters

Two different thruster designs were tested in these experiments. The first design is a proof of concept system that is a simple modification of a DC discharge tube. The second thruster design is an attempt to realise the proposed novel thruster concept.

Proof of Concept Design

The proof of concept design consists of a rectangular, acrylic plastic block, measuring 20 mm in length, 15 mm in width and 10 mm in height. Acrylic plastic was chosen as the construction material as it could be easily machined into the desired shape, it is reasonably robust with a melting point of 160° [80], and it is most commonly transparent, which allows for the interior of the thruster to be observed. A 2 mm diameter tube is drilled through the block along its length. A second 2 mm diameter tube is drilled along the width of the block, so that it intersects the first tube at right angles. This second tube is then widened to a 5 mm diameter up to half of its depth into the block. This widening is to facilitate the insertion of a gas connection attachment, which allows the thruster to be connected to the propellant supply system when inside the vacuum chamber. At either end of the first tube, circular, stainless steel electrodes, with 2 mm diameter holes drilled in them, are attached using an acid-free clear adhesive, so that the holes in the electrodes are collinear with the tube drilled along the thruster's length. Electrical leads are attached to the electrodes by wrapping the bare ends of the electrical wires around each electrode through the central hole before the electrodes are attached to the thruster body. Finally, the external surface of the electrodes exposed to the vacuum are insulated using an epoxy resin, so that the only exposed surface of the electrode is the inner surface of the hole drilled through it.

The purpose of this proof of concept design is to test if a discharge can be initiated and maintained if the ends of a DC discharge tube are removed, and if plasma plumes form at these open ends when a gas flow is maintained while the discharge is occurring. This proof of concept would also be useful as a test bed to study the lifetime, repeatability and erosion characteristics of a DC discharge based thruster when compared to the CorIon system, previously studied in the laboratory.

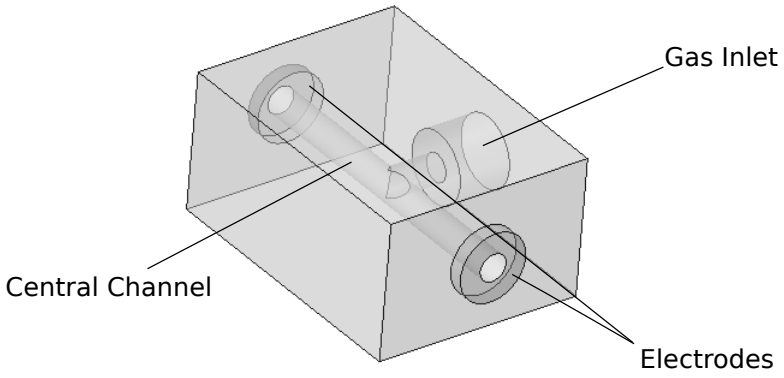

Figure 3.8.: A diagrammatic representation of an example, proof of concept, straight discharge tube, tested throughout these experiments

'U-Shaped' Thruster Design

The thruster consists of a 16 mm long and 3 mm diameter 'U-shaped' channel in which the DC discharge is expected to occur. These dimensions are chosen so as to ensure an electron mean free path that is not larger than the thruster under the available operating conditions. A gas inlet tube connects to the 'U-shaped' channel at its apex. Electrodes with attached wires are mounted to the open ends of the thruster channel, and a face plate is attached on top of the electrodes to prevent arcing between the electrodes during operation.

Both the thruster body and the faceplate were manufactured with a RepRap Omerod 2 3D printer using transparent polylactic acid (PLA) plastic as the construction material. 3D printing using PLA plastic was chosen as the construction technique as the acrylic plastic used previously proved to be too difficult to machine into the required shape. Since the melting point of PLA [81] is close to the melting point of acrylic plastic [80], it was assumed that PLA would perform just as well, if not better than acrylic plastic and 3D printing would allow it to be manipulated into the desired shape. Acrylonitrile butadiene styrene (ABS) plastic would also have been an option that could be used with the 3D printer, but its higher melting temperature would have proved problematic to print, while requiring substantial modifications to the 3D printer. Transparent PLA plastic allowed for the interior thruster channel to be monitored during thruster operation. The dimensions of the thruster body and faceplate were varied depending on the test being

conducted, while the dimensions of the interior 'U-shaped' channel were kept constant.

The electrodes were made of an aluminium rod and were hand cut to a thickness of approximately 1 mm. The electrodes were cleared of any burrs and cleaned in an ultrasonic bath to remove any dirt, contaminants, and oils. Bare copper wire was used to attach the electrodes to the electrical pressure contacts on the thruster mounting table, and was insulated after the thruster was completely assembled. The copper wire was sandwiched between an electrode and the body of a thruster. The electrode was heated using a soldering iron until it stared to melt into the plastic. Once the plastic cooled down and solidified, the assembly of the electrode and the copper wire would be held in place. A small amount of conductive silver paint was used to ensure good electrical contact between the electrode and the copper wire was maintained. This process was repeated for the second electrode. The faceplate was then clamped to the secured electrodes, and an acid-free clear adhesive was used to fill all the gaps between the electrodes. This was left to dry for 24 hours before mounting the thruster to the thruster mounting table. A diagrammatic representation of a 3D printed thruster and a faceplate are shown in Figures 3.9 and 3.10 respectively.

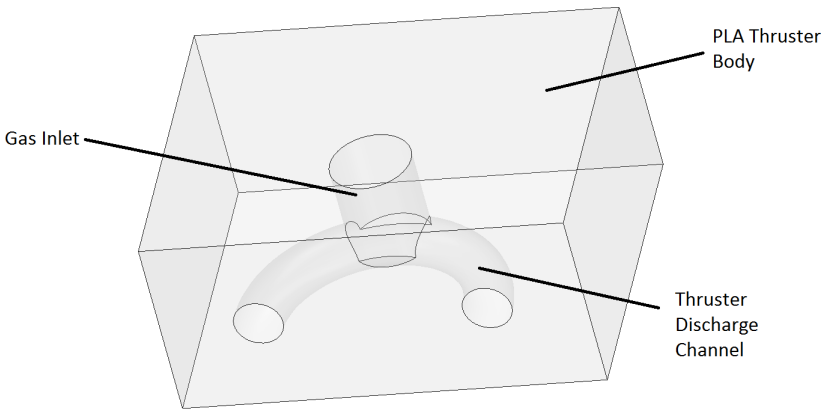

Figure 3.9.: A diagrammatic representation of an example, 'U-shaped' thruster body, tested throughout these experiments

3.2. Thrust Measurement Stand

In order to measure the thrust produced by the thruster under study, a suitable thrust measurement system needs to be devised that is able to resolve changes in thrust produced by the thruster when thruster parameters are varied. The thrust measurement system should also be easy to use, cost-effective, robust and impose a minimal impact on the

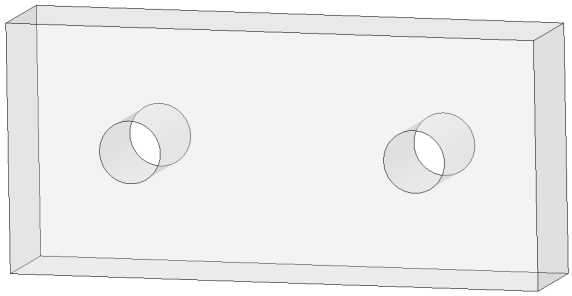

Figure 3.10.: A diagrammatic representation of an example, 'U-shaped' thruster faceplate, tested throughout these experiments

thruster's operation. There are accepted thrust measurement practices that have been written about extensively elsewhere [82], however, the balance developed in this work uses an original thrust measurement principle not typically used in conventional thrust measurement systems. Details of this system are given below.

3.2.1. Description

Figure 3.11 depicts a 3D schematic diagram of the thrust measurements stand. A horizontal lever, machined out of PVC plastic, is used as the foundation of the thrust stand. PVC was used to maintain sensitivity and stability, minimize the thrust stand's overall mass and retain cost-effectiveness, but it can be substituted by any suitable vacuum grade plastic. Interactions between the thrust stand and plasmas generated by electrical propulsion systems are mitigated by the use of PVC as a construction material. This is due to it being electrically inert. Thermal expansion due to heating of the plastic, is not expected to be an issue at the power ranges currently utilized in the laboratory. The low melting point of PVC is offset by its small linear coefficient of thermal expansion, especially when compared to other commercially available plastics [83]. An advantage of this thrust stand design is that it can easily accommodate different materials to adapt to a variety of experimental conditions.

The hollow PVC lever arm acts as a thrust support member. Holes are drilled across its length, weight relieving the thrust support member. The lever arm has an outer diameter of 16 mm, an inner diameter of 10 mm, a length of 425 mm and a mass of

28 g. A specially machined mounting table at one end of the thrust support member provides a point of attachment for the thruster to be studied. The mounting table is shown in the schematic drawing in Figure 3.12, and facilitates the connection of a variety of micro-thruster concepts via electrical and gas attachments.

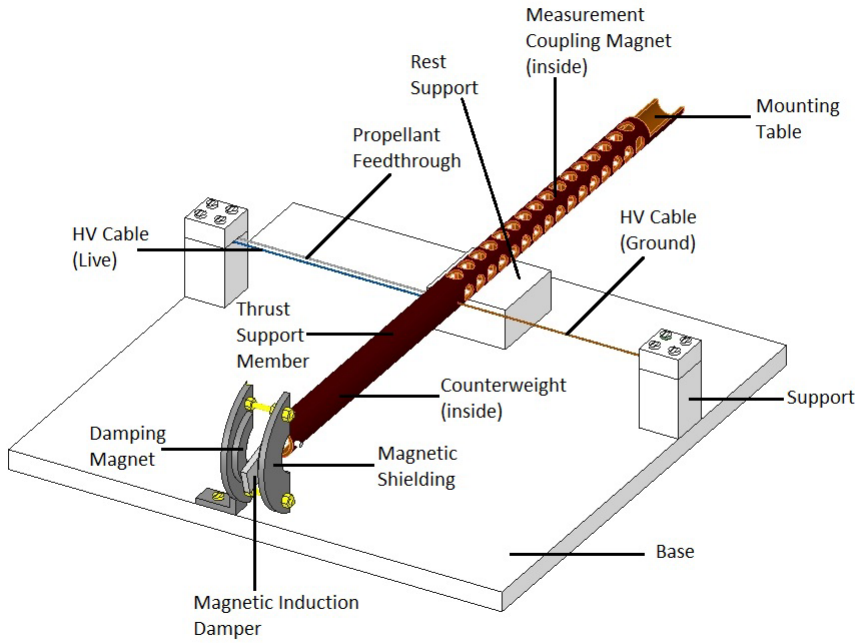

Figure 3.11.: The thrust measurement stand rendered in 3D. The mass balance used to take measurements is positioned underneath the thrust support member.

The thrust support member is kept horizontal using an adjustable PVC counterweight positioned inside the end of the thrust support member opposite the mounting table and, in this case, the counterweight has a length of 130 mm and a mass of 16 g. A fine screw mechanism can be used to adjust the counterweight, which in turn slightly alters the moment of the thrust support member. Greater adjustments to the moment can be made by altering the position of the counterweight inside the thrust support member, or by adding masses to the counterweight.

Figure 3.12 also shows an aluminium plate attached to the thrust support member at the same end as the counter weight. This aluminium plate has a mass of 6 g, a thickness of 3 mm and a length of 65 mm, and acts as a magnetic induction damper by moving between two Mu-Metal shielded, nickel-plated neodymium magnets, mounted on the base of the thrust stand. Passive damping is achieved via eddy currents, generated by the movement of the induction damper through the magnetic field [84]. The thrust support member is further stabilized by the magnetic induction damper due to its orientation at an angle of

30° to the axis of the thrust support member, as seen in Figure 3.12.

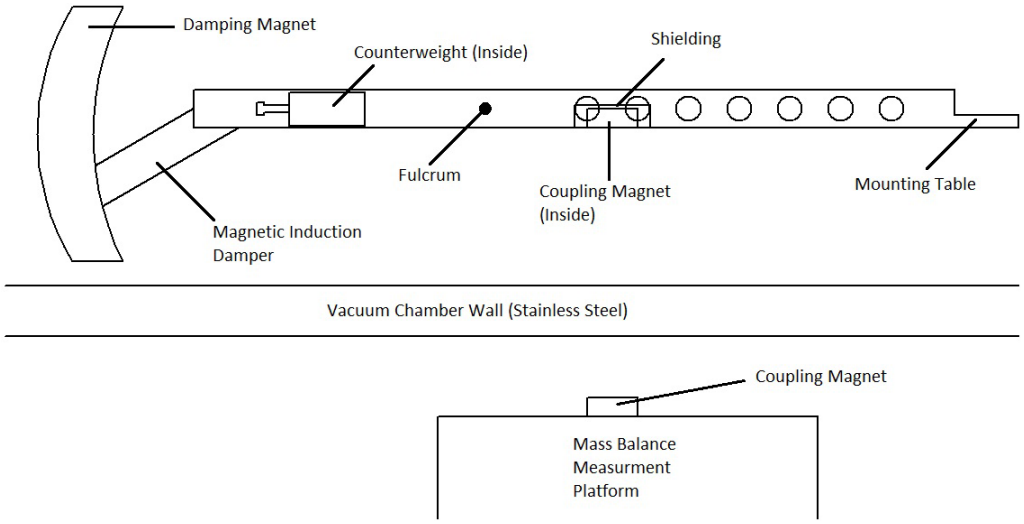

Figure 3.12.: A schematic diagram of the thrust measurement stand.

The thin, high-voltage cables used by electric propulsion systems being studied with the thrust measurement stand serve a dual-purpose; also acting as the fulcrum of the lever the thrust stand is based on. A small nulling torque is provided by the plastic insulation around the cables, acting to resist the motion of the thrust support member as it is displaced from its equilibrium position. Aligned parallel to the cables is a gas feed pipe. It is oriented in this way to minimize its interference with the operation of the thrust stand.

Two supports of height 30 mm are used to anchor the thrust support member to the 250 mm by 250 mm base. The two supports are placed on either side of the thrust support member, and the high voltage cables are clamped in place using the removable tops of the support stands. Tension in the cables can be released, which allows the thrust support member to rest on a third support on the base of the thrust stand (as shown in Figure 3.11) when the thrust stand is not in use. This allows for various tasks such as the mounting of new thrusters to be performed.

A new magnetic coupling system is used to measure thrust. A circular Alnico magnet, with a mass of 3 g and a diameter of 10 mm, can be placed at different points along the axis of the thrust support member, via a number of widened weight relief cavities. A Mettler Toledo AB204 digital mass balance is positioned outside of the vacuum chamber, as shown in Figure 3.12, and a rare earth magnet is placed in the center of its measurement platform. The motion of the thrust support member is coupled to the rare earth magnet via the Alnico magnet. The vacuum chamber should not interfere with the operation of the thrust stand as it is made from stainless steel, which is typically non-magnetic. The

walls of the vacuum chamber are 4 cm thick. This will offset any transitions to a ferritic phase because of mechanical deformation [85]. The two coupling magnets are vertically aligned via appropriate positioning of the mass balance using the visual judgement of the experimenter. The two coupling magnets are oriented so that they repel one another. Displacing the thrust support member a set amount and recording the readings displayed by the mass balance allows for the initial position of the balance to be refined. The point of correct magnet alignment is when, for a given thrust support member displacement, the readings displayed by the mass balance are the largest. It is important to note that the calibration procedure will capture any misalignment of the magnets, and therefore, the magnet alignment will not greatly impact experimental results. The sensitivity and measurement range of the balance can be adjusted by altering the position of the alnico magnet along the axis of the thrust support member.

3.2.2. Principle of Operation

The mass balance must be zeroed before any thrust measurements are made. The thruster on the mounting table generates a force by firing upwards during a thrust measurement. This force displaces the thrust support member from its equilibrium position by depressing it downwards. The repelling force between the two magnets will increase as they approach each other, and the thrust support member will come to a stop at a new equilibrium position. The measurement platform of the mass balance is depressed by the repelled rare earth magnet placed on it. This causes the mass balance to register a reading, which can be converted to Newtons. The measured thrust is extracted by comparing this reading to the calibration curve. It is important to note that the only feature of interest is the repulsive force component acting on the thrust support member, and the exact form of the magnetic field is immaterial. The reaction force of this magnetic repulsion force is what is measured by the mass balance.

3.2.3. Calibration Procedure

The system is calibrated within the thrust range of interest by using a number of previously prepared, known test masses. The masses of these test pieces are measured using a Sartorius LE225D digital mass balance, and they are fashioned into shapes that ccan be loaded onto the thrust stand, via a calibration perch attached to the mounting table. The calibration perch is made from stiff copper wire, and positioned parallel to the axis of the thrust support member.

For simplicity, the system is calibrated in open air. The heaviest mass is placed on the calibration perch after the mass balance has been zeroed. Software written in LabView is used to capture the readings from the mass balance at a sample rate of 1 Hz, which excludes transient noise, while allowing important features of the readings to be captured. The mass balance is connected to a computer via a recommended standard-232 (RS-232) connection.

Zero Drift

Mechanical loading and thermal deformations cause zero drift in many thrust measurement systems, which is difficult to avoid [86]. Any zero drift in the system is detected by monitoring and recording the mass reading on the balance for approximately half an hour. The repeatability of the zero drift is tested by removing the test mass from the balance and replacing it for a second reading once the balance has stabilized. If the zero drift is repeatable, it will give a consistent difference between the zero reading and the mass reading. Figure 3.13 depicts a graph which illustrates the output of such a test. The graph shows that the zero drift is no more than a few hundred micrograms over the test period, which is minimal compared to the test mass. It also shows that the same result is obtained when replacing the test mass. This indicates that the zero drift will not significantly affect any test results. It is important to note that different values of the zero offset can be recorded when the zero drift test is repeated. However, an identical mass reading is obtained when the measured mass is subtracted from the corresponding zero offset for the same test mass. This further illustrates the minimal impact that the zero drift has on the system.

Calibration

The balance is calibrated using the known masses once the zero drift test is complete. The calibration procedure involves hanging each test mass, starting with the heaviest, from the calibration perch in turn. The test mass is left to hang from the calibration perch for one minute, which allows the system to stabilize. This is aided by the magnetic induction damper, the effect of which is shown in Figure 3.14. The test mass is then removed, and the balance is allowed to stabilize at its zero value. Averaging and error analysis is made possible by repeating this process at least three times for each test mass. Once all the known masses have been used, an unknown test mass is hung from the calibration perch, and its reading on the mass balance recorded. This is done to test the accuracy of the calibration. Figure 3.15 depicts the raw data for an example calibration,

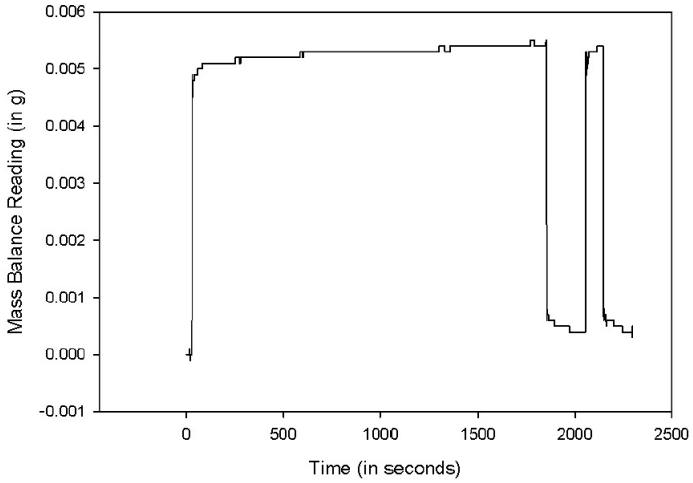

Figure 3.13.: The zero drift experienced by the thrust measurement stand over a period of approximately 30 minutes.

where only one reading is taken per test mass. This is done for illustrative purposes only. A calibration curve is obtained by plotting the mass balance readings against the masses of the test pieces. The unknown mass is then measured, and this value is compared to the value extracted from the calibration curve. The entire calibration procedure is rapid, and even novice operators have been able to complete a calibration in approximately half an hour.

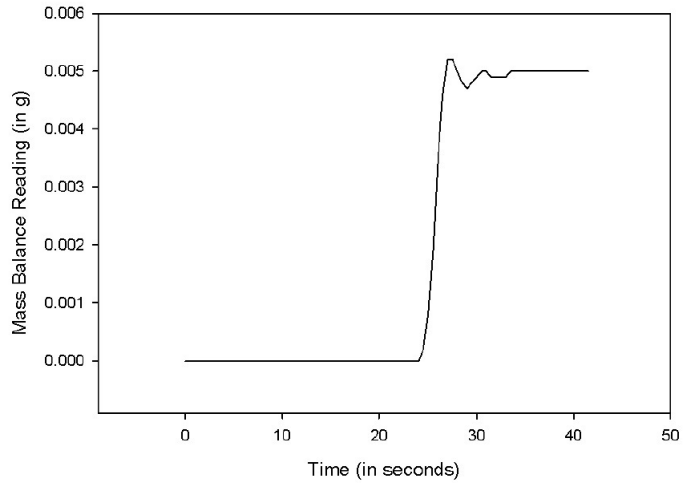

Figure 3.14.: Magnetic induction damper stabilization as indicated using the output from the thrust measurement stand.

Figure 3.16 shows a sample calibration curve. The data clearly shows a linear relationship as is desirable in thrust measurement systems [82]. Equation 3.5 shows a linear calibration curve that has been fitted to the data.

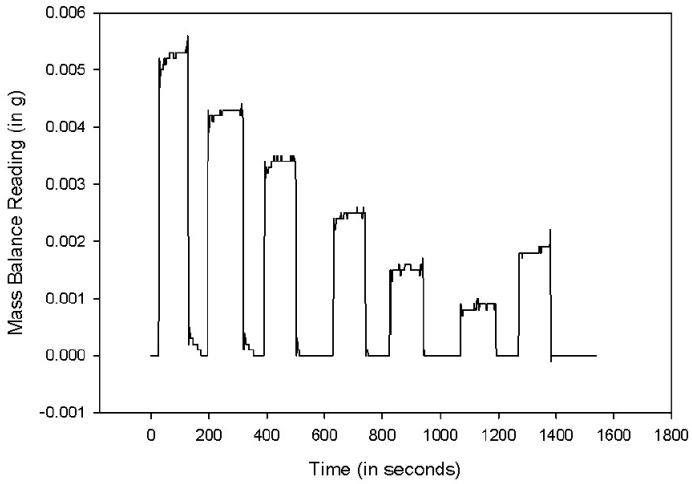

Figure 3.15.: The raw data obtained from the thrust stand for a single full calibration. The masses corresponding to the peaks from left to right are from largest to smallest and the unknown mass is the final peak.

$$M_T(x) = 2.33x + 9.61 \times 10^{-5} \tag{3.5}$$

where x is the measurement read from the thrust balance and M_T is the actual mass of the corresponding test mass. The error in the gradient was found to be 0.045 and the error in the intercept was calculated to be 10^{-5}. The actual mass of the unknown calibration mass was measured to be 0.00444 g and the extracted mass was calculated to be 0.00439 ± 0.00022 g. This shows that the predicted value is off by approximately 1% and the measured value is within experimental error tolerances.

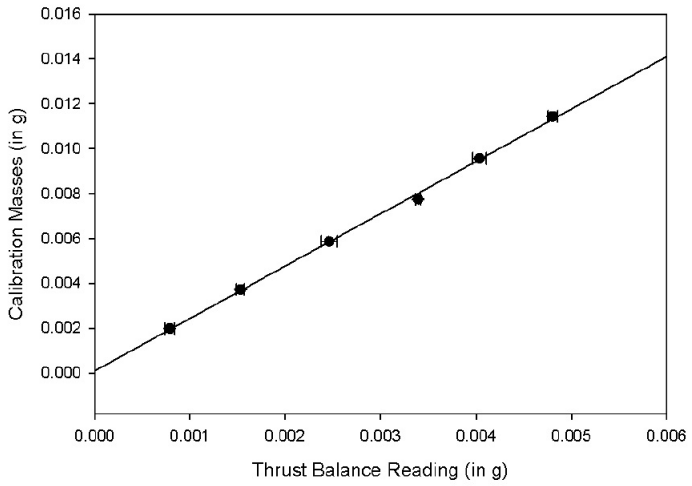

Figure 3.16.: A sample calibration curve obtained from the thrust measurement stand.

3.2.4. Theoretical Model

A similar approach to Moeller and Polzin was adopted to model the behavior of the thrust stand [87]. The application of a thrust is related to an angular displacement of the thrust support member using free body analysis. Details of the calculations involved are included in Appendix B. A free body diagram of the balance is depicted in Figure 3.17 and contains all the forces considered.

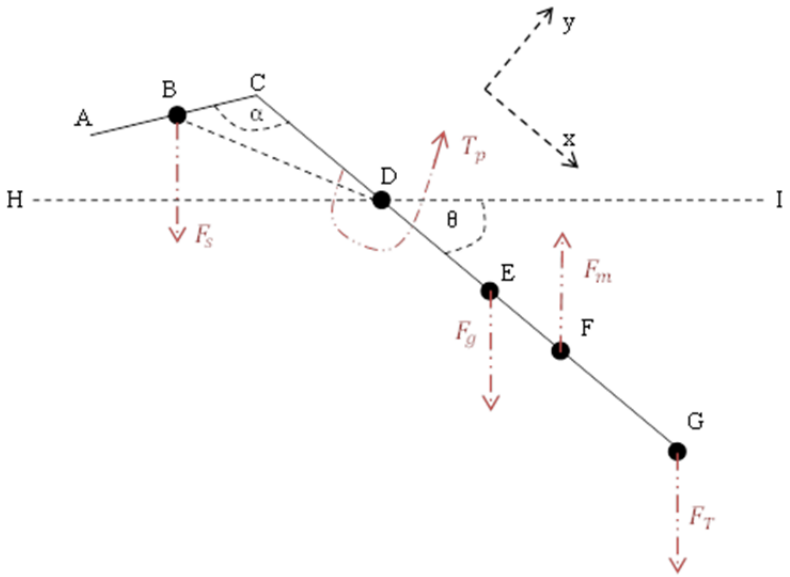

Figure 3.17.: A free body diagram of the thrust measurement stand showing all of the forces considered.

Equation 3.6 relates the angular displacement of the lever arm to the applied calibration test mass.

$$F_T(\theta) = \frac{k\theta + zm_b g \sin(\gamma) - m_a g d_1 \cos(\theta) + d_2 g M_m \cos(\theta)}{d_3 \cos(\theta)} \tag{3.6}$$

where θ is the angular displacement experienced by the thrust support member CG; F_T is the magnitude of the force applied; m_b is the mass of the magnetic induction damper AC; k is the torsion spring constant of the fulcrum of the balance; m_a is the mass of the thrust support member; g is magnitude of gravitational acceleration; d_2 is the length of DF, which is the distance from the fulcrum point to the position of the magnet inside the thrust support member; d_1 is the length of DE, which is the distance from the fulcrum point to the centre of gravity of the thrust support member; d_3 is the length of DG,

which is the distance from the fulcrum point to the mounting table and M_m is the mass measured from the mass balance outside of the vacuum chamber. These are all quantities that can be measured.

Equation 3.7 shows how to obtain the value of z in Equation 3.6, which is the length of the line segment BD. This is the distance from the fulcrum point to the center of gravity of the magnetic induction damper.

$$z = \sqrt{\left(\frac{1}{2}AC\right)^2 + CD^2 - \left(\frac{1}{2}AC\right)(CD)\cos(\alpha)} \tag{3.7}$$

The angle between the line segment BD and the gravitational force acting on the magnetic induction damper $\vec{F}_s$, as shown in Figure 3.17, is given by γ in Equation 3.6. γ can be calculated using Equation 3.8. Geometry and Trigonometry are used to obtain these expressions, and they are defined in terms of measured quantities.

$$\gamma = \theta - \arcsin\left(\frac{1}{2}AC\left(\frac{\sin(\alpha)}{z}\right)\right) + \frac{\pi}{2} \tag{3.8}$$

where α is the angle between the thrust support member and the magnetic induction damper and AC and CD are the length of the corresponding line segments.

Torsion Spring Constant

The fulcrum is approximated as a torsion spring in a manner similar to that described in [87]. This is to account for the nulling torque applied by it. The angles of deflection experienced by the thrust support member are not expected to push the fulcrum outside of the regime of Hooke's law. This means plastic deformation does not have to be considered when determining the value of the spring constant associated with the fulcrum. Slipping of the fulcrum is prevented by ensuring the high voltage cables that act as the fulcrum are tightly secured in the thrust support member and the base supports. Calculating the torsion spring constant is difficult, as the high voltage cables consist of two separate layers, a core of conducting wire and an insulating outer sheath. These form a non-trivial system to model. To circumvent this, the torsion spring constant can be measured experimentally. This process is discussed below.

The orientation of the magnetic induction damper can be altered so that $\alpha = \pi$. This will

cause the terms in Equation 3.6, accounting for the effect of the weight of the magnetic induction damper and the weight of the thrust support member, to cancel by altering the angle γ and the distance z. The magnet inside the thrust support member can be taken away, which will remove the term accounting for the force due to the magnet. The now altered model of the thrust stand is given in Equation 3.9.

$$F_T(\theta) = \frac{k\theta}{d_3 \cos(\theta)} \tag{3.9}$$

This shows that the spring constant can be extracted from the gradient of a linear fit to the angular displacement of the thrust support member, against the thrust measured from a series of known calibration masses. To obtain experimental data, the resultant angular displacement was noted when a test mass was placed on the calibration perch. Figure 3.18 depicts the resulting data and corresponding linear fit. The large errors in the angle can be reduced by increasing the length of the thrust support member.

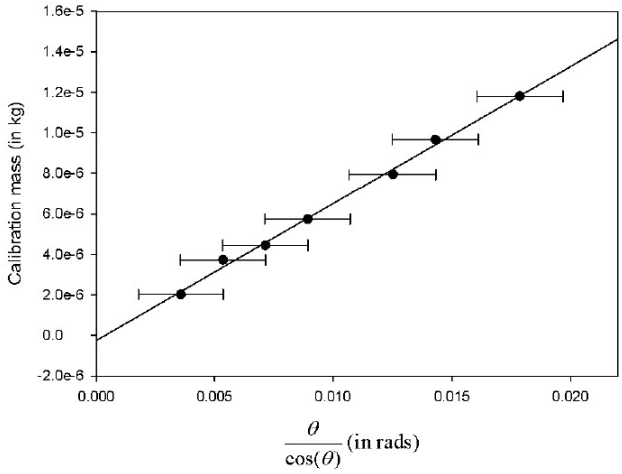

Figure 3.18.: A plot of the angular displacement of the lever arm against the known test masses used in calibration. The torsion spring constant of the fulcrum can be determined from this plot. Errors in the calibration mass are too small to appear on the plot.

From the gradient of the above graph, the torsion spring constant of the fulcrum was determined to be $0.00192 \pm 5.30 \times 10^{-5}$ Nm/rad.

Model Verification

The measured masses of the calibration test pieces are compared to their predicted masses obtained using the model. This is done to test the accuracy of the model. Table 3.1 shows

Measured Calibration Mass (in g)	Predicted Calibration Mass (in g)
0.0118 ± 0.00001	0.01151 ± 0.00033
0.00966 ± 0.00001	0.0095 ± 0.00028
0.00794 ± 0.00001	0.00752 ± 0.00025
0.00574 ± 0.00001	0.00549 ± 0.00020
0.00444 ± 0.00001	0.00363 ± 0.00016

Table 3.1.: A comparison between the measured calibration masses and the predicted calibration masses obtained from the model of the thrust measurement stand.

this comparison.

The comparison shows that the smallest calibration mass has the largest deviation associated with it, and the measured value is found to be within 18% of the predicted value. This error can be reduced by a more accurate measurement of the angular displacement of the thrust support member.

3.2.5. Adjusting Sensitivity

Figure 3.17 shows how the distances d_2 and d_1 can be varied independently by adjusting the counterweight and magnet positions. Altering the position of the magnet inside the thrust support member will alter the measurement range of the balance. This changes the repulsive force between the magnets. Three calibrations of the thrust stand were performed to test this. The same set of test masses was used, but the position of the magnet inside the thrust support member was varied to one of three different positions: a position closer to the mounting table (table magnet position); a position closer to the fulcrum of the thrust balance (fulcrum magnet position) and a central position between these two extremes (central magnet position). Figure 3.19 depicts the results of these tests. The results show a larger mass is measured by the mass balance if the magnet is located further from the fulcrum, for the same calibration mass. This indicates a rise in sensitivity if the magnet is closer to the balance.

3.2.6. Thrust Measurement

A number of cold gas thrust tests were performed on a simple cold gas thruster to test the operation of the thrust stand. The thruster used was similar to those used as the basis of the CorIon system [28], and consists of a 5 mm long needle, with an internal diameter of 0.184 mm. The thrust measurement stand was placed inside the vacuum

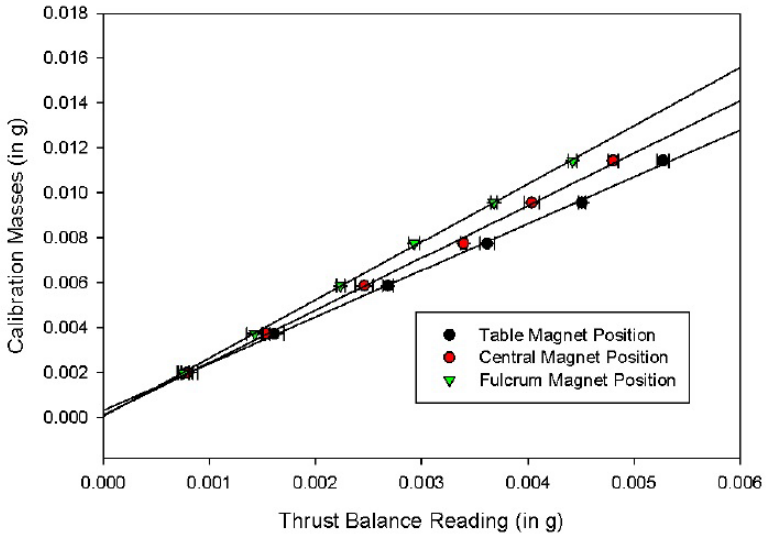

Figure 3.19.: A plot showing the effect of magnet position on thrust stand sensitivity.

chamber after the thruster was mounted to the mounting table, and the system was then calibrated. Vacuums of approximately 4×10^{-5} torr were used in all tests. The propellant used was air, at mass flow rates ranging from 0.1 mg/s to 0.3 mg/s. Averaging and error analysis were facilitated by taking three measurements for each mass flow rate. The process of calibrating the balance and taking a set of measurements takes no more than an hour. This excludes the time it takes to pump down the vacuum chamber. These short measurement times allow for rapid turnaround times and for multiple tests to be run.

The zero reading of the mass balance decreases steadily and then increases sharply when the vacuum chamber is initially pumped down upon. This change in the zero value of the balance when the thrust stand is under vacuum is because the medium that the thrust stand is in is changing as the chamber is being evacuated. This is similar to when a floating object is placed in a new medium with a different density. In this case, the thrust stand experiences an effective change in the buoyancy force, which was supporting the thrust stand when it was in air. Upon completion of this adjustment, a new equilibrium position is reached. If an in situ calibration system can be developed, the effect of these phenomena could be negated.

Results

Figure 3.20 shows the results of the cold gas thrust measurement. A linear relationship is clearly seen in the data, which corresponds to the results obtained by others [88].

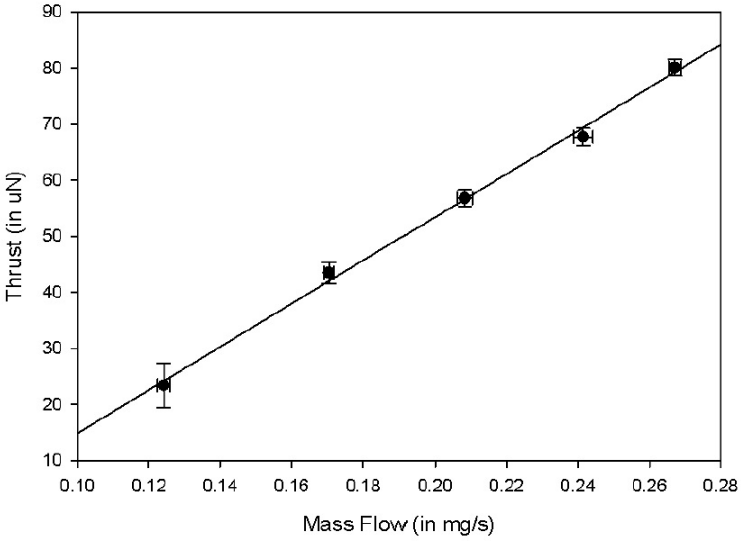

Figure 3.20.: A plot of the measured thrust of a simple cold gas thruster as the mass flow rate is varied.

Equation 3.10 gives the resulting curve that was fitted to the data.

$$F_T = 385\dot{m} - 23.7 \tag{3.10}$$

Repeatability

Any piece of measurement equipment needs to provide consistent results. Repeatability ensures that any flucuations experienced during an experiment are due to the system under study and not the measurement apparatus. Another two thrust measurements were performed on the cold gas thruster to test the repeatability of the thrust stand. Figure 3.21 shows the comparison between the results of all three thrust measurements.

The results of the tests indicated that the largest fluctuations in the data are within no more than 20%, but, when considering the rest of the data, it would appear that this data point is an outlier. This is because the fluctuations observed around other data points are much smaller. This suggests that the system exhibits good repeatability.

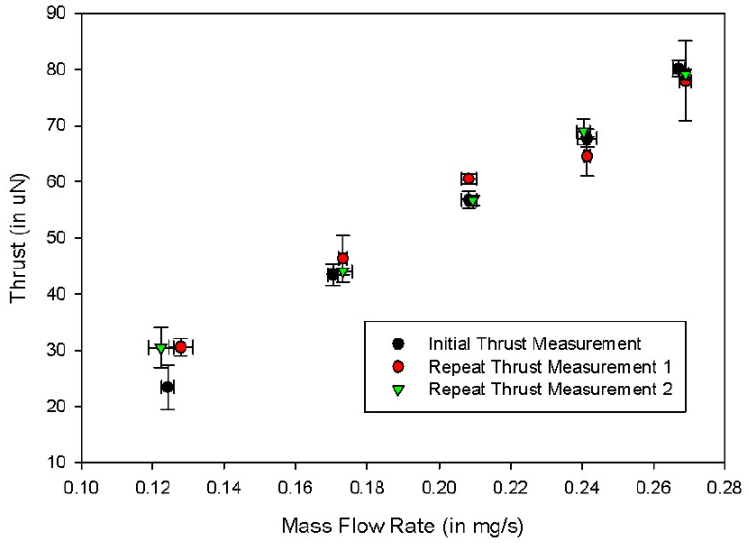

Figure 3.21.: A plot comparing the thrust measurements of the three identical thrust tests to check for repeatability

3.2.7. Costing

One of the primary advantages of using the system described above, is that it offers a much more cost-effective alternative to other available systems. Taking into account that the system was designed and built in South Africa, the material costs of the thrust measurement stand amounted to no more than 25 US dollars, using the exchange rate at the time of writing. A digital mass balance would be the most expensive component of the thrust stand, and this system was designed and built under the assumption that such a balance would be available in most laboratories. Including the price of a reasonably accurate mass balance, for example, a Sartorius ENTRIS124-1S Analytical Balance, would add between 1000 and 1500 US dollars to the cost of the thrust measurement stand at time of writing. The cost of labour is not taken into account when pricing the system, as constructing the thrust stand is a simple procedure and labour costs would not be appreciable.

A clear price advantage becomes apparent when comparing the system described here to more conventional thrust measurement systems. In South Africa, at the exchange rate at time of writing, a torsion style thrust measurement balance, that was designed and built in the laboratory [89], cost approximately 4500 US dollars in parts alone. The balance was complex in nature, and the time and labour spent on designing and developing the system added an additional 4500 US dollars to the price. These numbers indicate that the thrust stand described in this work holds a clear advantage over other more conventional systems in terms of cost. It is important to note that this design can be

modified by substituting construction materials that would improve its robustness and allow it to support a greater variety of thruster designs, much like more conventional thrust measurement systems. These modifications would not add substantial costs to the system.

3.3. Procedure

In this section, the process of performing certain general operations, such as mounting of thrusters, are discussed, and the details and experimental procedures of specific tests are presented.

3.3.1. Mounting Thrusters to the Thruster Mounting Table

Once a thruster has been assembled, as described previously, the thruster to be tested is attached to a PVC plastic mounting block, using silicone sealant, and the wires connected to the electrodes inside the thruster are fed to the underside of the mounting block via holes drilled through it. Figure 3.22 shows a photograph of an assembled proof of concept, straight, discharge tube, about to be mounted to the thruster mounting table. The wires are then fed into channels machined into the underside of the mounting block. These channels lead the exposed ends of the wires to points on the underside of the block, which correspond to the position of the pressure contact screws on the top half of the thruster mounting table. Nylon screws secure the mounting block to the thruster mounting table and facilitate the pressure contacts. This configuration prevents any wires from being exposed to the surrounding vacuum and plasma resulting from thruster operation. The gas inlet attachment is inserted into the gas inlet on the thruster to facilitate the connection of the thruster to the propellant flow system. The gas inlet attachment is secured in place with silicone sealant. Before any experiments are performed, the silicone is left to dry for one hour to ensure it is set and stable. Once this time period has elapsed, the gas inlet attachment is connected to the propellant flow system using a silicone tube.

3.3.2. Mounting Thrusters to the Thrust Measurement Stand

Once a thruster has been assembled, as described previously, a gas inlet attachment is inserted into the gas inlet of the thruster to facilitate the connection of the thruster to

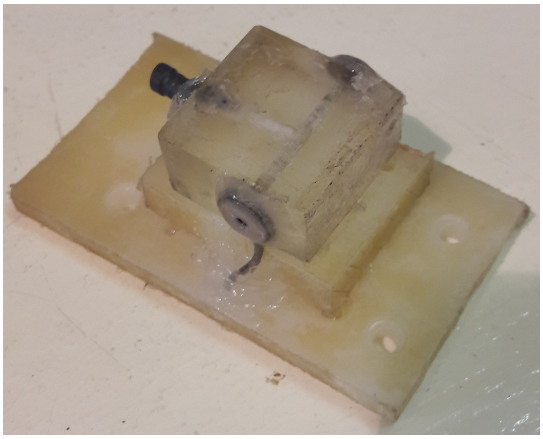

Figure 3.22.: A photograph depicting an assembled, proof of concept, straight, discharge tube ready to be mounted to the thruster mounting table.

the propellant flow system. The gas inlet attachment is secured in place with silicone sealant. The thruster to be tested is then attached to the mounting table at the end of the thrust support member using silicone sealant. Care is taken to ensure that the thruster is level and that it is not offset to one side. If the thruster is not level or is offset, the thrust vector will not be correctly aligned with the balance and results will be affected. The silicone sealant is allowed to dry for a period of one hour before any further connections are made. Figure 3.23 shows a photograph of an assembled thruster about to be mounted to the thruster mounting table

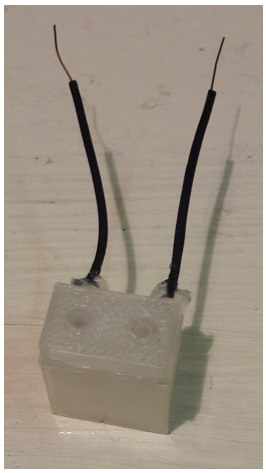

Figure 3.23.: A photograph depicting an assembled, 'U-shaped' thruster ready to be mounted to the thrust measurement stand. Note the hexagonal grain in the plastic, an artefact of the 3D printing process.

To provide electrical connections, two small pieces of electrical stripboard are used. Each piece of stripboard consists of no more than one connected strip and three holes. One piece of stripboard is used to connect the positive terminal of the power supply to the

thruster, and another is used to connect the grounded terminal of the power supply to the thruster. A wire connected to an electrode on the thruster is positioned in a hole on one end of each piece of stripboard and soldered in place. A high voltage lead used in the construction of the thrust measurement stand is positioned in a hole on the other end of the same piece of stripboard and soldered in place. The piece of stripboard and any exposed wires are then coated in silicone sealant to insulate them, as well as to prevent interactions with the resulting plasma. This process is repeated with the second piece of stripboard, after which the silicone is left to dry for one hour. Once the silicone is dry, these electrical connections are inserted into the hollowed thrust support member, so that they cannot interfere with the operation of the thrust measurement stand. The other ends of high voltage leads are connected to the copper high voltage connectors at one of the access ports via insulated crocodile clips.

3.3.3. Evacuating the Vacuum Chamber

A thruster is mounted in the chamber, as described previously, and the digital camera used in the data acquisition system is activated and focused on the thruster, while the vacuum chamber is open and there is sufficient light. The chamber is sealed and pumped down, using the roughing and backing pumps, until an appropriate vacuum is reached. Typically, pressures of 5×10^{-4} torr and lower are considered acceptable. This is because higher pressures would result in too soft a vacuum once propellant is introduced into the simulated space environment. Introducing a high voltage at such pressures could result in destructive ionization occurring in the chamber. If the pressure is too high upon the first pumping down of the chamber with a new thruster, the pumps are left to continue pumping on the chamber, in order to afford the plastics used the opportunity to outgas. If further problems are experienced, the pumps are deactivated and the chamber is vented so that all the relevant seals and vacuum connections can be checked.

3.3.4. Mass Flow Rate, Voltage and Current Tests

The primary goal of these tests is to determine under what operating conditions the thruster under study will fire. This has the added benefits of allowing different operating regimes and phenomena to be observed, as well as placing a boundary on the operating conditions that allow for stable system operation.

Procedure

The thruster under study is mounted to the thruster mounting table, and the procedure for pumping down the vacuum chamber is followed, as described previously. Air is the propellant used throughout these tests. The mass flow rates chosen for these tests were selected to span the entire calibrated range of the mass flow measurement system, and were spaced equally apart from one another. The mass flow rates studied were approximately 0.21 mg/s, 0.36 mg/s, 0.47 mg/s, 0.55 mg/s and 0.62 mg/s.

First, a set of current-varying measurements are performed. This is achieved by setting a constant voltage of 8000 V on the high voltage power supply, and varying the current from 200 μA to 4000 μA, in steps of 200 μA. Once the voltage and current are set, the high voltage supply is activated, and the digital video camera is used to record footage of the thruster in operation for 5 seconds. When 5 seconds have elapsed, the high voltage is deactivated. This is to minimize thruster damage that may result from any unexpected behavior. The current is then increased and the above process is repeated. When the entire current range has been explored, the mass flow rate is increased to the next value to be studied, and another set of current varying readings are taken. This procedure is repeated until all the mass flow rates under consideration have been explored.

The process for performing voltage-varying measurements is almost identical to that for taking current-varying measurements. When setting the parameters of the high voltage power supply, a constant current of 4000 μA is set, and the voltage is varied between 500 V and 8000 V, in steps of 500 V.

When a full set of current-varying and voltage-varying reading have been taken across all the mass flow rates of interest, the vacuum chamber is vented, and the pumps deactivated.

3.3.5. Lifetime and Erosion Tests

A trait that will determine the usability of any propulsion system, is how long it can operate without failure. If a system is highly efficient, but can only operate for short periods, then it has limited practical use. This is especially important when considering plasma based propulsion systems, where the erosion of system components hampers operation. By studying the erosion characteristics of a system, the greatest contributing factors to lifetime limitation can often be determined. These tests are particularly useful here, as one of the failings of the CorIon concept was its lifetime. This was due to the erosion

of the needles the system consisted of. Due to the proposed mechanism of operation of the new system, it is highly likely that the electrodes will also be the point of failure of the new system, and therefore, they will be the focus of erosion testing. These tests will show if the new system is able to address the operational failings of the CorIon system.

Procedure

The thruster under study is mounted to the thruster mounting table and the vacuum chamber is pumped down. Intermediate operating parameters of a 0.47 mg/s mass flow rate, a 2000 μA current and an 8000 V voltage are set and maintained throughout the experiment. The high voltage supply is activated, and the thruster being studied is left to run for a period of 5 hours. Every hour, the operating parameters are checked, and a visual inspection of the thruster is made to determine if there have been any changes to the thruster's operation. After 5 hours of operation or thruster failure, the high voltage supply is deactivated, the vacuum chamber is vented, and the vacuum pumps deactivated. The thruster being studied is then dismounted from the thruster mounting platform, taking care to not introduce any external contaminants or impurities. The thrusters are dismantled, and the electrodes removed. These electrodes are cleaned in an ultrasonicating bath, and placed inside a Topcon SM510 Scanning Electron Microscope (SEM), along with a control electrode, so that images can be taken of any damage.

3.3.6. Repeatability

If a thruster produces erratic and varying thrust for the same sets of operating parameters, then the thrust produced cannot be predicted and used when planning missions. Missions will frequently require that a thruster produces a set thrust for a set period of time to perform a manoeuvre. If the thrust produced is unstable, it is possible the thruster will either over- or undershoot its target, which could have catastrophic consequences. This means repeatability tests need to be performed, to ensure that when the thruster operates, it produces the same results, without extreme variations that could compromise its operation.

Procedure

The thruster under study is mounted to the thruster mounting table and the vacuum chamber is pumped down. Intermediate operating parameters of a 0.47 mg/s mass flow

rate, a 2000 μA current and an 8000 V voltage are set and maintained throughout the experiment. The high voltage supply is activated, and the thruster is left to fire for a period of one minute. Voltage, current and mass flow rate are recorded throughout the minute of operation. The high voltage power supply and the mass flow are then deactivated for a period of one minute. This process is repeated 20 times. Upon completion of the 20 thruster firings, the vacuum chamber is vented and the pumps deactivated.

3.3.7. Thrust Measurements

In this test, the variation of the thrust produced by the system, as the main operating parameters are varied, is measured. The three main operating parameters to be varied are the mass flow rate of propellant through the thruster, the current flowing through the electrodes, and the voltage drop across the electrodes.

Procedure

The thruster under study is mounted to the thrust stand, which is then positioned inside the vacuum chamber, and calibrated, as previously described. The vacuum chamber is pumped down. The propellant used throughout all these tests was argon. The mass flow rate is set using the commercial mass flow rate measurement system, described previously. The data acquisition system is prepared, and the voltage and current to be used for the thrust measurement are set.

When a reading is ready to be taken, the data acquisition system is activated, and the mass flow is turned on. This causes a cold gas thrust to be measured by the data acquisition system. The system is left to capture this data for a period of 30 seconds. Once this period has elapsed, the high voltage power supply is activated so that the thruster begins to generate a plasma. The thruster is observed through the viewing port, to ensure that it is firing correctly and that no anomalies are present. The data acquisition system is also set to record the voltage drop across the electrodes and the current flowing through the thruster. The system is left to capture this data for a period of 30 seconds. Once this period has elapsed, the high voltage power supply and the voltage and current data acquisition system are deactivated, and a cold gas thrust is measured for a period of 30 seconds. The propellant flow is then deactivated, and a zero measurement is made for 30 seconds. This process is repeated 20 times, while retaining the same mass flow rate, voltage and current. This is to obtain a number of data points for the facilitation of error analysis and averaging. Once 20 data points have been captured, the parameter

currently being studied (mass flow rate, voltage or current) is changed to the next value to be studied, and the process is repeated, until the entire range of the varied parameter has been explored. The process is then repeated for a different operating parameter, whose effect is to be studied.

The mass flow rates studied in these tests are: 10.1 sccm, 14.5 sccm, 17.5 sccm, 20.2 sccm and 22.2 sccm. The voltage range that was studied in these tests was between 2000 V and 8000 V, increasing in steps of 2000 V. The current range that was explored in these tests was between 1000 μA and 4000 μA, increasing in steps of 1000 μA.

Data Processing

From a single set of 20 data points, two readings can be obtained, namely a cold gas thrust, and a thrust obtained with the high voltage power supply active (a hot gas thrust). These are obtained by taking each individual cold gas reading recorded for 30 seconds, and averaging these readings. The same is done to the hot gas reading and the zero reading. The zero reading is then subtracted from both the hot gas and the cold gas readings. This is repeated 20 times for each of the 20 data points. The thrust measurement stand calibration curve is applied to each of these 20 data points. From these data points, an average and an error is calculated, while discarding any extreme outliers.

3.3.8. Ion Current Density Measurements

In these tests, the ICD produced by the thruster is measured using a Faraday cup probe. The ICD is measured, while the operating parameters of the thruster under study are varied. The position of the probe is also varied, so that an indication of the ICDD can be obtained.

Procedure

Varying Operating Parameters The thruster under study is mounted to the thruster mounting table, as previously described. The Faraday cup probe is initially positioned so that it is level with the outlets of the thruster. The probe is then moved backwards, so it is 20 cm away from the thruster outlets, and the procedure for pumping down the chamber is followed, as previously described.

First, a set of mass flow rate varying measurements are performed. The mass flow rates studied in these tests are: 10.1 sccm, 14.5 sccm, 17.5 sccm, 20.2 sccm and 22.2 sccm. A constant voltage of 8000 V and a constant current of 2000 μA, are set on the high voltage power supply. Next, the propellant flow is set and activated. The high voltage power is then activated. While the thruster is firing, the digital oscilloscope screen is monitored for signs of a voltage signal resulting from the ion current produced from the thruster. When a stable signal is obtained, the signal is saved by the digital oscilloscope onto an external storage device, and the high voltage power supply is deactivated. This process is repeated 10 times, so that a number of different voltage signals can be obtained for the same operating parameters. This allows for averaging and error analysis. Once all ten readings have been obtained, the gas flow is shut off, the next mass flow rate is set, and another set of readings is taken. This procedure is repeated until all the mass flow rates have been explored.

The process for performing varying voltage and varying current measurements is almost identical to that for taking varying mass flow rate measurements. In the varying current case, a constant voltage of 8000 V is set on the high voltage power supply, and a constant mass flow rate of 17.5 sccm is set on the mass flow measurement system, while the current is varied from 1000 μA to 4000 μA, in steps of 1000 μA. In the varying voltage case, a constant current of 2000 μA is set on the high voltage power supply, and a constant mass flow rate of 17.5 sccm is set on the mass flow measurement system, while the voltage is varied from 2000 V to 8000 V, in steps of 2000 V.

Varying Probe Position The thruster under study is mounted to the thruster mounting table, as previously described. The Faraday cup probe is initially positioned so that it is level with the outlets of the thruster. The probe is then moved backwards, so it is 20 cm away from the thruster outlets, and moved 10 cm to the right. The probe is rotated, so that the entrance hole is facing the thruster, and the procedure for pumping down the chamber is followed, as previously described.

A constant current of 2000 μA and a constant voltage of 8000 V are set on the high voltage power supply. A mass flow rate of 17.5 sccm is set on the mass flow measurement system and the gas flow is activated. The high voltage power supply is then activated. While the thruster is firing, the digital oscilloscope screen is monitored for signs of a voltage signal resulting from the ion current produced from the thruster. When a stable signal is obtained, the signal is saved by the digital oscilloscope onto an external storage device, and the high voltage power supply is deactivated. This process is repeated 10 times, so that a number of different voltage signals can be obtained for the same operating

parameters. This allows for averaging and error analysis. Once all ten readings have been obtained, the gas flow is shut off, and the vacuum chamber is evacuated.

Upon completion of a measurement, the probe is repositioned so that it is still 20 cm away from the thruster, but 10 cm to the left of the central position. The probe is once again rotated so that the entrance hole is facing the thruster. The same process for taking readings previously described is performed. Readings are taken for a total of 6 different positions around the vacuum chamber, which are illustrated in Figure 3.24.

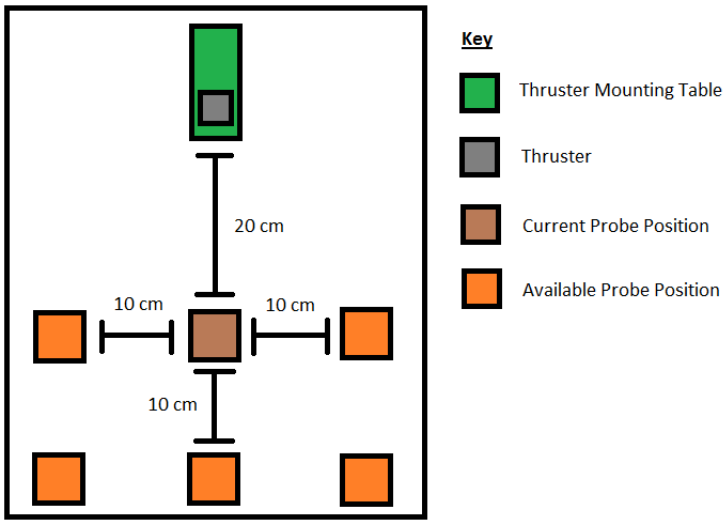

Figure 3.24.: A diagram illustrating the 6 probe positions ion current density measurements are taken from. In each case the probe is rotated so that the probe entrance faces the thruster.

4. Experimental: Results and Discussion

In this chapter, the results of the previously described experiments will be presented. These include: mass flow rate, voltage and current tests; lifetime, erosion and repeatability tests; thrust measurements and ICD measurements

4.1. Mass Flow Rate, Voltage and Current Tests

Here, the results of tests to determine if the proof of concept, straight, discharge tube and the 'U-shaped' thruster will fire are presented. The results of testing the 'U-shaped' thruster across the range of available operating conditions, to determine viable operating parameters are also given.

4.1.1. Proof of Concept Straight Discharge Tube

Test Firing

When the propellant flow is activated, and propellant gas is flowing through the proof of concept, straight discharge tube without any voltage drop across the electrodes, the interior of the vacuum chamber remains dark, due to the lack of a discharge. When the high voltage power supply is activated, and the current increased, a purple discharge becomes visible inside the discharge channel. The light emitted by the discharge increases in overall intensity as the current is increased. Different regions of the discharge are clearly visible across the length of the discharge channel, as indicated by variations in the colour and local intensity of the emitted light. At lower currents, the discharge appears to be confined to the discharge channel. As the current is increased further past a threshold value, plumes spontaneously appear from the open ends of the discharge tube. A large,

bright plume emanates from the end of the discharge tube to which the live electrode is attached, and a smaller less bright plume emanates from the end of the discharge tube to which the grounded electrode is attached. Figure 4.1 shows a photograph of the proof of concept, straight, discharge tube in operation. The two plumes and the discharge inside the discharge channel are all clearly visible. The formation of plumes at the open ends of the discharge channel is indicative of charged and excited particle species exiting the proof of concept system. This behavior supports the original design hypothesis, as charged and excited species could dominate over, or add to, the cold gas thrust produced by such a system. This confirms that the thruster concept could be viable.

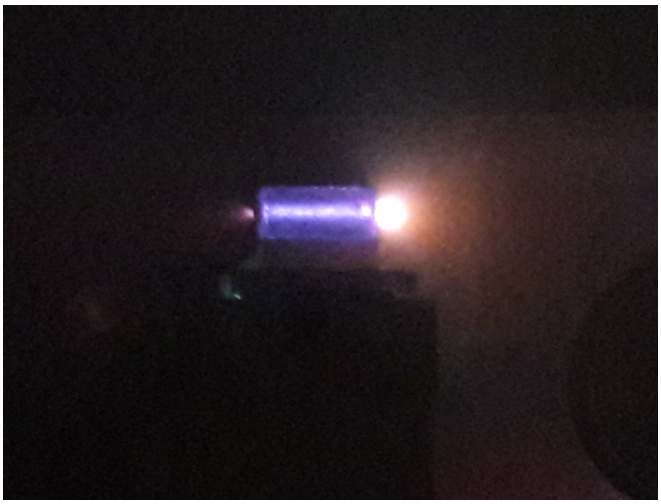

Figure 4.1.: A photograph of a proof of concept, straight, discharge tube in operation.

IV Characteristics

Figure 4.2 A) shows the voltage versus current curve for the proof of concept system taken at two different mass flow rates, 0.675 mg/s and 0.611 mag/s. The voltage curve show a rapid increase to a peak, followed by a drop in voltage and a near linear increase in voltage with increasing current. The initial sharp increase in voltage with increasing current corresponds with the discharge being confined between the electrodes in the discharge channel. The peak corresponds with initial plume formation, and the linear increase in voltage with increasing current corresponds with continuous plume formation at the electrodes. The higher mass flow rate exhibits lower voltages for the same current values in general. This is due to the greater gas density at higher mass flow rates. The shape of the voltage versus current curve for both mass flow rates is the same.

Figure 4.2 B) shows the power versus current curve for the proof of concept system taken at two different mass flow rates, 0.675 mg/s and 0.611 mag/s The power versus current

curve is linear with a slight deviation from linearity present at the point where continuous plume formation is observed to occur.

Figure 4.2 C) shows the resistance versus current curve for the proof of concept system taken at two different mass flow rates, 0.675 mg/s and 0.611 mg/s. The resistance versus current curve shows an exponential decrease with increasing current. This indicates the gas is becoming more conductive and points to greater ionization of the propellant gas as the current is increased.

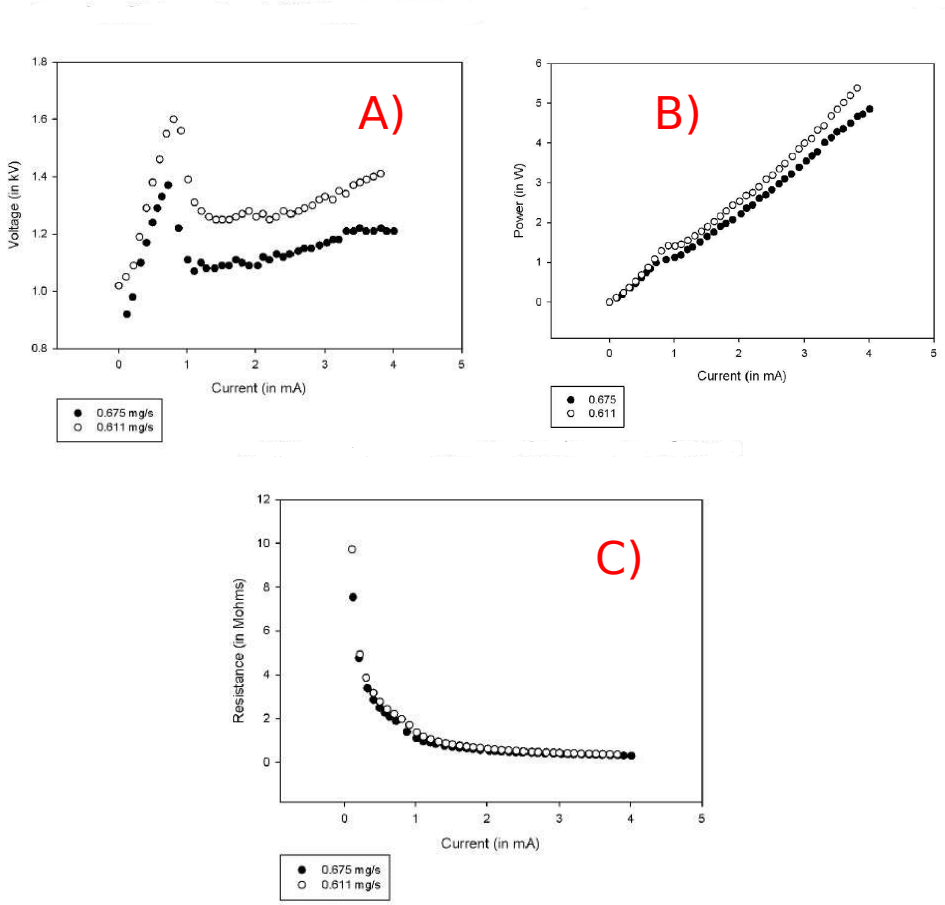

Figure 4.2.: A series of graphs depicting: A) the voltage versus current curves for the proof of concept system at two different mass flow rates, B) the power versus current curves for the proof of concept system at two different mass flow rates and C) the resistance versus current curves for the proof of concept system at two different mass flow rates

4.1.2. 'U-Shaped' Thruster

Test Firing

When the propellant flow is activated, and propellant gas is flowing through the 'U-shaped' thruster, without any voltage drop across the electrodes, the interior of the vacuum chamber remains dark, as seen previously with the proof of concept, straight, discharge tube. When the high voltage power supply is activated and the current increased, a purple discharge becomes visible inside the discharge channel. The light emitted by the discharge increases in overall intensity as the current is increased. It is more difficult to visually discern different regions of the discharge in the 'U-shaped' thruster than when studying the proof of concept system. At lower currents, the discharge appears to be confined to the discharge channel. As the current is increased further past a threshold value, plumes spontaneously appear from the open ends of the discharge tube. This is shown in Figure 4.3. A large, bright plume emanates from the end of the discharge tube to which the live electrode is attached, and a smaller, less bright plume emanates from the end of the discharge tube to which the grounded electrode is attached. The formation of plumes is indicative of the ejection of charged and excited particles that could dominate over, or improve on the cold gas thrust produced by the system. This suggests that further study is warranted.



Figure 4.3.: A photograph of a 'U-shaped' thruster in operation.

Current Varying Tests

In current varying tests, when the current is increased from its minimum value up to the maximum value studied, the light emitted by the discharge is observed to increase in intensity, irrespective of the mass flow rate being explored. This is to be expected, as with an increase in current, comes an increase in the number of electrons that can potentially participate in ionization and excitation collisions with neutrals. More excitation collisions will result in a greater intensity of emitted light [90].

At the lowest current values studied, less than 1000 μA, no plume formation is observed. A purple glow discharge is observed between the electrodes inside the discharge channel of the thruster. This can be seen in Figure 4.4 A). The intensity of the light emitted from the discharge increases as the current is increased. Once a threshold value is reached, typically around 1000 μA, plumes spontaneously appear from the open ends of the discharge channel.

At lower discharge currents, between 1000 μA and 2000 μA, plume formation is observed, but is not stable. The plumes splutter in and out of existence. Stable plume formation occurs in the region of 2000 μA to 3000 μA, whereas at higher discharge currents, greater than 3000 μA, there appears to be a transition from a stable DC discharge mode of operation, shown in Figure 4.4 B), to a 'corona' DC discharge mode of operation, shown in Figure 4.4 C). The stable DC discharge mode of operation is characterized by the presence of a visible discharge in the thruster discharge channel, from which the resulting plumes emanate. The 'corona' DC discharge mode of operation is characterized by the lack of a visible discharge in the thruster discharge channel, and one plume seemingly emanating directly from the electrode. Further investigation is required to verify that this is in fact the case.

Voltage Varying Tests

In voltage varying tests, when the voltage is increased from its minimum value up to the maximum value studied, smaller voltages (typically lower than 1500 V) yield no visible discharge, even when the maximum current limit was applied. This is to be expected, as these lower voltages are not enough to initiate breakdown in the propellant gas. Further increase in the voltage would result in breakdown.

As the mass flow rate is varied, it is observed that the breakdown voltage also changes. The lower the mass flow rate, the higher the breakdown voltage, the highest observed

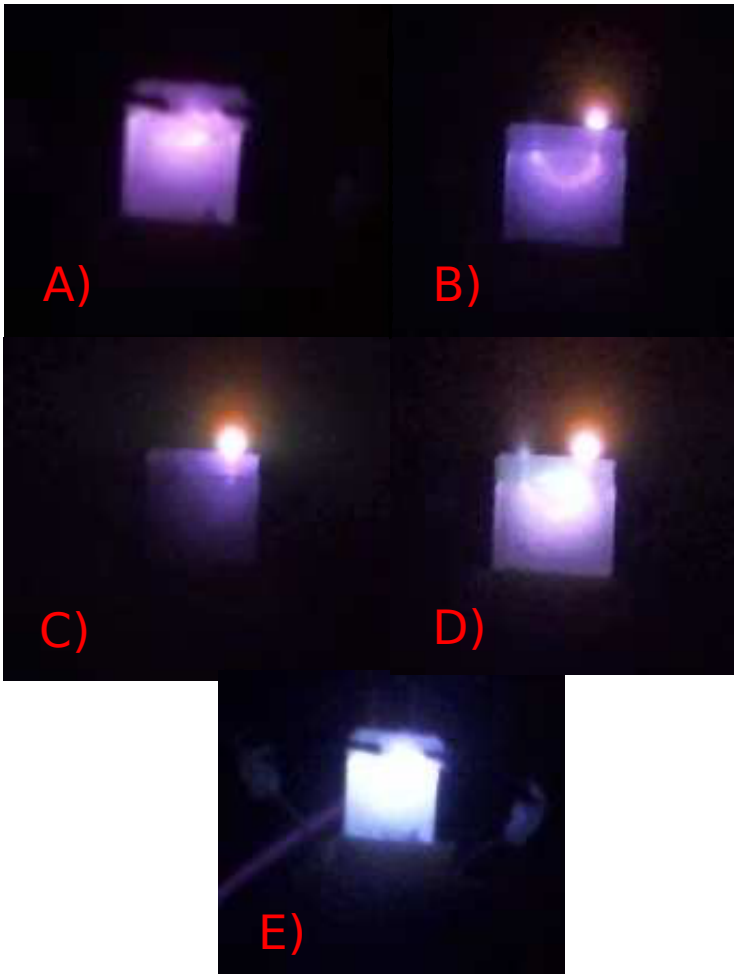

Figure 4.4.: A series of video stills depicting the 'U-shaped', direct current discharge based thruster in the various observed modes of operation: A) the discharge confined to the thruster channel with no visible plumes; B) the thruster exhibiting a stable direct current discharge mode of operation with a plume visible; C) the thruster in a 'corona' discharge mode of operation with a plume visible; D) the thruster exhibiting continued plume formation while arcing is occurring between electrodes and E) the thruster experiencing arcing between electrodes and discharge expansion into the supply pipe.

being approximately 2000 V. This phenomenon is expected, as it conforms to the predictions of Paschen's law [91]. Equation 4.1 shows the expression for the mass flow rate of an ideal, isentropic, compressible gas flow [92]:

$$\dot{m} = \frac{P_t}{\sqrt{RT_t}} A\sqrt{\gamma} M \left(1 + \frac{\gamma - 1}{2} M^2\right)^{\frac{\gamma+1}{2-2\gamma}} \tag{4.1}$$

where A is the area through which the fluid is flowing, P_t is the stagnation pressure of the flow, T_t is the stagnation temperature of the flow, γ is the ratio of the specific heats of the fluid, R is the gas constant of the fluid, and M is the Mach number of the flow. It can be clearly seen that the mass flow rate is dependent on the pressure of the flow. Therefore, a change in mass flow rate will change the pressure inside the discharge channel, assuming all other variables remain constant. Since the distance between the electrodes remains constant, the only parameter that will influence the breakdown voltage will be the mass flow rate. In the range of mass flow rates under study, no minimum in the breakdown voltage was observed. This could indicate that the minimum occurs at higher mass flow rates than those studied in this work.

Varying Mass Flow Rate Tests

The lowest mass flow rates explored (approximately 0.21 mg/s and 0.15 mg/s), result in the thruster exhibiting erratic behavior. The discharge would extend backwards into the propellant supply pipe, which connects the thruster to the mass flow measurement system. Arcing between electrodes is also observed, which would result in damage to the thruster. The arcing would occur inside the thruster body, which is indicative of damage to the acid free adhesive acting as an insulator between electrodes. These effects could be mitigated by a more appropriate choice of insulator material, which could better withstand such environments. The arcing and discharge expansion phenomena are shown in Figure 4.4 E).

In situations where the thruster was damaged due to the arcing observed at low mass flow rates, testing was extended to study the thruster's ability to continue functioning after experiencing damage or failure. It should be noted that, even after arcing damage, plume formation is still observed to occur, indicating that thrusters can still operate once they have been damaged. This is advantageous to note when considering this system for space flight. This phenomenon is shown in Figure 4.4 D). At mass flow rates greater than 0.21 mg/s, the thruster operated without arcing and plume formation was once again observed.

General Comments

Under circumstances where stable plume formation was observed, according to the hypothesized mechanism of operation, one would expect that stable plumes would form at both the grounded and live electrodes, but all observations of stable plume formation showed a stable plume emanating from the live electrode, and the sporadic formation of a plume at the grounded electrode, accompanied by sparking on the chamber walls. It is hypothesized that this phenomenon is caused by a charge build up, due to the inherent difference in production rates of charged species present at each electrode. This difference is because most heavy ions will be attracted towards the grounded electrode, where they will either be ejected from the thruster in the plume, or they will impact on the electrode, releasing more electrons via secondary emission. Because of this, many more electrons are produced at the grounded electrode than the positively charged electrode and, as the ends of the thruster are open, charged particles are allowed to escape, resulting in a charge imbalance. Further testing is required in order to confirm this. If such is the case, a possible solution would be to use electrodes with orifices of different sizes. The electrode with the smaller electrode orifice would be connected to the positive terminal of the power supply. This would expose more of the electrode surface area to the plasma, in an attempt to increase the charged species production rate at this electrode to mitigate charge imbalances.

It should be noted that in all footage taken, there appears to be yellow light emanating from the plasma plume resulting from the discharge. This was not the case when observed with the naked eye. The plume was observed to be predominately violet/pink, as is expected from nitrogen [93], the dominant component of air. This phenomenon is most likely an effect created by the digital camera used to record footage, which was not designed for scientific work.

It was generally noted, that stable operation could be observed at mass flow rates greater than 0.36 mg/s, at intermediate values of voltage (greater than 2000 V) and current (greater than 2000 μA). It was also noted that changing the current had a much greater impact on the visual characteristics of the system than changing the voltage.

4.2. Lifetime, Erosion and Repeatability Tests

Here, the results of the lifetime, erosion and repeatability tests performed on both the proof of concept, straight, discharge tube and the 'U-shaped' thruster are presented.

4.2.1. Proof of Concept Straight Discharge Tube

Lifetime

The purpose of these tests was to determine if the novel thruster concept proposed in this work could address the lifetime shortfalls of the CorIon system. To determine if this is the case, the new system should run in a stable configuration for an extended period of time, surpassing that of the CorIon system.

At this point, it is pertinent to provide a definition of stable operation in this context. After observing the thruster's behavior under a variety of different operating conditions in previous tests, stable operation is defined as being a state where a discharge is visible inside the thruster discharge channel, and two plumes are observed to be emanating from the electrodes. The sporadic formation of one of the plumes, due to charge imbalance, was deemed to be an acceptable feature when considering stable operation. However, the spluttering and sporadic formation of both plumes was deemed to be a disqualifying feature when considering stable operation. If only the discharge inside the thruster discharge channel was observed, without any plume formation, this was not considered to be stable operation. If arcing between the electrodes was observed, or if the discharged was observed to extend backwards into the gas supply pipe, the thruster would be deemed to be operating unstably. Finally, for stable operation, the fluctuations in the measured current, voltage and mass flow rate should be at a minimum. The accepted fluctuations in the operating parameters were determined to be $\pm$ 0.05 mg/s for the mass flow rate, $\pm$ 500 V for the voltage and $\pm$ 100 μA for the current.

Throughout the period of 5 hours over which the test was run, no obvious deviation from stable operation was observed. At every check-in period, the proof of concept system displayed both the required visual, and operational characteristics to declare the operation of the system as being stable. Even after 5 hours, when the thruster was deactivated, the system displayed stable operating characteristics, indicating the test could have been extended further to determine the full lifetime of the proof of concept, straight, discharge tube. However, this was deemed unnecessary, as the proof of concept configuration is not truly representative of the actual system to be studied.

Erosion

Figure 4.5 A) shows a SEM image of the inner rim of a control electrode that was not exposed to any discharges. All the features visible should then only be artefacts of the

manufacturing process. The cracks and fissures on the surface of the control electrode appear to be common surface features of untreated stainless steel of various grades [94]. The smoothed off edge, forming the inner rim of the electrode, could be an artefact of the machining process, as seen elsewhere [95].

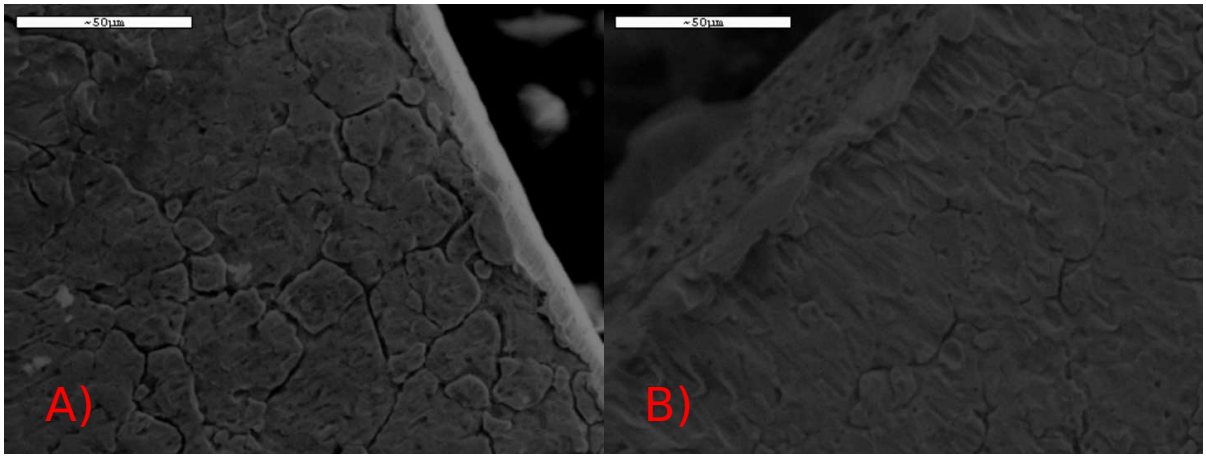

Figure 4.5.: Electron microscope images of the inner rims of: A) a control electrode that was not subjected to plasma exposure and B) an electrode that was used to generate and was exposed to the discharge in the proof of concept, straight, discharge tube.

When considering the SEM image of the electrode exposed to the larger, more stable plasma plume, shown in Figure 4.5 B), many of the same features observed on the control electrode are present, including the smoothed off edge of the inner rim, as well as the cracks and fissures. However, a new phenomenon is observed: the formation of streak-like features on the surface of the electrode, starting at the inner rim, and moving outwards towards the outer perimeter of the electrode. Due to the absence of these features in the images taken of the control electrode and their location, the logical conclusion is that these features result from the electrode's exposure to the plasma. These streaking features could be the result of sputtering material from the inner rim of the electrode [35]. Similar features are observed when material is sputtered from a copper surface, with a glow discharge ion source, creating a crater-like structure [96]. This could eventually be a point of failure for the thruster, but when compared to the erosion results for the CorIon system, as discussed below, it is a great improvement.

Figure 4.6 A) shows an optical microscope image of one of the needles used in the CorIon system, before the thruster was fired. The needle channel is free from any obstruction. Figure 4.6 B) depicts the needle tip after the thruster was fired. The needle becomes discoloured and its shape is distorted. This will affect the gas flow through the needle, as well as the resulting plasma. Thruster performance will be adversely affected. In some cases, erosion was so severe that the needles become blocked, and the thruster would cease

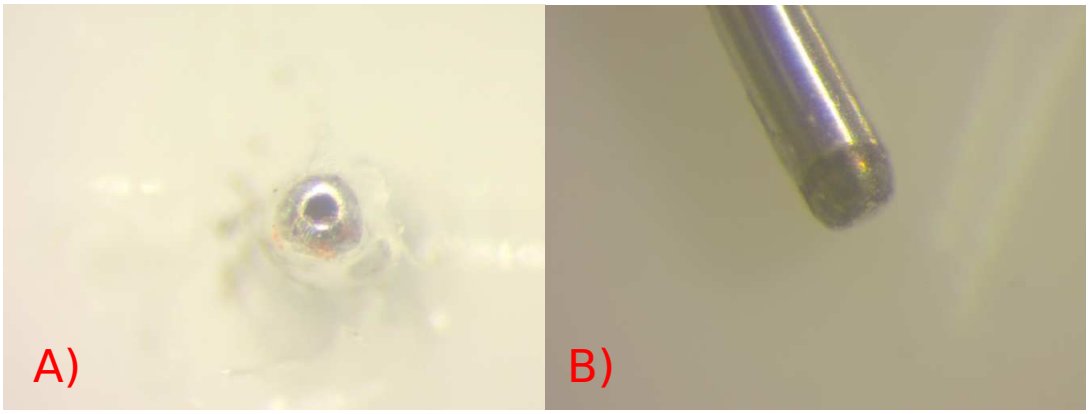

Figure 4.6.: Optical microscope images of the needles used as electrodes in the CorIon system: A) before firing and B) after firing. Note the lack of obstructions in the needle before firing and the discoloration of the needles after firing.

to operate entirely. Typically, this would happen after only tens of minutes of operation. Considering that after 5 hours of operation, the damage present on the inner rim of the electrodes of the proof of concept system was visible only with an electron microscope, it can be concluded that the stable DC discharge based configuration is an improvement on the DC corona ionization based CorIon system, in terms of lifetime.

Repeatability

Table 4.1 shows the results of performing repeatability tests on the proof of concept, straight, discharge tube. The mass flow rate fluctuations were limited to ± 0.001 mg/s, and the corresponding fluctuations in current and voltage were limited to ± 10 μA and ± 0.01 kV respectively. As was indicated in the mass flow rate, voltage and current tests, much larger variations in these quantities (typically value changes of 0.1 mg/s for mass flow rate, 500 μA for current) are required to alter thruster behavior. This indicates that the proof of concept system exhibits good repeatability characteristics. These results, coupled with the successful lifetime and erosion tests, mean further testing of the 'U-shaped' thruster concept can commence.

Mass Flow Rate (in mg/s)	Current (in μA)	Voltage (in kV)
0.677	1843	0.92
0.678	1851	0.92
0.676	1848	0.91
0.678	1847	0.92
0.675	1851	0.9
0.677	1847	0.93
0.675	1845	0.93
0.676	1839	0.92
0.675	1843	0.92
0.677	1840	0.91

Table 4.1.: A table showing the repeatability results of the proof of concept, straight, discharge tube.

4.2.2. 'U-Shaped' Thruster

Lifetime

Due to the successful lifetime test results displayed by the proof of concept, straight, discharge tube, it was expected that the 'U-shaped' thruster should display similar lifetime characteristics, or at least be able to surpass the lifetime of the CorIon system. The same definition of stable operation given previously is used here. The 'U-shaped' thruster was able to outperform the CorIon system, in terms of lifetime, by a substantial amount. However, it was not able to operate for longer periods than the proof of concept, straight, discharge tube. The 'U-shaped' thruster began to operate unstably after continued stable operation of approximately 2 hours and 45 minutes. A discharge was still present in the thruster discharge channel, but plumes were no longer forming, and the electrical behavior of the discharge was becoming erratic, with current and voltage values fluctuating outside of acceptable bounds. The thruster was deactivated to prevent further damage to the system. Although the thruster was unable to continue stable operation, the lifetime tests were considered successful, as it was able to surpass the lifetime of the CorIon system by a considerable amount. Reasons for the failure of the 'U-shaped' thruster are explored in the following section.

Erosion

Figure 4.7 depicts the damage incurred by the 'U-shaped' thruster while performing lifetime tests. Figure 4.7 A) shows a top down view of the thruster, focusing on the

outlets of the thruster from which the ionized propellant is expelled. The outlet on the left-hand side of the image (corresponding to the grounded electrode) appears to be completely obscured by blackened debris, while the outlet on the right-hand side of the image (corresponding to the live electrode) is largely unobstructed, and appears unaffected aside from discoloration of the plastic faceplate.

Figure 4.7 B) shows a side profile, focusing on the surface of the thruster into which the gas attachment is inserted. Note that in this image, the grounded electrode is on the right-hand side of the image, whereas the live electrode is on the left-hand side of the image. Once again, the damage appears to be concentrated around the grounded electrode, where the layers of PLA plastic that form the body of the thruster have warped and discoloured. The layers have even separated from one another around the grounded electrode. The cavity that is left appears to be filled with blackened debris.

Figure 4.7 C) depicts another top down view of the thruster, but in this image, the thruster has been disassembled, so that the interior of the thruster and the electrodes can be studied. The distortion and discoloration of the PLA plastic and the acid-free clear adhesive used to assemble the thruster, can be seen to extend into the body of the thruster. Of particular interest is the blackening of the grounded electrode and the corresponding blackened area of plastic to which the electrode is attached.

Figure 4.8 shows SEM images of 3 electrodes. Figure 4.8 A) depicts the inner rim of the live electrode, Figure 4.8 B) depicts the inner rim of the grounded electrode and Figure 4.8 C) depicts the inner rim of a control electrode that was not subjected to any discharge. In all three images, the underlying surface of the electrode is very course, exhibiting features such and peaks, valleys and large canyons appearing to be dug out of the aluminium surface. These features are most likely due to the mechanical manufacturing process. The electrodes were also not polished before being used in the thruster or placed in the SEM. Polishing would remove any remnants of manufacturing [97].

The image of the live electrode shows similar streaking phenomena when compared to the electrode studied from the proof of concept, straight, discharge tube, but now the addition of small dots in the surface of the electrode is also observed. These dots could be indications of pitting [98], or other markings relating to material removal. While the electrodes were cleaned in an ultrasonic bath, these markings could also be residual thruster construction material, such as PLA plastic or acid-free adhesive. Irrespective of the true nature of these features, they are small when compared to the size of the electrode and, assuming they do not result from sputtering, do not indicate significant radiation damage from ion bombardment.

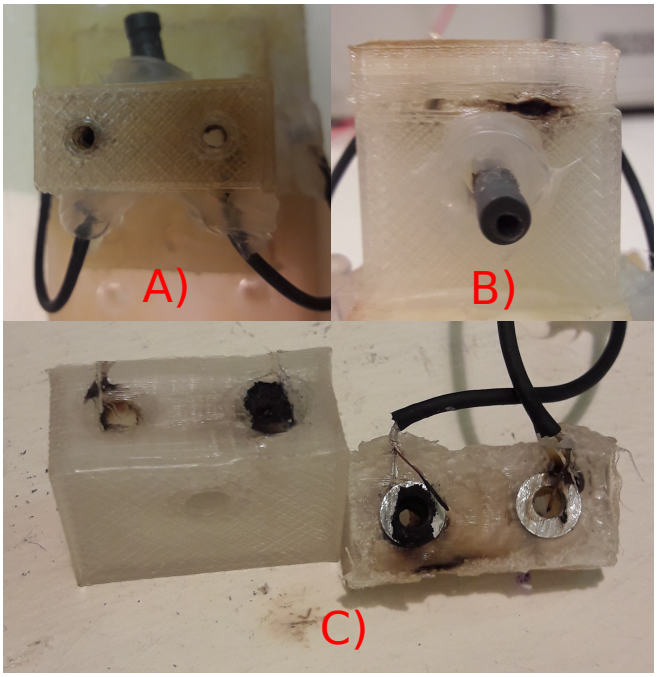

Figure 4.7.: Photographs of the 'U-shaped' thruster that failed while conducting lifetime tests: A) a top down view of the outlets of the thruster; B) a side profile of the thruster, showing the face into which the gas insert is attached and C) a top down view of the thruster having been disassembled so that the damage can be further studied.

The effect on the grounded electrode is much more pronounced. A large amount of debris is present on the surface of the grounded electrode as well as inside the inner rim. This deposited material is most likely a combination of PLA plastic and acid-free adhesive glue used in the construction of the thruster. These construction materials have clearly been damaged, and have affixed themselves onto the surface of the electrode in a manner that requires more forceful cleaning to remove. When considering the underlying electrode, there does not appear to be significant structural damage to the electrode itself due to ion bombardment.

By studying these images, the most likely cause of failure of the thruster would be the blocking of the thruster channel with debris. This debris most probably originates from the body of the thruster itself, either from the heat of the discharge burning the interior of the thruster channel, or from the heat generated at the grounded electrode. The grounded electrode is the most plausible generator of debris when considering the location and extent of damage to the thruster body and the presence of debris on the electrode even after cleaning. The mechanism of failure of the thruster is therefore not the erosion of the electrodes, as was in the case of the CorIon system, but rather the unsuitability of the construction materials.

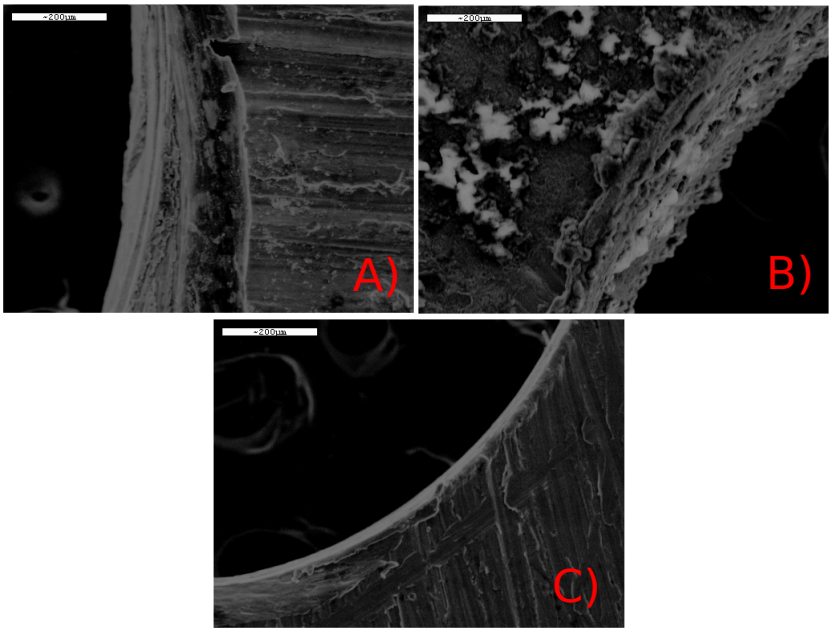

Figure 4.8.: Electron microscope images of the inner rims of: A) the electrode connected to the positive terminal of the high voltage power supply; B) the grounded electrode and C) a control electrode.

The construction materials in these tests are not ideal for use in space propulsion systems, but serve the purpose of testing and evaluation of the concept. The use of more appropriate construction materials, such as ceramics, would mitigate these erosion effects and allow for a considerably longer thruster lifetime. An example would be alumina, a ceramic commonly used in thruster construction [99], [100].

Repeatability

Table 4.2 gives the results of the repeatability experiments performed on the 'U-shaped' thruster. One can see that when compared to the repeatability results of the proof of concept discharge tube, the fluctuations between readings is larger, in particular when considering the voltage. This may be due to the fact that, in the 'U-shaped' thruster design studied here, the plasma plumes that are observed to form at both thruster openings are in close proximity, which means they can interact and influence the resulting plasma potential. This is especially pertinent when considering the spluttering phenomena observed in plume formation during thruster operation. However, even though the fluctuations are larger, they are not large enough to result in large changes in the operational behavior of the thruster. In light of this, the repeatability test on the 'U-shaped' thruster can be considered a success.

Mass Flow Rate (in mg/s)	Current (in mA)	Voltage (in kV)
0.479	2.054	1.29
0.479	2.128	1.38
0.482	2.004	1.20
0.480	2.101	1.46
0.480	2.121	1.45
0.482	2.147	1.44
0.481	2.098	1.43
0.481	2.133	1.45
0.480	2.157	1.46
0.481	2.087	1.35

Table 4.2.: A table showing the repeatability results of the 'U-shaped' thruster.

4.3. Thrust Measurement

In the following subsections, the results of the thrust measurements performed on the 'U-shaped' thruster will be discussed. If the readings being discussed are conventional cold gas readings, they will be referred to as 'cold gas' readings. If the readings being discussed are readings performed with the high voltage power supply activated, so that the propellant is ionized, they will be referred to as 'hot gas' readings.

4.3.1. Varying Mass Flow Rate

Cold Gas

Figure 4.9 shows a plot of the cold gas thrust readings of the 'U-shaped' thruster as the mass flow rate is varied. A clear linear trend is observed in the data and this is further evidenced by the relatively small error bars. A linear expression is fitted to the data:

This fit is also shown in Figure 4.9.

$$T = 270\dot{m} + 15.9 \tag{4.2}$$

This expression is of the form of the expression shown below shown below:

$$T = \dot{m}v_e\left(1 + \frac{a^2}{v_e^2}\right) \tag{4.3}$$

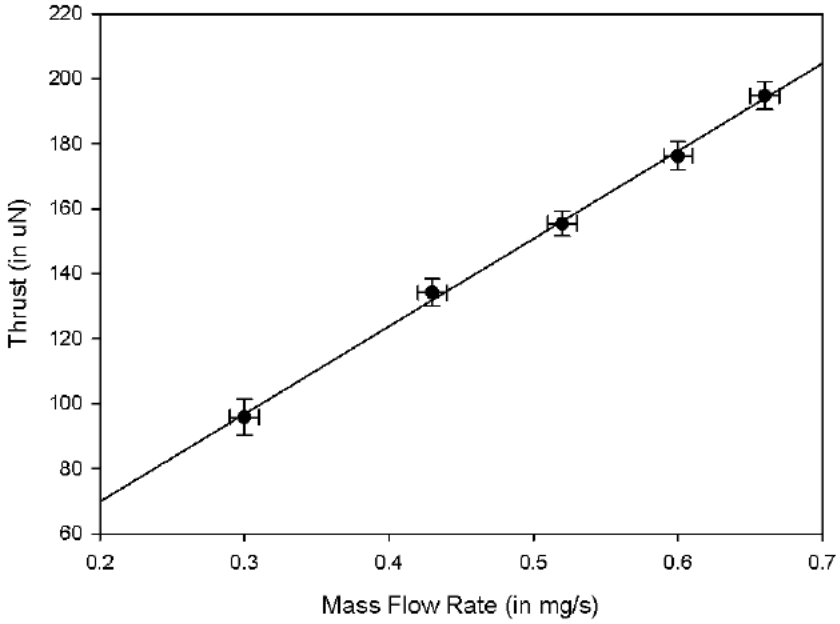

Figure 4.9.: A graph depicting the cold gas thrust test of the 'U-shaped' thruster design as the mass flow rate is varied. A linear expression is fitted to the data.

where a is the speed of sound in the propellant gas. This equation relates the thrust to the propellant mass flow rate in the absence of a background gas. From this expression, the value for the propellant exhaust velocity (v_e in Equation 2.2) can be determined to be (270±6.42) m/s. Considering that the speed of sound in argon is approximately 320 m/s near atmospheric pressure [101], this indicates that the flow exiting the thruster is not yet choked, but is still at a higher Mach Number [102]. At the mass flow rates explored, the thrust ranged from 95 μN to 195 μN, equating to a cold gas thrust range of 100 μN. Using Equation 2.1 and the propellant exit velocity obtained above, the specific impulse of the cold gas thrust can be calculated. The thruster in its current form has a specific impulse of (28 ± 1) s. This value is considerably lower than the value typically obtained for argon as a cold gas propellant, which is approximately 56 s [103]. It should be noted, that this thruster design is not optimised for cold gas thrust, and with design improvements and propellant changes, the cold gas specific impulse value can be greatly improved.

Hot Gas

Figure 4.10 shows a plot of the cold gas thrust readings of the 'U-shaped' thruster compared with the hot gas readings of the same thruster as the mass flow rate is varied. Comparing these results shows that using the thruster in its hot gas mode of operation

results in an increase in the thrust produced. A definite increase in thrust is noted, as the error bars of the cold and hot gas thrust measurements do not overlap. The increase in thrust by activating the high voltage power supply remains approximately constant as the mass flow rate is increased. The thrust increase varies slightly between 11 μN and 13 μN, the only outlier being the 1st data point with a thrust increase of 17 μN. The approximately constant thrust increase in the range studied means the percentage thrust increase drops from 17 % to 6 %, as the mass flow rate is increased. It should be noted, that while the error bars do not cross, they are large when compared to the thrust increase between the hot and the cold gas thrusts. This means the thrust increase could in fact be smaller than the figures reported here. However, the thruster does produce a definite positive increase in thrust when the power supply is activated, showing that the system successfully operates as an electric propulsion system.

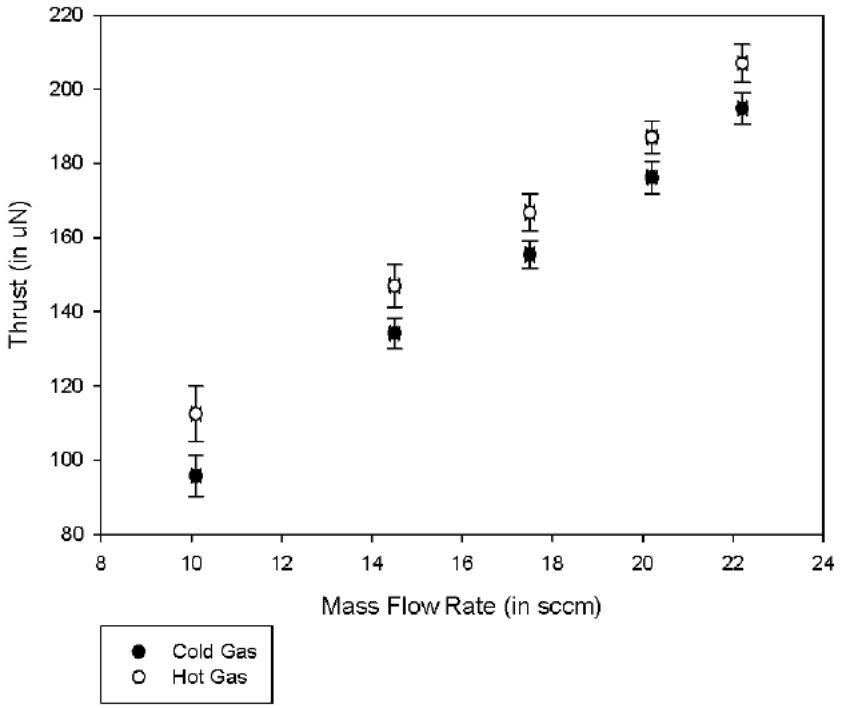

Figure 4.10.: A graph comparing the thrust measurements of the 'U-shaped' thruster before the power supply is activated (cold gas) and after the power supply is activated (hot gas) as the mass flow rate is varied.

Table 4.3 lists some competing technologies in electric micropropulsion and some of their comparable performance parameters. In the case of the CorIon system, only an expected thrust is available, and for the masses given, some values of the thruster mass only were not available so the mass of the entire system is given. When considering these competing technologies, the novel DC discharge based space propulsion concept appears to compare favourably.

System	Thrust (in μN)	Mass (in g)	Power Used (in W)	References
CorIon	50 (expected)	5 (thruster)	1.5	[28]
Vacuum Arc	10 - 200	50 (thruster)	1 - 20	[104], [105]
Laser Ablation	680	750 (thruster)	9	[54]
FEEP	0.1 - 150	1400 (system)	6	[106]
PPT	850	350 (thruster)	5 - 33	[107], [108]
Gridded Ion	200 - 500	210 (thruster)	30	[109]

Table 4.3.: A table showing a comparison between some performance parameters of competing electric micropropulsion systems.

Figure 4.11 depicts how the measured power varies as the mass flow rate is varied. The power is calculated from the measured voltage and current from the digital multimeters. A near linear decrease in power is measured as the mass flow rate is increased. An outlying point occurs at 14.5 sccm, but the error bars associated with this data point are large enough to encapsulate the linear trend. The decreasing power is due to the decrease in the measured voltage as the mass flow rate is varied, and the measured current remains constant as the mass flow rate is varied. This decrease in power with increasing mass flow rate could be a consequence of Paschen's law. A higher mass flow rate results in a corresponding higher pressure as indicated previously. This higher pressure in turn results in a lower breakdown voltage of the gas. The power obtained from these measurements varies between 2.3 W and 0.9 W. These values compared favourably with those seen in competing systems given in Table 4.3.

4.3.2. Varying Current

Figure 4.12 shows a plot of the cold gas thrust readings of the 'U-shaped' thruster compared with the hot gas readings of the same thruster as the current is varied. It would appear that varying the current has a minimal effect on thrust production as indicated by these measurements. There appears to be no improvement in thrust stability (reduction in hot gas error bars) or increase in thrust as the current is increased. At the highest current measured, it appears that the thrust decreases, but considering the size of the error bars this cannot be said with absolute certainty. The thrust increase varies from 9 μN to 14 μN. The percentage thrust increase varies from 6 % to 9 %.

Figure 4.13 depicts how the measured power varies as the current is varied. The power is calculated from the measured voltage and current. A near linear increase in power is measured, as the current is increased. An outlying point occurs at 2000 μA, but the error bars associated with this data point are not large enough to encapsulate the

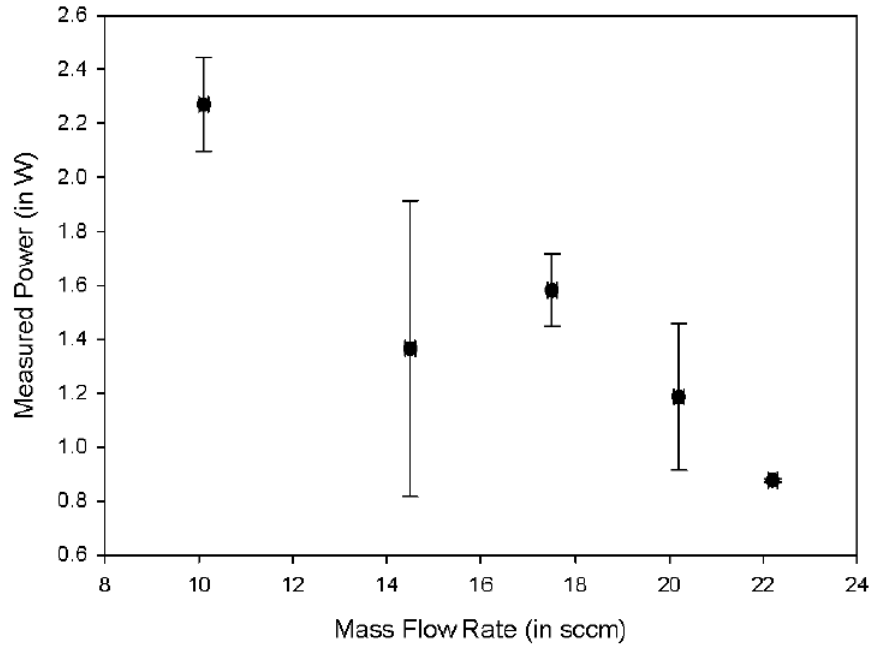

Figure 4.11.: A graph showing how the power obtained from measuring the voltage and current at the thruster electrodes varies as the mass flow rate is varied.

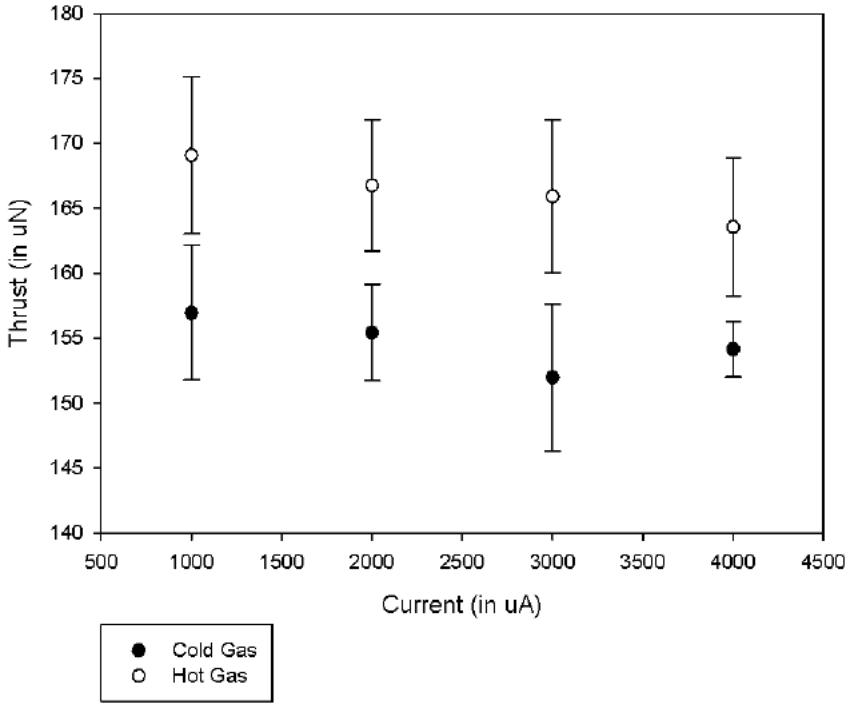

Figure 4.12.: A graph comparing the thrust measurements of the 'U-shaped' thruster before the power supply is activated (cold gas) and after the power supply is activated (hot gas) as the discharge current is varied.

linear trend. This spike in measured power could be attributed to the initial onset of stable plume formation, as this typically occurs at approximately 2000 μA. The increasing power is due to the increase in the measured current, which is the varied parameter in the experiment. The measured voltage remained constant as the current was varied. The power obtained from these measurements varied from between 1.9 W and 0.9 W.

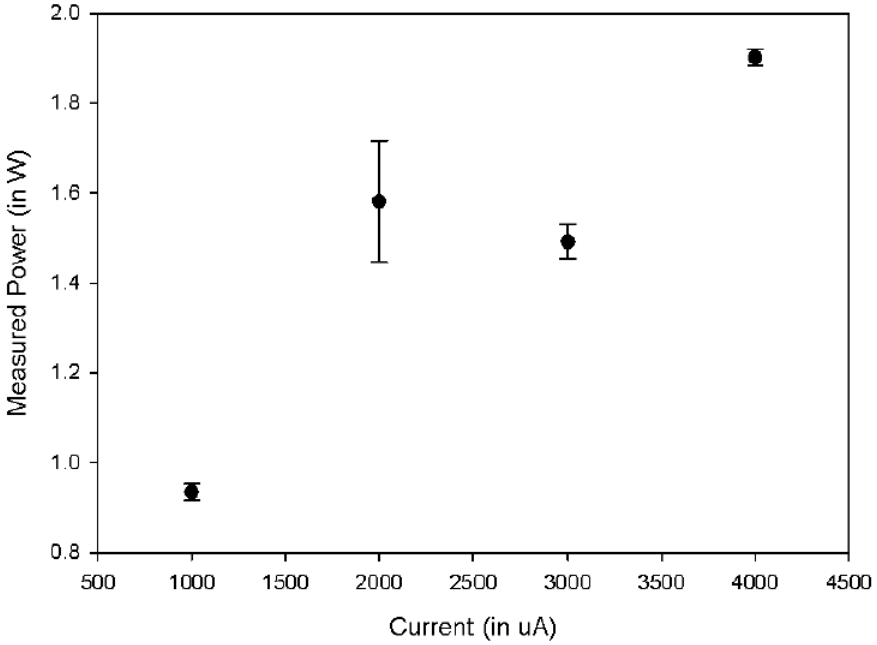

Figure 4.13.: A graph showing how the power obtained from measuring the voltage and current at the thruster electrodes varies as the discharge current is varied.

4.3.3. Varying Voltage

Figure 4.14 shows a plot of the cold gas thrust readings of the 'U-shaped' thruster compared with the hot gas readings of the same thruster as the voltage is varied. It would appear that varying the voltage has a minimal effect on thrust production as indicated by these measurements. There appears to be no improvement in thrust stability (reduction in hot gas error bars) or increase in thrust as the voltage is increased. In the case of the reading at 4000 V, in spite of averaging, the error bars overlap, nullifying the measurement. At the highest voltage measured, it appears that the thrust decreases, but considering the size of the error bars, this cannot be said with absolute certainty. The thrust increase varies between 8 μN to 12 μN. The percentage thrust increase varies from 5 % to 8 %.

Figure 4.15 depicts how the measured power varies as the voltage is varied. The power is calculated from the measured voltage and current. As opposed to the linear relationships

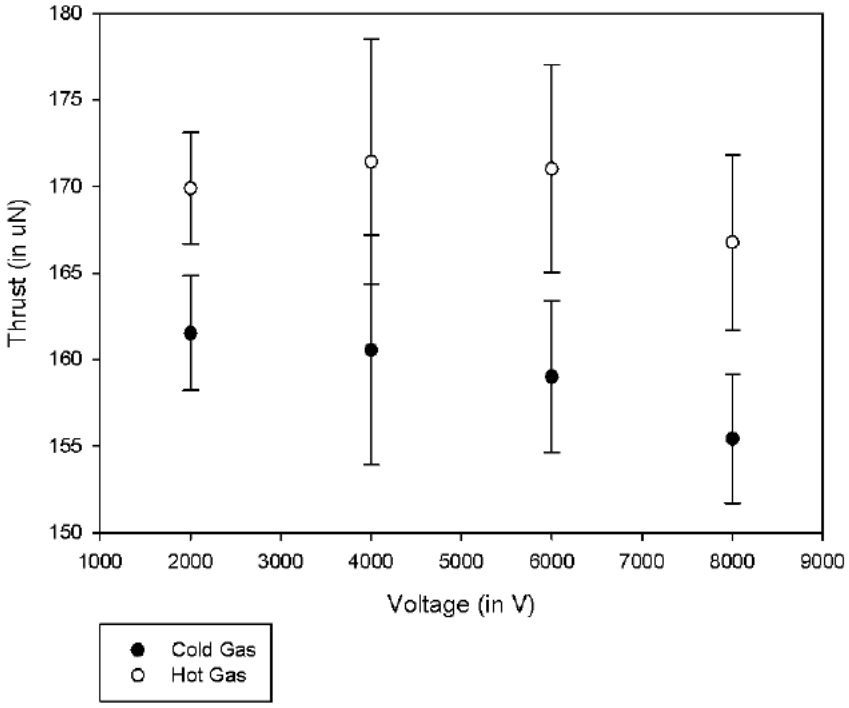

Figure 4.14.: A graph comparing the thrust measurements of the 'U-shaped' thruster before the power supply is activated (cold gas) and after the power supply is activated (hot gas) as the discharge voltage is varied.

observed previously, a discontinuous, increasing, step-like behavior is observed in the measured power as the voltage is increased. The step occurs at 6000 V and, even though the accompanying error bars for the subsequent points are large, they are not larger than the step itself. The increasing power is due to an increase in the measured voltage. The measured current remains constant as the voltage is varied. This could be indicative of some sort of transition phenomenon, but more testing is required to confirm this. The power obtained from these measurements varies between 1 W and 1.6 W.

4.4. Ion Current Density Measurements

Figure 4.16 shows the commonly observed lineshapes in the raw data. The raw data observed shows unexpected results. Considering the system is operated with a DC voltage source, a DC ion current signal was expected. However, all of the lineshapes observed are pulses. These pulses are not transient phenomena, and are largely stable throughout thruster firing. The two most commonly occurring lineshapes are shown in Figure 4.16 A) and Figure 4.16 B). Figure 4.16 A) shows a sawtooth-like, single peaked profile, while Figure 4.16 B) shows a similar curve, but with two peaks present. The first peak is sharp

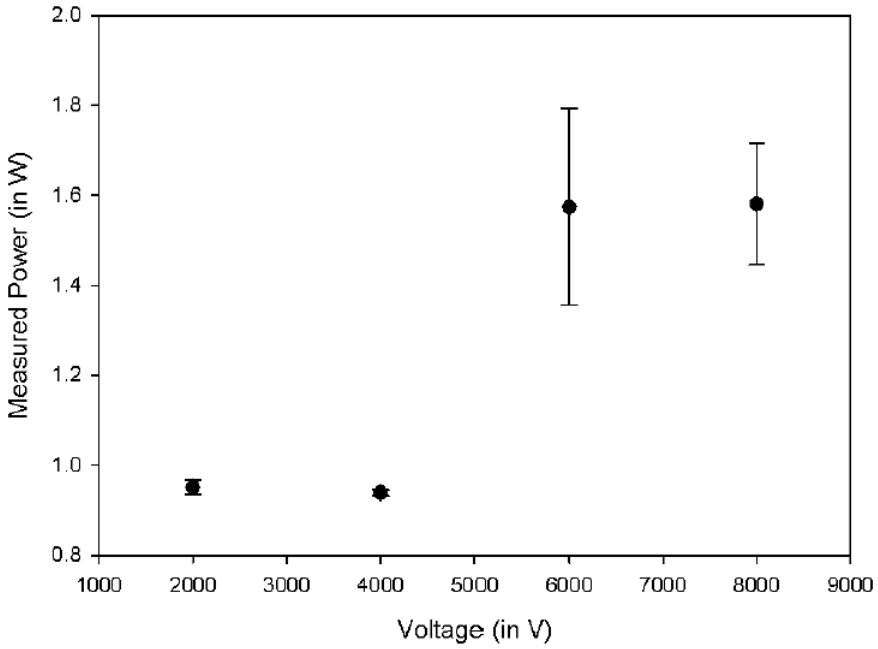

Figure 4.15.: A graph showing how the power obtained from measuring the voltage and current at the thruster electrodes varies as the discharge voltage is varied.

and well-defined, while the second peak is wider, and of a lower voltage than the first. Figure 4.16 C) shows a magnified image of the curve shown in Figure 4.16 B) to allow the peaks to be more easily resolved. These line shapes are similar to those observed for other pulsed propulsion systems, such as VAT's, although the VAT's ICD Raw Data displays a slightly broader lineshape with less sawtooth-like features, exhibiting a smoother curve [79], [77].

Typically, only single peaks are observed in the ICD readings of pulsed DC discharges, like those used in time-of-flight mass spectrometry [110], and to study secondary electron emission [111]. However, dual peak Faraday cup probe signals have been observed while studying lower energy plasma focus devices [112] and pseudospark discharges [113]. In the case of plasma focus devices, the first peak is lower in intensity than the second, and is associated with X-ray generation. X-rays have been generated in small, helium glow discharge systems, using electrical parameters similar to those used in this work [114]. In the case of the pseudospark discharge, the first peak is comparable in height to the second, and is attributed to ultraviolet (UV) radiation. However, to confirm if the first peak observed in the thruster's ICD profile is in fact the result of X-ray or UV radiation production, additional testing outside of the scope of this work would be required. Another possibility, is that the first peak corresponds to the build up of slower ions in the forefront of the ion pulse. This is observed in heavy ion driver, used in fusion experiments, and is caused by the finite amount of rise time in the source voltage. Other

phenomena, such as image currents and latent capacitances in the probe, are also possible causes [115]. Both peaks will be considered where applicable in the following analysis.

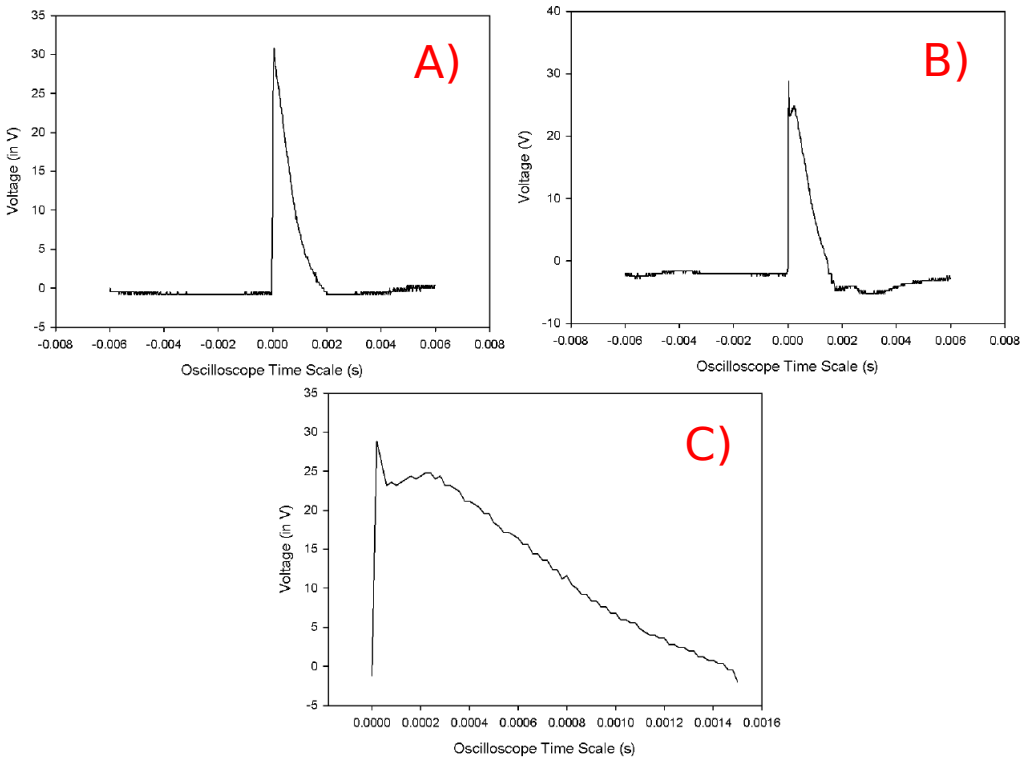

Figure 4.16.: Graphs depicting the common lineshapes observed in the raw data obtained from ion current density measurements: A) the lineshape depicting a single peaked, sawtooth-like curve; B) the lineshape depicting a double-peaked curve and C) the curve depicted in B) magnified, so that the double-peak is clearly seen.

4.4.1. Varying Operating Parameters

When studying the ICD of a system, the space charge limited current density becomes an important factor for consideration. This quantity will place a bound on the amount of current the Faraday cup probe is able to capture, and is dependent on a number of factors. The Child-Langmuir Law [116] allows for the space charge limited current density to be calculated for the one-dimensional case of two infinite, parallel plates, separated by a finite distance:

$$J_{cl} = \frac{I_{cl}}{A} = \frac{4}{9}\varepsilon_0 \left(\frac{2e}{m_i}\right)^{\frac{1}{2}} \frac{V_0^{\frac{3}{2}}}{s^2} \tag{4.4}$$

where I_{cl} is the space charge current limit, A is the area of the collector plate that is exposed to the plasma, V_0 is the voltage drop across the collector plate, m_i is the mass of the ions under consideration and s is the distance between the two infinite, parallel electrodes. This is of little use for the current experimental configuration. In [117], the law is expanded to higher dimensions, in [79] it is modified to describe the configuration used in this work, and the space charge limited current is calculated for a number of different ions. The ion considered in this work is argon, and calculations are performed in [79] for aluminium and iron. Argon possesses an atomic mass between that of aluminium and iron. This means that the space charge limited current for Argon should exist between the values for aluminium and iron, namely between 73 μA and 91 μA. The largest value measured in this work is 52 μA, well below 73 μA. This means that space charge current limiting will not affect the results of this work.

The results of the variation of the mass flow rate of propellant through the thruster, the voltage drop across the electrodes and the current flow through the electrodes on the ICD are discussed below.

Mass Flow Rate

Figure 4.17 shows how the measured ICD varies as the mass flow rate of the propellant through the thruster is altered. Both the values of the first peak and the second peak are given. It is quite clear that as the mass flow rate is increased, the ICD decreases, reaching a plateau at higher mass flow rate values. This phenomenon of decreasing ICD with increasing mass flow rate has been observed in high current, low emittance, DC electron cyclotron resonance proton sources [118].

A possible cause of this phenomenon is that as the mass flow rate increases, propellant atoms flow through the system at a faster rate. This would mean that more propellant atoms could flow through the discharge inside the thruster without being ionized, and simply exit the thruster either as a neutral or as an excited atom. It should be noted that as the mass flow rate is increased, the discharge voltage decreases. This means that the average ion speed will decrease and this could result in a drop in the ICD.

When comparing these results to the thrust measurements, one sees that as the mass flow rate is increased, the ICD decreases, but the amount of thrust increase between the cold gas and hot gas measurements remains constant. This would suggest that the acceleration of ions away from the thruster does not contribute significantly to the generation of thrust, and therefore some other effect is the dominant thrust producing mechanism.

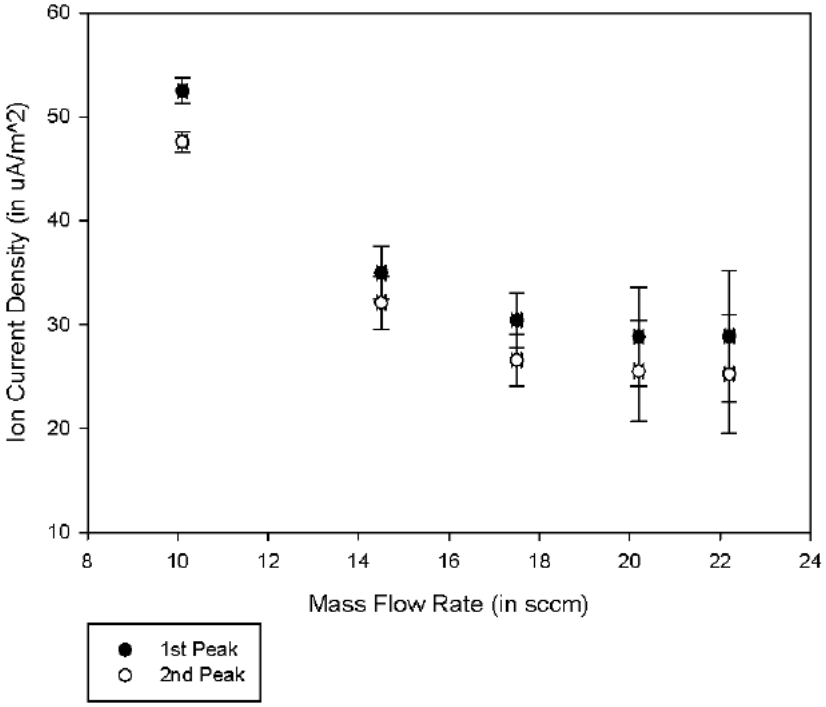

Figure 4.17.: A graph depicting the measured ion current density generated by the 'U-shaped' thruster as the mass flow rate is varied. The ion current densities obtained from both the first and second peaks are shown.

Current

Figure 4.18 shows how the measured ICD varies as the current flowing through the thruster's electrodes is altered. The ICD appears to remain relatively constant at low and higher current values, with slight fluctuations that are encapsulated by the error bars. However, it appears that at 2000 μA, a drop in the ICD occurs. While the error bars for this data point are large, this point still exhibits a lower ICD, and is outside of the error bars of the other data points. This corresponds with the drop in power observed when the current is varied.

The electron current density of glow, arc and capillary discharges is observed to increase with increasing discharge current [119], [120]. However, the operating currents and voltages used in [119] are substantially higher than those used in this work. The ICD is also observed to increase with increasing discharge current in electrostatic ion gun designs, with similar operating parameters to those used in this work [121]. This suggests that the behavior observed here is somewhat anomalous. A hypothesis for the dip in the ICD at 2000 μA is that this could be an artefact of the transition from where the discharge is contained in the thruster, to where stable plume formation begins to occur. This typically occurs between 1000 μA and 2000 μA, as previously confirmed by visual inspection.

Relating these readings to the thrust measurements obtained as the current is varied provides more evidence to suggest that ion momentum transfer is not the primary contributor to thrust generation. This is noticeable when considering the 2000 μA point in both curves. At 2000 μA a distinct dip is noted in the ICD, but no appreciable corresponding drop in thrust is measured.

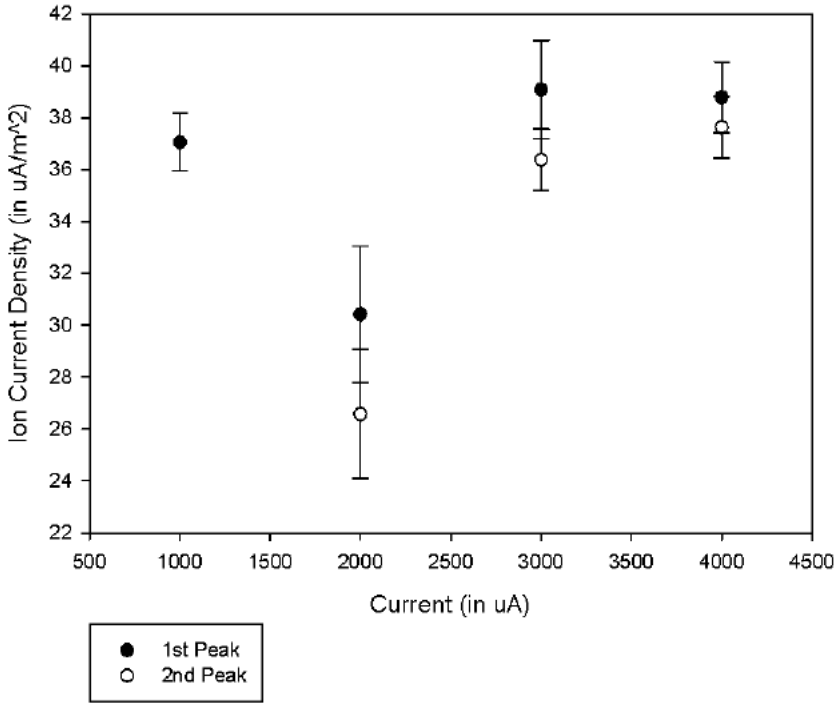

Figure 4.18.: A graph depicting the measured ion current density generated by the 'U-shaped' thruster as the discharge current is varied. The ion current densities obtained from both the first and second peaks are shown.

Voltage

Figure 4.18 shows how the measured ICD varies as the voltage flowing through the thruster's electrodes is altered. While variation is observed in the ICD as the voltage drop across the thruster electrodes is increased, these fluctuations are all within the error bars of all points considered. This means that the ICD can be taken to be approximately constant, as the discharge voltage is varied.

In small multicusp H^- sources, the extracted ICD is shown to increase slowly, but then reach a plateau, and decrease as the discharge voltage is increased [122]. This behavior was mirrored in the extraction of positive hydrogen ions [123]. The 'U-shaped' thruster could be operating in this plateau regime, which would explain the lack of fluctuation in the ICD, as the discharge voltage is increased.

When comparing these results to the thrust measurement results, a similar trend is observed, as in previous comparisons. There appears to be little fluctuation in the measured thrust and ICD with changes in discharge voltage.

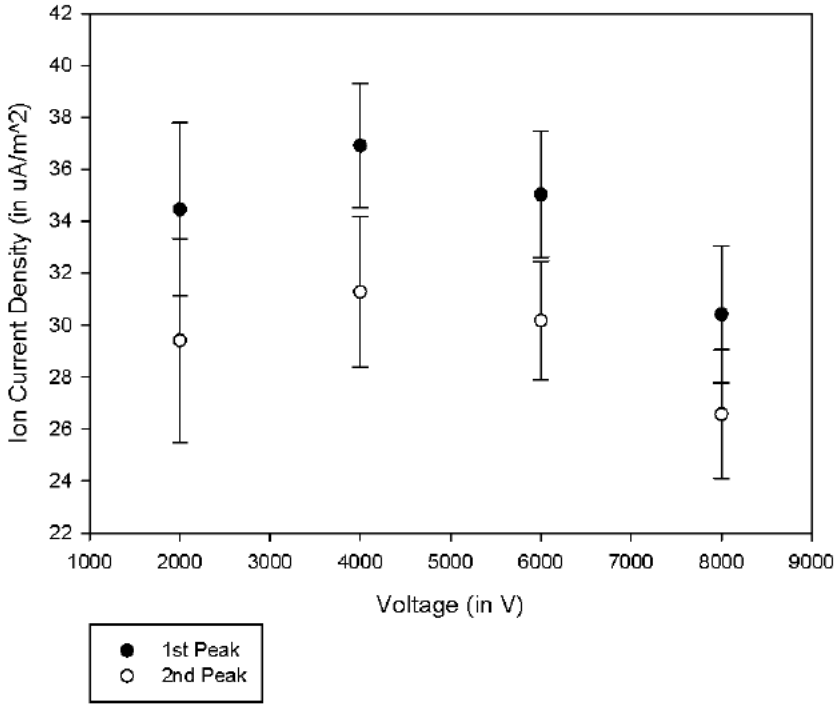

Figure 4.19.: A graph depicting the measured ion current density generated by the 'U-shaped' thruster as the discharge voltage is varied. The ion current densities obtained from both the first and second peaks are shown.

4.4.2. Ion Current Density Distribution

Figures 4.20 and 4.21 show the ICDD for the first peak and second peak of the signals obtained by the Faraday cup probe, in the 6 different vacuum chamber positions respectively. In the case of the two points along the centreline of the thruster and 10 cm to the right of the thruster, the ICD measurements show a decrease in the ICD as the Faraday cup probe is moved radially away from the thruster. The large error bars can be reduced by taking more measurements. The decrease in the ICD with increasing radial distance is a phenomenon that is expected, and is observed in various unique plasma sources, such as vacuum arcs [124]. However, the two points recorded 10 cm to the left of the thruster indicate that there is a substantial increase in the ICD as the radial distance from the thruster to the probe is increased. The exact cause of this feature is unknown at this time, and further testing outside the scope of this work is required to determine its cause.

Another interesting feature is that, while a Gaussian trend is typically observed in the ICDD [124], a decrease in the ICD is observed at the centreline and the ICD increases as the probe is moved to the edges of the beam. A possible explanation for this is that in the centreline, the two plumes emanating from the thruster combine, which allows for a greater incidence of ion neutralization by emitted electrons, which would result in a lower ICD. Langmuir probe measurements of different points in the plumes would be required to confirm this.

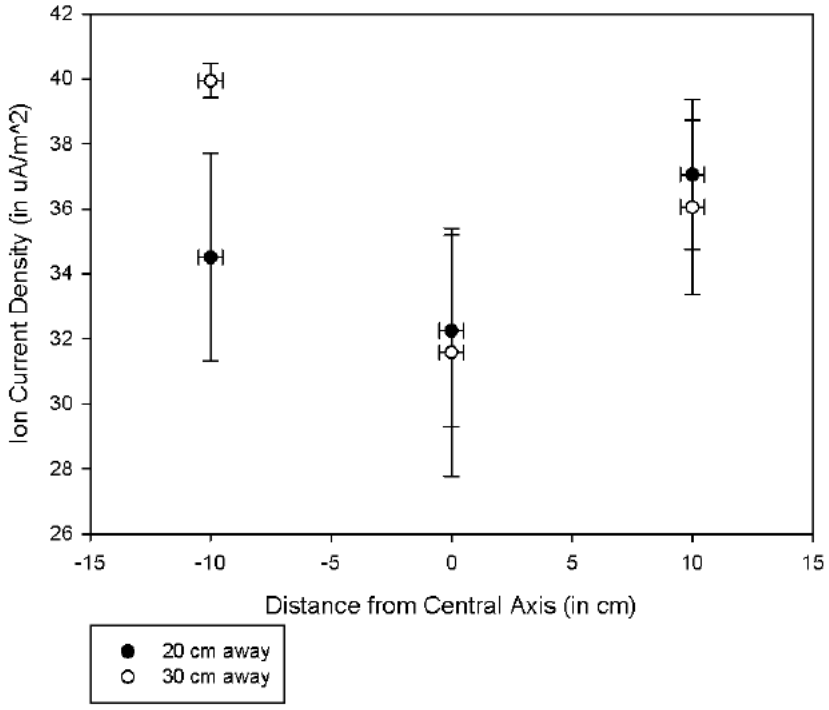

Figure 4.20.: A graph depicting the ion current density distribution generated by the 'U-shaped' thruster determined from the first peak of the measured ion current signals.

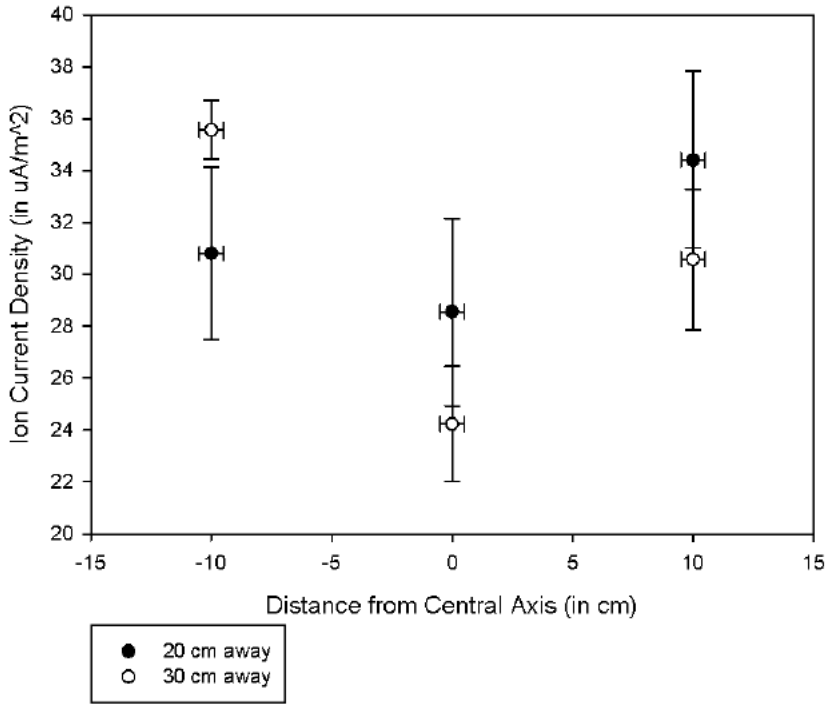

Figure 4.21.: A graph depicting the ion current density distribution generated by the 'U-shaped' thruster determined from the second peak of the measured ion current signals.

5. Simulations: Framework and Development

In this chapter, the computational machinery used to construct simulations of the novel microthruster concept developed in this work are presented. A general outline of the software packages used will be given, and the specific simulation geometry and parameters are discussed.

5.1. COMSOL Multiphysics

In order to better interpret the experimental results obtained in this work, a theoretical analysis of the system under study is required. Due to the intractable nature of the equations used to study plasma phenomena, which only possess analytical solutions in the simplest cases, numerical methods are used to develop computational simulations. These will give insight into the underlying physics of the system. The software package used to achieve this is COMSOL Multiphysics.

5.1.1. General Overview

COMSOL Mutiphysics is a patented software package, developed by COMSOL Inc. It is used to create simulations based on partial differential equations, which are then solved numerically. COMSOL Multiphysics is particularly useful in applications where a number of different physical phenomena are coupled. A number of optional modules are available, which allow for different physics to be added to a model. This allows for complex problems to be solved. An example of this is the simulation of the thermal effects of galvanostatic discharges in lithium-ion batteries [125].

The software package primarily uses finite element analysis to generate solutions to the

boundary value problem under consideration. The finite element method is a technique used to solve systems of partial differential equations numerically. This is achieved by dividing up the domain to be studied into simpler sections, called mesh elements. A diagrammatic representation of a domain divided up into such mesh elements is shown in Figure 5.1. The calculus of variations is then applied to each mesh element to obtain a solution in that subdivision by minimizing an associated error function [126].

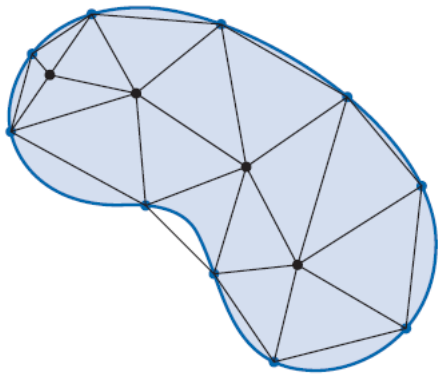

Figure 5.1.: A diagrammatic representation of an arbitrary domain divided up into triangular mesh elements [126]

Other numerical methods used by COMSOL include: the finite volume method, the boundary element method, and particle tracing methods. Finite volume methods are similar to finite element methods in that solutions to partial differential equations are evaluated on grid points of a meshed geometry. In the case of the finite volume method, the fluxes of the physical quantities across the surfaces of a finite volume that is constructed around each grid point are calculated [127].

The boundary element method is used to solve numerous engineering and scientific problems by dividing a boundary on which a function is applied into elements that are approximated by a straight line. The function applied is then assumed to be constant over the element [128].

Finally, particle tracing methods are used to model the transport of solute mass. Advection is simulated using the velocity field obtained by solving the flow equation of the system, and a random walk displacement is used to simulate dispersion [129].

COMSOL Multiphysics has been successfully utilized in a number of commercial and research contexts, including food technology [130], electrochemistry [131] and biotechnology [132]. Three multiphysics modules are used throughout this work, namely: the plasma module, the fluid flow module and the heat transfer module. These modules are discussed below.

5.1.2. The Plasma Module

Three common approaches are used to study the physics of plasmas using simulations. These approaches are a kinetic approach, a fluid approximation and hybrid techniques. Kinetic methods typically solve either a Boltzmann Equation, or an approximation to the Boltzmann Equation to obtain the electron and ion velocity distribution functions. Approximations to the Boltzmann Equation, such as the Fokker-Planck Equation, ease computation by simplifying physical phenomena such as collision effects. The distribution functions are then used to solve Maxwell's Equations to obtain the resulting electric and magnetic fields [133]. The most popular computational implementation of kinetic methods are various forms of particle-in-cell (PIC) methods. PIC methods group electrons and ions together into much larger particles. These larger particles are allowed to exist in a continuous phase space, while their properties are evaluated at fixed grid points [134]. While PIC codes obtain accurate results, they are computationally expensive, and some more advanced codes require very sophisticated hardware to be used effectively.

As opposed to kinetic codes, fluid approximation techniques assume a form of the distribution function for the species to be modelled, and velocity moments of the Boltzmann Equation are taken. The distribution function is obtained by considering the macroscopic properties of the plasma [135]. The resulting partial differential equations are much less computationally expensive to solve than those which result from kinetic approaches. COMSOL Multiphysics uses this formalism when constructing plasma simulations.

Finally, hybrid techniques utilize a combination of the above two formalisms. This achieves a balance between the accurate results of kinetic methods, and the computational speed and ease of use of the fluid approximation. Kinetic methods can be used to determine the behavior of heavier species, such as ions, while electrons are modelled as a fluid, but the reverse can also be implemented [136]. It is not uncommon to see Monte Carlo methods being utilized in hybrid solving techniques.

The Theory of The Plasma Module

The plasma module utilizes three theoretical frameworks to effectively simulate a wide variety of plasma environments. These frameworks are: a Boltzamann Equation Two Term Approximation, to calculate the electron energy distribution function (this retains a balance between fluid and kinetic approaches); Drift Diffusion Theory, which is used to calculate electron density and electron energy, using a fluid approximation as well as electron transport properties; and a Heavy Species Transport Framework, that utilizes

mass transport and conservation via Fick's Law or Mixture Averaging, to determine the transport of all non-electron species: charged, excited and neutral. A brief discussion of these frameworks will be presented here, as more comprehensive treatments can be found in the COMSOL Multiphysics documentation and the references cited therein [137].

Boltzmann Equation Two Term Approximation The Boltzmann Equation is a complex differential equation that is used to describe the evolution of a distribution function. It can be written as the sum of the effects of external forces acting on the system under study, the diffusion of particles through the system, and the effects of collisions between particles in the system:

$$\frac{\partial f}{\partial t} + \vec{v} \cdot \nabla f - \frac{e}{m}(\vec{E} \cdot \nabla_{\vec{v}} F) = C(f) \tag{5.1}$$

where f is the distribution function, $\vec{v}$ is the velocity field, e is the charge of an electron, m is the mass of an electron, $\vec{E}$ is the electric field and $C(f)$ are the terms describing the effects of collisions on the system. By following the treatment shown in [138], the Boltzmann equation shown above can be approximated by first expanding using spherical harmonics and then truncating the resulting expression at the required level of accuracy. If the electron energy distribution function is close to symmetric, then this can occur after the second term. Once collision terms, which account for elastic collisions, excitation/de-excitation, ionization, attachment and electron-electron collisions are considered, the resulting Boltzmann equation can be written in the following form:

$$\frac{\partial}{\partial \varepsilon}\left(Wf - D\frac{\partial f}{\partial \varepsilon}\right) = S \tag{5.2}$$

Equation 5.2 can be interpreted as a convection-diffusion continuity equation in energy space (indicated by the variable ε), where the convective part has a negative flow velocity W, the diffusive part has a diffusion coefficient D and a source term on the right-hand side of the equation given by S. W represents elastic collisional cooling and contains information like the total cross-section of elastic collisions, and the density of the background gas, while D represents heating via fields and collisions and contains information like the temperature of the background gas, and the electron density. Solving Equation 5.2 requires a special approach as the coefficients W and D depend on the integral of the solution to Equation 5.2 itself, and the source term is non-local as it represents quantized energy loss due to inelastic collisions. A possible numerical method used to solve Equation 5.2 is detailed in [138]. This technique utilizes an exponential scheme to discretize

the equation [139].

An important quantity that can be extracted from this treatment is the electron drift velocity. This can be easily measured, so it provides a way for the results of this analysis to be compared with experimental data. The drift velocity is extracted by evaluating the integral:

$$\omega = -\left(\frac{\gamma}{3}\right)\left|\frac{E}{N_n}\right|\int_0^\infty \frac{\varepsilon}{\sigma_m}\left(\frac{\partial f}{\partial \varepsilon}\right)d\varepsilon \tag{5.3}$$

where E is the electric field, N_n is the background gas density, σ_m is the total collision cross-section, and γ is:

$$\gamma = \left(\frac{2e}{m}\right)^{\frac{1}{2}} \tag{5.4}$$

Drift Diffusion Theory Approximating an ionized gas as a fluid is a frequently utilized technique in the field of plasma physics. Magnetohydrodynamics has been successful in describing the phenomena observed in both laboratory and cosmic plasmas [140]. Typically, both electrons and ions are modelled as two interacting fluids that are able to influence each other with their resulting electric and magnetic fields.

The way in which the fluid equations used by COMSOL Multiphysics are obtained, is based on the method of [141]. Velocity moments are taken of a Boltzmann equation that has been multiplied by a weighting function. This results in 3 equations: one that describes the electron number density, one that describes the mean electron momentum and one that describes the mean electron energy. The electron number density is obtained from:

$$\frac{\partial n_e}{\partial t} + \nabla \cdot \vec{\Gamma}_e = R_e \tag{5.5}$$

where n_e is the electron density, $\vec{\Gamma}_e$ is the electron flux vector, derived from momentum conservation and R_e is an electron source or sink term, and is determined using the plasma chemistry of the system. The mean electron momentum is obtained from:

$$\frac{\partial}{\partial t}(n_e m\vec{\omega}) + \nabla \cdot n_e m\vec{\omega}\vec{\omega}^T = -(\nabla \cdot \boldsymbol{p_e}) + en_e\vec{E} - n_e m\vec{\omega}\nu_m \tag{5.6}$$

where $\boldsymbol{p_e}$ is the electron pressure tensor and ν_m is the momentum transfer frequency. Drift diffusion theory is obtained by ignoring the terms on the left had side of Equation 5.6. Finally, the electron energy density is obtained from:

$$\frac{\partial n_\varepsilon}{\partial t} + \nabla \cdot \vec{\Gamma}_\varepsilon + \vec{E} \cdot \vec{\Gamma}_e = R_\varepsilon \tag{5.7}$$

where $\vec{\Gamma}_\varepsilon$ is the electron energy flux vector, n_ε is the electron energy density and R_ε is the energy gain or loss as a result of inelastic collisions, and is determined using the plasma chemistry of the system. The above three equations can be simplified by making assumptions regarding the momentum transfer frequency and the thermal velocity of the electrons, as well as assuming a Maxwellian velocity distribution. This results in a simplification of the electron pressure tensor, which becomes:

$$\boldsymbol{p_e} = n_e \kappa T_e \boldsymbol{I} \tag{5.8}$$

where κ is Boltzmann's Constant, $\boldsymbol{I}$ is the Identity matrix and T_e is the electron temperature. With these simplifications, the drift velocity can be calculated and finally, expressions for the electron and energy flux vectors can be obtained. With this information and appropriate boundary conditions, the above differential equations can be solved numerically. The numerical method used to solve the equations resulting from this treatment is detailed in [142].

This drift diffusion approximation is only useful when the plasma to be studied is weakly ionized and collisional. It's validity is also reliant on the reduced electric field not being too high and the background pressure not being too low.

Heavy Species Transport The most comprehensive way to describe the diffusive transport of heavy, excited, charged and neutral species is to utilize the Maxwell-Stephan Equations [143]. These equations describe the force balance of a species $\imath$ and, in general, are:

$$-\frac{1}{\xi_\imath}\nabla\xi_\imath = \sum_{\jmath \neq \imath} \frac{1}{D_{\imath\jmath}} \xi_\jmath (u_\imath - u_\jmath) \tag{5.9}$$

where $D_{\imath\jmath}$ is the binary diffusivity between species $\imath$ and species $\jmath$, $\xi_\imath$ is the mole fraction

of each species $\imath$, and $u_\imath$ is the molar velocity of the same species. The Maxwell Stephan's approach is the only one which conserves the total mass of the system, but it is difficult to implement as it is very computationally expensive. This means alternative techniques need to be considered. Fick's Laws of diffusion are one such alternative [144], and are given in one dimension:

$$F = -D\frac{\partial C}{\partial x} \tag{5.10}$$

$$\frac{\partial C}{\partial t} = D\frac{\partial^2 C}{\partial x^2} \tag{5.11}$$

where F is the rate of transfer of the diffusive substance, D is the diffusion coefficient, C is the concentration of the diffusing substance, t is time and x is the spatial coordinate under consideration. Fick's Laws can be derived from the Maxwell-Stephan's Equations by assuming all binary diffusion coefficients are equal, i.e. $D_{\imath\jmath} = D$. This means that certain phenomena can't be captured by Fick's Laws, but implementing them is much less computationally expensive. A compromise between these two methods is the Mixed Average Approximation.

In the Mixed Average Approximation, all other gases' velocities are assumed to be the same. This allows the diffusion velocity for each gas to be obtained [145]. The result being that only one diffusion coefficient is calculated for each species, i.e. $D'_{\imath m}$ instead of $D_{\imath\jmath}$. By applying this approximation to the Maxwell-Stephan Equation and rearranging as in [145], the Mixed Average Approximation Equation is:

$$D'_{\imath m} = \frac{1 - Y_\imath}{\sum_{\jmath \neq \imath} \frac{\xi_\imath}{D_{\imath\jmath}}} \tag{5.12}$$

where $Y_\imath$ is the mass fraction of each species $\imath$. These approximations are implemented by COMSOL Multiphysics in the following way: The equation describing the flow of $k = 1, ..., Q-1$ species and N reactions is:

$$\rho\frac{\partial Y_k}{\partial t} + \rho(\vec{u}\cdot\nabla)Y_k = \nabla\cdot\vec{j}_k + R_k \tag{5.13}$$

where ρ is the density of the flow, R_k is the rate expression for species k, $\vec{u}$ is the mass averaged fluid velocity vector and $\vec{j}_k$ is the diffusive flux vector:

$$\vec{j}_k = \rho Y_k \vec{V}_k \tag{5.14}$$

where $\vec{V}_k$ is the multicomponent diffusion velocity for species k, and will change depending on whether the Mixed Average Approximation is chosen, or Fick's Laws are chosen to determine the heavy species transport properties. Equation 5.13 is appropriate for describing the transport of ions. If the Mixed Average Approximation is chosen, the multicomponent diffusion velocity is:

$$\vec{V}_k = D'_{km}\frac{\nabla Y_k}{Y_k} + D'_{km}\frac{\nabla M_n}{M_n} + \frac{D_k^T}{\rho Y_k}\frac{\nabla T}{T} - z_k \mu_{km}\vec{E} \tag{5.15}$$

where M_n is the mean molar mass of the mixture, T is the gas temperature, D_k^T is the thermal diffusion coefficient for species k, z_k is the charge number for species k, μ_{km} is the mixture averaged mobility for species k and $\vec{E}$ is the electric field. If Fick's Laws are chosen, the multicomponent diffusion velocity is:

$$\vec{V}_k = D_{kf}\frac{\nabla Y_k}{Y_k} + D_{kf}\frac{\nabla M_n}{M_n} + \frac{D_k^T}{\rho Y_k}\frac{\nabla T}{T} - z_k \mu_{km}\vec{E} \tag{5.16}$$

where D_{kf} is a user defined diffusion coefficient that must be specified for each species.

5.1.3. The Computational Fluid Dynamics Module

The computational fluid dynamics module in COMSOL Mutiphysics, is able to solve a number of different fluid flow problems, that can involve a wide variety of interacting phenomena. For example, chemical reactions in multi-species flows can be studied as well as non-isothermal turbulent flows. In general, these flows are solved by considering the laws of momentum, mass and energy in fluids. To explain the ability of the module to solve all possible flows would be beyond the scope of this work, so the features of the particular type of flow used in these simulations will be explored here, namely, a single-phase laminar flow.

Single-Phase Laminar Flow

Laminar flow is characterized by a fluid flowing in parallel layers, where mixing between layers does not occur [146]. Laminar flow typically occurs at lower velocities (depending on the fluid properties), and phenomena such as swirls or eddies are not observed. If the velocity is increased past a threshold velocity, laminar flow transitions into turbulent flow. A single-phase laminar flow was considered for this work because the propellant flow used in the thrusters under study consists of a pure monatomic gas (argon), flowing at low to intermediate Reynolds numbers.

COMSOL Multiphysics is able to simulate laminar flows by solving for the velocity and pressure fields of a flow using the Navier-Stokes equations for momentum conservation, and the continuity equations for the conservation of mass. The Navier-Stokes Equation for compressible flow [147] (the flow considered in this case), as solved by COMSOL Multiphysics, is given by Equation 5.17 and the continuity equations for the conservation of mass [148], is given by Equations 5.18:

$$\rho\frac{\partial\vec{u}}{\partial t}+\rho(\vec{u}\cdot\nabla)\vec{u}=\nabla\cdot\left[-p\mathbf{I}+\mu\left(\nabla\vec{u}+(\nabla\vec{u})^{T}\right)-\frac{2}{3}\mu(\nabla\cdot\vec{u})\boldsymbol{I}\right]+\vec{F} \tag{5.17}$$

$$\frac{\partial\rho}{\partial t}+\nabla\cdot(\rho\vec{u})=0 \tag{5.18}$$

where ρ is the density, $\vec{u}$ is the velocity field, p is the pressure and μ is the dynamic viscosity of the fluid under study, while $\boldsymbol{I}$ is the identity matrix and $\vec{F}$ are the accelerating forces that are acting on the fluid such as the force of gravity.

5.1.4. The Heat Transfer Module

A brief discussion of the heat transfer module is given here, which applies only to the specific situation detailed in this work. More detail is available in the COMSOL Multiphysics user guide and the associated references [137].

The heat transfer module takes into account the transfer of thermal energy in a system under study by including the effects of the three mechanisms of thermal energy transport, namely, conduction (the process by why heat is transferred through collisions between the microscopic particles that constitute a body); convection (the transport of heat energy

throughout a system via the movement of fluids) and radiation (the transport of heat energy via the emission and absorption of electromagnetic waves). In order to achieve this, the heat transfer module attempts to solve the heat equation, which is a representation of the first law of thermodynamics. The form of the equation given in Equation 5.19 has been expressed for a fluid, and is written in terms of the temperature, T, as opposed to the internal energy. This makes the system of equations easier to solve:

$$\rho C_p \left(\frac{\partial T}{\partial t} + (\vec{u} \cdot \nabla) T \right) = -(\nabla \cdot \vec{q}) + \boldsymbol{\tau} : \boldsymbol{S} - \frac{T}{\rho} \frac{\partial \rho}{\partial t}\bigg|_p \left(\frac{\partial p}{\partial t} + (\vec{u} \cdot \nabla) p \right) + Q \quad (5.19)$$

where $\vec{u}$ is the velocity field of the fluid under study, ρ is the density of the fluid heat is being transferred through, T is the absolute temperature of the fluid, C_p is the heat capacity at a constant pressure, p is the pressure of the fluid, $\boldsymbol{\tau}$ is the viscous stress tensor, $\vec{q}$ is the heat flux through the system via conduction, Q represents heat sources other than viscous heating, which is represented by the second term on the right of the equation, and $\boldsymbol{S}$ is the strain-rate tensor, which can be written as:

$$\mathbf{S} = \frac{1}{2}(\nabla \vec{u} + (\nabla \vec{u})^T) \quad (5.20)$$

Equation 5.19 is derived ensuring that conservation of mass is taken into account. This is embodied in the expression given in Equation 5.18. Fourier's law of heat conduction is used to determine the conductive heat flux, $\vec{q}$, which is given to be proportional to the temperature gradient across the system under study:

$$q_i = -k \frac{\partial T}{\partial x_i} \quad (5.21)$$

where k is the thermal conductivity of the system under study. k becomes a tensor in the case of heat transfer in a solid where anisotropy is considered. In the viscous heating term, the : symbol is a contraction operator, and can be written as:

$$\boldsymbol{\tau} : \boldsymbol{S} = \sum_n \sum_m \tau_{nm} S_{nm} \quad (5.22)$$

The third term on the right-hand side of Equation 5.19 represents adiabatic compression

heating from the work done via pressure, but these phenomena, as well as viscous heating effects, can be neglected, and this gives a more recognisable form of the heat equation:

$$\rho C_p \frac{\partial T}{\partial t} + \rho C_p \vec{u} \cdot \nabla T = \nabla \cdot (k \nabla T) + Q \tag{5.23}$$

Finally, if the fluid under consideration is stationary, the equation for purely convective heat transfer is obtained:

$$\rho C_p \frac{\partial T}{\partial t} + \nabla \cdot (-k \nabla T) = Q \tag{5.24}$$

5.2. Simulation Geometry

An example of the geometry used in these simulations is shown in Figure 5.2. It depicts a two-dimensional representation of the 'U-Shaped', DC discharge thruster channel and gas inlet, with electrodes installed, and a region of the open vacuum chamber into which the discharge and gaseous propellant will expand. The dimensions are chosen to reflect the size of the experimentally studied system as accurately as possible.

The DC discharge thruster channel is represented by the semicircular tube extending from $y = 0.003$ m to $y = -0.011$ m. The gas inlet is represented by the rectangular block extending from the apex of the thruster channel at $x = 0$ m, downwards to the line $y = -0.014$ m. The electrodes are represented by the rectangles extending inwards into the thruster channel, from the line $y = 0.001$ m. The region of the vacuum chamber is represented by the large rectangle extending from the line $y = 0.003$ m, to the line $y = 0.012$ m. The geometry is constructed in such a way that the cathode is the electrode to the left of the origin, while the anode is the electrode to the right of the origin. The discharge channel length is set to a value of 0.022 m, and the discharge channel radius is set to a value of 0.0025 m. The diameter of the hole in the electrodes is the same for both cathode and anode, and is set to a value of 0.0036 m. The thickness of the electrodes is set to 0.0005 m. The gas inlet measures 0.005 m wide and 0.0025 m long. The region of the vacuum chamber measures 0.021 m wide and 0.009 m long.

Extra edges are added to the geometry at a number of different positions. Edges are added near the cathode to act as mesh control edges. These edges do not form part of the physical geometry of the simulation, but allow for a more refined mesh to be developed near the cathode. This is to resolve the more complex phenomena that typically occur

here. Extra edges are also added across the openings of the thruster channel, where the thruster channel connects to the vacuum region. These edges are also not part of the physical geometry of the system, but are used as integration paths when extracting thrust values from the simulations.

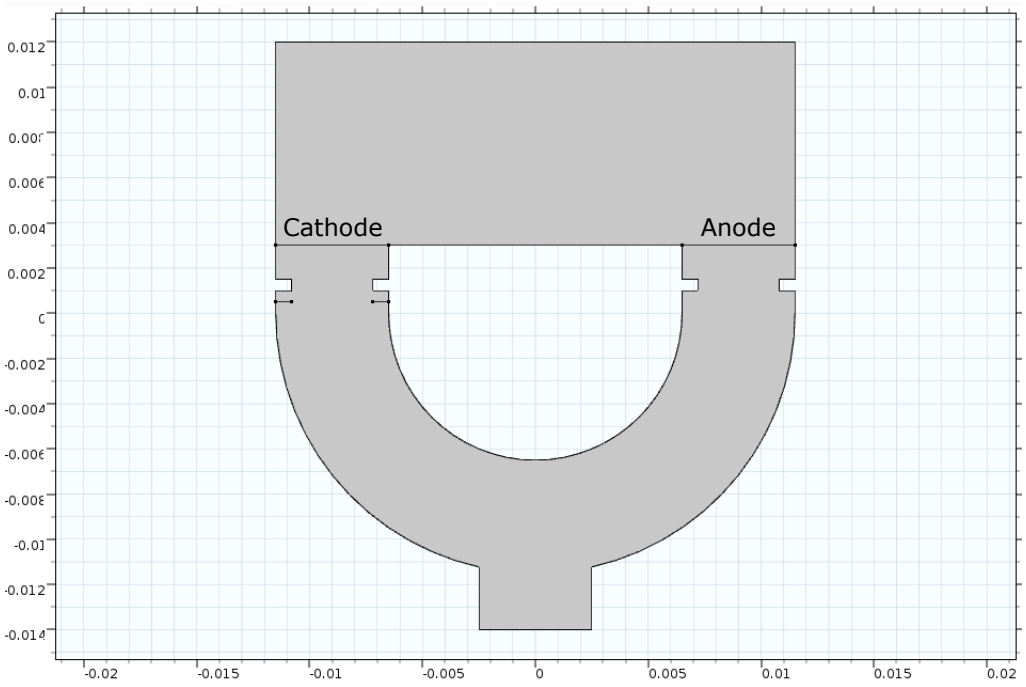

Figure 5.2.: An example geometry used to study the 'U-shaped', direct current discharge based, electric microthruster. The units of the horizontal and vertical axes are meters

5.3. Simulation Parameters

Two sets of simulations are performed, a base case, where the fundamental features of thruster operation are studied, and varying parameter simulations, where parameters corresponding to experimental variables are altered, to study their affect on the fundamental features of thruster operation.

5.3.1. Base Case

The discharge to be simulated occurs in argon gas, set at a mass flow rate of 0.6 mg/s, flowing from the gas inlet. The discharge tube is powered by a circuit with a ballast resistor value of 1 kΩ. This circuit is used to generate a potential difference of 425 V

No.	Reaction	Reaction Type	$\Delta\varepsilon$ (in eV)
1	$e + Ar \rightarrow e + Ar$	Elastic	0
2	$e + Ar \rightarrow e + Ar^*$	Excitation	11.5
3	$e + Ar^* \rightarrow e + Ar$	Superelastic	-11.5
4	$e + Ar \rightarrow 2e + Ar^+$	Direct Ionization	15.8
5	$e + Ar^* \rightarrow 2e + Ar^+$	Stepwise Ionization	4.24
6	$Ar^* + Ar^* \rightarrow e + Ar + Ar^+$	Penning Ionization	-
7	$Ar^* + Ar \rightarrow Ar + Ar$	Metastable Quenching	-

Table 5.1.: A list of the reactions occurring in the plasma chemistry of argon as found in [149].

across the electrodes. The cathode is set to have a work function of 5 and a secondary electron emission coefficient of 0.25. In order to model the plasma chemistry inside the argon discharge, a number of reactions have to be specified, along with their rate coefficients. The reactions considered are given in Table 5.1. The species considered in the reactions are: neutral argon (Ar), excited argon neutrals (Ar^*), argon ions (Ar^+) and electrons (e). A simple argon plasma chemistry, where only singly charged ions are considered, is used in this work. The collision frequency of the reactions is determined from cross-section information for reactions 1, 3 and 5, and from Townsend coefficients for reactions 2 and 4, as they provide a more accurate result for these reactions. Reactions 6 and 7 are specified in terms of forward rate coefficients.

5.3.2. Initial and Boundary Conditions

The initial conditions provide the simulation with a point from which the model will evolve. The initial electron number density is set to 10^{13} particles/m^{-3}, the initial mean electron energy is set to 4 V, and the initial electric potential is set to 0 V. The initial population of neutral argon atoms is obtained from mass conservation constraints and the initial population of argon ions is obtained from an electroneutrality constraint. The initial background pressure is set to a value of 0.17 torr, and the initial temperature of the whole system is set to a value of 300 K.

All the walls that comprise the thruster, including the electrodes, but excluding the surface through which the propellant enters the simulation, have no slip boundary conditions imposed upon them. This is to simulate the greater strength of the force of adhesion compared to the force of cohesion when the gaseous propellant interacts with the thruster walls. The horizontal surface defining the bottom of the gas inlet pipe is set to be the surface through which neutral propellant enters the simulation domain. The surfaces that

No.	Reaction
1	$Ar^* \rightarrow Ar$
2	$Ar^+ \rightarrow Ar$

Table 5.2.: A list of the surface reactions occurring in the plasma chemistry of argon, as the different particle species interact with the boundaries.

define the boundary of the vacuum are set as neutral outflow points. This is enforced by imposing a pressure at these boundaries, which is equal to the initial background pressure.

The DC discharge is set to act as a heat source, which will alter the temperature of the unionised propellant fuelling it. To simplify the computation, the surfaces of the thruster channel are kept at a constant temperature of 300 K. This means that the plasma resulting from the DC discharge heats only the gaseous propellant. The surfaces which define the boundary of the vacuum are set to act as an outflow of thermal energy, representing the loss of heated gas to the vacuum.

The walls of the discharge channel are constructed from an insulating material and, as a result, a charge accumulation boundary condition is imposed on the walls to simulate the formation of a plasma sheath. The surfaces that define the boundaries of the vacuum outside of the thruster have boundary conditions imposed upon them that allow them to act is outlets of electrons, ions and excited atoms, as well as neutrals. This simulates different charged and excited species being lost to the vacuum when they interact with the boundary. The cathode is grounded and the anode is connected to the external electric circuit, which drives the discharge with the circuit values described previously. The vacuum boundary directly opposite the thruster channel openings is also grounded. This is to simulate the grounded vacuum chamber used in experiments, the presence of which influences electron and ion behavior. The temperature, pressure and velocity fields used in the plasma component of the simulation are obtained from the heat transfer and laminar fluid flow components respectively.

A number of surface reactions also need to be specified, as they will define how the different species in the plasma will interact with the boundaries. These reactions are given in Table 5.2. Both Reaction 1 and 2 are applied to the discharge tube walls and the electrodes. However, in the case of the cathode, reaction 2 is specified so that it results in secondary electron emission, which will sustain the discharge.

5.3.3. Mesh Choice

A free triangular geometry was used in the bulk of the simulation domain, with a finer edge mesh used around the anode and the cathode to capture the physics in these areas with greater accuracy. The mesh element sizes were altered depending on the convergence requirements of the simulation being considered. The mesh refinement edges placed near the cathode, allow for a finer mesh in this area, as interactions that will sustain the discharge will occur here. An example of the mesh used is shown in Figure 5.3.

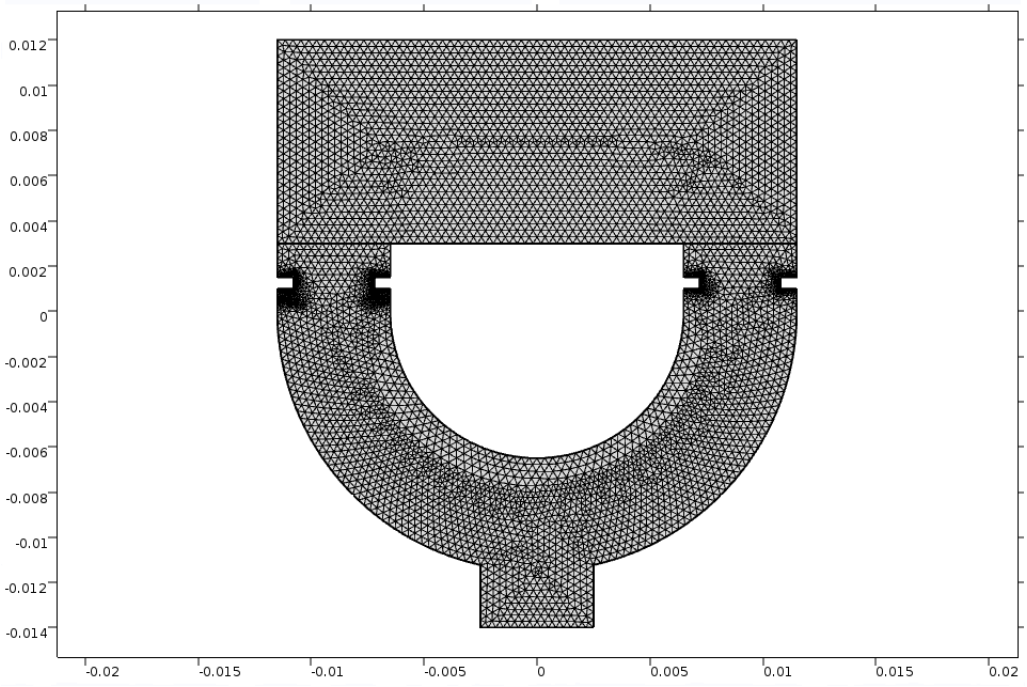

Figure 5.3.: An example of the mesh geometry used to study the 'U-shaped', direct current discharge based, electric microthruster. The units of the horizontal and vertical axes are meters

5.3.4. Varying Parameter Simulations

To ensure the simulations can model the experimental behavior of the thruster, various simulation parameters that correspond to physical thruster parameters are varied, and the effect on the simulation results are studied. These simulation parameters are the discharge voltage and the mass flow rate. The discharge voltage is varied between 200 V and 400 V, in steps of 50 V, and the mass flow rate is varied between 0.2 mg/s and 0.8 mg/s, in steps of 0.2 mg/s. In simulations where the discharge voltage is varied, a mass flow rate of 0.6 mg/s is used. In simulations where the mass flow rate is varied,

a discharge voltage of 425 V is used. All other simulation parameters and initial and boundary conditions are identical to those used in the base case simulation.

6. Simulations: Results and Discussion

In this chapter, the results of the simulations described previously are presented. The distributions of important physical quantities across the simulation domain are provided. Results for both a base case scenario, and a scenario where thruster operating parameters are varied are given. Connections between the simulation results and the experimental results previously described are made.

6.1. Base Case

The following sections describe the features observed in the profiles of the electron number density, ion number density, electron temperature, electric potential, ion flux, neutral gas velocity and neutral gas temperature profiles of the base case simulation. These profiles are shown in Figure 6.1. These results are compared and contrasted with experimental results where possible in an attempt to explain the trends observed in the experimental data.

Upon reviewing the literature, a particular reference is of considerable interest. The work done in [150] focuses on simulating a micrometer sized, DC discharge based, electric microthruster. However, contrary to the mechanism of operation proposed in this work, the DC discharge is used to heat a gaseous propellant, the expulsion of which generates thrust. The geometry studied in [150] differs from that studied here, but still provides an invaluable source of comparison.

6.1.1. Electron Number Density

As shown in Figure 6.1 A), the simulation results indicate two distinct regions of elevated electron number density: a region around the live electrode, which exists both inside the thruster channel, and extends outwards into the vacuum region, and a region inside the

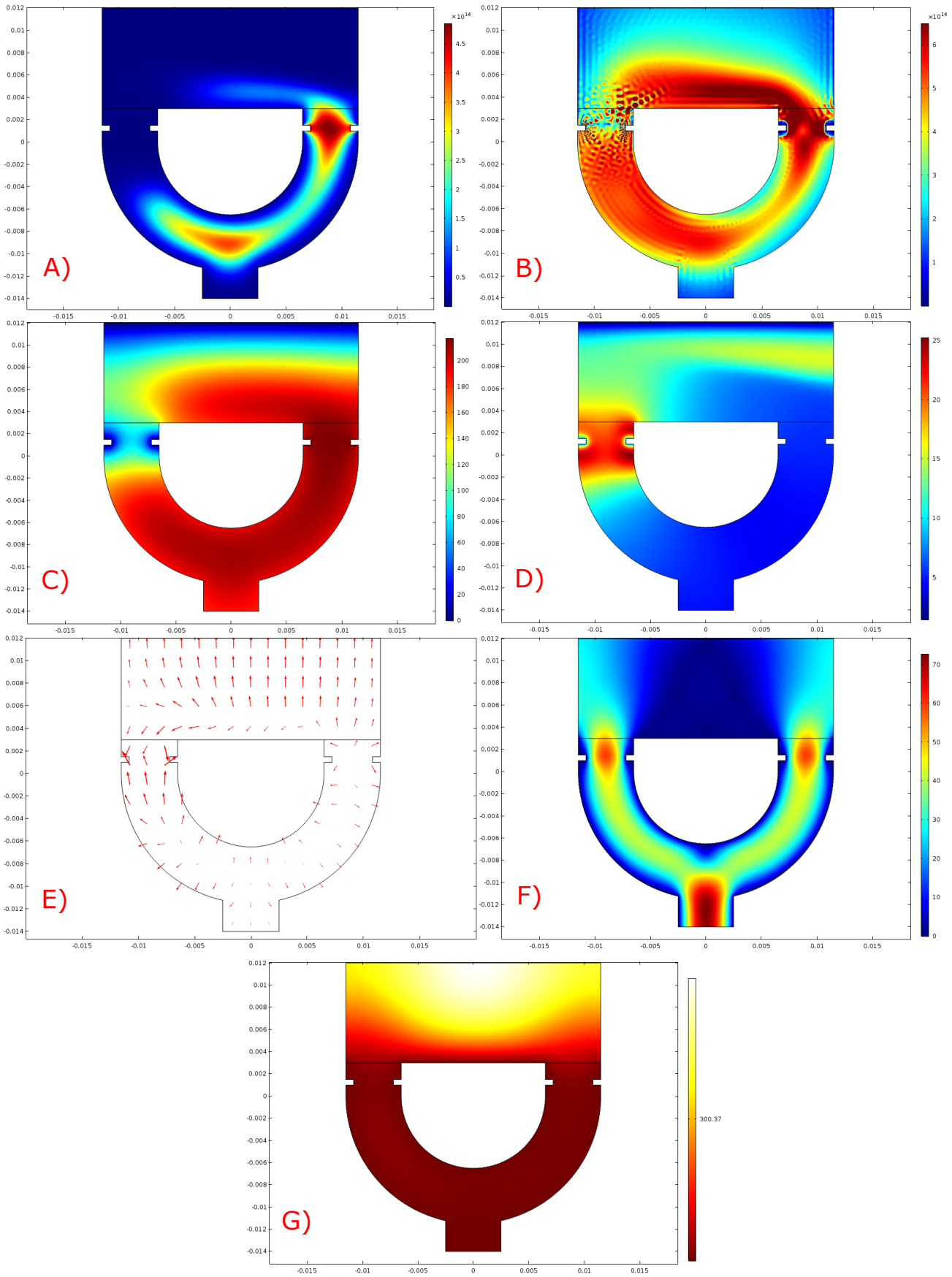

Figure 6.1.: The results of the simulation of the 'U-shaped', direct current discharge based, electric microthruster: A) electron number density (in particles/m^3); B) ion number density (in particles/m^3); C) electric potential (in V); D) electron temperature (in V); E) ion flux; F) neutral gas velocity (in m/s) and G) neutral gas temperature (in K)

thruster channel, which corresponds to the electron number density profile present in a conventional DC discharge. While no obvious plume formation occurs, this observation is consistent with the hypothesis of the system's mechanism of operation, which states that electrons will be attracted towards the live electrode and be ejected outwards.

The discharge present in the thruster channel would result in the creation of electrons at the grounded electrode, due to secondary electron emission developing from ion bombardment, and would in turn create an elevated electron density between the electrodes. This is a result of further ionization collisions deeper inside the channel. The existence of these phenomena are supported by experimental observations, which show a discharge present in the thruster discharge channel during thruster operation.

The remaining areas of the simulation domain are characterized by a significantly lower density of electrons. However, there is a region of elevated electron density present outside of the thruster channel, which extends along the exterior surface of the thruster towards the grounded electrode. The presence of electrons outside the thruster channel can be attributed to the attractive influence of ions as they leave the thruster channel.

The region of highest electron number density is in the center of the hole in the live electrode, with values of approximately 4.5×10^{14} particles/m^3, 9 times higher than the background electron number density. No plume formation is also observed in [150], and the electron number density profile appears to be similar to that observed in a conventional DC discharge, with the region of highest electron number density nearest the grounded electrode.

6.1.2. Ion Number Density

As shown in Figure 6.1 B), the simulation results indicate an ion number density profile that possesses some similarities to the electron number density profile. However, the profile appears to be less well resolved, and a number of small, isolated regions have greatly elevated number densities with no physical phenomenon suggesting why these regions should exist. It is most likely that these features and the lack of resolution are due to numerical artefacts. Further evidence of this is provided by mesh refinements, which result in some of these regions disappearing and the resolution of the ion number density profile improving. However, these improvements were limited, as attempting to continually refine the mesh in its current configuration resulted in convergence issues. More mesh refinements should be performed, so that a smooth ion number density profile can be obtained.

In contradiction to the original hypothesis of the system's mechanism of operation, the region of highest ion number density is present nearest the live electrode. Studying the evolution of the ion density profile from discharge initiation until it reaches a steady state, indicates that while ion formation does occur on the inside of the thruster discharge channel, initially, the highest ion density occurs nearest the live electrode, corresponding with the high electron density also present there. This suggests that the majority of ionization is initiated by the electrons being attracted to the live electrode, resulting in a higher ion density. The ions in this region are then attracted towards the grounded vacuum boundary wall, causing them to exit the thruster channel at the opening associated with the live electrode. Ions are not ejected from the opening in the thruster associated with the grounded electrode, as the majority of ions accelerated towards the grounded electrode, collide with the electrode and emit secondary electrons.

There is also a region of elevated ion number density outside of the thruster that appears to be attracted towards the grounded electrode. These ions may hamper thruster operation by charging the exterior spacecraft surface. The more massive ions drag electrons along with them as they move towards the grounded electrode, resulting in the region of increased electron number density outside of the thruster discharge channel along the exterior of the thruster. The region of increased ion number density inside the thruster channel is a consequence of the conventional DC discharge mode of operation.

These results could explain the asymmetry observed in the ICD measurements. The ICD is slightly greater on the side of the thruster associated with the live electrode according to experimental data. A different result is observed in the ion number density observed in [150]. The singly charged ion number density is concentrated nearest the grounded electrode, as would be expected in a conventional DC discharge.

6.1.3. Electric Potential

As shown in Figure 6.1 C), the simulation results indicate that the electric potential is highest around the live electrode, which corresponds with the region of highest electron and ion number density. This area of high potential corresponds with the plasma potential seen in conventional DC discharges, where the discharge is confined between the two electrodes. The plasma potential is determined to be approximately 200 V in this region. Langmuir probe measurements would be required to experimentally verify these results. A cathode fall region is observed in the potential near the grounded electrode, as is expected with such a discharge. Similar features, including the cathode fall region, are observed in [150] as well. Another cathode fall region is observed around the grounded

vacuum region boundary

6.1.4. Electron Temperature

As shown in Figure 6.1 D), the simulation results indicate that the electron temperature is highest nearest the grounded electrode. The electron temperature in this region is calculated to be approximately 25 V, 5 times higher than the background electron temperature. This phenomenon is expected, as electrons are ejected from the grounded electrode as secondary electrons when it is bombarded by ions. Electrons will gain energy as they are accelerated away from the grounded electrode, but will then lose their energy as they participate in ionization and excitation collisions. It is interesting to note that some of the highest energy electrons are present on the side of the grounded electrode open to the vacuum chamber area. This phenomenon is due to the ions ejected from the region around the live electrode being attracted to the grounded cathode, and impacting on its outward facing surface. The resulting electrons are then accelerated towards the positive plasma potential outside of the thruster channel. This will result in an increase in electron energy, and a corresponding increase in electron temperature in this region.

It is interesting to note that the areas of highest electron temperature are nearest the inner wall of the discharge channel. The fact that the highest energy electrons are present at these surfaces implies that these surfaces are bombarded by high energy ions, and will in turn be subjected to increased erosion. This is consistent with experimental observations, which show that the grounded electrode experiences the greatest erosion and is the point of failure of the thruster. However, the experimental data is not sufficient to determine which surface of the electrode experiences the most erosion, and more studies are required to confirm this. In [150], the region of highest electron temperature also occurs at the grounded electrode, as is expected for a DC discharge, and corresponds with the results seen here.

6.1.5. Ion Flux

As shown in Figure 6.1 E), the ion flux is primarily directed outwards towards the grounded vacuum boundary, with a small portion of the flux directed backwards towards the grounded electrode. These results indicate that ions should contribute to the generation of thrust, as they are ejected and accelerated away from the thruster under the influence of the grounded vacuum chamber boundary. The ion flux seen in [150] appears to also be predominantly attracted to the grounded electrode, but the ions are largely

confined to the discharge tube. This means the detrimental effect of ions being directed backwards, towards the thruster are avoided. The thrust geometry also helps mitigate this affect.

6.1.6. Neutral Gas Velocity

As shown in Figure 6.1 F), the simulation results indicate that there are constriction points in the neutral gas velocity profile at the openings in the electrodes. These constriction points result in an increase in the gas velocity before they expand out into the vacuum. However, the greatest constriction occurs as the gas enters the simulation domain at the gas inlet. This results in a maximum neutral gas velocity of 70 m/s, which indicates a subsonic flow. The neutral gas velocity profile is symmetric about the line $x = 0$ m. The neutral gas expands into the vacuum domain and forms plumes at the thruster channel openings.

6.1.7. Neutral Gas Temperature

As shown in Figure 6.1 G), there is an increase in the neutral gas temperature as the gas expands outwards into the vacuum domain. This shows that the DC discharge is heating the neutral gas. The gas is heated to less than a degree above the initial temperature. This differs from the results of [150] where increases of hundreds of degrees kelvin are measured. Considering that the thruster in [150] was studied as an electrothermal system, where thrust production ws predominantly the result of neutral gas heating, these results suggest neutral gas heating only forms a small component of thrust generation in this system. However, no experimental data exists to confirm these results.

6.2. Varying Parameter Simulations

The following sections describe the effect that varying some of the simulation parameters, which correspond to actual thruster operational parameters, have on the profiles of the same physical quantities studied in the base case.

6.2.1. Voltage

In the following subsections, the results of varying the discharge voltage, and the effect it has on the physical quantities extracted from the simulations are given.

Electric Potential

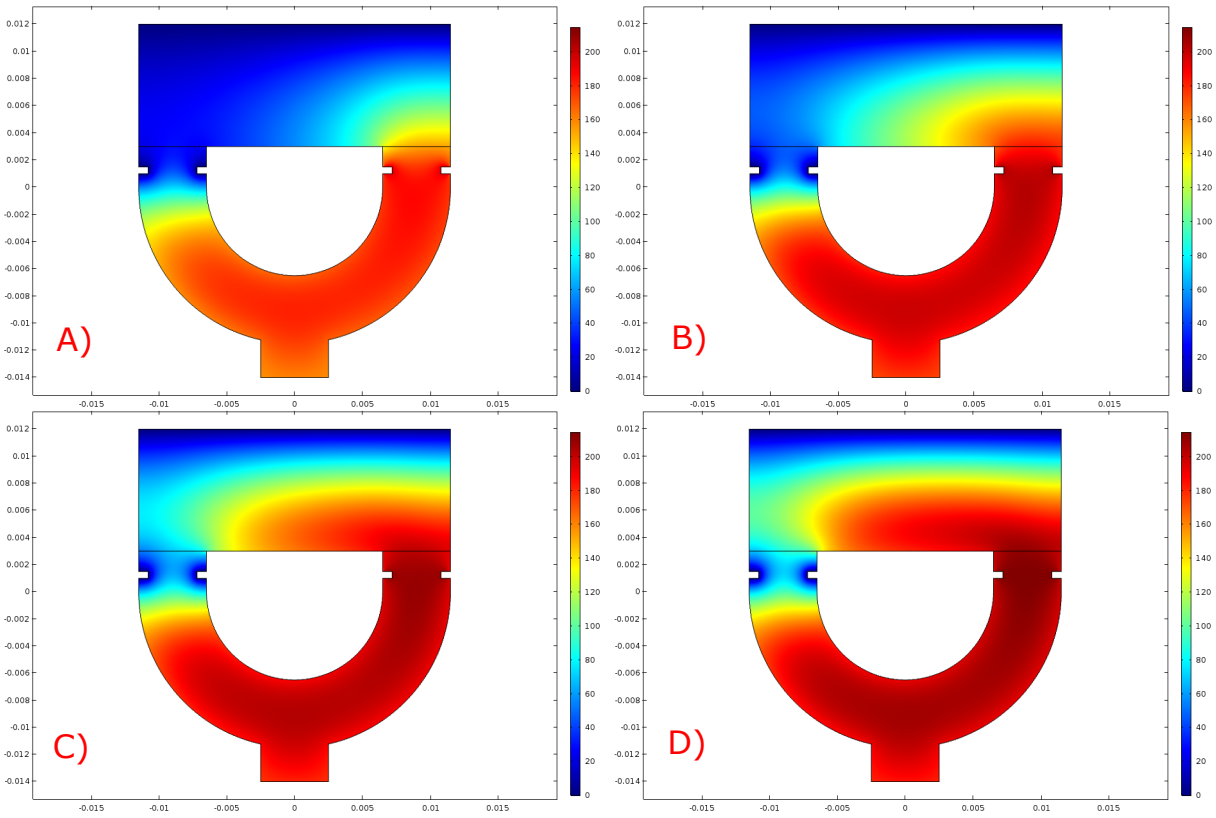

Figure 6.2.: The electric potential obtained from the simulation of the 'U-shaped', direct current discharge based, electric microthruster, as the discharge voltage is varied between the values of A) 250 V; B) 300 V; C) 350 V and D) 400 V

Figure 6.2 shows how the electric potential changes as the voltage drop across the electrodes is increased. The plots A) through D) show how increasing the voltage results in an increase in the plasma potential. The maximum electric potential increases from approximately 180 V to 200 V. The increase results in a steeper potential gradient between the plasma and the grounded electrode, and between the plasma and the grounded vacuum boundary. An interesting phenomenon is noted at lower discharge voltages. Here, the plasma potential is almost completely confined to the thruster discharge channel, but as the discharge voltage is increased, the plasma potential begins to expand outwards into the vacuum region, and extend towards the grounded electrode and the grounded

vacuum boundary. This could represent the different modes of operation observed experimentally, where the discharge is initially confined to the discharge channel, followed by plume formation as the discharge voltage increases.

Electron Number Density

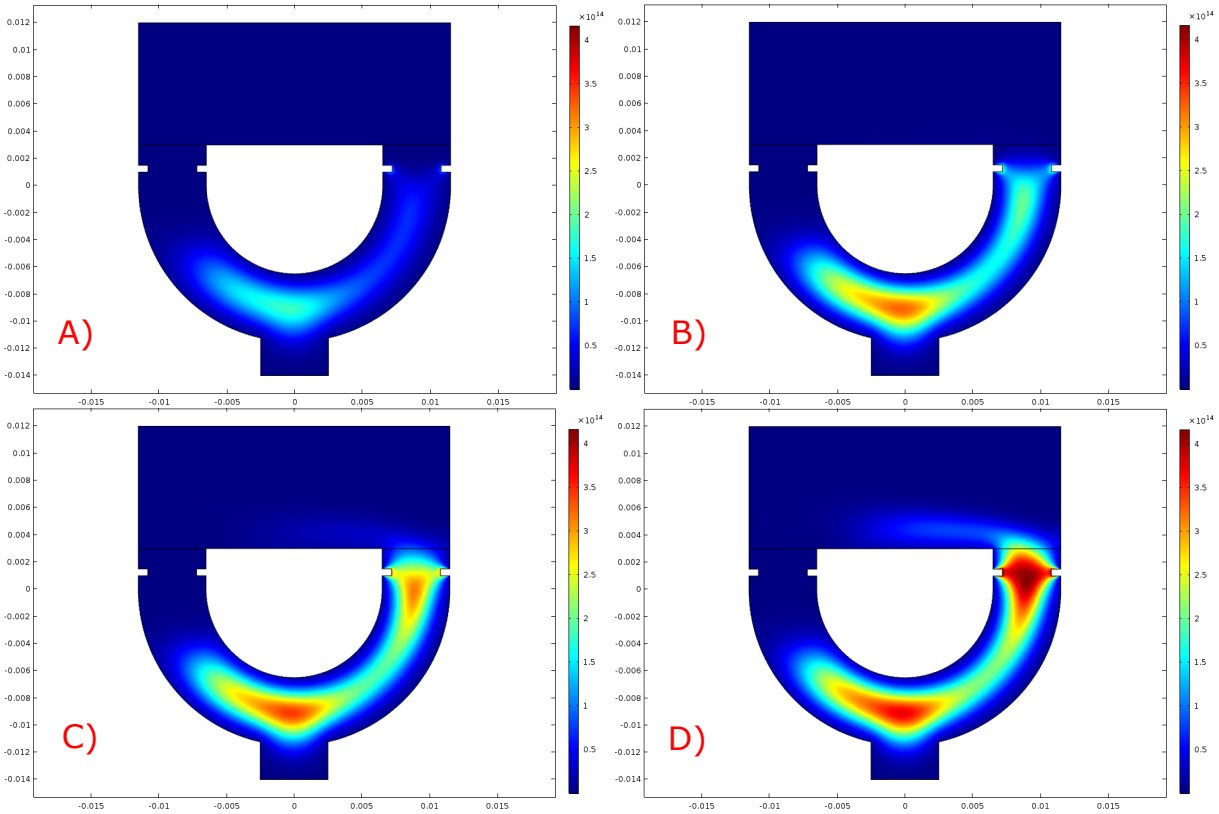

Figure 6.3.: The electron number density obtained from the simulation of the 'U-shaped', direct current discharge based, electric microthruster, as the discharge voltage is varied between the values of A) 250 V; B) 300 V; C) 350 V and D) 400 V

Figure 6.3 shows how the electron number density changes as the voltage drop across the electrodes is increased. The plots A) through D) show how increasing the voltage results in an increase in the electron number density. The maximum electron number density increases from approximately 1.5×10^{14} particles/m^3 to 4×10^{14} particles/m^3. This result is expected, because a larger potential drop results in the initial electron population being accelerated to greater velocities, which results in more ionization reactions and a greater electron number density. The electron population appears to be confined to the thruster discharge channel at low discharge voltages, but as the discharge voltage is increased, the electron number density increases around the live electrode, resulting in a high electron number density present outside of the thruster channel near the live electrode. These

results agree with the trends observed in the electric potential results and experimental observations.

Electron Temperature

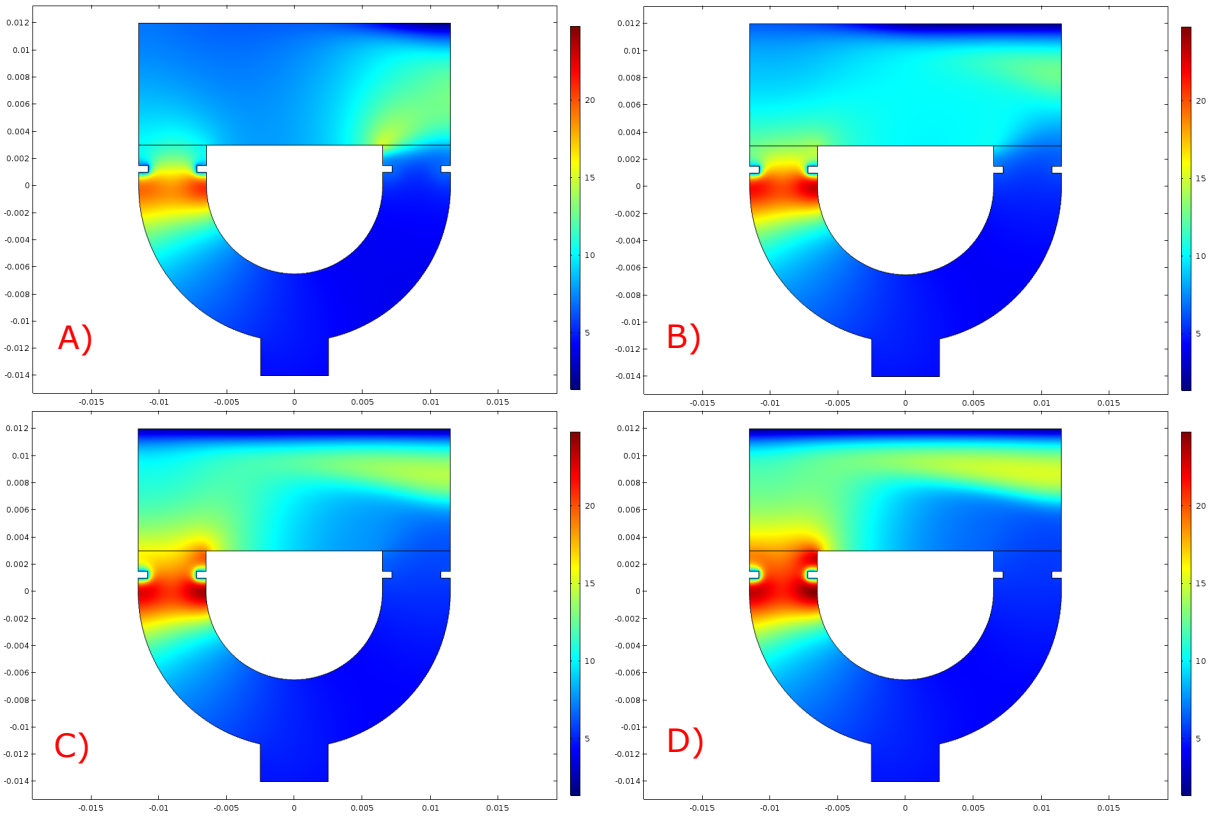

Figure 6.4.: The electron temperature obtained from the simulation of the 'U-shaped', direct current discharge based, electric microthruster, as the discharge voltage is varied between the values of A) 250 V; B) 300 V; C) 350 V and D) 400 V

Figure 6.4 shows how the electron temperature changes as the voltage drop across the electrodes is increased. The plots A) through D) show how increasing the voltage results in an increase in the electron temperature. The maximum electron temperature increases from approximately 18 V to 25 V. This is because a larger potential drop results in a larger plasma potential, which creates a larger potential gradient between the live and grounded electrodes through which the ions and electrons, resulting from secondary electron emission, can be accelerated. This means that electrons can be accelerated to higher energies and corresponding higher temperatures.

At lower discharge voltages, the region of high electron temperature is initially confined to the internal surface of the grounded electrode. As the discharge voltage is increased, a region of high electron temperature begins to form at the external surface of the grounded

electrode. This could be because ions in the discharge are no longer confined to the discharge channel at higher discharge voltages and are ejected away from the thruster. Ions outside of the thruster channel can then become attracted to the grounded electrode and be accelerated towards the external surface, where they collide with the electrode and release secondary electrons. These electrons are then accelerated to higher energies by the plasma potential outside of the thruster discharge channel.

Ion Number Density

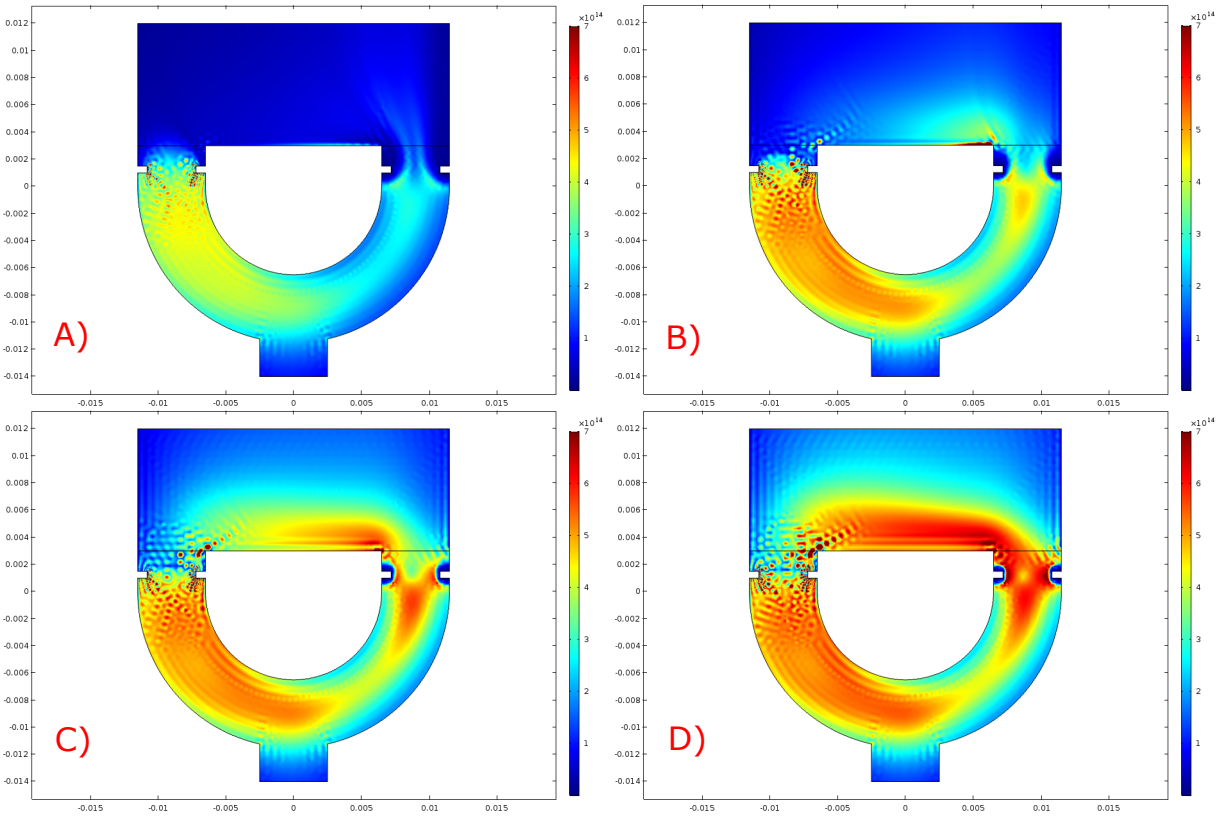

Figure 6.5.: The ion number density obtained from the simulation of the 'U-shaped', direct current discharge based, electric microthruster, as the discharge voltage is varied between the values of A) 250 V; B) 300 V; C) 350 V and D) 400 V

Figure 6.5 shows how the ion number density changes as the voltage drop across the electrodes is increased. The plots A) through D) show how increasing the voltage results in an increase in the ion number density. The maximum ion number density increases from approximately 4.5×10^{14} particles/m^3 to 7×10^{14} particles/m^3. This is due to the greater electron population resulting from the higher number of ionizing collisions by higher energy electrons. This in turn produces a higher ion number density.

The ion number density results correlate with the trends seen in the other results extracted

from these simulations. Initially the ion population is largely confined to the thruster discharge channel, with a small stream of ions ejected from the live electrode towards the grounded vacuum boundary. This suggests that even at low voltages, where the discharge is confined to the thruster channel, ions are ejected away and contribute to thrust. As the discharge voltage is increased, the ion number density increases, and more of the ion population is able to escape from the thruster.

ICD measurements show that increases in voltage have little effect on the ICD, in spite of the simulations indicating an increase in ion number density with increasing voltage. It is possible that no increase is measured because the increased ion number density could be directed backwards towards the grounded electrode.

Ion Flux

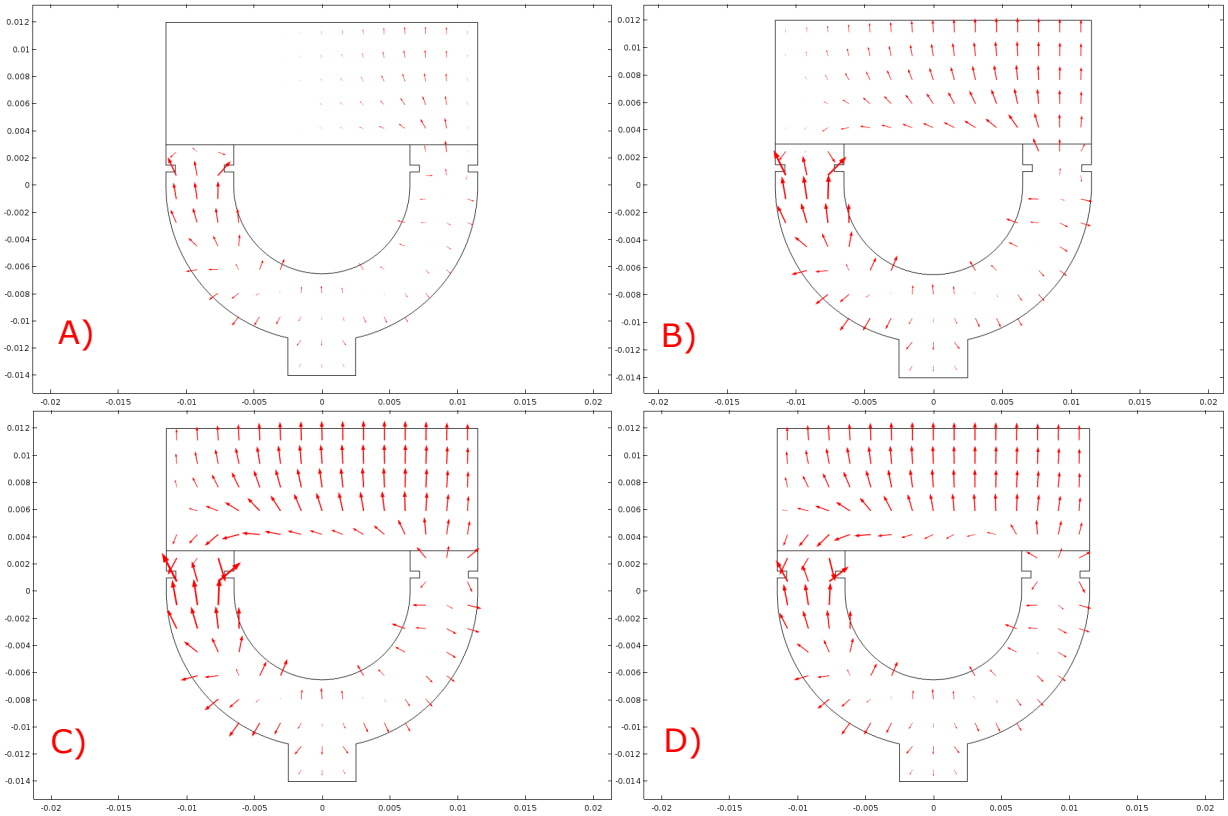

Figure 6.6.: The ion flux obtained from the simulation of the 'U-shaped', direct current discharge based, electric microthruster, as the discharge voltage is varied between the values of A) 250 V; B) 300 V; C) 350 V and D) 400 V

Figure 6.6 shows how the ion flux changes as the voltage drop across the electrodes is increased. The plots A) through D) show how increasing the voltage results in an increase in the ion flux. At low discharge voltages, the ion flux is entirely directed away

from the thruster towards the grounded vacuum boundary. This suggests that spacecraft surface charging could be mitigated by running the thruster at lower discharge voltages. As the discharge voltage is increased, more ion flux is extracted from the thruster and directed towards the grounded vacuum boundary, but ion flux also begins to be directed backwards towards the grounded electrode. This corresponds with the simulation results seen previously. It should be noted that only a small portion of the ion flux is directed backwards towards the thruster. This discredits the previous hypothesis, stating that no increase in thrust is measured experimentally when the discharge voltage is varied because the increased ion flux is directed backwards towards the thruster.

Temperature Profile

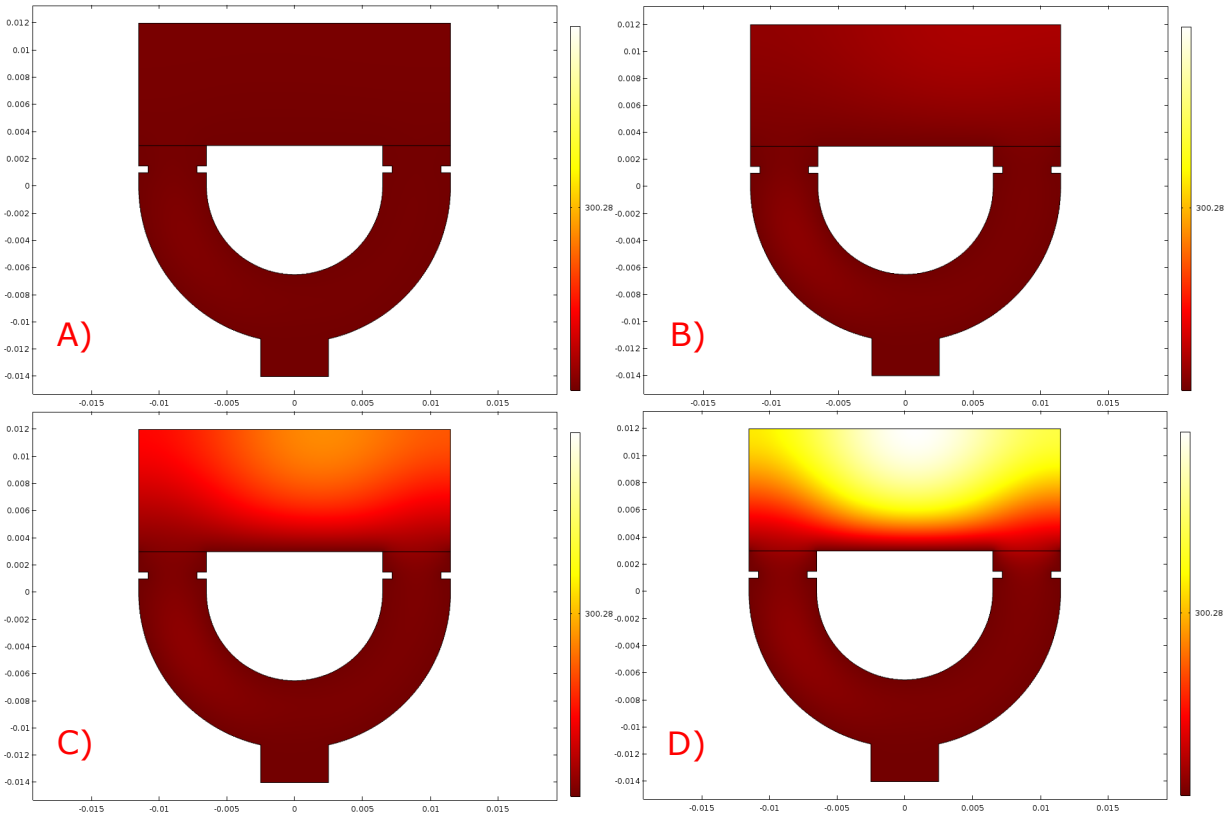

Figure 6.7.: The neutral gas temperature profile obtained from the simulation of the 'U-shaped', direct current discharge based, electric microthruster, as the discharge voltage is varied between the values of A) 250 V; B) 300 V; C) 350 V and D) 400 V

Figure 6.8 shows how the temperature profile of the background gas changes as the voltage drop across the electrodes is increased. The plots A) through D) show how increasing the voltage results in an increase in the temperature of the background gas. The maximum temperature increases from approximately 300 K to 301 K. This is due to the greater

heating imparted to the gas via the greater number of ionization and excitation collisions occurring between neutral gas atoms, ions and electrons. If the heating of the background gas is a contributing mechanism of thrust generation, this could explain why increases in the voltage do not result in increases in thrust as is observed experimentally. The increases in voltage simply do not result in an appreciable increase in gas temperature to create meaningful thrust increases.

Neutral Gas Velocity Profile

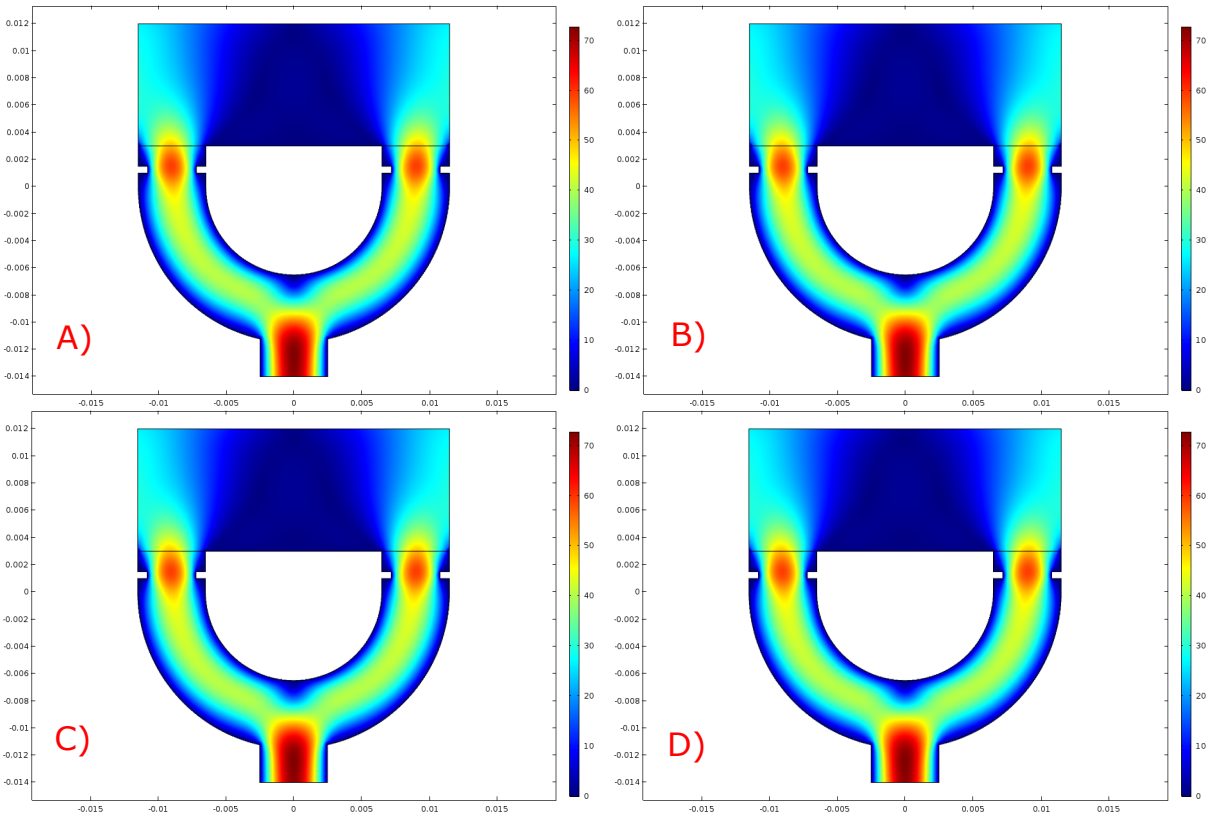

Figure 6.8.: The neutral gas velocity profile obtained from the simulation of the 'U-shaped', direct current discharge based, electric microthruster, as the discharge voltage is varied between the values of A) 250 V; B) 300 V; C) 350 V and D) 400 V

No change in the neutral gas velocity profile was observed, as the discharge voltage is varied.

6.2.2. Mass Flow Rate

In the following sub sections, the results of varying the inlet mass flow rate, and the effect it has on the physical quantities extracted from the simulations are given.

Neutral Gas Velocity Profile

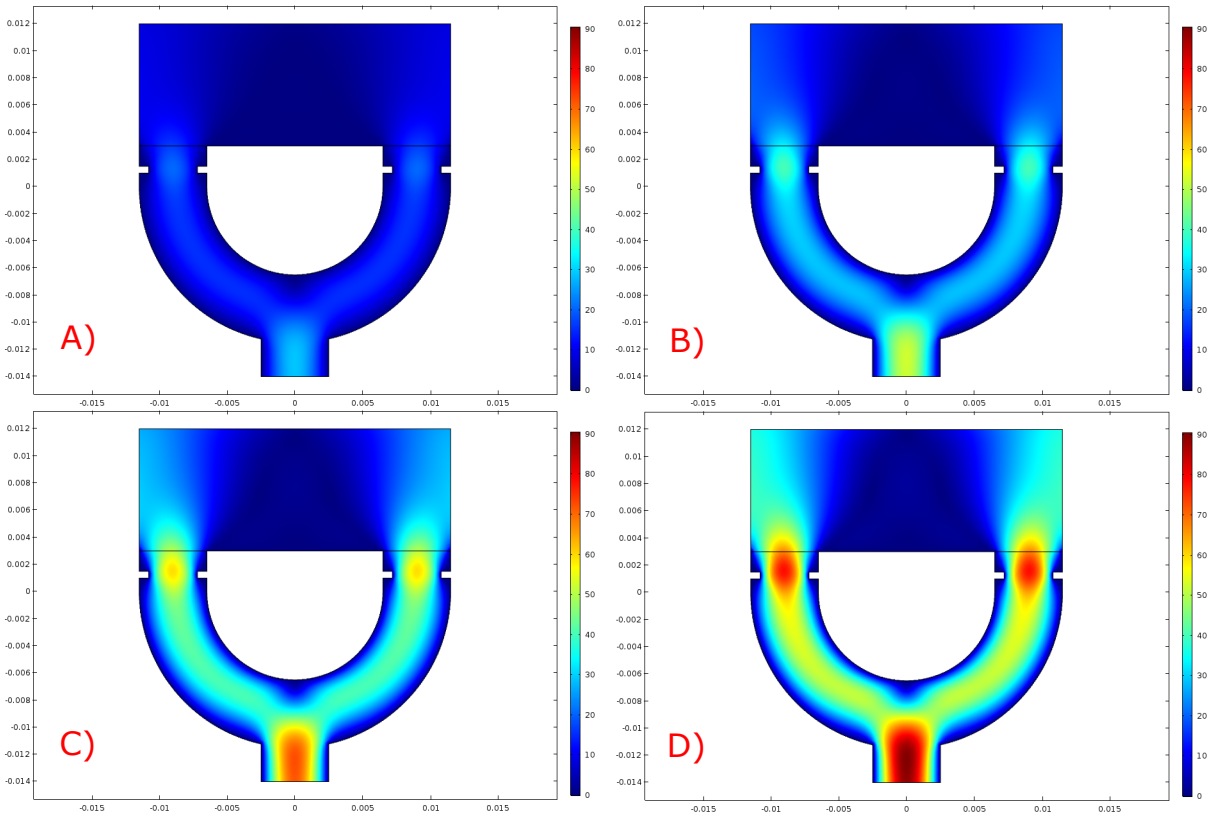

Figure 6.9.: The neutral gas velocity profile obtained from the simulation of the 'U-shaped', direct current discharge based, electric microthruster, as the mass flow rate of the gaseous propellant is varied between the values of A) 0.2 mg/s; B) 0.4 mg/s; C) 0.6 mg/s and D) 0.8 mg/s

Figure 6.9 shows how the background gas velocity profile changes as the mass flow rate at the inlet of the system is increased. The plots A) through D) show how increasing the mass flow rate results in an increase in the background gas velocity profile. This is the expected result. The maximum neutral gas velocity increases from approximately 30 m/s to 90 m/s. This increase in neutral gas velocity will result in an increase in the cold gas thrust component.

Neutral Gas Temperature Profile

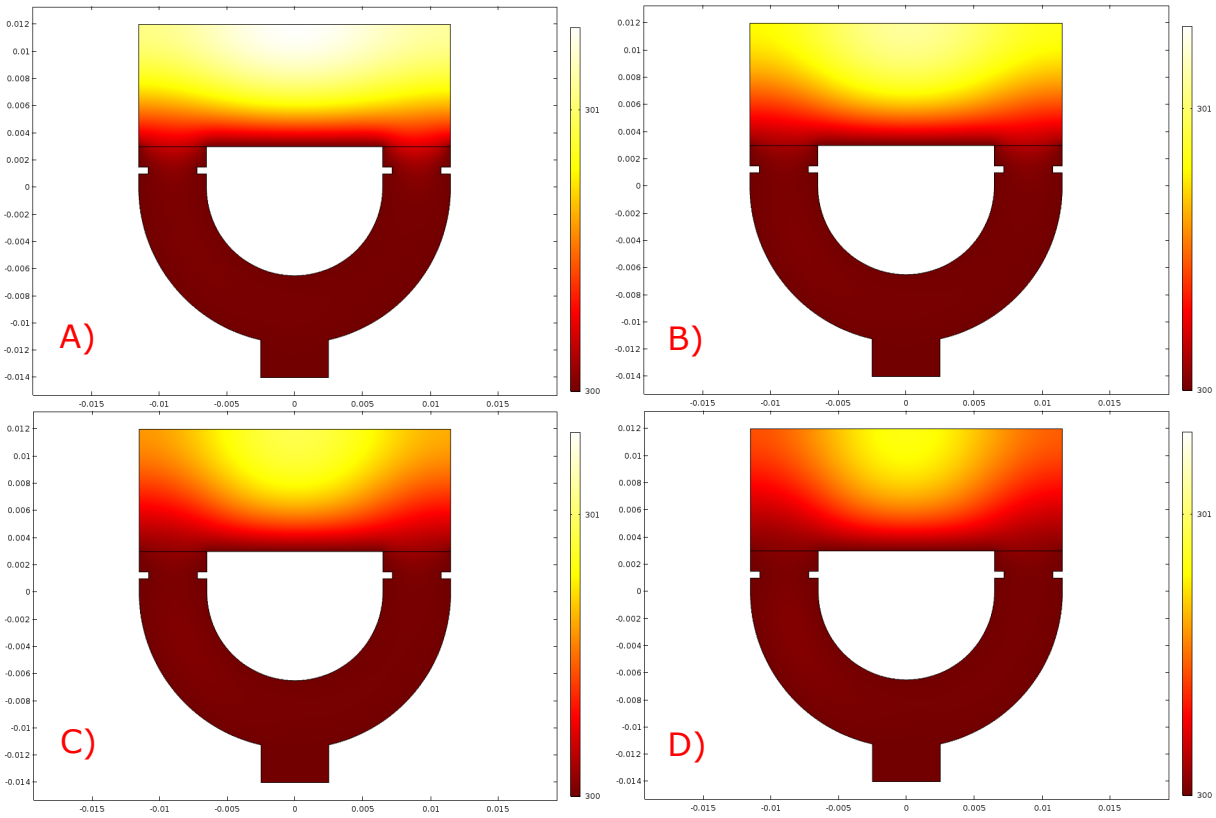

Figure 6.10.: The neutral gas temperature profile obtained from the simulation of the 'U-shaped', direct current discharge based, electric microthruster, as the mass flow rate of the gaseous propellant is varied between the values of A) 0.2 mg/s; B) 0.4 mg/s; C) 0.6 mg/s and D) 0.8 mg/s

Figure 6.10 shows how the neutral gas temperature profile changes as the mass flow rate at the inlet of the system is increased. The plots A) through D) show how increasing the mass flow rate results in a decrease in the neutral gas temperature profile. This is due to the greater velocity of the flowing neutral gas. The gas is present in the discharge for a shorter period of time, reducing the ability of the discharge to heat the neutral gas.

Electron Density

Figure 6.11 shows how the electron number density profile changes as the mass flow rate at the inlet of the system is increased. The plots A) through D) show how increasing the mass flow rate results in an increase in the electron number density, specifically in the thruster discharge channel, whereas the electron number density at the live electrode remains unchanged. The electron number density in the thruster discharge channel region increases from approximately 4.5×10^{14} particles/m^3 to 5×10^{14} particles/m^3.

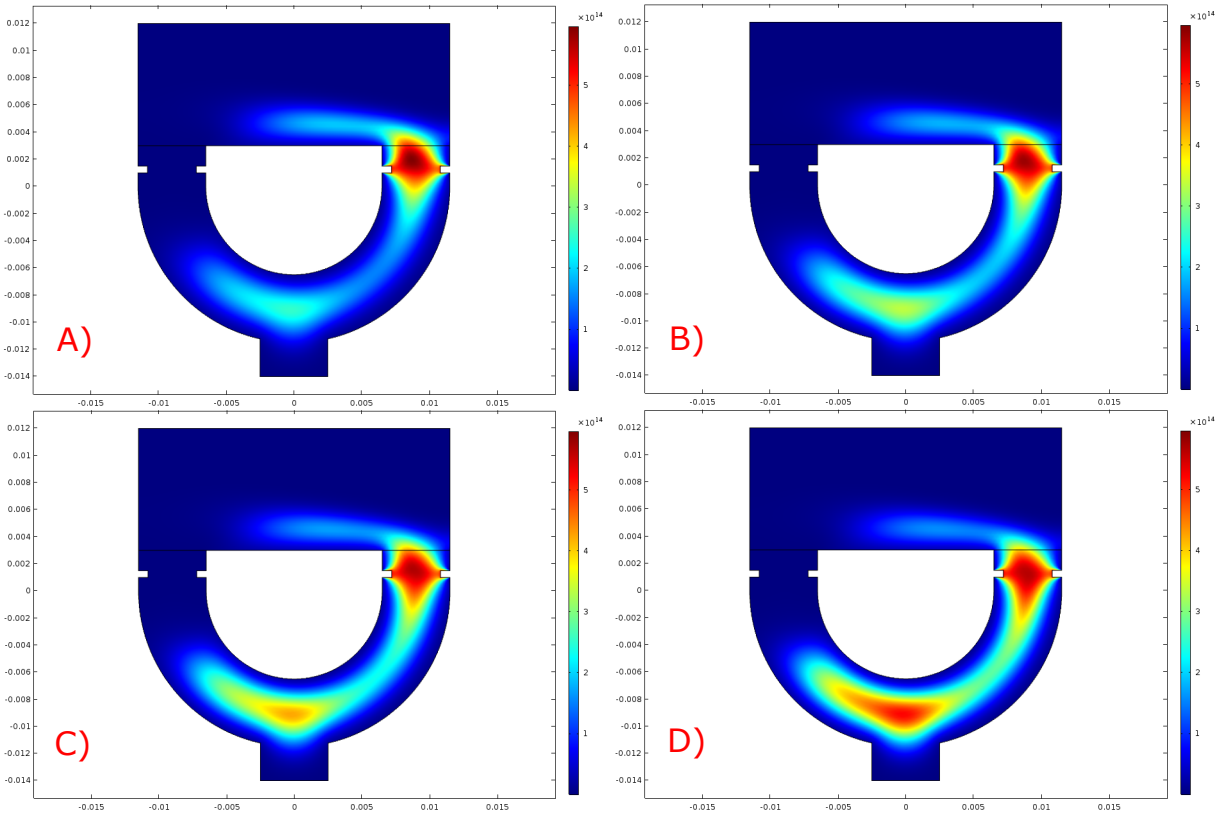

Figure 6.11.: The electron density profile obtained from the simulation of the 'U-shaped', direct current discharge based, electric microthruster, as the mass flow rate of the gaseous propellant is varied between the values of A) 0.2 mg/s; B) 0.4 mg/s; C) 0.6 mg/s and D) 0.8 mg/s

At lower mass flow rates, a lower neutral gas density is present. This means that the probability of ionizing collisions occurring between energetic electrons and neutral atoms decreases. Less ionizing collisions means a reduction in the number of electrons produced through these collisions, and subsequent secondary electron emission from the resulting ions. This results in a reduced electron number density in the thruster discharge channel.

These results indicate that the electron population around the live electrode is influenced by changes in the electrical parameters of the system, and, while the mass flow rate will have an impact on the sustaining the discharge, it will not impact the electrical characteristics of thrust generation.

Electron Temperature

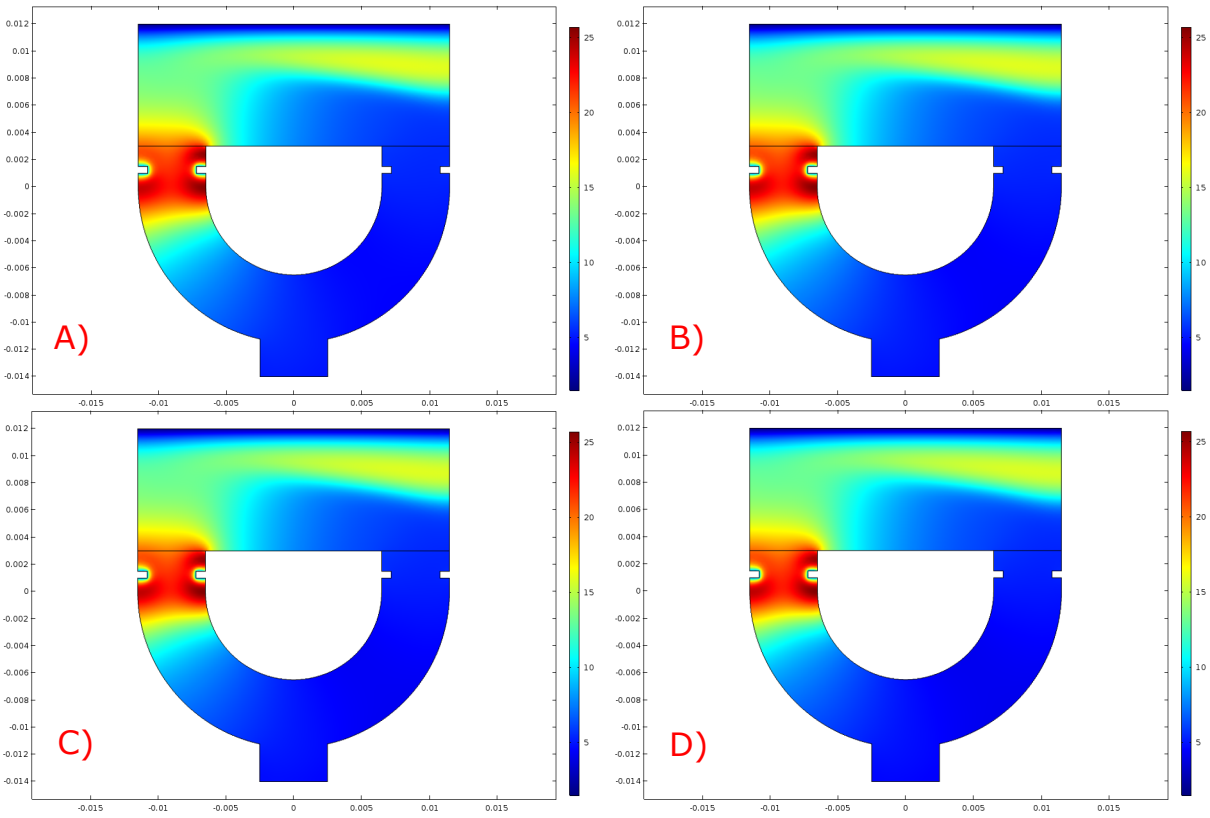

Figure 6.12.: The electron temperature profile obtained from the simulation of the 'U-shaped', direct current discharge based, electric microthruster, as the mass flow rate of the gaseous propellant is varied between the values of A) 0.2 mg/s; B) 0.4 mg/s; C) 0.6 mg/s and D) 0.8 mg/s

Figure 6.12 shows how the electron temperature profile changes as the mass flow rate at the inlet of the system is increased. The plots A) through D) show how increasing the mass

flow rate results in relatively little change in the magnitude of the electron temperature. The region of heightened electron temperature around the grounded electrode decreases in size slightly as the mass flow rate is increased. This is due to the increased neutral gas density, which results from an increased mass flow rate. The increased neutral density means the probability of an energetic electron exciting or ionizing a neutral atom increases so the region in which energetic electrons exist will decrease.

Electric Potential

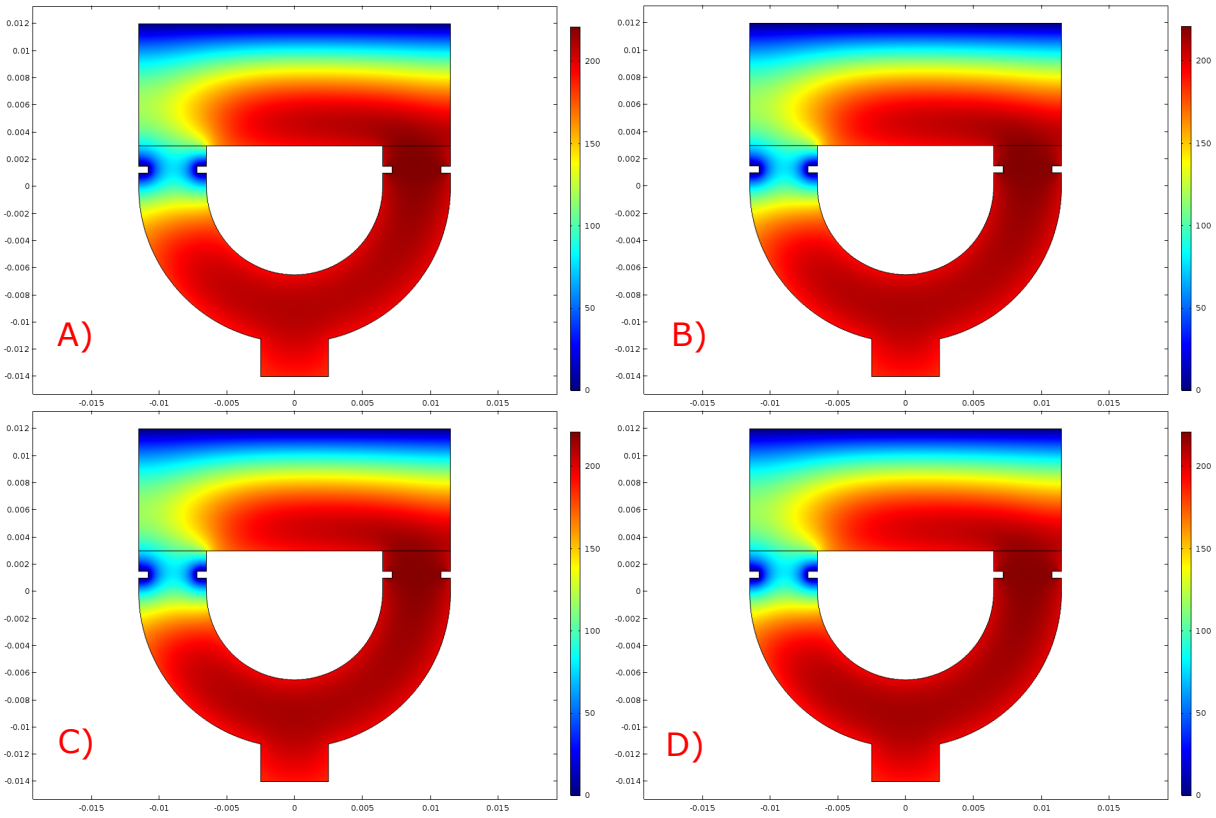

Figure 6.13.: The electric potential profile obtained from the simulation of the 'U-shaped', direct current discharge based, electric microthruster, as the mass flow rate of the gaseous propellant is varied between the values of A) 0.2 mg/s; B) 0.4 mg/s; C) 0.6 mg/s and D) 0.8 mg/s

Figure 6.13 shows how the electric potential profile changes as the mass flow rate at the inlet of the system is increased. The plots A) through D) show how increasing the mass flow rate results in relatively little change in the electric potential. There is a slight increase in the potential in the region in the thruster discharge channel, which corresponds to the region where the electron number density increases with increasing mass flow rate.

Ion Number Density

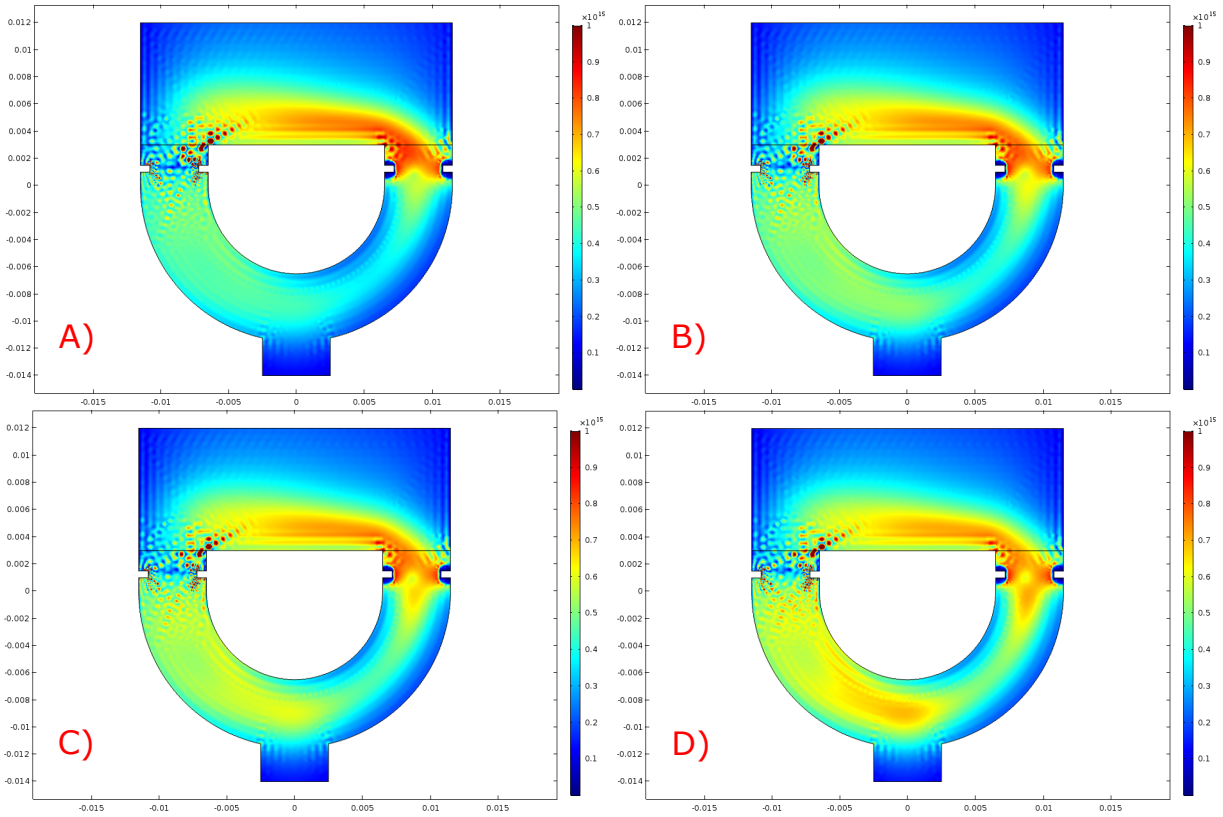

Figure 6.14.: The ion number density profile obtained from the simulation of the 'U-shaped', direct current discharge based, electric microthruster, as the mass flow rate of the gaseous propellant is varied between the values of A) 0.2 mg/s; B) 0.4 mg/s; C) 0.6 mg/s and D) 0.8 mg/s

Figure 6.14 shows how the ion number density profile changes as the mass flow rate at the inlet of the system is increased. The plots A) through D) show how increasing the mass flow rate results in an increase in the ion number density in the thruster discharge channel, but a decrease in the ion number density outside the thruster discharge channel. This is an interesting result, as it does not mirror the behavior of the electron number density. This behavior could account for the decrease in ICD as the mass flow rate is increased as was measured experimentally, but this could also be a numerical artefact.

Ion Flux

Figure 6.15 shows how the ion flux profile changes as the mass flow rate at the inlet of the system is increased. The plots A) through D) show how increasing the mass flow rate results in little change in the ion flux. This suggests that the decrease in the ion number density obtained as the mass flow rate is increased could be a numerical artefact.

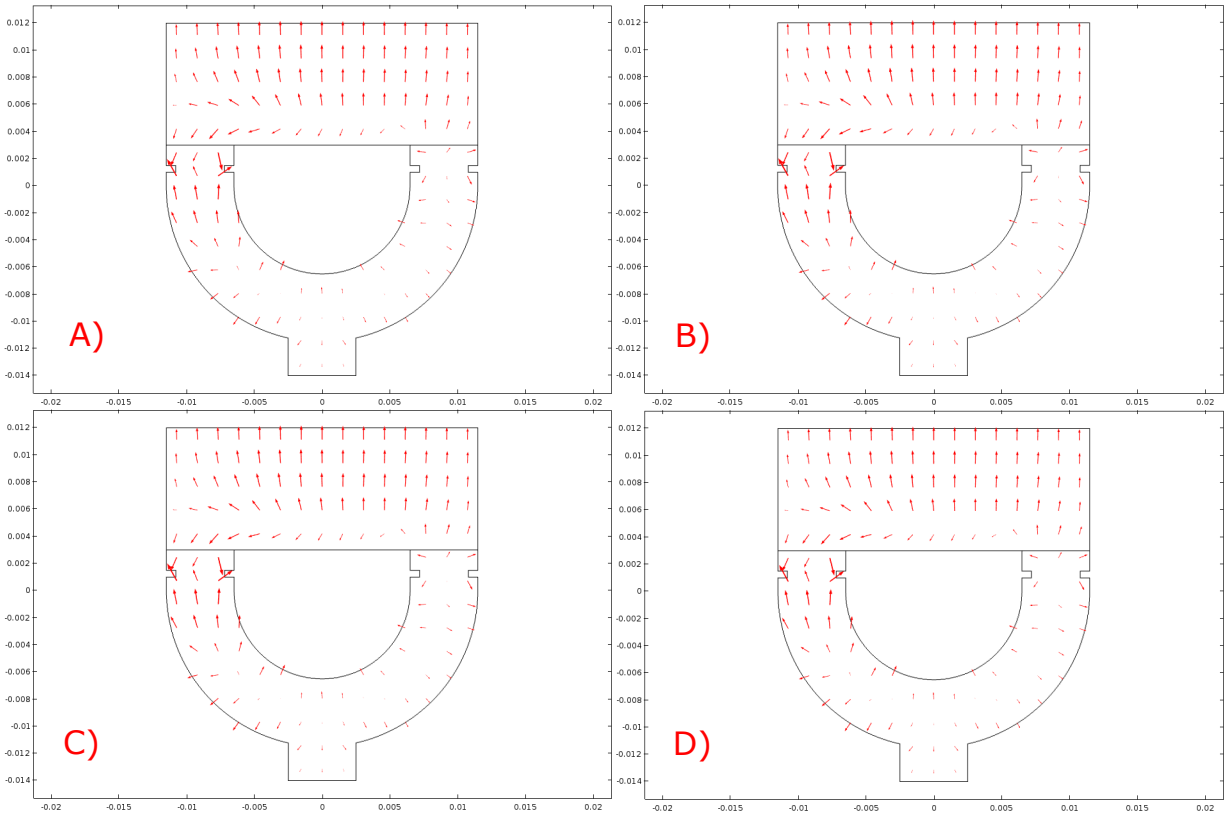

Figure 6.15.: The ion flux profile obtained from the simulation of the 'U-shaped', direct current discharge based, electric microthruster, as the mass flow rate of the gaseous propellant is varied between the values of A) 0.2 mg/s; B) 0.4 mg/s; C) 0.6 mg/s and D) 0.8 mg/s

6.3. Thrust Extraction

In order to firmly link the experimental results with the data obtained from these simulations, the thrust that the simulated thruster produces must be determined and compared with the experimentally measured thrust. This is achieved using the generalised thrust expression, shown in Equation 2.4. By applying this expression to the simulation geometry and parameters, the expression used to extract the thrust from these simulations is determined:

$$F_T = \sum_s \int_{2)} -\rho_s v_{sy} v_{sy} dl + \sum_B \int_B (p_B - p_0)\hat{n}_B dl \tag{6.1}$$

where s represents each of the heavy particle species: argon ions (Ar^+), argon neutral atoms (Ar) and excited, neutral argon atoms (Ar^*), the subscript y represents the y-component of the quantity under consideration, B represents each of the boundaries along which the neutral argon gas pressure is considered: 4) and 5), p_B is the neutral argon gas pressure across the boundary B and p_0 represents the background gas pressure. All other quantities retain their previously defined meanings. Figure 6.16 shows all of the boundaries that were considered in this analysis, along with their corresponding labels. Appendix C contains a full discussion of how Equation 6.1 is obtained. All of the required integrals are performed numerically using COMSOL Multiphysics.

6.3.1. Results

The thrust obtained by varying both the mass flow rate and the discharge voltage are extracted from the simulations and compared to experimental data.

Varied Mass Flow Rate

Cold Gas Thrust Figure 6.17 shows the cold gas thrust that was extracted from the simulations as the mass flow rate was varied. This is obtained by considering only the heavy species that are not charged or excited as a result of the discharge. Mass flow rates between 0.3 mg/s and 0.8 mg/s are considered. A linear curve is fitted to the data in order to extract the exhaust velocity, so it can be compared with experimental results. The cold gas thrust extracted from the simulations varies from between 14 μN and 65 μN. At the largest mass flow rate studied, the experimentally measured cold gas thrust

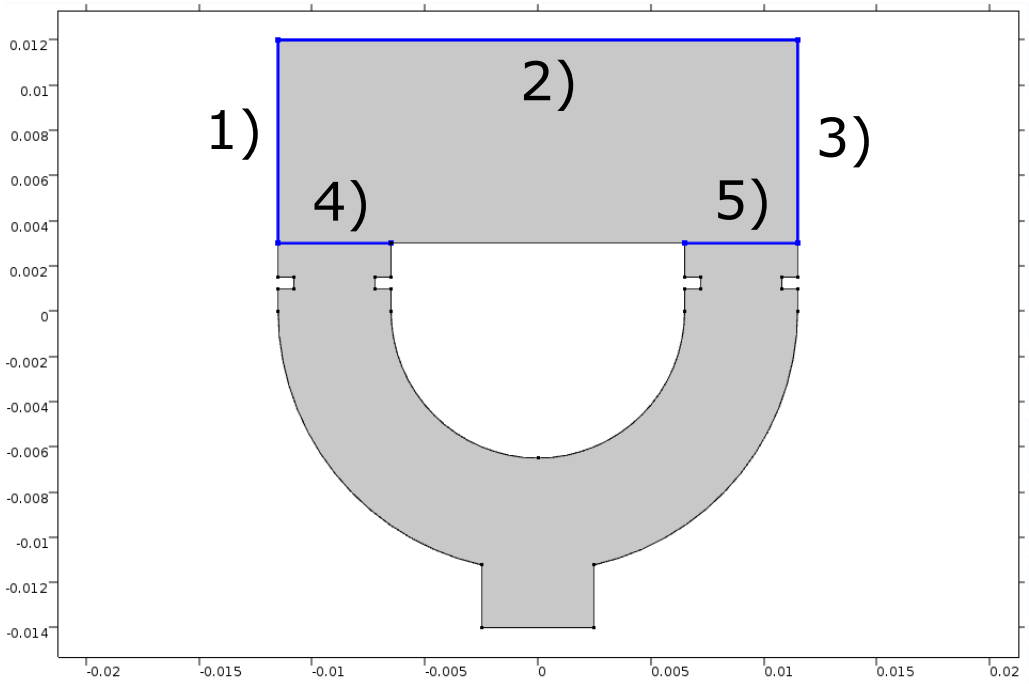

Figure 6.16.: A diagram depicting the entire simulation geometry and all of the labelled boundaries considered in calculating the thrust generated by the simulated thruster.

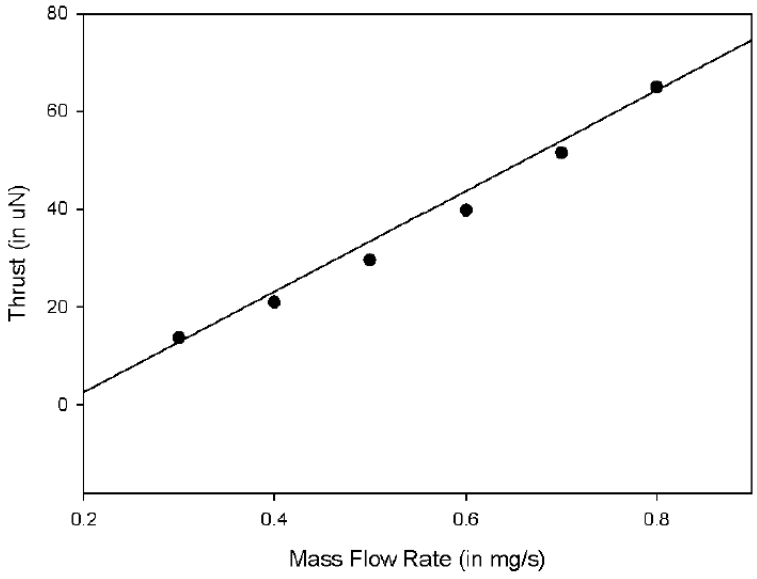

Figure 6.17.: The cold gas thrust extracted from the simulations as the mass flow rate through the system is varied. A linear curve is fitted to the data.

is approximately three times greater than the simulated cold gas thrust. The expression fitted to the simulated cold gas thrusts is:

$$\vec{F_T} = 103\dot{m} - 18 \tag{6.2}$$

The results of this fit indicate that the exhaust velocity of the simulated cold gas propellant is 103 m/s. The experimentally determined cold gas exhaust velocity is approximately three times greater than this value.

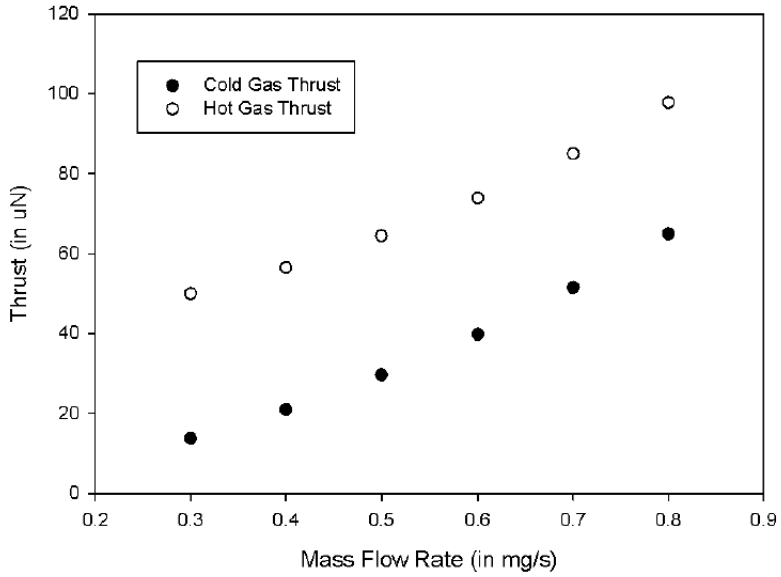

Figure 6.18.: A comparison between the hot gas thrust and the cold gas thrust extracted from the simulations as the mass flow rate is varied

Hot Gas Thrust Figure 6.18 shows a comparison between the hot gas thrust and the cold gas thrust extracted from the simulations as the mass flow rate is varied. The simulation results indicate that, as the mass flow rate increases, the increase in thrust imparted to the base cold gas thrust remains constant. This is the same phenomena observed in the experimental results, and indicates that the mass flow rate has a negligible effect on the thrust produced by the electrical component of the system in the range of operating parameters studied here. The increase in thrust imparted by the discharge fluctuates slightly around a value of 37 μN, which is approximately three time higher than the experimental value measured. The recurrence of the factor of three in the difference between the experimental and simulated value could indicate the influence of a scaling factor that needs to be taken into consideration in the design of simulations.

Varied Voltage

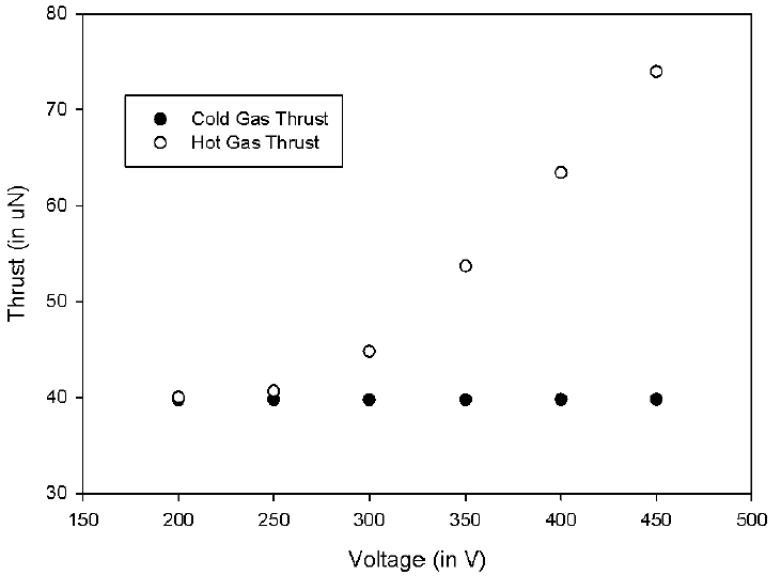

Figure 6.19.: A comparison between the hot gas thrust and the cold gas thrust extracted from the simulations as the discharge voltage is varied

Figure 6.19 shows a comparison between the hot gas thrust and the cold gas thrust extracted from the simulations as the discharge voltage is varied. These results differ markedly from experimental results. Experimentally, when the discharge voltage is varied, no change in the hot gas thrust increase is measured. The thrust increase extracted from the simulation is shown to increase as the discharge voltage is increased. This increase results in the electrostatic thrust component becoming the dominant mechanism for thrust production, producing close to the same thrust produced by the base cold gas thrust.

6.3.2. General Comments

There are substantial differences noted when the experimentally obtained thrust measurements are compared to the thrust values extracted from the simulations. However, it should be noted that there are two fundamental differences between the experimental and simulated configurations, which could account for the differences in observed behavior. Firstly, the two-dimensional nature of the simulation means there are inherent differences in the geometry of the simulated system and the experimentally studied system. When extrapolated to three dimensions, the simulated geometry consists of a square discharge channel, as opposed to a round one, and the electrode geometry consists of two bars on either side of the discharge channel, as opposed to the ring electrodes used in experi-

mental work. It is also important to note that the grounded vacuum chamber boundary is in very close proximity to the thruster when compared to experiment, and this could have an impact on the electric component of thrust generation, making it more prominent than is observed in the experimental situation. Secondly, the simulated system is a system where no limit is placed on the current in the discharge, whereas experimentally, both the voltage and the current were individually controlled and limited. This difference will have a profound impact on the simulated system. These issues should be addressed in future work by attempting to place a limit on the current produced in the simulated system (or running experiments without current limitations), and attempting to implement a full, three-dimensional simulation, which will ensure that the experimental and simulated geometries are identical. Implementing these changes should result in better correspondence between experimental and simulated results, which will allow for greater insight into the system to be obtained.

6.4. Estimated Power Lost to Heating

Power is utilized by the system in a variety of different ways, including ionization of the propellant gas and accelerating the resulting ions away, via an electrostatic mechanism, generating thrust. However power can also be lost in ways that may be less than ideal, a prominent example being heating of the propellant gas and heating of the electrodes used to generate the plasma. Using simulated and experimental data, the amount of power lost due to general heating is estimated below.

6.4.1. Calculation

Firstly, by considering the experimental evidence from erosion testing, only heating of the cathode is considered. This is because the thruster material around the cathode showed the most amount of heat damage when compared to the anode. Secondly, only the vacuum region of the simulation will be considered when determining heating effects. This is because the neutral gas temperature profiles from the simulations indicate the the area of greatest temperature increase lie outside the thruster channel. This suggests that the mechanism of heating in this case would be heating due to the inelastic collision of ions with neutral particles as they are accelerated towards the cathode. In order to approximate the maximum effect of this heating, the simulation results from approximating the highest experimentally tested mass flow rate will be used. The vacuum region of the simulation domain is divided up into 8 separate regions, which are each considered

in turn. These subdivisions are shown in Figure 6.20 and Figure 6.21.

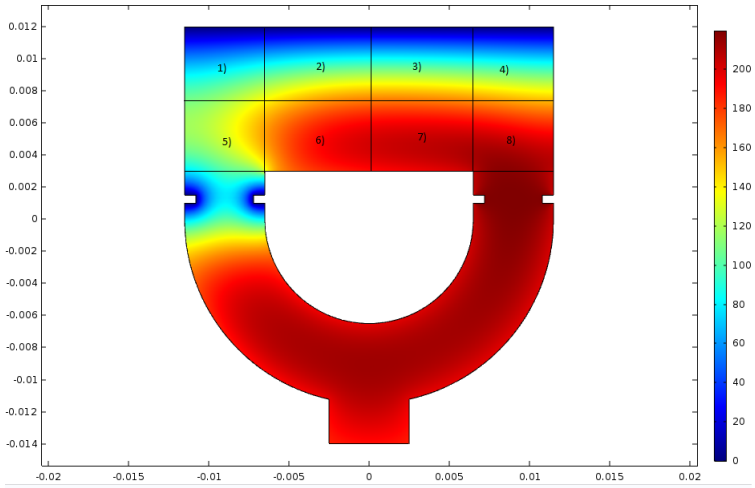

Figure 6.20.: A plot showing the spatial variation of the electric potential under the conditions used in these calculations. The division of the vacuum region into several smaller regions is shown.

Using the spacial variation of the electric potential shown in Figure 6.20, the maximum voltage drop between the point of highest potential and the cathode in each subdivision of the vacuum region is determined. With the maximum voltage drop known, the electric potential energy is:

$$E_V = eV_{max} \tag{6.3}$$

where e is the charge of an electron and V_{max} is the voltage drop between the point of highest electric potential and the cathode. This electric potential energy must be the energy that a single ion loses through all collisions and electron emissions as it traverses the gap from its position of highest electrical potential energy to the cathode. To determine the total energy of all ions, the maximum number of ions possible in each subdivision must be determined. This is calculated using the maximum ion number density in each subdivision, shown in Figure 6.21, and the dimensions of each region.

With the dimensions of each subdivision known (a common depth of 5 mm is assumed to agree with the dimensions of the experimentally studied thruster), the volume of each subdivision can be calculated. The product of the volume of each subdivision and the maximum ion number density in each region gives the maximum possible number of ions in each subdivision. This means that the maximum amount of energy lost due to heating in each subdivision is:

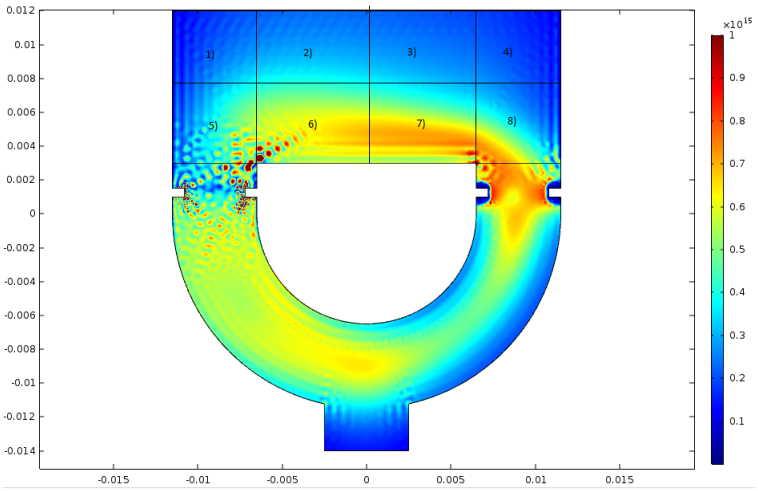

Figure 6.21.: A plot showing the spatial variation of the ion number density under the conditions used in these calculations. The division of the vacuum region into several smaller regions is shown.

$$E_H = NE_V \tag{6.4}$$

where N is the maximum number of ions in a subdivision. The total energy lost due to heating would then be the sum of this energy in each of the 8 subdivisions. However it should be noted that this figure includes the energy that is lost due to electron emission from the cathode. The total energy lost due to secondary electron emission must be subtracted from the above value to obtain the energy lost to heating. The work function of the cathode is known and because the maximum total number of ions has been previously calculated, the maximum total energy lost due to electron emission is simply the product of the work function and N is Equation 6.4. Subtracting the resulting value from E_H gives the maximum total energy lost due to heating. Now this calculated value must be related to something that was measured experimentally, to do so, the maximum total power lost due to heating must be calculated.

The measured circuit current for readings performed at the highest explored mass flow rate was 0.00205 A. This current represents the current that circulates in the plasma between the electrodes. This current can be converted to an ion number flow rate by dividing the measured circuit current by the elementary charge of an electron, e. Using this value, a ratio of the maximum total number of ions in the subdivisions to the measured number of ions can be determined. This ratio acts as a multiplier, for example, if the measured number of ions flowing is double the maximum total number of ions in the simulation, the maximum total power lost to heating must be double the maximum

total energy lost to heating. By multiplying this ratio by the calculated maximum total energy lost due to heating, a value of 0.362 W is obtained. This value is approximately a third of the total experimentally measured power.

7. Conclusions

In this chapter, the final conclusions drawn from this work are presented. The success of the research as a whole is evaluated by determining whether the goals originally established at the onset of the research were achieved. This is accomplished by considering the experimental and simulation components in turn. Suggestions of future work, which could be conducted to better understand this system, are given.

7.1. Experimental

In this work, a novel electrostatic microthruster concept was proposed that would exploit the ionization-acceleration coupling mechanism initially explored in the CorIon system, to achieve miniaturization, and to generate thrust. If successfully developed and tested, this thruster could be a viable propulsion system for use on microsatellites, such as CubeSats. The thruster operates by using a DC glow discharge to generate a plasma inside a discharge channel, and the electric fields set up by the same electrodes used to generate the plasma, would be used to accelerate charged species away from the thruster, generating thrust.

7.1.1. Proof of Concept

Initially, the DC discharge needed to be tested to see if it could be used in the proposed configuration to generate a plasma for space propulsion. This was achieved by developing a proof of concept, straight, discharge tube, that resembled a miniaturized, conventional florescent light tube. Instead of closed off ends to confine the gas, the ends of the tube are opened up, to allow propellant gas to flow into a vacuum, and ring shaped electrodes that will initiate and sustain the discharge, while allowing the propellant to flow, are positioned at the open ends of the discharge channel. Tests across a wide range of operating parameters showed that a DC discharge did form in the central discharge

channel, and plasma plumes were observed to form at the open ends of the discharge tube. This indicates the DC discharge does operate in a manner that would be useful as a space propulsion system.

7.1.2. 'U-Shaped' Thruster

Due to the observation of plume formation in the proof of concept system, the design representative of the thruster concept itself could be tested. This design is also based off of a miniaturized, conventional florescent light tube, but the discharge channel in which the discharge will occur, is bent into a 'U-shape', so that the openings in the discharge channel face the same direction. This ensures that measurable thrust will be generated in one direction only. The ring electrodes are placed at the open ends of the discharge channel, and a faceplate is placed over the electrodes, to prevent arcing occurring during thruster operation. When this design was fired in the vacuum chamber, using a wide range of operating parameters, a number of different operating regimes were discovered via visual inspection, one of which matching the mechanism of operation described previously was found, and the operating parameters that result in this regime were determined. It was discovered that the plume emanating from the grounded electrode would splutter in and out of existence, accompanied by sparking on the interior of the vacuum chamber. This reaction was hypothesised to be due to charge imbalances from differing charged species production rates at the electrodes. The other operating regimes maybe useful in thrust generation, but further investigation is required to determine this. These successes allowed for further testing to determine if this design is an improvement on the CorIon design to continue.

7.1.3. Lifetime

One of the critical points of failure of the CorIon system, was an impractically short lifetime, resulting from the high erosion rates of the electrodes. Lifetime testing is therefore a crucial factor determining the future viability of the system. Both the proof of concept system, and the 'U-shaped' thruster outlasted the CorIon system in terms of operating lifetime. The proof of concept system was able to operate stably for the entire test duration, while showing signs of being able to continue operating past this point. This was not explored, as the proof of concept does not represent the actual thruster design being investigated. The 'U-shaped' design was not able to operate stably for the entire test duration. This was due to thruster failure, the cause of which was explored in erosion

testing. However, the fact that the 'U-shaped' thruster was able to greatly surpass the CorIon system's performance, tendered the lifetime testing successful, and allowed for the erosion testing to commence.

7.1.4. Erosion

Once the lifetime tests were completed, both the proof of concept, straight, discharge tube and the 'U-shaped' thruster were removed from the vacuum chamber and inspected for damage. The electrodes were then removed and cleaned, before being studied along with a control electrode using a SEM. The proof of concept, straight, discharge tube showed little to no damage, aside from body discoloration and minor damage to the electrodes. The 'U-shaped' thruster exhibited body distortion and discoloration, as well as blocking of the discharge channel with debris. However, the electrodes showed minor signs of damage from plasma exposure, so electrode erosion was ruled out as the primary cause of thruster failure. Thruster failure was attributed to body distortion and destruction, due to either heating by the gas, or the plasma itself. These effects can be mitigated by a more appropriate use of construction material, and so further testing of the thruster could commence.

7.1.5. Repeatability

Both the proof of concept, straight, discharge tube and the 'U-shaped' thruster were tested to see if they produce repeatable results in terms of measured operating parameters. This is important for determining consistency and reliability when the thruster is applied in actual space missions. The proof of concept, straight, discharge tube passed repeatability tests, with any parameter fluctuations well within the imposed bounds. The 'U-shaped' thruster also passed repeatability tests, but with larger fluctuations in the operating parameters. It was hypothesised that this results from the interactions between the two plumes, which now face the same direction. Another possible cause of this could be a difference in effective gap length between the proof of concept system and the 'U-shaped' thruster.

7.1.6. Thrust Measurement Stand Development

In order to experimentally determine the thrust produced by the 'U-shaped' thruster, a thrust measurement stand was constructed that utilizes a novel magnetic coupling mechanism to measure thrust. The sensitivity of the balance can be altered by adjusting the novel magnetic coupling system. Fluctuations in thrust measurements are smoothed using a magnetic induction damper. The thrust measurement stand is cost-effective to build, flexible in design and easily operated from calibration to measurement.

The thrust measurement stand is calibrated using a number of known test masses, and the calibration is checked using an unknown mass. The resulting linear calibration curve allows for thrusts across the calibrated range to be determined. The thrust measurement stand was theoretically modelled using a free body analysis. The results of thrusts obtained from the model correspond with experimental calibration data. Thrust measurements were performed on a cold gas thruster to test the operation of the thrust measurement stand. The measurements produced the expected results for such a system, with a linear change in thrust as the mass flow rate through the thruster is varied. Repeatability tests showed the system produces consistent results, as multiple measurements of the same thrust are performed, across the entire calibrated thrust range. All of these tests show that the thrust measurement stand is a suitable instrument to measure the thrust produced by the 'U-shaped' thruster.

7.1.7. Thrust and Power Measurements

A variety of different thrust measurements were performed to study the effect of varying operating parameters on the thrust produced by the 'U-shaped' thruster. Measurements of the power deposited into the thruster were also taken as the operating parameters were varied. The varied operating parameters were the mass flow rate, voltage drop across the electrodes and current flowing through the electrodes.

7.1.8. Cold Gas Thrust

Cold gas thrust measurements were performed in each case to provide a baseline to compare the corresponding hot gas thrust to at the same operating parameters.

7.1.9. Hot Gas Thrust

Hot gas thrust measurements is the term given to the thrust measurements performed on the thruster when the high voltage power supply is activated and a plasma is observed to form.

Varying Mass Flow Rate

The cold gas thrust produced by the 'U-shaped' thruster increases linearly as the mass flow is increased as is expected for a cold gas thruster. The exit velocity of the propellant is extracted from the fit, indicating subsonic flow. The specific impulse is calculated, giving a lower value that expected for an argon cold gas thruster. This is anticipated, as the design is not optimized for cold gas flow. The hot gas thrust produced by the system also increases linearly as the mass flow rate is increased, but with the same gradient as the cold gas thrust, indicating the thrust increase between hot and cold gas thrust remains constant. The measured power is shown to decrease as the mass flow rate is increased, even though an anomalous point is measured. This decrease is attributed to a decreasing voltage as the mass flow rate is increased, which can be linked to Paschen's law. This performance data compares favourably with those of other competing micropropulsion systems.

Varying Current

There appears to be little to no increase in hot gas thrust, or improvement to hot gas thrust stability, as the discharge current is increased. This casts into doubt the proposed mechanism of operation because, if the system operates as hypothesised, increases in discharge current should result in an increase in measured thrust. The measured power increases as the discharge current increases. The discharge voltage remains constant, so the increase in measured power is only due to the increasing discharge current. An anomalous point is present in the measured power data, and this is hypothesised to be due to the onset of stable plume formation.

Varying Voltage

There appears to be little to no increase in hot gas thrust, or improvement to hot gas thrust stability as the discharge voltage is increased. This casts into doubt the proposed

mechanism, of operation because if the system operates as hypothesised, increases in discharge voltage should result in an increase in measured thrust. The measured power displays an increasing 'step-like' feature as the discharge voltage is increased. At this time, the cause of this step feature is unknown, and further study is required to determine its source.

7.1.10. Ion Current Density Measurements

The lineshapes observed in the ICD measurements contradict the hypothesised mechanism of operation of the 'U-shaped' thruster, which was assumed to operate continuously due to a DC power supply being used. The lineshapes obtained from the ICD measurements are pulses, similar to those seen in other pulsed electric propulsion systems. There could be a relationship between the plume spluttering observed experimentally and this behavior. Two types of pulses were observed. A single-peaked pulse and a double-peaked pulse. Potential causes for the double-peak were explored.

The space charge limited current density for the probe geometry, and the propellant used, was estimated and was found to be larger than the maximum ion currents measured in this work. This means space charge current limiting should not affect the results of these measurements.

7.1.11. Ion Current Density as Operating Parameters are Varied

The ICD was measured as various operating parameters were varied. These include: the mass flow rate, discharge voltage and discharge current. These measurements provide insight on the DC discharge plasma generator as operating conditions are varied.

Varying Mass Flow Rate

The measured ICD shows a clear decrease as the mass flow rate is increased, reaching a plateau at higher mass flow rates. This phenomenon has been observed in other DC plasma sources and a possible explanation for this behavior is given. These results elucidate on the operating mechanism of the 'U-shaped' thruster. If the acceleration of ions is the primary thrust production mechanism, the decrease in ICD should correspond with a decrease in the thrust difference between cold and hot gas thrust as the mass flow rate is increased. This is not observed in the thrust measurements.

Varying Current

The measured ICD remains approximately constant, as the discharge current is increased. An anomaly is present at lower currents in the same position where the anomalous power reading was located. The same reasoning is applied to explain this artefact. The constant current density with increasing current appears to be anomalous behavior when considering the literature, and more research is required to determine the reason for this behavior. These results provide further evidence to cast into doubt the hypothesised mechanism of operation. The drop in ICD at the anomalous data point did not result in a drop in thrust. This supports the idea that the acceleration of ions away from the thruster is not the primary thrust production mechanism.

Varying Voltage

The measured ICD remains approximately constant as the discharge voltage is increased. This behavior has been observed in the literature for other DC plasma sources. The same trend is observed in the thrust measurements, however the ICD measurements do not shed light on the anomalous power measurements as the discharge voltage is varied.

7.1.12. Ion Current Density Distribution

The ICDD was obtained by placing the Faraday cup probe in 6 different locations inside the vacuum chamber. This was to provide information on the plume shape and behavior. Moving the probe radially away from the thruster results in a drop in the ICD as is expected, except in the case of the readings 10 cm to the left of thruster centreline, which showed a large increase in ICD as the radial distance is increased. This phenomenon is unexplained, but could be an experimental artefact. The side of the thruster associated with the live electrode exhibits a higher ICD than the grounded side. This is contrary to the hypothesized mechanism of operation. The large error bars can be mitigated by increasing the number of measurements for averaging and error analysis. A lower ICD is measured along the centreline. According to the hypothesized mechanism of operation, this could be explained by the neutralization of the different plumes, but experiments have brought this hypothesis into doubt. Langmuir probe measurements and more detailed ICDD measurements are required to confirm these results.

7.2. Simulation

Simulations were constructed using COMSOL Multiphysics, so a better understanding of the underlying physical processes in the thruster could be obtained. A base simulation was created to understand the general features of the 'U-shaped' thruster. This base case was then used as a framework to test the effects of varying different physical parameters in the simulation, that correspond to operating parameters of the physical thruster.

7.2.1. Base Case

The base case simulation consists of a 2D representation of the 'U-shaped' thruster channel, with the attached gas inlet, and a rectangular region of simulation domain representing a region of the vacuum.

Electron Number Density

The electron number density results show the formation of two distinct regions of increased electron number density, one inside the thruster discharge channel, and one protruding out into the vacuum region at the thruster opening associated with the live electrode. This is in line with the expected result from the hypothesized mechanism of operation.

Ion Number Density

The ion number density results show the formation of two distinct regions of increased ion number density, one inside the thruster discharge channel, and one protruding out into the vacuum region at the thruster opening associated with the live electrode. This contradicts the results from the hypothesized mechanism of operation. These results are accounted for. The ion number density results are not as refined as the other results extracted from the simulations. This could be due to the choice of mesh, but further attempts at mesh refinements resulted in convergence issues. This should be addressed in future work.

Electric Potential

The electric potential results show the region of highest electric potential corresponds with the plasma potential, and cathode fall regions are present near the grounded electrode and the grounded vacuum boundary as expected. These results can be experimentally confirmed using Langmuir probe measurements.

Electron Temperature

The electron temperature results show the region of highest electron temperature is at the grounded electrode, as is expected, but some of the highest electron temperatures are noted at the external electrode surface, facing the the vacuum region, as opposed to the interior of the thruster discharge channel. These results are contrary to the hypothesized mechanism of operation. This result is accounted for, but can be experimentally verified using Langmuir probe measurements. The region of high electron temperature also explains why the point of failure of the thruster is the region around the grounded electrode.

Ion Flux

The ion flux results show that the majority of the ion flux is directed away from the thruster, towards the grounded vacuum boundary, but a portion of the ion flux is also directed backwards, towards the thruster body, specifically the grounded electrode. While this corresponds to the hypothesis of the source of the high electron temperature, it does provide firm evidence to suggest that the ions can hamper thruster operation by charging external spacecraft surfaces.

Neutral Gas Velocity

The neutral gas velocity profile shows that constriction points in the flow are present at the openings in the electrodes and at the gas inlet. The velocity measured in the these simulations is lower than that seen experimentally. Future work should include refining the simulations to allow for greater correlation between experimental and simulated results.

Neutral Gas Temperature

The neutral gas temperature profile shows that the neutral gas temperature increases in the vacuum region, indicating that the gas is heated by the discharge. The heating of the expelled propellant could possibly be a contributing mechanism of thrust generation. However, the increase in gas temperature is small.

7.2.2. Varying Simulation Parameters

In this work, various physical parameters in the simulation, namely, the inlet mass flow rate and the discharge voltage, were varied. These parameters correspond to parameters that can be altered experimentally. These tests will determine if the simulated thruster is effected by these parameters in the same way that the experimental thruster is.

Varying Discharge Voltage

Here, the discharge voltage is varied, and the effect on the simulated thruster presented.

Electric Potential The simulation results indicate that the electric potential across the simulation domain increases as the discharge voltage increases. This is the obvious result. A corresponding steeper potential gradient is observed in the cathode fall region. A region of increased electron number density begins to extend into the vacuum region as the discharge voltage is increased. This is accounted for.

Electron Number Density The simulation results indicate that the electron number density increases in the regions of elevated electron number density, previously observed, as the discharge voltage is increased. This is the expected result, and is accounted for by an increase in the number of ionization and excitation collisions. A region of increased electron number density begins to extend into the vacuum region as the discharge voltage is increased. This is accounted for.

Electron Temperature The simulation results indicate that the electron temperature, particularly around the grounded electrode, increases as the discharge voltage increases. This result is accounted for by the steeper potential gradient in the cathode fall region.

A region of increased electron temperature begins to appear on the external surface of the grounded electrode, as the discharge voltage is varied. This is accounted for by the attraction of ions that are ejected into the vacuum region by thruster operation.

Ion Number Density The simulation results indicate that the ion number density increases as the discharge voltage increases. This is accounted for by the increase in the number of ionization and excitation collisions. A region of increased ion number density begins to extend into the vacuum region as the discharge voltage is increased. This is accounted for.

Ion Flux The simulation results indicate that the ion flux increases in magnitude as the discharge voltage is increased. Initially, the ion flux is directed entirely towards the grounded vacuum boundary. As the discharge voltage is increased, a portion of the flux is directed backwards, towards the grounded electrode. This suggests that ions should contribute to thrust generation, and higher discharge voltages could have a negative impact on thruster operation.

Neutral Gas Velocity No changes in the neutral gas velocity profile are observed, as the discharge voltage is increased.

Neutral Gas Temperature The simulation results show that the neutral gas temperature increases in magnitude, as the discharge voltage is increased. This indicates that the gas is being heated more as it exits the thruster. The increase in temperature is noted to be small. This means that the heating of neutral gas can only play a small roll in thrust generation.

Mass Flow Rate

Here, the inlet mass flow rate is varied, and the effect on the simulated thruster presented.

Neutral Gas Velocity The simulation results indicate that, as the inlet mass flow rate is increased, the neutral gas velocity increases. This results in an increase in the cold gas thrust component.

Neutral Gas Temperature The simulation results show that, as the inlet mass flow rate is increased, the heating effect of the discharge begins to decrease. This phenomena is accounted for.

Electron Number Density The simulation results indicate that, as the inlet mass flow rate is increased, the electron number density in the thruster discharge channel increases, whereas the electron number density present around the live electrode remains constant. This indicates that the electrons around the live electrode are influenced predominantly by electromagnetic phenomena.

Electron Temperature The simulation results show that, as the inlet mass flow rate is increased, the magnitude of the electron temperature remains unchanged, but the size of the region of elevated electron number density decreases slightly. This is accounted for.

Electric Potential The simulation results indicate that, as the inlet mass flow rate is increased, the magnitude of the electric potential increases slightly in the thruster discharge channel, this is accounted for by the increase in charged species number density in this region.

Ion Number Density The simulation results show that, as the inlet mass flow rate is increased, the ion number density in the thruster discharge channel increases, whereas, the ion number density present around the live electrode remains constant. This behavior is mirrored in the electron number density, and variations are accounted for by numerical anomalies.

Ion Flux The simulation results indicate that, as the inlet mass flow rate is increased, the ion flux remains approximately constant.

7.2.3. Thrust Extraction

In order to connect the experimental results to the simulations, an expression that enables thrust values to be extracted from the simulations is developed, and thrust values are obtained from the simulations, which can be compared to experimental thrusts.

Varying Mass Flow Rate

Cold Gas Thrust A linear trend is observed in the cold gas thrust extracted from the simulations. This trend is also observed in experimental data, and an appropriate curve is fitted to the simulated cold gas thrust. The exhaust velocity extracted from the curve is lower than the experimentally obtained value.

Hot Gas Thrust Including the hot gas thrust component imparted by the discharge results in an increase in the thrust extracted from the simulations. This thrust increase is larger than the experimentally observed increase, but it remains constant as the mass flow rate is increased, which corresponds with the experimental observations.

Varying Discharge Voltage

The thrust increase obtained by including the effect of the discharge is shown to increase as the discharge voltage is increased. This differs from the experimental result, where the thrust increase remains constant as the discharge voltage is increased. Possible reasons for the differences in simulated and experimental behavior are given.

7.2.4. Power Lost To Heating

An estimation of the power used by various mechanisms in heating of various thruster features is made using experimental data and information extracted from the simulations.

7.3. Summary and Future Work

Here, a final summary of this work is given and suggestions for future research on this system are presented.

7.3.1. Summary

In this work, a novel electrostatic microthruster concept is proposed and tested both experimentally, using an in-house developed thrust measurement system, and using numerical techniques, with COMSOL Multiphysics. This is to simulate thruster operation and gain insight into the underlying physical phenomena which will explain the experimental results.

The experimental results indicated that the system not only operates and generates thrust, but it also compares favourably with other more established systems in terms of performance. The system has an improved lifetime on the CorIon system from which it draws inspiration and erosion tests indicate that this lifetime could be improved with a different choice of construction materials.

However, many of the experimental results obtained cast doubt on the proposed mechanism of operation and whether the system in fact operates in the manner it is hypothesised to. This is evidenced in thrust increases that do not change as various operating parameters, namely the propellant mass flow rate, the discharge voltage and the discharge current, are varied. It is worthwhile nothing that these tests were performed with limits imposed on the discharge voltage and discharge current. Future tests should be performed without these limits imposed to test if the thruster behaviour remains unchanged.

The ICD and ICDD measurements also provided unexpected results that suggests the thruster operates via a pulsed mechanism as opposed to continuous operation. This may be linked to the spluttering behaviour observed in thruster plume formation, but further testing is required to confirm this.

It was anticipated that the simulations would provide greater insight into the system's behaviour, but unfortunately differences between the simulated geometry and operating conditions and the experimental system means that the simulations are useful for qualitative analysis only. However this qualitative analysis is still useful as it provides some explanation for why the experimental results differ from the hypothesised mechanism of operation. For example, the greater ICD measured to emanated from the live electrode as opposed to the grounded electrode as hypothesised is explained by a significantly higher ion number density present in the region around the live electrode and the ion flux accelerated away from the thruster emanating from this region.

The novel electrostatic microthruster concept proposed in this work shows substantial promise and while the system does not operate as initially expected, the results obtained

by this study suggested that it would be worthwhile to dedicate more research into understanding and optimizing the system until the technology is at a state of readiness high enough to be tested in a space mission.

7.3.2. Future Work

All of the goals defined at the onset of this work were achieved, but much of this research has lead to more questions regarding the novel electric microthruster's operation. Here, a series of suggestions for future work that can be conducted on this system are given:

- Refining ICD measurements, to reduce errors, and to obtain a more detailed ICDD.
- Determine the true nature of the dual peaks observed in the ICD data.
- Perform Langmuir probe measurements on the thruster, to determine the plasma potential, electron density and electron temperature, which can be compared to simulations.
- Develop three dimensional simulations, which more closely represent the experimental thruster.
- Conduct experiments without current limitations imposed, to facilitate better correlation between simulations and experiment.
- Impose current limitations in the simulated discharge, to facilitate better correlation between simulations and experiment.
- Gas temperature measurements should be performed, to determine the extent of neutral gas heating as a thrust production mechanism in the experimental system.
- Vary the holes in the electrodes, in an attempt to improve the stability of the thruster operation, and explore the pulsed mode of operation.
- Study the effect of varying the dimensions of the system on thruster operation.
- Optimize the design for both cold gas and hot gas operation.
- Develop a prototype system out of more suitable materials.

- Alter the design in an attempt to enhance the electrostatic component of thrust generation.

References

[1] A. Ketsdever. System considerations and design options for microspacecraft propulsion systems. *Progress in Astronautics and Aeronautics*, 187:139 – 161, 2000.

[2] J. Gonzalez del Amo. European space agency activities in electric propulsion. In *Proceedings of the 33rd International Electric Propulsion Conference*, pages IEPC–2013–37, Washington D.C., USA, 2013. Electric Rocket Propulsion Society.

[3] H. Kuninaka and K. Kajiwara. Overview of JAXA's activities on electric propulsion. In *Proceedings of the 32nd International Electric Propulsion Conference*, pages IEPC–2011–332, Wiesbaden, Germany, 2011. Electric Rocket Propulsion Society.

[4] N. Püttmann and K. Ruf. Electric propulsion in Germany: System activities today, institutions involved, challenges coming up. In *Proceedings of the 33nd International Electric Propulsion Conference*, pages IEPC–2013–257, Washington D.C., USA, 2013. Electric Rocket Propulsion Society.

[5] A. Semenkin. Overview of electric propulsion activity in Russia. In *Proceedings of the 30th International Electric Propulsion Conference*, pages IEPC–2007–275, Florence, Italy, 2007. Electric Rocket Propulsion Society.

[6] S. Persson, P. Bodin, E. Gill, J. Harr, and J. Jörgensen. PRISMA an autonomous formation flying mission. In *Proceedings of the ESA Small Satellite Systems and Services Symposium*, pages Section 10 – 1, Sardinia, Italy, 2006. ESA Publications Division.

[7] F. Hechler and W. Folkner. Mission analysis for the laser interferometer space antenna (LISA) mission. *Advances in Space Research*, 32:1277 – 1282, 2003.

[8] J. Schilling, R. Spores, and G. Spanjers. Micropropulsion options for the TechSat21 space based radar flight. *Progress in Astronautics and Aeronautics*, 187:3–23, 2000.

[9] J. Mueller. Thruster options for microspacecraft: a review and evaluation of state-

of-the-art and emerging technologies. *Progress in Astronautics and Aeronautics*, 187:45 – 137, 2000.

[10] R. Goldstein, M. Boehm, E. Cutting, H. Javadi, L. Miller, B. Pain, J. Randolph, P. Turner, and K. Lynch. A fully integrated micro-magnetometer/microspacecraft for multipoint measurements: The free flyer magnetometer. *Geophysical Monograph Series*, 103:305 – 310, 1998.

[11] L. Muller. Miniaturization methods for deep space microspacecraft. In *Proceedings of the AIAA/USU Conference on Small Satellites*, page Technical Session V, Utah, USA, 1994. Utah State University.

[12] M. Martinez-Sanchez and J. Pollard. Spacecraft electric propulsion-an overview. *Journal of Propulsion and Power*, 14:688 – 699, 1998.

[13] B. Palaszewski, L. Ianovski, and P. Carrick. Propellant technologies: Far-reaching benefits for aeronautical and space-vehicle propulsion. *Journal of Propulsion and Power*, 14:641 – 648, 1998.

[14] G. Sutton and O. Biblarz. *Rocket Propulsion Elements*. Wiley, New York, USA, 2001.

[15] M. Rayman and D. Lehman. Deep Space 1: NASAs first deep-space technology validation mission. *Acta Astronautica*, 41:289 – 299, 1997.

[16] M. Rayman, P. Varghese, D. Lehman, and L. Livesay. Results from the Deep Space 1 technology validation mission. *Acta Astronautica*, 47:475 – 487, 2000.

[17] J. Mueller. Thruster options for microspacecraft: A review and evaluation of existing hardware and emerging technologies. In *Proceedings of the 33rd Joint Propulsion Conference*, pages AIAA Paper 97–3058, Washington, USA, 1997. AIAA.

[18] C. Rossi, S. Orieux, B. Larangot, T. Do Conto, and D. Estéve. Design, fabrication and modeling of solid propellant microrocket-application to micropropulsion. *Sensors and Actuators A*, 99:125 – 133, 2002.

[19] I. Hrbud, G. Kemp, A. Yan, and J. Gedrimas. Review of RF plasma thruster development. In *Proceedings of the 30th International Electric Propulsion Conference*, pages IEPC–2007–309, Florence, Italy, 2007. Electric Rocket Propulsion Society.

[20] J. Mitterauer. Prospects of liquid metal ion thrusters for electric propulsion. In

Proceedings of the 22nd International Electric Propulsion Conference, pages IEPC–1991–105, Viareggio, Italy, 1991. Electric Rocket Propulsion Society.

[21] A. Mehrparvar. Cubesat design specification. Technical report, California State Polytechnic University, 2014.

[22] R. Van Zyl, D. Visser, P. Cilliers, and B. Opperman. ZACUBE-1 space weather mission: Characterize the SuperDARN HF radar antenna array at SANAE-IV. *Space Weather*, 11:52–54, 2013.

[23] A Toorian, K. Diaz, and S. Lee. The CubeSat approach to space access. In *Proceedings of the 2008 IEEE Aerospace Conference*, pages 1–16, Big Sky, USA, 2008. IEEE Aerospace and Electronic Systems Society.

[24] D. Beckett and B. Carpenter. Rapid de-orbit of LEO space vehicles using towed rigidizable inflatable structure (TRIS) technology: Concept and feasibility assessment. In *Proceedings of the 18th Annual AIAA Small Satellite Conference*, pages SSC04–IV–3, Utah, USA, 2004. AIAA Meeting Papers.

[25] F. Rysanek, J. Hartmann, J. Schein, and R. Binder. Microvacuum arc thruster design for a cubesat class satellite. In *Proceedings of the 16th Annual AIAA/USU Conference on Small Satellites*, pages SSC02–I–2, Utah, USA, 2002. Utah State University.

[26] T. Roy, V. Hruby, N Rosenblad, P. Rostler, and D. Spence. CubeSat propulsion using electrospray thrusters. In *Proceedings of the 23rd Annual AIAA/USU Conference on Small Satellites*, pages SSC09–II–6, Utah, USA, 2009. Utah State University.

[27] T. Lafleur. Corona discharge as an ionization mechanism for electrostatic propulsion applications. Honours project, University of the Witwatersrand, 2007.

[28] P. Ferrer and M. Tchonang. Miniaturization of electrostatic ion engines by ionization and acceleration coupling. *Journal of Physics D: Applied Physics*, 44:335204, 2011.

[29] M. Tchonang. Modeling of the corona ionization space propulsion system. Masters dissertation, University of the Witwatersrand, 2011.

[30] M. Hirsh and H. Oskam (Eds.). *Gaseous Electronics: Volume 1 Electrical Discharges*. New York: Academic Press, New York, USA, 1978.

[31] Y. Raizer. *Gas Discharge Physics*. Springer-Verlag, Berlin, Germany, 1991.

[32] C. Dougherty, T. Foulke, J. Harnden, T. Hewitt, F. Peters, R. Smith, and J. Tuttle. *General Electric Glow Lamp Manual*. General Electric Company, Cleveland, USA, 1966.

[33] N. Yamamoto, S. Kondo, T. Chikaoka, H. Nakashima, and H. Masui. Effects of magnetic field configuration on thrust performance in a miniature microwave discharge ion thruster. *Journal of Applied Physics*, 102:123304, 2007.

[34] G. Roy. *Advances in Chemical Propulsion: Science to Technology*. CRC Press, Boca Raton, USA, 2010.

[35] D. Goebel and I. Katz. *Fundamentals of Electric Propulsion: Ion and Hall Thrusters*. Wiley, New Jersey, USA, 2008.

[36] K. Cheah, P. Khiew, and J. Chin. Fabrication of a zirconia MEMS-based microthruster by gel casting on PDMS soft molds. *Journal of Micromechanics and Microengineering*, 22:095013, 2012.

[37] T. Kammash, R. Tang, and A. Gallimore. Alpha particle dynamics in muon-boosted fusion propulsion system. In *Proceedings of the 44th AIAA/ASME/SAE/ASEE Joint Propulsion Conference and Exhibit*, pages AIAA 2008–4674, Hartford, USA, 2008. AIAA Meeting Papers.

[38] A. Ketsdever. Micropropulsion. *Encyclopedia of Aerospace Engineering*, 7:1 – 12, 2010.

[39] S. Greenwood. Definition of specific impulse. *Journal of Spacecraft and Rockets*, 12:62, 1975.

[40] R. Hofer, P. Peterson, A. Gallimore, and R. Jankovsky. A high specific impulse two-stage hall thruster with plasma lens focusing. In *Proceedings of the 27th International Electric Propulsion Conference*, pages IEPC–2001–036, Pasadena, USA, 2001. Electric Rocket Propulsion Society.

[41] M. Tanaka, Y. Suzuki, K. Araki, and R. Suzuki. Microstrip antenna with solar cells for microsatellites. *Electronics Letters*, 31:5 – 6, 1995.

[42] K. Burton. Atmospheric fueled ion engine. Patent, 2000. US6145298.

[43] P. Balachandran. *Fundamentals of Compressible Fluid Dynamics*. Prentice-Hall of India, Delhi, India, 2006.

[44] M. Krommenhoek. Modelling of the propulsion mechanism for a miniaturized corona ionization thruster. Master's thesis, University of the Witwatersrand, March 2015.

[45] H. Leiter et al. RIT-μX - The new modular high precision micro ion propulsion system. In *Proceedings of the 30th International Electric Propulsion Conference*, pages IEPC–2007–209, Florence, Italy, 2007. Electric Rocket Propulsion Society.

[46] I. Dey, Y. Toyoda, N. Yamamoto, and H. Nakashima. Microwave plasma interaction in a miniature plasma ion thruster. In *Proceedings of the 33rd International Electric Propulsion Conference*, pages IEPC–2013–223, Washington DC, USA, 2013. Electric Rocket Propulsion Society.

[47] P. Taunay, Sven G. Bilén, and M. Micci. Numerical simulations of a miniature microwave ion thruster. In *Proceedings of the 33rd International Electric Propulsion Conference*, pages IEPC–2009–194, Washington DC, USA, 2013. Electric Rocket Propulsion Society.

[48] R. Jahn and E. Choueiri. *Electric Propulsion*, volume 5 of *Encyclopedia of Physical Science and Technology*. New York: Academic Press, New York, USA, 3rd edition, 2002.

[49] P. Molina-Cabrera, G. Herdrich, M. Lau, S. Fausolas, T. Schoenherr, and K. Komurasaki. Pulsed plasma thrusters: a worldwide review and long yearned classification. In *Proceedings of the 32nd International Electric Propulsion Conference*, pages IEPC–2011–340, Wiesbaden, Germany, 2011. Electric Rocket Propulsion Society.

[50] P. Gessini, L. Hably, M. Barcelos, J. Ferreira, R. Marques, and M. Coletti. Low power ablative pulsed plasma thrusters. In *Proceedings of the 33rd International Electric Propulsion Conference*, pages IEPC–2013–344, Washington DC, USA, 2013. Electric Rocket Propulsion Society.

[51] V. Hruby et al. Colloid thrusters for the new millennium, ST7 DRS mission. In *Proceedings of the 2004 IEEE Aerospace Conference*, pages 202 – 213. IEEE Computer Society, 2004.

[52] J. Mitterauer. Micropropulsion for small spacecraft: a new challenge for field ef-

fect electric propulsion and microstructured liquid metal ion sources. *Surface and Interface Analysis*, 36:380 – 386, 2004.

[53] J. Ziemer. Laser ablation microthruster technology. In *Proceedings of the 33rd Plasmadynamics and Lasers Conference*, pages AIAA–2002–2 153, Maui, USA, 2002. AIAA Meeting Papers.

[54] C. Phipps, J. Luke, T. Lippert, M. Hauer, and A. Wokaun. Micropropulsion using a laser ablation jet. *Journal of Propulsion and Power*, 20:1000 – 1011, 2004.

[55] J. Polk, M. Sekerak, J. Ziemer, J. Schein, N. Qi, and A. Anders. A theoretical analysis of vacuum arc thruster and vacuum arc ion thruster performance. *IEEE Transactions On Plasma Science*, 36:2167 – 2179, 2008.

[56] H. Goedbloed and S. Poedts. *Principles of Magnetohydrodynamics with Applications to Laborotory and Astrophysical Plasmas*. Camebridge University Press, New York, USA, 2008.

[57] P. Sturrock. *Plasma Physics: An Introduction to the Theory of Astrophysical, Geophysical and Laboratory Plasmas*. Camebridge University Press, New York, USA, 1994.

[58] D. Gurnett and A. Bhattacharjee. *Introduction to Plasma Physics: With Space and Laboratory Applications*. Camebridge University Press, Camebridge, UK, 2005.

[59] M. Haverkorn and S. Spangler. Plasma diagnostics of the interstellar medium with radio astronomy. *Microphysics of Cosmic Plasmas*, 47:407–435, 2013.

[60] B. Smirnov. *Physics of Ionized Gases*. Wiley, New Jersey, USA, 2001.

[61] K. Rawer. *Wave Propagation in the Ionosphere*. Springer Netherlands, Dordrecht, Netherlands, 2010.

[62] J. Ratcliffe. *An Introduction to Ionosphere and Magnetosphere*. Camebridge University Press, Camebridge, UK, 1972.

[63] M. Aschwanden. *Physics of the Solar Corona: An Introduction*. Praxis Publishing, Chichester, UK, 2004.

[64] M. Uman. *Lightning*. Praxis Publishing, Chichester, UK, 2004.

[65] A. Montaser. *Inductively Coupled Plasma Mass Spectrometry*. Wiley, Danvers, USA, 1998.

[66] P. Chabert and N. Braithwaite. *Physics of Radio Frequency Plasmas*. Cambridge University Press, New York, USA, 2011.

[67] K. Jankowski and E. Reszke. *Microwave Induced Plasma Analytical Spectrometry*. RCS Publishing, Cambridge, UK, 2011.

[68] R. Noll. *Laser-Induced Breakdown Spectroscopy: Fundamentals and Applications*. Springer, Berlin, Germany, 2012.

[69] Y. Razier. *Gas Discharge Physics*. Springer-Verlag, Berlin, Germany, 1991.

[70] A. Schütze, J. Jeong, S. Babayan, J. Park, G. Selwyn, and R. Hicks. The atmospheric-pressure plasma jet: A review and comparison to other plasma sources. *IEEE Transactions on Plasma Science*, 26:1685–1694, 1998.

[71] K. Burm. Calculation of the townsend discharge coefficients and the paschen curve coefficients. *Contributions to Plasma Physics*, 47:177–182, 2007.

[72] R. Barton and R. Govier. A mass spectrometric study of the outgassing of some elastomers and plastics. *Journal of Vacuum Science and Technology*, 2:113–122, 1965.

[73] R. Baker. *Flow Measurement Handbook: Industrial Designs, Operating Principles, Performance and Applications*. Cambridge University Press, Cambridge, UK, 2000.

[74] F. de Buyl. Silicone sealants and structural adhesives. *International Journal of Adhesion and Adhesives*, 21:411–422, 2001.

[75] M. Ehsani, H. Borsi, E. Gockenbach, G. Bakhshandeh, and J. Morshedian. Modified silicone rubber for use as high voltage outdoor insulators. *Advances in Polymer Technology*, 24:51–61, 2005.

[76] R. Merlino. Understanding langmuir probe current-voltage characteristics. *American Journal of Physics*, 75:1078–1085, 2007.

[77] M. Sekerak. Plasma plume characterization of a vacuum arc thruster. Master's thesis, California Institute of Technology, March 2005.

[78] I. Brown, J. Galvin, R. MacGill, and R. Wright. Improved time-of-flight ion charge state diagnostic. *Review of Scientific Instruments*, 58:1589–1592, 1987.

[79] J. Lun. *Performance Improvements of Vacuum Arc Thrusters*. PhD thesis, University of the Witwatersrand, 2015.

[80] W. Smith and J. Hashemi. *Foundations of Materials Science and Engineering*. McGraw-Hill, New York, USA, 2006.

[81] J. Lunt. Large scale production, properties and commercial applications of polylactic acid polymers. *Polymer Degradation and Stability*, 59:145–152, 1998.

[82] J. Polk, A. Pancotti, T. Haag, S. King, M. Walker, J. Blakley, and J. Ziemer. Recommended practices in thrust measurements. In *Proceedings of the 33rd International Electric Propulsion Conference*, pages IEPC–2013–440, Washington DC, USA, 2013. Electric Rocket Propulsion Society.

[83] American Water Works Association. *PVC Pipe - Design and Installation*. American Water Works Association, Denver, USA, 2002.

[84] J. Soni and S. Roy. Design and characterization of a nano-newton resolution thrust stand. *Review of Scientific Instruments*, 84:095103, 2013.

[85] E. Collings. Magnetic evaluation of machining induced deformation transformation in austentic stainless steels. *Cryogenics*, 19:215–216, 1979.

[86] J. Gong, L. Hou, and W. Zhao. Experimental study of a low-thrust measurement system for thruster gound tests. *Review of Scientific Instruments*, 85:035102, 2014.

[87] T. Moeller and K. Polzin. Thrust stand for vertically oriented electric propulsion performance evaluation. *Review of Scientific Instruments*, 81:115108, 2010.

[88] S. Pottinger, D. Lamprou, A. Knoll, and V. Lappas. Impact of plasma noise on a direct thrust measurement system. *Review of Scientific Instruments*, 81:033504, 2012.

[89] J. Lun and C. Law. Direct thrust measurement stand with improved operation and force calibration technique for performance testing of pulsed micro-thrusters. *Measurement Science and Technology*, 25:095009, 2014.

[90] W. Tao and H. Yasuda. Measurement of spatial distributions of electron density and

electron temperature in direct current glow discharge by double langmuir probes. *Plasma Chemistry and Plasma Processing*, 22:297–311, 2002.

[91] F. Paschen. On the potential difference required for spark initiation in air, hydrogen, and carbon dioxide at different pressures. *Annalen der Physik*, 273:69–75, 1889.

[92] S. Klein and G. Nellis. *Thermodynamics*. Cambridge University Press, New York, USA, 2012.

[93] M. Elwenspoek and H. Jansen. *Silicon Micromachining*. Cambridge University Press, Cambridge, UK, 1998.

[94] M. Pashaeiyan and A. Bahari. Nano structural properties of stainless steel for ultra high vacuum chambers. *International Journal of ChemTech Research*, 3:403–407, 2011.

[95] L. Yan, W. Yang, H. Jin, and Z. Wang. Microstructure changes of machined surfaces on austenitic 304 stainless steel. *World Academy of Science, Engineering and Technology*, 81:823–827, 2011.

[96] N. Jakubowski, D. Stuewer, and G. Toelg. Improvement of ion source performance in glow discharge mass spectrometry. *International Journal of Mass Spectrometry and Ion Processes*, 71:183–197, 1986.

[97] P. Stutzman and J. Clifton. Specimen preparation for scanning electron microscopy. In *Proceedings of the 21st International Conference on Cement Microscopy*, pages 10–22, Nevada, USA, 1999. International Cement Microscopy Association.

[98] W. Biller, D. Heyden, D. Müller, and G. Wolf. Modification of steel and aluminium by pulsed energetic ion beams. *Surface and Coatings Technology*, 116-119:537–542, 1999.

[99] N. Gascon, M. Dudeck, and S. Barral. Wall material effects in stationary plasma thrusters. i. parametric studies of an SPT-100. *Physics of Plasmas*, 10:4123–4136, 2003.

[100] M. Tartz, T. Heyn, C. Bundesmann, and H. Neumann. Measuring sputter yields of ceramic materials. In *Proceedings of the 31st International Electric Propulsion Conference*, pages IEPC–2009–240, Ann Arbour, USA, 2009. Electric Rocket Propulsion Society.

[101] A. Estrada-Alexanders and J. Trusler. The speed of sound in gaseous argon at temperatures between 110 K and 450 K and at pressures up to 19 MPa. *The Journal of Chemical Thermodynamics*, 27:1075–1089, 1995.

[102] D. Green and J. Maloney. *Perry's Chemical Engineer's Handbook*. McGraw-Hill, New York, USA, 1997.

[103] H. Nguyen, J. Köhler, and L. Stenmark. The merits of cold gas micropropulsion in state-of-the-art space missions. In *Proceedings of the 2nd World Space Congress*, pages IAC–02–S.2.07, Houston, USA, 2002. International Astronautical Federation.

[104] I. Kronhaus, K. Schilling, S. Jayakumar, A. Kramer, M. Pietzka, and J. Scheink. Design of the UWE-4 picosatellite orbit control system using vacuum-arc-thrusters. In *Proceedings of the 33rd International Electric Propulsion Conference*, pages IEPC–2013–195, Washington DC, USA, 2013. Electric Rocket Propulsion Society.

[105] J. Lun and C. Law. Influence of cathode shape on vacuum arc thruster performance and operation. In *Proceedings of the 33rd International Electric Propulsion Conference*, pages IEPC–2013–177, Washington DC, USA, 2013. Electric Rocket Propulsion Society.

[106] L. Paita, F. Ceccanti, M. Spurio, U. Cesari, L. Priami, F. Nania, A. Rossodivita, and M. Andrenucci. Altas FT-150 FEEP microthruster: Development and qualification status. In *Proceedings of the 31st International Electric Propulsion Conference*, pages IEPC–2009–186, Ann Arbor, USA, 2009. Electric Rocket Propulsion Society.

[107] M. Coletti, S. Ciaralli, and S. Gabriel. PPT development for nanosatellites applications: experimental results. In *Proceedings of the 33rd International Electric Propulsion Conference*, pages IEPC–2013–198, Washington DC, USA, 2013. Electric Rocket Propulsion Society.

[108] A. Bogatiy and G. Diakonov. Development of vernier propulsion system for micro satellite on the basis of ablative pulsed plasma thruster. In *Proceedings of the 30th International Electric Propulsion Conference*, pages IEPC–2007–130, Florence, Italy, 2007. Electric Rocket Propulsion Society.

[109] D. Feili, B. Lotz, S. Bonnet, B. Meyer, H. Loeb, and N. Puetmann. μNRIT-2.5 - a new optimized microthruster of giessen university. In *Proceedings of the 31st International Electric Propulsion Conference*, pages IEPC–2009–174, Ann Arbor, USA, 2009. Electric Rocket Propulsion Society.

[110] W. Harrison and W. Hang. Development of multi faraday cup assembly for ion beam measurements from a low energy plasma focus device. *Journal of Analytical Atomic Spectrometry*, 11:835–840, 1996.

[111] S. Qin, M. Bradley, P. Kellerman, and K. Saadatmand. Measurements of secondary electron emission and plasma density enhancement for plasma exposed surfaces using an optically isolated faraday cup. *Review of Scientific Instruments*, 73:1153–1156, 2002.

[112] S. Mohanty, H. Bhuyan, N. Neog, R. Rout, and E. Hotta. Development of multi faraday cup assembly for ion beam measurements from a low energy plasma focus device. *Japanese Journal of Applied Physics*, 44:5199–5205, 2005.

[113] K. Frank and J. Christiansen. The fundamentals of the pseudospark and its applications. *IEEE Transactions in Plasma Science*, 17:748–753, 1989.

[114] K. Tsuji and K. Wagatsuma. Compact glow discharge x-ray tube. *Review of Scientific Instruments*, 69:4006–4007, 1998.

[115] A. Sefkow et al. Fast faraday cup to measure neutralized drift compression in intense ion charge bunches. *Physical Review Special Topics*, 9:052801, 2006.

[116] Y. Lau. Simple theory for the two-dimensional child-langmuir law. *Physical Review Letters*, 87:278301, 2001.

[117] W. Bridges, J. Frey, and C. Birdsall. Limiting stable currents in bounded electron and ion streams. *IEEE Transactions on Electron Devices*, 12:264–272, 1965.

[118] T. Taylor and J. Wills. A high current low emittance dc ECR proton source. *Nuclear Instruments and Methods in Physics Research A*, 309:37–42, 1991.

[119] V. Devyatkov et al. Generation and propagation of high-current low-energy electron beams. *Laser and Particle Beams*, 21:243–248, 2003.

[120] J. Rocca, M. Marconi, and F. Tomasel. Study of soft X-ray emission from carbon ions in a capillary discharge. *IEEE Journal of Quantum Electronics*, 29:182–191, 1993.

[121] G. Rushton, K. O'Shea, and R. Fitch. Modes of operation of an electrostatic ion gun. *Journal of Physics D: Applied Physics*, 6:1167–1172, 1973.

[122] K. Leung, K. Ehlers, C. Hauck, W. Kunkel, and A. Lietzke. Small multicusp H^- source. *Reviews of Scientific Instruments*, 59:453–456, 1988.

[123] K. Leung, K. Ehlers, and R. Pyle. Optimization of H^- production in a magnetically filtered multicusp source. *Reviews of Scientific Instruments*, 56:364–368, 1985.

[124] I. Brown. Vacuum arc ion sources. *Reviews of Scientific Instruments*, 65:3061–3081, 1994.

[125] L. Cai and R. White. Mathematical modeling of a lithium ion battery with thermal effects in COMSOL Inc. Multiphysics (MP) software. *Journal of Power Sources*, 196:5985–5989, 2011.

[126] R. Burden and J. Faires. *Numerical Analysis*. Thomson Higher Education, Belmont, USA, 2005.

[127] R. Leveque. *Finite Volume Methods for Hyperbolic Functions*. Cambridge University Press, Cambridge, UK, 2004.

[128] P. Salamon, D. Fernández-Garcia, and J. Gómez-Hernández. A review and numerical assessment of the random walk particle tracking method. *Journal of Contaminant Hydrology*, 87:277–305, 2006.

[129] W. Hall. Boundary element method. In *The Boundary Element Method*, volume 27 of *Solid Mechanics and Its Applications*, pages 61–83. Springer Netherlands, 1994.

[130] D. Salvi, D. Boldor, G. Aita, and C. Sabliov. COMSOL Multiphysics model for continuous flow microwave heating of liquids. *Journal of Food Engineering*, 104:422–429, 2011.

[131] A. Lavacchi, U. Bardi, C. Borri, S. Caporali, A. Fossati, and I. Perissi. Cyclic voltammetry simulation at microelectrode arrays with COMSOL Multiphysics. *Journal of Applied Electrochemistry*, 39:2159–2163, 2009.

[132] M. Wang and L. Jang. A systematic investigation into the electrical properties of single HeLa cells via impedance measurements and COMSOL simulations. *Biosensors and Bioelectronics*, 24:2830–2835, 2009.

[133] F. Chen. *Introduction to Plasma Physics and Controlled Fusion*. Plenum Press, New York, USA, 1984.

[134] J. Verboncoeur. Particle simulation of plasmas: review and advances. *Plasma Physics and Controlled Fusion*, 47:A231–A260, 2005.

[135] E. Havlíčková. Fluid model of plasma and computational methods for solution. In *WDS'06 Proceedings of Contributed Papers, Part III*, pages 180–186, Prague, Czech Republic, 2006. Matfyzpress.

[136] P. Rambo. Numerical heating in hybrid plasma simulations. *Journal of Computational Physics*, 133:173–180, 1997.

[137] A COMSOL. *COMSOL Multiphysics Plasma Module User Guide*. COMSOL Inc., Stockholm, Sweden, 2013.

[138] G. Hagelaar and L. Pitchford. Solving the boltzmann equation to obtain electron transport coefficients and rate coefficients for fluid models. *Plasma Sources Science and Technology*, 14:722–733, 2005.

[139] D. Scharfetter and H. Gummel. Large-signal analysis of a silicon read diode oscillator. *IEEE Transactions of Electron Devices*, 16:64–77, 1969.

[140] E. Witalis. Hall magnetohydrodynamics and its applications to laboratory and cosmic plasma. *IEEE Transactions on Plasma Science*, 14:842–848, 1986.

[141] E. Gogolides and H. Sawin. Continuum modelling of radio frequency glow discharges. i. theory and results for electropositive and electronegative gases. *Journal of Applied Physics*, 72:3971–3987, 1992.

[142] E. Gogolides, H. Sawin, and R. Brown. Direct calculation of time-periodic steady-states of continuum models of radio-frequency plasmas. *Chemical Engineering Science*, 47:3839–3855, 1992.

[143] L. Boudin, B. Grec, and F. Salvarani. A mathematical and numerical analysis of the maxwell-stefan diffusion equations. *Discrete and Continuous Dynamical Systems - Series B*, 17:1427–1440, 2012.

[144] J. Crank. *The Mathematics of Diffusion*. Oxford University Press, Oxford, UK, 1975.

[145] M. Torstensson. A comparison of the multicomponent model and the mixture averaged approximation. Master's thesis, Lund University, January 2014.

[146] D. Young, B. Munson, T. Okiishi, and W. Huebsch. *A Brief Introduction To Fluid Mechanics*. Wiley, New York, USA, 2011.

[147] G. Batchelor. *An Introduction to Fluid Dynamics*. Cambridge University Press, Cambridge, UK, 1967.

[148] J. Pedlosky. *Geophysical Fluid Dynamics*. Springer, New York, USA, 1979.

[149] E. Bogdanov, S. Adams, V. Demidov, A. Kudryavtsev, and J. Williamson. Influence of the transverse dimension on the structure and properties of dc glow discharges. *Physics of Plasmas*, 17:103502, 2010.

[150] T. Deconick, S. Mahadevan, and L. Raja. Computational simulation of a coupled nonequilibrium discharge and compressible flow phenomena in a microplasma thruster. *Journal of Applied Physics*, 106:063305, 2009.

[151] H. Leiter, B. Lotz, D. Feili, M. Tartz, H. Neumann, and D. Cara. Design development and test of the RIT-μX mini ion engine system. In *Proceedings of the 31st International Electric Propulsion Conference*, pages IEPC–2009–179, Ann Arbor, USA, 2009. Electric Rocket Propulsion Society.

[152] D. Cara et al. Experimental validation of RIT micro-propulsion subsystem performance at EPL. In *Proceedings of the 33rd International Electric Propulsion Conference*, pages IEPC–2013–90, Washington DC, USA, 2013. Electric Rocket Propulsion Society.

[153] C. Altmann, H. Leiter, and R. Kukies. The RIT-μX miniaturized ion engine system way to TRL 5 for an extended thrust range. In *Proceedings of the 34th International Electric Propulsion Conference*, pages IEPC–2015–274, Hyogo-Kobe, Japan, 2015. Electric Rocket Propulsion Society.

[154] R. Henrich, D. Feiliy, and C. Heiligerz. Self-consistent simulation of the coupling between plasma and neutral gas in μN-RIT. In *Proceedings of the 32nd International Electric Propulsion Conference*, pages IEPC–2001–323, Wiesbaden, Germany, 2011. Electric Rocket Propulsion Society.

[155] R. Henrich and C. Heiliger. Three dimensional simulation of micro newton RITs. In *Proceedings of the 33rd International Electric Propulsion Conference*, pages IEPC–2013–301, Washington DC, USA, 2013. Electric Rocket Propulsion Society.

[156] C. Collingwood, S. Gabriel, M. Corbett, N. Wallace, and P. Jameson. Development

of a differential radio frequency ion thruster for precision spacecraft control. *Journal of Plasma and Fusion Research*, 8:1564 – 1568, 2009.

[157] J. Foster. Compact plasma accelerator for micro-propulsion applications. In *Proceedings of the 27th International Electric Propulsion Conference*, pages IEPC–2001–221, Pasadena, USA, 2001. Electric Rocket Propulsion Society.

[158] T. Trudel, S. Bilén, and M. Micci. Design and performance testing of a 1-cm miniature radio-frequency ion thruster. In *Proceedings of the 31st International Electric Propulsion Conference*, pages IEPC–2009–167, Ann Arbor, USA, 2009. Electric Rocket Propulsion Society.

[159] H. Koizumi and H. Kuninaka. Performance evaluation of a miniature ion thruster μ1 with a unipolar and bipolar operation. In *Proceedings of the 32nd International Electric Propulsion Conference*, pages IEPC–2011–297, Wiesbaden, Germany, 2011. Electric Rocket Propulsion Society.

[160] Y. Takao, K. Eriguchi, K. Ono, Y. Sugita, H. Koizumi, and K. Komurasaki. Three-dimensional particle-in-cell simulation of a miniature microwave discharge ion thruster μ1. In *Proceedings of the 33rd International Electric Propulsion Conference*, pages IEPC–2013–186, Washington DC, USA, 2013. Electric Rocket Propulsion Society.

[161] R. Tsukizaki, H. Koizumi, K. Nishiyama, and H. Kuninaka. Number density measurement of Xe I in the ECR ion thruster μ10 using optical fiber probe. In *Proceedings of the 32nd International Electric Propulsion Conference*, pages IEPC–2011–318, Wiesbaden, Germany, 2011. Electric Rocket Propulsion Society.

[162] R. Tsukizaki, T. Ise, H. Koizumi, H. Togo, K. Nishiyama, and H. Kuninaka. Plasma diagnostics of the μ10 ECR ion thruster using optical fiber probes. In *Proceedings of the 33rd International Electric Propulsion Conference*, pages IEPC–2013–270, Washington DC, USA, 2013. Electric Rocket Propulsion Society.

[163] A. Hine and K. Lemmer. Effect of plasma plume on CubeSat structures as a function of thrust vectoring. In *Proceedings of the 34th International Electric Propulsion Conference*, pages IEPC–2015–157, Hyogo-Kobe, Japan, 2015. Electric Rocket Propulsion Society.

[164] M. Nakano and H. Koizumi. Grid wear analysis of a miniature ion engine. In

Proceedings of the 34th International Electric Propulsion Conference, pages IEPC–2015–187, Hyogo-Kobe, Japan, 2015. Electric Rocket Propulsion Society.

[165] M. Tsay, J. Frongillo, and K. Hohman. Iodine-fueled mini RF ion thruster for cubesat applications. In *Proceedings of the 34th International Electric Propulsion Conference*, pages IEPC–2015–273, Hyogo-Kobe, Japan, 2015. Electric Rocket Propulsion Society.

[166] R. Wirz. Miniature ion thrusters: A review of modern technologies and mission capabilities. In *Proceedings of the 34th International Electric Propulsion Conference*, pages IEPC–2015–275, Hyogo-Kobe, Japan, 2015. Electric Rocket Propulsion Society.

[167] N. Egami, T. Matsuoka, M. Sakamoto, Y. Inoue, T. Ikeda, and H. Tahara. R&D, launch and initial operation of the Osaka Institute of Technology's 1st PROITERES nano-satellite with electrothermal pulsed plasma thrusters and development of the 2nd satellite. In *Proceedings of the 33rd International Electric Propulsion Conference*, pages IEPC–2013–100, Washington DC, USA, 2013. Electric Rocket Propulsion Society.

[168] S. Kisaki, R. Muraoka, C. Huanjun, M. Tanaka, H. Tahara, and T. Wakizono. Research and development of electrothermal pulsed plasma thruster systems onboard Osaka Institute of Technology PROITERES nano-satellites. In *Proceedings of the 33rd International Electric Propulsion Conference*, pages IEPC–2013–097, Washington DC, USA, 2013. Electric Rocket Propulsion Society.

[169] C. Huanjun, R. Muraoka, S. Kisaki, M. Tanaka, H. Tahara, and T. Wakizono. Performance prediction of electrothermal pulsed plasma thrust systems onboard Osaka Institute of Technology PROITERES nano-satelite series. In *Proceedings of the 33rd International Electric Propulsion Conference*, pages IEPC–2013–102, Washington DC, USA, 2013. Electric Rocket Propulsion Society.

[170] K. Kanaoka, R. Fujita, R. Muraoka, H. Tahara, and T. Wakizono. Research and development of high-power electrothermal pulsed plasma thruster systems for osaka institute of technology 2nd PROITERES nano-satellite. In *Proceedings of the 34th International Electric Propulsion Conference*, pages IEPC–2015–22, Hyogo-Kobe, Japan, 2015. Electric Rocket Propulsion Society.

[171] R. Fujita, R. Muraoka, K. Kanaoka, C. Huanjun, M. Tanaka, H. Tahara, and T. Wakizono. Flowfield simulation and performance prediction of electrothermal

pulsed plasma thrusters onboard osaka institute of technology PROITERES nanosatellite series. In *Proceedings of the 34th International Electric Propulsion Conference*, pages IEPC–2015–207, Hyogo-Kobe, Japan, 2015. Electric Rocket Propulsion Society.

[172] M. Coletti, R. Marques, and S. Gabriel. Design of a two-stage PPT for CubeSat application. In *Proceedings of the 31st International Electric Propulsion Conference*, pages IEPC–2009–244, Ann Arbor, USA, 2009. Electric Rocket Propulsion Society.

[173] S. Gabriel, E. Rogers, and M. Leomanni. The applicability of pulsed plasma thrusters to rendezvous and docking of cubesats. In *Proceedings of the 33rd International Electric Propulsion Conference*, pages IEPC–2013–424, Washington DC, USA, 2013. Electric Rocket Propulsion Society.

[174] A. Mingo Pérez, M. Coletti, and S. Gabriel. Development of a microthruster module for nanosatellite applications. In *Proceedings of the 32nd International Electric Propulsion Conference*, pages IEPC–2011–144, Wiesbaden, Germany, 2011. Electric Rocket Propulsion Society.

[175] F. Guarducci, M. Coletti, and S. Gabriel. Design and testing of a micro pulsed plasma thruster for CubeSat application. In *Proceedings of the 32nd International Electric Propulsion Conference*, pages IEPC–2011–239, Wiesbaden, Germany, 2011. Electric Rocket Propulsion Society.

[176] S. Ciaralli, M. Coletti, and S. Gabriel. Qualification of a pulsed plasma thruster for cubesat propulsion (PPTCUP). In *Proceedings of the 34th International Electric Propulsion Conference*, pages IEPC–2015–208, Hyogo-Kobe, Japan, 2015. Electric Rocket Propulsion Society.

[177] S. Pottinger and C. Scharlemann. Micro pulsed plasma thruster development. In *Proceedings of the 30th International Electric Propulsion Conference*, pages IEPC–2007–125, Florence, Italy, 2007. Electric Rocket Propulsion Society.

[178] D. Krejci, B. Seifert, and C. Scharlemann. Endurance testing of a pulsed plasma thruster for nanosatellites. *Acta Astronautica*, 91:187 – 193, 2013.

[179] C. Scharlemann, M. Tajmar, I. Vasiljevich, N. Buldrini, D. Krejci, and B. Seifert. Propulsion for nanosatellites. In *Proceedings of the 32nd International Electric Propulsion Conference*, pages IEPC–2011–171, Wiesbaden, Germany, 2011. Electric Rocket Propulsion Society.

[180] W. Ling, H. Koizumi, and T. Schönherr. Use of liquid propellants in pulsed plasma thrusters for small satellites. In *Proceedings of the 34th International Electric Propulsion Conference*, pages IEPC–2015–139, Hyogo-Kobe, Japan, 2015. Electric Rocket Propulsion Society.

[181] E. Ahedo and J Gallardo. Scaling down hall thrusters. In *Proceedings of the 28th International Electric Propulsion Conference*, pages IEPC–2003–104, Toulouse, France, 2003. Electric Rocket Propulsion Society.

[182] K. Dannenmayer and S. Mazouffre. Elementary scaling laws for sizing up and down hall effect thrusters: Impact of simplifying assumptions. In *Proceedings of the 31st International Electric Propulsion Conference*, pages IEPC–2009–077, Ann Arbor, USA, 2009. Electric Rocket Propulsion Society.

[183] M. Dabiri, M. Dudeck, M. Guyot, S. Barral, and J. Kurzyna. Plasma properties inside a small hall effect thruster. In *Proceedings of the 33rd International Electric Propulsion Conference*, pages IEPC–2013–415, Washington DC, USA, 2013. Electric Rocket Propulsion Society.

[184] R. Conversano, D. Goebel, R. Hofer, T. Matlock, and R. Wirz. Magnetically shielded miniature hall thruster: Development and initial testing. In *Proceedings of the 33rd International Electric Propulsion Conference*, pages IEPC–2013–201, Washington DC, USA, 2013. Electric Rocket Propulsion Society.

[185] R. Conversano, D. Goebel, R. Hofer, I. Mikellides, I. Katz, and R. Wirz. Magnetically shielded miniature hall thruster: Design improvement and performance analysis. In *Proceedings of the 34th International Electric Propulsion Conference*, pages IEPC–2015–100, Hyogo-Kobe, Japan, 2015. Electric Rocket Propulsion Society.

[186] R. Eytan, D. Lev, G. Alon, A. Warshavsky, A. Kapulkin, and M. Rubanovitz. Wall material selection process for cam200 low power hall thruster. In *Proceedings of the 34th International Electric Propulsion Conference*, pages IEPC–2015–103, Hyogo-Kobe, Japan, 2015. Electric Rocket Propulsion Society.

[187] A. Leufroy, T. Gibert, and A. Bouchoule. Characteristics of a permanent magnet low power hall thruster. In *Proceedings of the 31st International Electric Propulsion Conference*, pages IEPC–2009–083, Ann Arbor, USA, 2009. Electric Rocket Propulsion Society.

[188] A. Loyan and T. Maksymenko. Performance investigation of SPT-20M low power hall effect thruster. In *Proceedings of the 30th International Electric Propulsion Conference*, pages IEPC–2007–100, Florence, Italy, 2007. Electric Rocket Propulsion Society.

[189] M. Titov, A. Loyan, O. Rybalov, and T. Maksymenko. The comparison of results of tests of low-power hall thrusters: SPT and TAL. In *Proceedings of the 32nd International Electric Propulsion Conference*, pages IEPC–2011–199, Wiesbaden, Germany, 2011. Electric Rocket Propulsion Society.

[190] T. Ikeda, K. Togawa, T. Nishida, and H. Tahara. Research and development of very low power cylindrical hall thrusters for nano-satellites. In *Proceedings of the 32nd International Electric Propulsion Conference*, pages IEPC–2011–039, Wiesbaden, Germany, 2011. Electric Rocket Propulsion Society.

[191] T. Ikeda, Y. Mito, M. Nishida, T. Kagota, T. Kawamura, and H. Tahara. Development of low-power cylindrical type hall thrusters for nano satellite. In *Proceedings of the 33rd International Electric Propulsion Conference*, pages IEPC–2013–109, Washingto DC, USA, 2013. Electric Rocket Propulsion Society.

[192] T. Kakuma, T. Ikeda, M. Nishida, T. Kagota, Y. Takahata, and H. Tahara. Research and development of low-power cylindrical-type hall thrusters for nano/microsatellites. In *Proceedings of the 34th International Electric Propulsion Conference*, pages IEPC–2015–302, Hyogo-Kobe, Japan, 2015. Electric Rocket Propulsion Society.

[193] M. Gamero-Castaño and V. Hruby. Characterization of a colloid thruster performing in the micro-newton thrust range. In *Proceedings of the 27th International Electric Propulsion Conference*, pages IEPC–2001–282, Pasadena, USA, 2001. Electric Rocket Propulsion Society.

[194] K. Huhn, M. Piechotka, T. Henning, and P. Klar. Investigation of the emission behavior of miniaturized SU-8 based colloid emitters. In *Proceedings of the 33rd International Electric Propulsion Conference*, pages IEPC–2013–141, Washington DC, USA, 2013. Electric Rocket Propulsion Society.

[195] R. Krpoun, M. Räber, H. Shea, K. Smith, and J. Stark. Design and fabrication of an integrated MEMS-based colloid micropropulsion system. In *Proceedings of the 30th International Electric Propulsion Conference*, pages IEPC–2007–099, Florence, Italy, 2007. Electric Rocket Propulsion Society.

[196] P. Lozano, B. Glass, and M. Martinez-Sanchez. Performance characteristics of a linear ionic liquid electrospray thruster. In *Proceedings of the 29th International Electric Propulsion Conference*, pages IEPC–2005–192, Princeton, USA, 2005. Electric Rocket Propulsion Society.

[197] K. Smith, M. Alexander, M. Paine, and J. Stark. Scaling of a colloid thruster system for micronewton to millinewton thrust levels. In *Proceedings of the 30th International Electric Propulsion Conference*, pages IEPC–2007–112, Florence, Italy, 2007. Electric Rocket Propulsion Society.

[198] K. Smith, J. Stark, R. Krpoun, and H. Shea. Performance of a micro-fabricated colloid thruster system. In *Proceedings of the 31st International Electric Propulsion Conference*, pages IEPC–2009–189, Ann Arbor, USA, 2009. Electric Rocket Propulsion Society.

[199] I. Funaki, Y. Nakayama, H. Horisawa, and M. Ando. Micro-thruster options for the Japanese space gravitational wave observatory missions. In *Proceedings of the 32nd International Electric Propulsion Conference*, pages IEPC–2011–308, Wiesbaden, Germany, 2011. Electric Rocket Propulsion Society.

[200] M. Capacci, G. Matticari, M. Materassi, E. Artina, and V. Vettorello. Electric propulsion diagnostic package for the FEEP thruster on LISA path finder: Review of status of achievements at TAS-1. In *Proceedings of the 30th International Electric Propulsion Conference*, pages IEPC–2007–150, Florence, Italy, 2007. Electric Rocket Propulsion Society.

[201] C. Scharlemann, A. Genovese, R. Schnitzer, N. Buldrini, P. Sattler, M. Tajmar, R. Killinger, and H. Früholz. Test results of the qualification tests for the In-FEEP technology for LISA PF. In *Proceedings of the 31st International Electric Propulsion Conference*, pages IEPC–2009–50, Ann Arbor, USA, 2009. Electric Rocket Propulsion Society.

[202] L. Ceruti, A. Antimiani, and A. Polli. Power control unit for μN FEEP propulsion subsystem. In *Proceedings of the 30th International Electric Propulsion Conference*, pages IEPC–2007–283, Florence, Italy, 2007. Electric Rocket Propulsion Society.

[203] C. Scharlemann, A. Genovese, N. Buldrini, R. Schnitzer, M. Tajmar, H. Frholz, and R. Killinger. Status of the indium FEEP micropropulsion subsystem development for LISA pathfinder. In *Proceedings of the 30th International Electric Propulsion*

Conference, pages IEPC–2007–122, Florence, Italy, 2007. Electric Rocket Propulsion Society.

[204] J. Makela and L. King. Progress on re-generable field emission cathodes for low-power electric propulsion. In *Proceedings of the 30th International Electric Propulsion Conference*, pages IEPC–2007–152, Florence, Italy, 2007. Electric Rocket Propulsion Society.

[205] A. Reissner, N. Buldrini, B. Seifert, F. Plesescu, C. Scharlemann, and J. Gonzales del Amo. mN-FEEP thruster module design and preliminary performance testing. In *Proceedings of the 33rd International Electric Propulsion Conference*, pages IEPC–2013–207, Washington DC, USA, 2013. Electric Rocket Propulsion Society.

[206] D. Bock, A. Kramer, P. Bangert, K. Schilling, and M. Tajmar. NanoFEEP on UWE platform - formation flying of cubesats using miniaturized field emission electric propulsion thrusters. In *Proceedings of the 34th International Electric Propulsion Conference*, pages IEPC–2015–121, Hyogo-Kobe, Japan, 2015. Electric Rocket Propulsion Society.

[207] C. Phipps, J. Luke, T. Lippert, M. Hauer, and A. Wokaun. Micropropulsion using laser ablation. *Applied Physics A*, 79:1385 – 1389, 2004.

[208] S. Yokoyama, H. Horisawa, I. Funaki, and H. Kuninaka. Fundamental study of laser micro propulsion using powdered-propellant. In *Proceedings of the 33rd International Electric Propulsion Conference*, pages IEPC–2013–207, Washington DC, USA, 2013. Electric Rocket Propulsion Society.

[209] H. Tahara. Research and development of compact laser ablative thrusters for small satellites. In *Proceedings of the 30th International Electric Propulsion Conference*, pages IEPC–2007–339, Florence, Italy, 2007. Electric Rocket Propulsion Society.

[210] H. Yonamine, K. Hagiwara, H. Horisawa, Y. Oshio, H. Sato, and I. Funaki. Experimental investigation on CW laser microthruster. In *Proceedings of the 32nd International Electric Propulsion Conference*, pages IEPC–2011–320, Wiesbaden, Germany, 2011. Electric Rocket Propulsion Society.

[211] T. Sakai, A. Osamura, and H. Horisawa. Characteristics of a laser-electrostatic hybrid propulsion system. In *Proceedings of the 33rd International Electric Propulsion Conference*, pages IEPC–2013–260, Washington DC, USA, 2013. Electric Rocket Propulsion Society.

[212] S. Scharring, S. Karg, R. Lorbeer, N. Dahms, and H. Eckel. Low-noise thrust generation by laser-ablative micropropulsion. In *Proceedings of the 34th International Electric Propulsion Conference*, pages IEPC–2015–143, Hyogo-Kobe, Japan, 2015. Electric Rocket Propulsion Society.

[213] T. Zhuang, A. Shashurin, L. Brieda, and M. Keidar. Development of micro-vacuum arc thruster with extended lifetime. In *Proceedings of the 31st International Electric Propulsion Conference*, pages IEPC–2009–192, Ann Arbor, USA, 2009. Electric Rocket Propulsion Society.

[214] T. Suaris and M. Keidar. Analysis of micro-vacuum arc thrusters for earth-orbiting and lunar missions. In *Proceedings of the 32nd International Electric Propulsion Conference*, pages IEPC–2011–031, Wiesbaden, Germany, 2011. Electric Rocket Propulsion Society.

[215] S. Haque, M. Keidar, and T. Lee. Low-thrust orbital maneuver analysis for CubeSat spacecraft with a micro-cathode arc thruster subsystem. In *Proceedings of the 33rd International Electric Propulsion Conference*, pages IEPC–2013–365, Washington DC, USA, 2013. Electric Rocket Propulsion Society.

[216] L. Brieda and M. Keidar. Numerical studies of micro-cathode arc thruster plume expansion. In *Proceedings of the 34th International Electric Propulsion Conference*, pages IEPC–2015–57, Hyogo-Kobe, Japan, 2015. Electric Rocket Propulsion Society.

[217] G. Teel, J. Lukas, A. Shashurin, and M. Keidar. Analysis of ignition of the micro cathode arc thruster. In *Proceedings of the 34th International Electric Propulsion Conference*, pages IEPC–2015–53, Hyogo-Kobe, Japan, 2015. Electric Rocket Propulsion Society.

[218] M. Pietzka, S. Kirner, M. Kauffeldt, C. Arens, J. Marques-Lopez, G. Forster, and J. Schein. Development of vacuum arc thrusters and diagnostic tools. In *Proceedings of the 32nd International Electric Propulsion Conference*, pages IEPC–2011–080, Wiesbaden, Germany, 2011. Electric Rocket Propulsion Society.

[219] M. Pietzka, M. Kühn-Kauffeldt, J. Schein, I. Kronhaus, K. Schilling, T. Mai, and A. Lebeda. Innovative vacuum arc thruster for cubesat constellations. In *Proceedings of the 33rd International Electric Propulsion Conference*, pages IEPC–2013–306, Washington DC, USA, 2013. Electric Rocket Propulsion Society.

[220] S. Fuchikami, M. Nakamoto, K. Toyoda, and M. Cho. Development of vacuum arc thruster for nanosatellite. In *Proceedings of the 33rd International Electric Propulsion Conference*, pages IEPC–2013–264, Washington DC, USA, 2013. Electric Rocket Propulsion Society.

A. Appendix - Electric Micropropulsion: Latest Developments to Date

This appendix contains a brief summary of some of the latest developments in mainstream micropropulsion systems. There are other novel systems that are not mentioned here, due to them still being in early development.

A.1. Ion Thrusters

Testing of miniaturized GITs has been initiated by numerous academic and industrial research groups, that have completed the conceptual phase of thruster development. Astrium Satellites based in Germany, is developing a system called the RIT-μX [45]. In this thruster, propellant gas is ionized and accelerated using radio frequency electron acceleration, which requires no external magnetic field for electron confinement. The RIT-μX has been able to achieve specific impulses ranging between 500 s and 3500 s, and a thrust range of 40 μN to 718 μN, with a power consumption in the range of 10 W to 70 W [151], in performance tests. These experimental results show a great improvement over the original calculated values for the system [45]. The laser interferometer space antenna (LISA) mission is a proposed, space-based, gravitational wave detector and in 2013, the complete RIT-μX thruster, having a mass of 500 g and operating at a mass flow rate of 5 μg/s, and its supporting subsystems, were tested by the ESA for viability as a propulsion system for the mission [152], [153]. The full system has moved onto the qualification phase, after being deemed suitable for fine attitude control. Giessen University in Germany is developing a similar system called μNRIT, which has been able to achieve thrusts between 200 μN and 500 μN, while obtaining fuel efficiencies between 29.9 % to 49.1 %, and specific impulses in the range of 1236 s and 2609 s. Mass flow rates ranging from 0.0047 sccm to 0.216 sccm were used, while performing measurements [109]. The thruster has a power consumption of 30 W, measures 2.5 cm in length, and has a mass of 210 g. Interactions between the plasma and neutral gas in this system have

been modelled using simulations. The results of these simulations will be used to aid in optimizing the system [154], [155].

A collaboration between the University of Southampton and QinetiQ, has resulted in a thruster that utilizes a radio frequency electric field to ionize xenon propellant. The thruster has been called MiDGIT. Precision thrust is generated by the system, using the differential control of opposing ion beams. Thrusts in the range of 200 μN to 480 μN have been measured using a breadboard system, at mass flow rates of between 0.03 mg/s and 0.05 mg/s, and power consumptions of between 22 W and 29 W [156].

Magnetic cusps are being used to circumvent the ionization issues with conventional, miniaturized Kaufman-type GITs. Attempts have been made to calculate the upper limits of the specific impulse and thrust that can be achieved with such a system. These values were determined to be 990 s and 500 μN respectively, using a mass flow rate of 0.48 sccm and power consumption values of between 20 W and 40 W. Additionally, the system was found to have a fuel efficiency of 88 % [157]

Theoretical and experimental studies of the fundamental properties of microwave induced plasma sources for GITs, are being conducted at Kyushu University [46]. The system under study was operated at a mass flow rate of 20 μg/s and a power of 8 W, and was able to obtain thrusts of 740 μN and a specific impulse of 7588 s

Both microwave and radio frequency ion thrusters are currently being researched at Pennsylvania State University, in the USA. A 1 cm long thruster has been studied experimentally and computationally. By running the system at mass flow rates of between 0.02 sccm and 0.1 sccm, a specific impulse of 5480 s and a thrust of 59 μN were achieved, with power consumptions as low as 13 W. Poor electrical efficiency has reduced the overall efficiency of the system, despite being able to achieve a propellant efficiency of just under 80% [158]. Experimental studies on the microwave ion thruster has yielded a fuel efficiency and a thrust of 46 % and 217 μN respectively, while consuming 8 W of power at mass flow rates ranging from 0.01 sccm to 1 sccm [47].

Unipolar and bipolar microwave based, ion thrusters have been studied in an attempt to create novel effects. In unipolar operation, external spacecraft surface charging is prevented by using a single thruster, in conjunction with a conventional neutraliser. In bipolar operation, external spacecraft surface charging is prevented, by using a second thruster, which is configured to generated electrons to replace the neutraliser. With a power consumption of 15.1 W, a bipolar thruster configuration was able to achieve a specific impulse of 1100 s and a thrust of 297 μN. When operating the system in a unipolar configuration, a greater thrust and specific impulse were obtained (379 μN and

1410 s respectively), but at the cost of a higher power consumption of 19.9 W. The fuel efficiency of the system was found to be 37 %, at a mass flow rate of 14.6 μg/s [159]. A number of techniques are being used to try to develop a greater understanding of how the plasma is generated in the system, to improve the thrust generated. These techniques include, numerical simulation [160], laser absorption spectroscopy [161] and optical fibre probes [162].

The charging of the external surfaces of CubeSats by electric propulsion systems (specifically miniturized GITs), is being studied at the Western Michigan University, in the USA. Tests showed that there was some evidence of high energy neutrals at large divergence angles, which could degrade and damage the surface of the CubeSat [163]

At the University of Tokyo, numerical simulations are being conducted to study the erosion effects of the extraction and acceleration grids in miniature GITs. The study showed that erosion effects have a drastic effect on performance. However, the system under study would still meet lifetime requirements [164].

At Busek Co. Inc. in the USA, a miniaturized radio frequency GIT is being developed called the BIT-3. This is due to its 3 cm diameter grids. The thruster is suitable for use on CubeSats, as it is able to generate thrusts up to 1.35 mN, with a specific impulse of 3200 s. The system consumes 60 W of power and operates with a thrust efficiency of approximately 35 % [165]

A more comprehensive review of some of the specifics of miniaturized GIT technologies and mission capabilities can be found elsewhere [166].

A.2. Pulsed Plasma Thrusters

The PROITERES program was originally designed as a platform to test the technology to be used in microspacecraft, and as of 2013, the Osaka Institute of technology, in Japan, has included an electrothermal PPT in the program [167]. The program's first satellite included the thruster as a test system, and design improvements for the second satellite are in progress [168]. Using both computational and experimental data, maximum impulse bits of 2.5 Ns were predicted [169]. The latests experimental and numerical results obtained from the thruster to be used on the second satellite, have shown the system produces impulse bits of between 1794 μNs and 2600 μNs, with specific impulses between 352 s and 464 s. The thrust efficiencies the system was able to achieve were between 12 % and 14 % [170], [171].

A collaboration between the University of Southampton, in the UK, Mars Space Ltd and Clyde Space Ltd, has resulted in the development of a two stage PPT, with a mass of 350 g, for CubeSat applications. The second stage will add a redundancy to the system, while also allowing for the lifetime of CubeSat missions to be extended [172]. The system has been deemed suitable for CubeSat missions using computational [173], theoretical [174] and experimental [175] data. Using this information, a specific impulse of 640 s at a power consumption of 5 W, was obtained for the system, which is 16 % higher than the required amount [107]. The system is currently undergoing qualification testing [176].

In an attempt to increase the lifetime of microspacecraft, the Research Institute of Applied Mechanics and Electrodynamics in Moscow is engaged developing an ablative pulsed plasma thruster, as part of a microspacecraft attitude control system. The system was able to achieve a thrust efficiency of 15 %, and thrusts of 850 μN, by consuming 33 W of power. [108].

By using the geometric scaling laws of PPTs, researchers at the Austrian Research Center are attempting to determine optimal strategies for the miniaturization of conventional PPTs [177]. A number of different PPT systems are being developed in Austria, including a 1.7 Ns impulse bit coaxial system, which has a lifetime of up to 1 million discharges, as well as an average mass bit of 0.37 μg/s and a specific impulse of 904 s [178]. A miniaturized prototype system is also being developed, which is small enough to have 4 thrusters installed on a single printed circuit board [179].

A research group at the University of Tokyo is exploring the use of liquid propellants in PPTs, via two separate mechanisms: a PPT fuelled with a non-volatile propellant, and a PPT fuelled with a volatile propellant, where the propellant delivery system is aided with the use of an electrospray system. The first technique has the added benefit of not requiring complex feeding systems needed by solid propellant PPTs, whereas the second technique allows for the direct control of each mass shot [180].

A.3. Hall Thrusters

Currently, a series of scaling laws for Hall thrusters have been developed, and are providing good predictions when compared with experimental results for Hall thruster miniaturization [181], [182]. Miniaturized Hall thrusters are also being studied using numerical simulations, but the results of this work have yet to be compared with experiment [183].

The lifetime of the 4 cm thruster being developed at the University of California, was

greatly improved by using magnetic shielding of the discharge chamber. This is indicated by a 3 order of magnitude reduction in the erosion rates. The specific impulse of the system was found to be 1870 s, with a thrust of 19 mN. A total system efficiency was found to be 43 %, at a power consumption of 325 W [184]. In an attempt to improve performance and efficiency, the same magnetic shielding techniques were applied to a 6 cm Hall thruster design. By operating at powers ranging from 160 W to 750 W and mass flow rates ranging from 12 sccm to 28 sccm, the 6 cm thruster was able to produce thrusts of between 8 mN and 33 mN, with specific impulses between 730 s and 1370 s and anode efficiencies of between 21 % and 29 % [185].

A number of different construction materials are being considered for the CAM200 Low Power Hall Thruster, being developed by Rafael Advanced Defense Systems Ltd and the Israel Institute of Technology. Different materials are being considered to help improve erosion characteristics of the thruster. M26-BN was found to be the optimal material studied as, while it didn't offer any noticeable performance increase, it experienced no dimension reduction when compared to the other materials studied [186].

Small permanent magnets are being used, instead of electromagnets, to generate the magnetic field required for Hall thrusters at The GREMI laboratory at the Orléans University, France. This reduces the power consumption and mass of the system, by limiting the power processing circuitry required. Thrusts of between 4 mN and 18 mN were obtained by a proof of concept system, operating at mass flow rates of between 0.8 mg/s and 1.6 mg/s, and powers of between 50 W and 300 W [187].

A miniature Hall thruster with a total system mass of 260 g, is currently being developed at the National Aerospace University in the Ukraine. While operating at a mass flow rate of 0.4 mg/s and consuming 100 W of power, the system was able to achieve a thrust efficiency of 38 %, while generating a thrust of 4 mN, and a specific impulse of 1400 s. The predicted lifetime of the system is quoted to be 1000 hours [188]. Miniature versions of a conventional stationary plasma thruster (SPT), and a thruster with an anode layer (TAL) have been compared at the National Aerospace University, and the TAL was able to achieve a total efficiency of 18 % by consuming between 25 W and 150 W of power and with mass flow rates between 0.2 mg/s and 0.34 mg/s. This efficiency was obtained while generating thrusts of up to 3 mN with a specific impulse of 1200 s [189].

A cylindrical Hall thruster, designed to be operated at powers as low as 10 W, is being studied at the Osaka Institute of Technology, in Japan [190]. By consuming 115 W of power and using mass flow rates of between 0.6 mg/s and 0.8 mg/s, a thrust efficiency of 19.5 % was obtained, while generating thrusts of up to 7.3 mN and a specific impulse of 940s [191]. A cylindrical Hall thruster is also being developed at the Osaka Institute of

Technology, as the propulsion system for the third satellite in the PROITERS program. The thruster is able to achieve thrusts in the range of 1.1 mN to 5 mN, with a specific impulse of between 366 s and 1853 s. For input powers in the range of 23 W to 163 W, the system is able to obtain thrust efficiencies between 8.6 % and 34 % [192].

A.4. Colloid Thrusters

An array of microfabricated colloid thrusters is currently under development at Busek Co. Inc. in the USA. For mass flow rates in the range of 0.159 mg/s and 0.005 mg/s, the thruster array can obtain fuel efficiencies of between 85 % and 70 %, and can produce thrusts between 20 μN to 189 μN, with a maximum specific impulse of 389 s. The variances in these values come from altering the propellant, or the number of thrusters in the array [193]. This thruster array system is being developed with the technology requirements of large space missions, like LISA, in mind [51].

Colloid thrusters require the use of high voltages to operate effectively, and this is problematic when considering construction materials for the thruster. Initial designs incorporated silicon as a construction material, which can experience electrical breakdown at these voltages. Epoxy polymers, such as SU-8, are being tested at the Institute of Experimental Physics in Germany, as potential replacement construction materials. Tests have shown how positive species of the ionic liquid EMI-BF_4, could be extracted from an emitter made from this material [194].

Thruster array geometry is yet another important thruster performance influencing factor. A MEMS based system, configured into a variety of different geometries, is currently under study by a collaboration between the Ecole Polytechnique Fédérale de Lausanne, in Switzerland, and the Queen Mary University of London, in the UK. The IV characteristics of the system can potentially be explained using a simple model proposed by the researchers [195]. This group is not the only team exploring different geometries, with MIT currently developing a flat linear arrangement of thrusters. This configuration is predicted to achieve thrusts in the range of 2 μN and 19 μN [196].

Unfortunately, some formation flying missions require thrust levels that are outside the range of the μN-thrust levels provided by colloid thrusters. Up-scaling of thruster systems may provide a solution to the problem. By increasing the number of colloid thrusters in a thruster array, researchers at the Queen Mary University of London in the UK have shown that larger thrust levels can be achieved. By increasing the number of microfabricated thrusters in an array, thrust ranges of between 0.5 μN to 10 mN can be

achieved, while operating at specific impulses of between 400 s to 1500 s. This makes colloid thrusters a realistic option as a propulsion system, for executing formation flying manoeuvres [197]. The researchers also performed tests on different varieties of colloid thruster, namely, commercially available electrospray emitters, and in-house developed microfabricated thrusters. By analysing these systems, two distinct modes of operation were discovered: a low specific impulse mode (with a specific impulse of 1178 s and a thrust of 442 μN), and a high specific impulse mode (with a specific impulse of 7570 s and a thrust of 25 μN). These results were obtained at a power consumption of 0.05 W/μN [198].

A.5. Field Emission Electric Propulsion

The LISA Pathfinder mission is a space test of all the technologies that have been selected to eventually be a part of the LISA mission. FEEP has been selected to be included in this project, as well as part of the Japanese Space Gravitational Wave Observatory [199]. This is because FEEP has already become an established technology in the field of micropropulsion. With any electric space propulsion system, a complex environment exists between the external surfaces of the spacecraft, emitted charged ions, and other space plasmas. As such, a diagnostic package has been designed to study this environment, with the inclusion of the FEEP system on the LISA Pathfinder mission [200]. A backup indium needle design is still being actively developed, in spite of the caesium slit thruster design being chosen to be included on the LISA Pathfinder project [201].

The power supply to be used in conjunction with the FEEP thruster on the LISA Pathfinder mission, is currently undergoing rigorous testing [202]. Astrium Space Transportation, in France, has collaborated with the Austrian Research Center, to build a breadboard version of the thruster, and measurements have shown that an electrical efficiency as high as 95 % can be obtained, and the system has a lifetime of over 3000 hours [203].

The dry mass of the current iteration of the thruster developed by ALTA SpA in Italy, is quoted as being 1.4 kg, and is able to generate thrusts between 0.1 μN and 150 μN. Also while consuming 6 W of power, the thruster is able to obtain specific impulses in the range of 3000 s to 4500 s [106].

Attempts to develop re-generatable field emission cathodes, are currently in the proof of concept phase at the Michigan University of Technology in the USA. These cathodes promise a significant improvement in performance [204].

FOTEC, in Austria, are currently developing a higher power FEEP system, based on an a indium crown needle emitter design. This design will be capable of generating thrusts of order mN. It is the hope that this system will find usage on future space missions, such as Next Generation Gravity Mission being planned by ESA [205].

A FEEP system, designed to be used on CubeSat formation flying missions, is being developed by the Institute of Aerospace Engineering, in Germany. The system is called NanoFEEP, and each thruster has a mass of 6 g, while using gallium as a propellant. The thruster has been able to generate thrusts of up to 22 μN of thrust, at a specific impulse of 1000 s [206].

A.6. Laser Ablation Thrusters

Much work is currently being done to establish the theoretical basis for the principle of operation of laser ablation thrusters. System performance is being predicted using simulations [207]. Photonics Associates, in New Mexico, are in the process of developing a test bed system, with a total system mass of 750 g. This system has produced thrusts of up to 680 μN, at a specific impulse of 400 s. With these parameters, a thrust efficiency of 8 % has been achieved, as well as a thrust to power ratio of 75 μN/W. The lifetime of a single tape in the system is 1.8 hours. These tests have lead to the proposal of parameters for a commercial system [54]. Along with these tests, different laser powers [208] and different propellants [209] have been studied.

A variation of the thruster concept, where the mechanism of thrust production is still under study, is being developed at Tokai University, in Japan. In this thruster, a metallic aluminium propellant is used to obtain thrusts of up to 15 μN, with a laser power of 20 W. In these tests, no extreme ablation of the propellant has been observed [210].

It has been shown at Tokai University, that a dramatic increase in the ion velocity obtained from a conventional laser ablation thruster, is achieved with accelerating electrodes. This results in an increase in measured thrust [211].

At the German Aerospace Center, a novel laser ablation based micropropulsion system is under study. This system is advantageous, in that it lacks moving parts, and generates thrust using high intensity laser pulses to ablate the propellant material. Experimental tests and theoretical calculations have shown the 15 μN/W can be achieved with this system[212].

A.7. Vacuum Arc Thrusters

The effect of magnetic fields on VAT performance, is currently being studied at the George Washington University, in the USA. A 50-fold improvement in performance was measured, when a magnetic field was included in thruster operation, when compared to tests without one [213]. When compared with experimental data, numerical simulations showed good agreement, and VATs can be considered as a viable propulsion system for use on nanosatellites [214], [215], [216]. A series of tests to develop a greater understanding of the triggering process in VATs, are currently under way at the George Washington University. These tests will hopefully allow for the lifetime of VATs to be extended [217].

The University of the Federal Armed Forces, in Germany, are in the process of upgrading their facilities so that they can perform diagnostics tests on VATs. Some of the tests that can already be performed at the institute include: computer tomography, direct thrust measurements and high speed imaging [218]. Work to improve the lifetime of thrusters being studied at the institute is being done concurrently [219].

The UWE-4 iU CubeSat mission, which will be used to test formation flying in CubeSats, will use VATs as the propulsion system as of 2013. VATs were chosen due to their ability to acurately resolve low thrusts (1 μN - 2 μN), as well as achieve specific impulse values of 1000 s at a low mass of 200 g [104].

Cathode shape has a large impact on the thrust properties of VATs, and this effect is being studied at the University of the Witwatersrand, South Africa. Three different cathode material were used in manufacturing the new conical shapes, which were found to increase thruster performance. However, the underlying mechanism behind this improvement in thrust is still unknown. Specific impulses of up to 440 s were obtained, using power ranges of between 1 W and 20 W [105].

The Kyushu Institute of Technology, in Japan, is currently working to measure the plasma plume velocity (which was found to be 12 km/s), and impulse bit (which was found to be of the order of μNs) of a VAT [220].

B. Appendix - Theoretical Model of Thrust Balance

This appendix contains a detailed account of the development of the theoretical model, used to understand the principle of operation of the thrust measurement stand that was developed in this work.

A free body analysis is performed in order to model the thrust stand. This entails considering the thrust stand, while taking a measurement and pinpointing and explaining all of the forces acting on the thrust stand. When the thrust stand is in it final equilibrium position, the moments corresponding to the forces can be calculated, and the angular displacement of the thrust support member can be related to the measured thrust. Figure B.1 depicts a copy of the free body diagram of the balance with all of the identified forces.

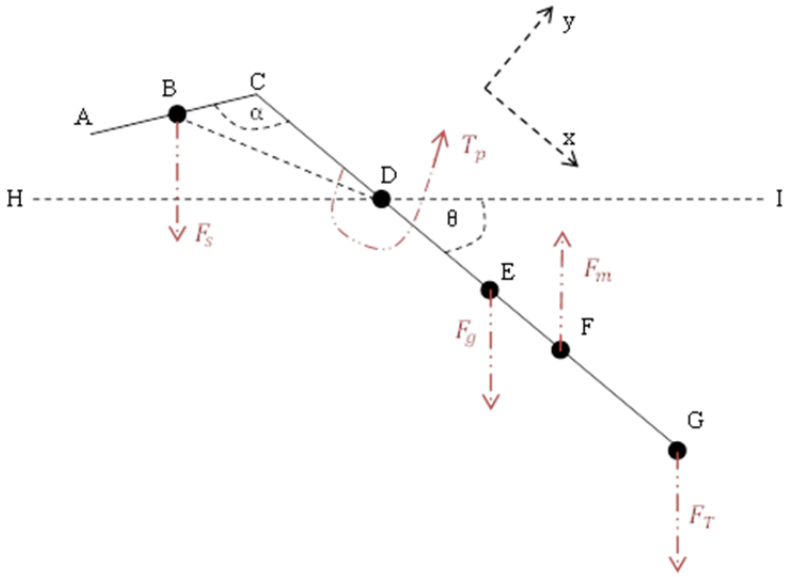

Figure B.1.: A reprint of the free body diagram of the thrust balance showing all of the forces considered.

Point F is taken to be the point inside the thrust support member, where the coupling magnet is mounted. Point D is taken to be the fulcrum of the thrust support member (the lever arm). Point G is taken to be the the point of attachment of the thruster on the mounting table. Point E is taken to be the center of gravity of the thrust support member. The center of gravity is made to coincide with the center of mass of the thrust support member, as it can be approximated as a uniform rod. However, the thrust support member has been non-uniformly weight relieved, and so the center of mass is shifted away from the center of the rod and closer to the fulcrum. Point B is taken to be the center of gravity of the magnetic induction damper. This is taken to be the center of mass of the magnetic induction damper, as it can be approximated as a uniform rod. The line segment HI is taken to be the initial equilibrium position of the thrust support member. The y-axis is taken to be perpendicular to the thrust support member, and the x-axis is taken to be parallel to the thrust support member.

All of the moments acting on the system must balance when it is in static equilibrium, and therefore this is assumed to be its final state. $\vec{T_p}$ is the nulling torque exerted by the fulcrum point. $\vec{F_s}$ is the force of gravity acting on the magnetic induction damper. $\vec{F_m}$ is the force of repulsion exerted by the two coupling magnets. $\vec{F_g}$ is the force of gravity acting on the thrust support member, and $\vec{F_T}$ is the thrust to be measured. For this analysis, the weight of the calibration mass is substituted for the thrust and therefore, will always act downwards. The impact of thrust generated from an actual thruster, can be modelled with the modification that the force $\vec{F_T}$, is made to always be perpendicular to the thrust support member.

The angle that the thrust support member moves through, under the influence of the thruster, is called θ. This angle will be measured when all of the moments balance, and the thrust support member reaches its equilibrium position. The angle between the thrust support member and the magnetic induction damper, is called α, and remains constant throughout a measurement.

The moments generated by the forces can be calculated, now that all the forces, angles and points have been identified. All symbols retain the meanings described previously. The fulcrum point is approximated as a torsion spring, and this allows the magnitude of the moment $\vec{T_p}$ to be calculated:

$$T_p = k\theta \tag{B.1}$$

All other moments are obtained by multiplying the magnitude of the force, with the

perpendicular distance between the fulcrum and the point of action of the force. The magnitude of the moment $\vec{T_T}$ generated by the force $\vec{F_T}$ is:

$$T_T = F_T d_3 \cos(\theta) \tag{B.2}$$

The magnitude of the moment $\vec{T_m}$, generated by the force $\vec{F_m}$ is:

$$T_m = M_m g d_2 \cos(\theta) \tag{B.3}$$

The magnitude of the moment $\vec{T_g}$, generated by the force $\vec{F_g}$ is:

$$T_g = m_a g d_1 \cos(\theta) \tag{B.4}$$

The magnitude of the final moment T_s, generated by the force F_s must be calculated from the more general definition of a moment's magnitude, given by:

$$T = rF \sin(\phi) \tag{B.5}$$

where F is the magnitude of the applied force, T is the magnitude of the applied moment, ϕ is the angle between the vector $\vec{r}$ and the vector $\vec{F}$, and r is the magnitude of the position vector connecting the point where the force is applied and the point about which the moment acts.

Equation B.6 shows how the magnitude of the force $\vec{F_s}$ is easily obtained:

$$F_s = m_b g \tag{B.6}$$

The triangle $\triangle BCD$ is considered when calculating r. The Cosine Rule is applied to obtain the required line segment BD, which is shown in Equation B.7:

$$|r| = z = \sqrt{\left(\frac{1}{2}AC\right)^2 + CD^2 - \left(\frac{1}{2}AC\right)(CD)\cos(\alpha)} \tag{B.7}$$

By first visualizing $\vec{F_s}$ at the fulcrum point, the angle ϕ can be obtained. The angle ϕ can then be found to be the sum of the angle $B\widehat{D}H$ and $\frac{\pi}{2}$. Equation B.8 shows how the angle $B\widehat{D}H$ can be calculated:

$$B\widehat{D}H = \theta - B\widehat{D}C \tag{B.8}$$

Equation B.9 shows how the Sine rule can be used to calculate $B\widehat{D}C$:

$$B\widehat{D}C = \arcsin\left(\frac{1}{2}AC\left(\frac{\sin(\alpha)}{z}\right)\right) \tag{B.9}$$

An expression for the angle ϕ is shown in Equation B.10:

$$\phi = \gamma = \theta - \arcsin\left(\frac{1}{2}AC\left(\frac{\sin(\alpha)}{z}\right)\right) + \frac{\pi}{2} \tag{B.10}$$

This allows for a final expression for T_s to be obtained, as is shown in Equation B.11:

$$T_s = zm_b g\sin(\gamma) \tag{B.11}$$

Finally, by adding up all of the moments, equating them to zero, and rearranging the resulting expression, the final form of the model describing the behavior of the thrust stand can be obtained, as is shown in Equation B.12:

$$F_T(\theta) = \frac{k\theta + zm_b g\sin(\gamma) - m_a g d_1\cos(\theta) + d_2 g M_m\cos(\theta)}{d_3\cos(\theta)} \tag{B.12}$$

C. Appendix - Thrust Extraction

This appendix contains a description of the process followed to extract the thrust produced by the simulated 'U-shaped' electric microthruster.

The generalized thrust expression, developed using a conservation of momentum approach in [44], is applied to the simulation geometry, so that different thrust components can be extracted for the different species considered in the simulation. These thrust components are then summed, to determine both the hot gas thrust, and cold gas thrust under a variety of different operating parameters.

The generalized thrust expression, derived in [44] is given in Equation C.1:

$$\vec{F_T} = \iiint_{V_c} \vec{b} dV + \oiint_{\partial V_c} \rho \vec{v}([\vec{w} - \vec{v}] \cdot \hat{n}) dA + \oiint_{\partial V_c} \boldsymbol{\sigma} \cdot \hat{n} dA \tag{C.1}$$

where V_c is the volume enclosing the generalized body that is to be moved, $\vec{b}$ is a body force density or a vector momentum density, dV is a volume differential, ∂V_c is the boundary of the volume V_c, ρ is the mass density of the system, v is the propellant velocity, $\vec{w}$ is the velocity at which ∂V_c moves, $\hat{n}$ is the unit vector normal to ∂V_c, dA is an area differential and $\boldsymbol{\sigma}$ is the stress tensor.

The expression for the generalized thrust consists of three separate terms. The first term on the right hand side accounts for thrusts from body forces, or momentum sources in the volume V_c. The second term on the right hand side accounts for thrust from momentum flux across the boundary ∂V_c, relative to the velocity $\vec{w}$ at which the boundary moves. The third term on the right hand side accounts for thrusts from applied stresses over the boundary ∂V_c.

Body forces acting on the thruster, such as gravity and electromagnetic interactions, are neglected due to the negligible impact they have on the thrust produced. This means the first term on the right hand side of Equation C.1 can be dropped, and the generalized thrust expression becomes Equation C.2:

$$\vec{F_T} = \oiint_{\partial V_c} \rho\vec{v}([\vec{w} - \vec{v}\cdot]\hat{n})dA + \oiint_{\partial V_c} \boldsymbol{\sigma} \cdot \hat{n}dA \tag{C.2}$$

In the simulations considered here, the thruster is taken to be stationary. This means the relative velocity $\vec{w}$ can be taken to be zero in Equation C.2, and the generalized thrust expression becomes Equation C.3:

$$\vec{F_T} = \oiint_{\partial V_c} \rho\vec{v}(-\vec{v} \cdot \hat{n})dA + \oiint_{\partial V_c} \boldsymbol{\sigma} \cdot \hat{n}dA \tag{C.3}$$

First, the momentum flux component of Equation C.3 will be considered, and is given in Equation C.4:

$$\vec{F_{Tp}} = \oiint_{\partial V_c} \rho\vec{v}(-\vec{v} \cdot \hat{n})dA \tag{C.4}$$

There are four particle species under consideration in these simulations: argon ions, argon neutral atoms, excited, neutral argon atoms and electrons. Each of these species will be involved in momentum transfer, but the mass of the electrons is negligible when compared with the masses of the other species, so only the heavier species will be considered here. The momentum flux components of all the species must be summed, to obtain the total momentum transfer. Equation C.4 then becomes Equation C.5:

$$\vec{F_{Tp}} = \sum_s \oiint_{\partial V_c} \rho_s\vec{v}_s(-\vec{v}_s \cdot \hat{n})dA \tag{C.5}$$

where s represents each of the heavy particle species: argon ions (Ar^+), argon neutral atoms (Ar) and excited, neutral argon atoms (Ar^*).

Consider the boundary of the control volume under study. Figure C.1 depicts the simulation domain. The highlighted regions are considered to be the boundary of the control volume. Each of the boundaries are labelled: 1), 2) and 3). If a particle interacts with a boundary, the particles is lost, and is considered to be travelling away from the thruster. These lost particles are taken to have participated in momentum transfer. Each of these boundaries must be integrated over, and the results summed to obtain the total momentum contribution. Equation C.5 then becomes Equation C.6:

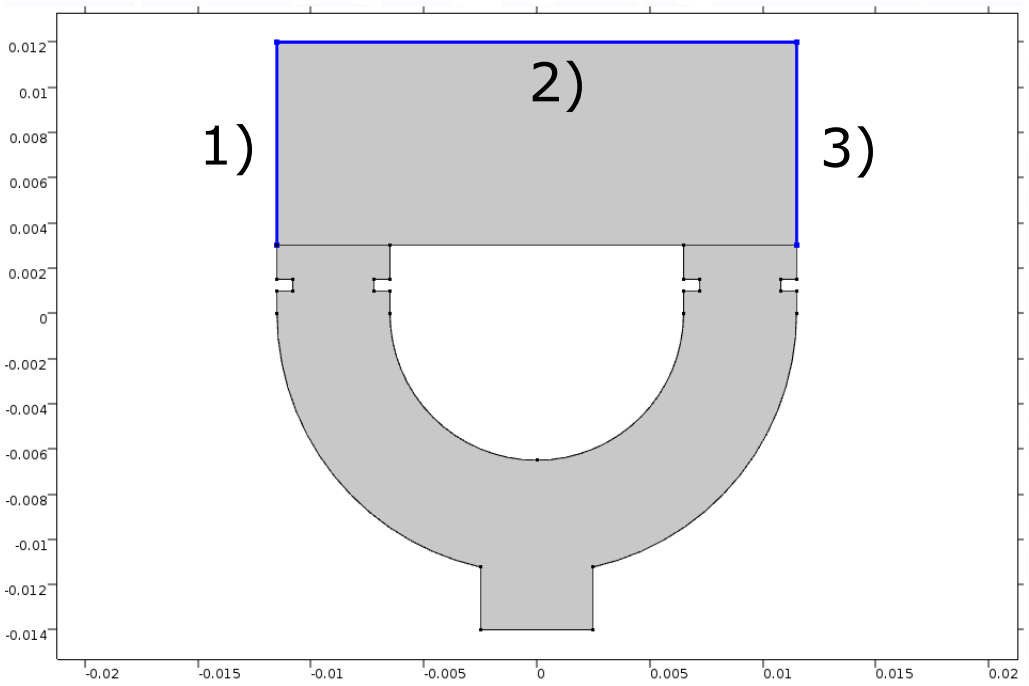

Figure C.1.: The simulation domain studied in this work. The highlighted regions represent the boundary of the control volume.

$$\vec{F_{Tp}} = \sum_b \sum_s \int_b \rho_s \vec{v}_s (-\vec{v}_s \cdot \hat{n}_b) dl \tag{C.6}$$

where b represents each of the boundaries that together enclose the control volume: 1), 2) and 3). Each of the unit vectors, $\hat{n}_b$, represents the unit outward normal of the corresponding surface. This means nine separate integrals must be solved, and summed, to obtain the total momentum flux thrust component.

When considering thrust, the component of greatest interest would be the component perpendicular to the thruster face. This component will propel the thruster in a straight line, without requiring additional control. The direction of this thrust component is parallel to the y-axis of the simulation. This means that this thrust component can be obtained, by considering the y-component of the respective particle species only. Equation C.6 then becomes Equation C.7:

$$F_{Tpy} = \sum_b \sum_s \int_b \rho_s v_{sy} (-\vec{v}_s \cdot \hat{n}_b) dl \tag{C.7}$$

Taking into account that the outward unit normals of boundaries 1) and 3) are perpen-

dicular to the y-component of the barycentric velocities, the resulting dot products in these integrals will result in zero. This means that all integrals over the boundaries 1) and 3) will result in a zero contribution to the momentum transfer thrust component. Equation C.7 then becomes Equation C.8:

$$F_{Tpy} = \sum_s \int_{2)} \rho_s v_{sy}(-\vec{v}_s \cdot \hat{n}_{2)})dl \tag{C.8}$$

Finally, the unit outward normal of the remaining boundary, 2), and the y-component of the barycentric velocities are in the same direction, so the momentum transfer component of the generalized thrust becomes the expression given in Equation C.9:

$$F_{Tpy} = \sum_s \int_{2)} -\rho_s v_{sy} v_{sy} dl \tag{C.9}$$

Now, the stress component of the thrust vector is considered. This is the third term on the right hand side of the generalized thrust expression, and is given in Equation C.10:

$$\vec{F_{Ts}} = \oiint_{\partial V_c} \boldsymbol{\sigma} \cdot \hat{n} dA \tag{C.10}$$

The stress considered in this work is the pressure exerted by the neutral argon atoms that leave the thruster exits. The boundaries over which the pressure is applied are the exits from which the gas and plasma escape, and are shown as the highlighted regions labelled 4) and 5) in Figure C.2.

The unit normals for boundaries 4) and 5) are directed in the positive y direction. Taking this into account, the stress component of thrust generation become the expression shown in Equation C.11:

$$\vec{F_{Ts}} = \sum_B \int_B (p_B - p_0)\hat{n}_B dl \tag{C.11}$$

where B represents each of the boundaries along which the pressure is considered: 4) and 5), p_B is the neutral argon gas pressure across boundary B and p_0 is the background pressure. Using this analysis, the total thrust generated by the simulated thruster can be determined, with the expression given in Equation C.12:

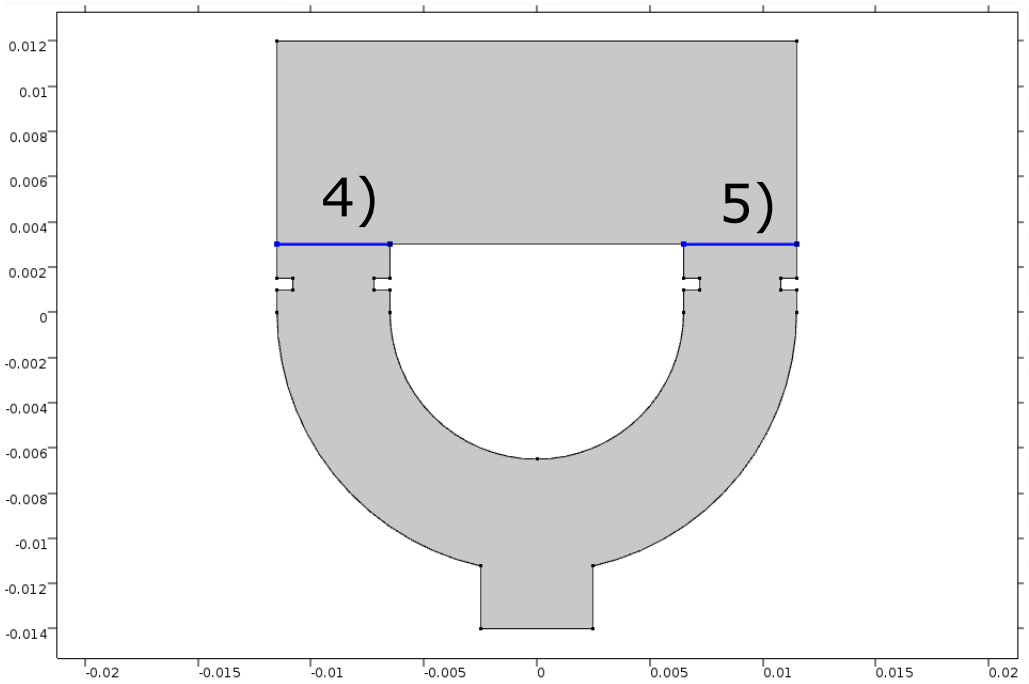

Figure C.2.: The simulation domain studied in this work. The highlighted regions represent the boundaries over which the pressure is considered

$$F_T = F_{Tpy} + F_{Ts} = \sum_s \int_{2)} -\rho_s v_{sy} v_{sy} dl + \sum_B \int_B (p_B - p_0)\hat{n}_B dl \tag{C.12}$$